REPORT NO.
UCB/EERC-97/10
NOVEMBER 1997

EARTHQUAKE ENGINEERING RESEARCH CENTER

PB99-106056

# FATIGUE LIFE EVALUATION OF CHANGEABLE MESSAGE SIGN STRUCTURES

## VOLUME 1: AS-BUILT SPECIMENS

by

AMIR S. GILANI
JUAN W. CHAVEZ
ANDREW S. WHITTAKER

Report to the California Department of Transportation
for Research under Contract RTA-59A131

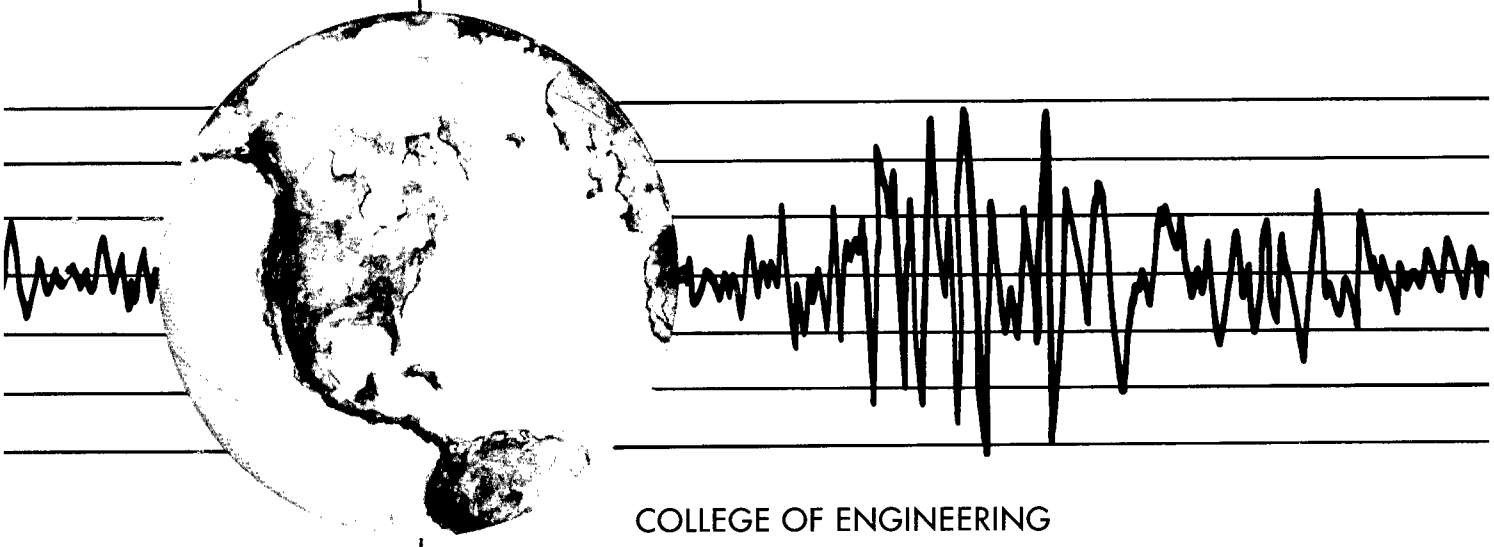

COLLEGE OF ENGINEERING

UNIVERSITY OF CALIFORNIA AT BERKELEY

REPRODUCED BY:
U.S. Department of Commerce
National Technical Information Service
Springfield, Virginia 22161

For sale by the National Technical Information Service, U.S. Department of Commerce, Springfield, Virginia 22161

See back of report for up to date listing of EERC reports.

DISCLAIMER

Any opinions, findings, and conclusions or recommendations expressed in this publication are those of the authors and do not necessarily reflect the views of the Sponsor or the Earthquake Engineering Research Center, University of California at Berkeley.

# FATIGUE LIFE EVALUATION OF CHANGEABLE MESSAGE SIGN STRUCTURES VOLUME 1: As-Built Specimens

by

Amir S. Gilani
Juan W. Chavez
and
Andrew S. Whittaker

Report No. UCB/EERC-97/10
Earthquake Engineering Research Center
College of Engineering
University of California at Berkeley

November, 1997

PROTECTED UNDER INTERNATIONAL COPYRIGHT
ALL RIGHTS RESERVED.
NATIONAL TECHNICAL INFORMATION SERVICE
U.S. DEPARTMENT OF COMMERCE

## Disclaimer

The contents of this report reflect the views of the authors who are responsible for the facts and the accuracy of data presented herein. The contents do not necessarily reflect the official views or policies of the State of California. The report does not constitute a standard, specification, or regulation.

**Technical Report Documentation Page**

| 1. Report No. | 2. Government Accession No. | 3. Recipients's Catalog No. |
|---|---|---|
| UCB/EERC-97/10 | | |

| 4. Title and Subtitle | 5. Report Date |
|---|---|
| Fatigue Life Evaluation of Changeable Message Sign Structures<br>Volume 1: As-Built Specimens | October 1997 |
| | **6. Performing Organization Code**<br>UCB ENG-8789 |
| **7. Authors**<br>Gilani, A.S., Chavez, J.W., and Whittaker, A.S. | **8. Performing Organization Report No.**<br>UCB/EERC-97/10 |
| **9. Performing Organization Name and Address**<br>Earthquake Engineering Research Center<br>University of California, Berkeley<br>1301 S. 46th Street; Richmond, California 94804 | **10. Work Unit No. (TRAIS)** |
| | **11. Contract or Grant No.**<br>RTA 59A131 |
| **12. Sponsoring Agency Name and Address**<br>California Department of Transportation<br>Division of Structures<br>1801 30th Street; Sacramento, California 95814 | **13. Type of Report and Period Covered**<br>Final, 4/1/96-10/31/97 |
| | **14. Sponsoring Agency Code**<br>RTA 59A131 |

**15. Supplementary Notes**

**16. Abstract**

This report outlines the research program undertaken at the Earthquake Engineering Research Center (EERC) to investigate the fatigue life of Changeable Message Structures (CMSs). These types of sign structures are inverted "L" shape structures, fabricated from steel pipe sections, and composed of a vertical (post) section that is connected to a horizontal (mast arm) section by a flanged connection. The sign structures are inherently flexible and have low structural damping.

Following the failure of one CMS structure in Southern California, field studies were undertaken that indicated that the groove-welded mast arm (post)-flange plate and post-base plate connections are susceptible to wind-induced fatigue cracking. Caltrans then identified seven topics for urgent study. This report addresses four of these topics: evaluation of the fatigue life of as-built connection details; assessment of the stress increase in CMS components adjacent to the conduit holes; estimation of the dynamic characteristics of CMS structures; and preparation of draft recommendations for improving the fatigue life of as-built CMS structures. To investigate the fatigue life of as-built CMS structures, laboratory tests of three mast arms and one cantilever post were undertaken. Two of the mast arm specimens sustained four million cycles without failing. One mast arm specimen and the post specimen developed fatigue cracks in the groove-welded connection. In both cases, the fatigue cracks propagated through the wall of the specimens. A mathematical (finite element) model of the CMS structure was developed, and analysis demonstrated that the presence of the conduit hole significantly increased the local stresses. Analysis of available field data showed that the CMS structures have closely spaced modes, are flexible, and have minimal structural damping. It is recommended that Caltrans consider: relocating and reconfiguring the conduit hole; developing a pre-qualified welding procedure (WPS) for groove-welded connections; develop improved quality control and inspection procedures; and specify tolerances for the flanged, mast arm-post connections.

| 17. Key Words | 18. Distribution Statement |
|---|---|
| Changeable Message signs, As-built<br>Fatigue life, Conduit hole, Low damping,<br>Fatigue crack propagation, Welding procedure,<br>Quality control and Inspection | Unlimited |

| 19. Security Classif. (of this Report) | 20. Security Classif. (of this Page) | 21. No. of Pages | 22. Price |
|---|---|---|---|
| Unclassified | Unclassified | 182 | |

# ABSTRACT

This report outlines the research program undertaken at the Earthquake Engineering Research Center (EERC) to investigate the fatigue life of Changeable Message Structures (CMSs). These types of sign structures are inverted "L" shape structures, fabricated from steel pipe sections, and composed of a vertical (post) section that is connected to a horizontal (mast arm) section by a flanged connection. The sign structures are inherently flexible and have low structural damping.

Following the failure of one CMS structure in Southern California, field studies were undertaken that indicated that the groove-welded mast arm (post)-flange plate and post-base plate connections are susceptible to wind-induced fatigue cracking. Caltrans then identified seven topics for urgent study. This report addresses four of these topics: evaluation of the fatigue life of as-built connection details; assessment of the stress increase in CMS components adjacent to the conduit holes; estimation of the dynamic characteristics of CMS structures; and preparation of draft recommendations for improving the fatigue life of as-built CMS structures. To investigate the fatigue life of as-built CMS structures, laboratory tests of three mast arms and one cantilever post were undertaken. Two of the mast arm specimens sustained four million cycles without failing. One mast arm specimen and the post specimen developed fatigue cracks in the groove-welded connection. In both cases, the fatigue cracks propagated through the wall of the specimens. A mathematical (finite element) model of the CMS structure was developed, and analysis demonstrated that the presence of the conduit hole significantly increased the local stresses. Analysis of available field data showed that the CMS structures have closely spaced modes, are flexible, and have minimal structural damping. It is recommended that Caltrans consider: relocating and reconfiguring the conduit hole; developing a pre-qualified welding procedure (WPS) for groove-welded connections; develop improved quality control and inspection procedures; and specify tolerances for the flanged, mast arm-post connections.

# ACKNOWLEDGMENTS

The work described in this report was funded by the California Department of Transportation (Caltrans) under Grant No. RTA 59A131. Numerous Caltrans engineers made significant contributions to the work described in this report, including Mr. Anthony Gugino, the Caltrans Technical Monitor for the project, and Messrs. George Amaro, John Dusel, Tim Leahy, James Roberts, Richard Shepard, Walt Winter, and Jeff Woody. The support and advice of these individuals, and the financial support of Caltrans, is gratefully acknowledged.

The authors wish to thank Mr. Mark Kaczinski, formally of Lehigh University, PA, for his advice over the course of this experimental program.

The timely completion of the experimental work presented in this report was made possible by the outstanding efforts of the laboratory staff at the Earthquake Engineering Research Center (EERC). The authors are indebted to Messrs. Don Clyde, Wesley Neighbor, and Changrui Yin, each of whom enthusiastically supported this research program and enabled, through many evenings and weekends of additional work, the work to be completed in a timely manner. Ms. Carol Cameron of EERC edited this report, and her efforts are sincerely appreciated.

The findings, conclusions, opinions, and recommendations expressed in this report are solely those of the authors, and do not necessarily represent the views of the sponsor.

# TABLE OF CONTENTS

# LIST OF TABLES

# LIST OF FIGURES

# CHAPTER 1: INTRODUCTION

## 1.1 Geometry of Changeable Message Signs

Changeable Message Sign (CMS) structures are widely used in California by the California Department of Transportation (Caltrans) for communicating information on road conditions to the driving public. The CMSs are composed of an electronic message sign hung from a mast arm, which is supported by a vertical cantilever post. The approximate weight of the sign is 2.5 kips (11 kN). Figure 1.1 shows a typical CMS structure.

The tubular, standard pipe, mast arm is 25 ft (7.6 m) long with an outside diameter of 18 in. (457 mm) and a wall thickness of 3/8 in. (9.5 mm). The cantilever post, fabricated using extra strong pipe, is approximately 24 ft (7.3 m) tall, with an outside diameter of 18 in. (457 mm) and a wall thickness of 1/2 in. (12.7 mm). The post is straight for approximately 16 ft (4.9 m), and has an eight ft (2.4 m) radius 90° arc at the top. Annular flange plates, with an outside diameter of 24 in. (610 mm), an inside diameter of 16 in. (406 mm), and a thickness of 1-3/8 in. (35 mm) are groove welded to the ends of the mast arm and the post, and 26 3/4 in. (19 mm) bolts are used to connect these plates (herein termed the mast arm-post connection). The post is welded at the bottom to an octagonal 2-3/4 in. (70 mm) thick base plate (herein termed the post-base plate connection), which, in turn, is attached to a reinforced concrete foundation using eight high-strength, 2-1/4 in. (57 mm) diameter anchor bolts. Figure 1.2 shows the dimensions of a Model 500 CMS structure.

CMSs are relatively flexible structures with little structural damping and are subjected to variable environmental and wind vibration conditions. They are designed by Caltrans using the AASHTO Standard Specifications for Structural Supports for Highway Signs, Luminaries, and Traffic Signals (AASHTO, 1994). Two weld details are used for the post-base plate connection: a full-penetration detail, and a socket detail. In some of the full-penetration connections, a drainage hole is flame cut close to the groove weld to facilitate the galvanizing process. All posts have a large diameter circular hole in the center of the base plate. A rectangular reinforced conduit hole measuring 4 by 6 in. (102 x 152 mm) is flame cut in the post. This conduit hole is located approximately 18 in. (457 mm) above the base plate on the post face opposite to the mast arm (herein termed the tension side of the post). An additional 3 in. (76 mm) circular access hole is located above the rectangular conduit hole on the face opposite to on-coming traffic. Two additional 2-1/2 in. (63 mm) circular conduit holes, one on the post and one on the mast arm, are located approximately 6 in. (152 mm) from the flange connection on the underside of the mast arm (herein termed

the compression side of the mast arm).

### 1.2 Caltrans Field Investigations

On 28 November 1995, a CMS structure located on Interstate I-15 in San Bernardino County, California, failed. The failure of the CMS structure led Caltrans investigators to inspect all CMS structures in the state of California, and to study the response of CMS structures.

More than 200 CMS structures in use throughout the state of California were inspected to determine the extent of wind-induced fatigue cracking in their welded components. The field examinations indicated that a number of the CMS structures that were exposed to sustained high winds had fatigue-related cracks at the post-to-base plate connections In addition, the field results did not rule out the possibility of fatigue cracks at the mast arm-to-post welded connection.

Several field structures were instrumented to characterize the dynamic response of the CMS structures. The available field data indicated that the welded connections were subjected to stress levels that substantially exceeded the allowable stress levels recommended by the AASHTO specifications (AASHTO, 1994).

As a result of these investigations, Caltrans identified seven topics for urgent study:

1. Development of an understanding of the fatigue life of the as-built welded connection details through full-scale experimental studies.
2. Development of mathematical models of CMS structures to a) estimate their dynamic properties, and b) assess the increase in stress adjacent to the conduit holes in the post and the mast arm.
3. Analysis of the available field data to establish the dynamic characteristics of CMS structures.
4. Preparation of draft recommendations for improving the fatigue life of CMS structures through improved fabrication, construction, and installation practices.
5. Development of retrofit schemes for the vulnerable groove-welded connections.
6. Estimation of the wind loads and forces on CMS structures as a function of wind speed and direction.
7. Development of vibration mitigation techniques.

### 1.3 Objectives and Scope

Caltrans contracted with the Earthquake Engineering Research Center (EERC) to study the first five of the seven topics identified in the previous section. This report addresses the first four topics; a soon-to-be-published EERC report (Chavez, et al., 1997) will present the findings on the fifth topic.

## 1.4 Organization of the Report

Chapter 2 provides limited background information on the subjects of wind loading and fatigue. Chapter 3 presents the results of the preliminary analysis of field data that were used to determine some of the dynamic properties of as-built CMS structures. Chapter 4 presents the results of the finite element modeling of the post and the mast arm specimens. Chapter 5 describes the experimental program, and Chapters 6 and 7 detail the experimental results for the post and mast arm specimens, respectively. Conclusions and recommendations are presented in Chapter 8. The appendices provide a more detailed description of the material summarized in Chapter 2 and include a trial analysis and design of a CMS structure (see Appendix A6).

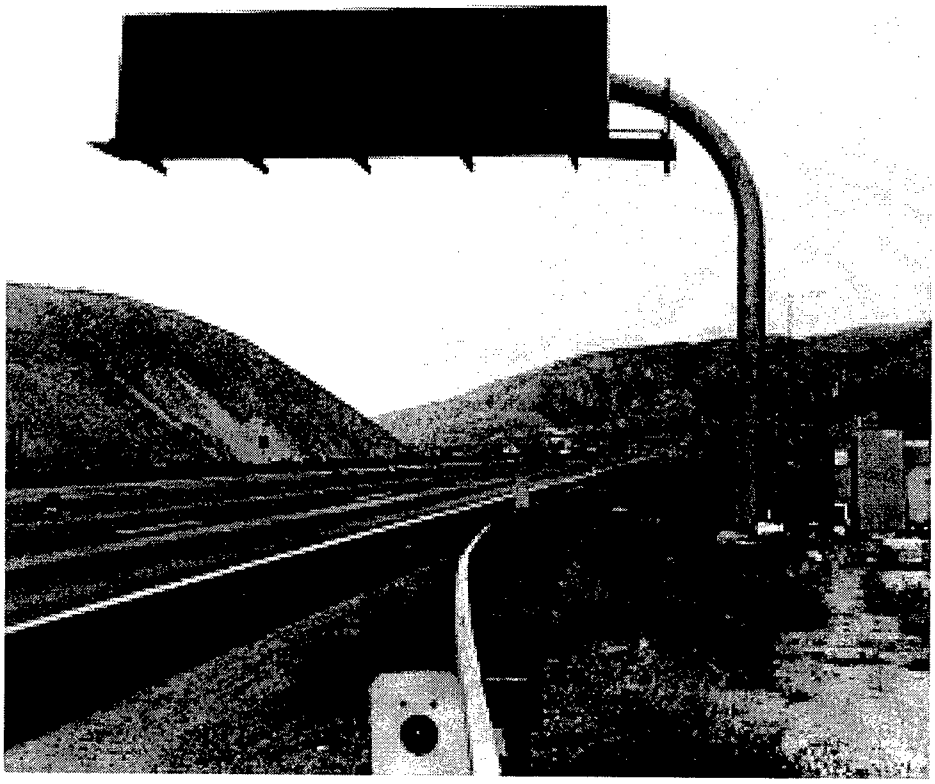

Figure 1.1: A typical as-built CMS structure

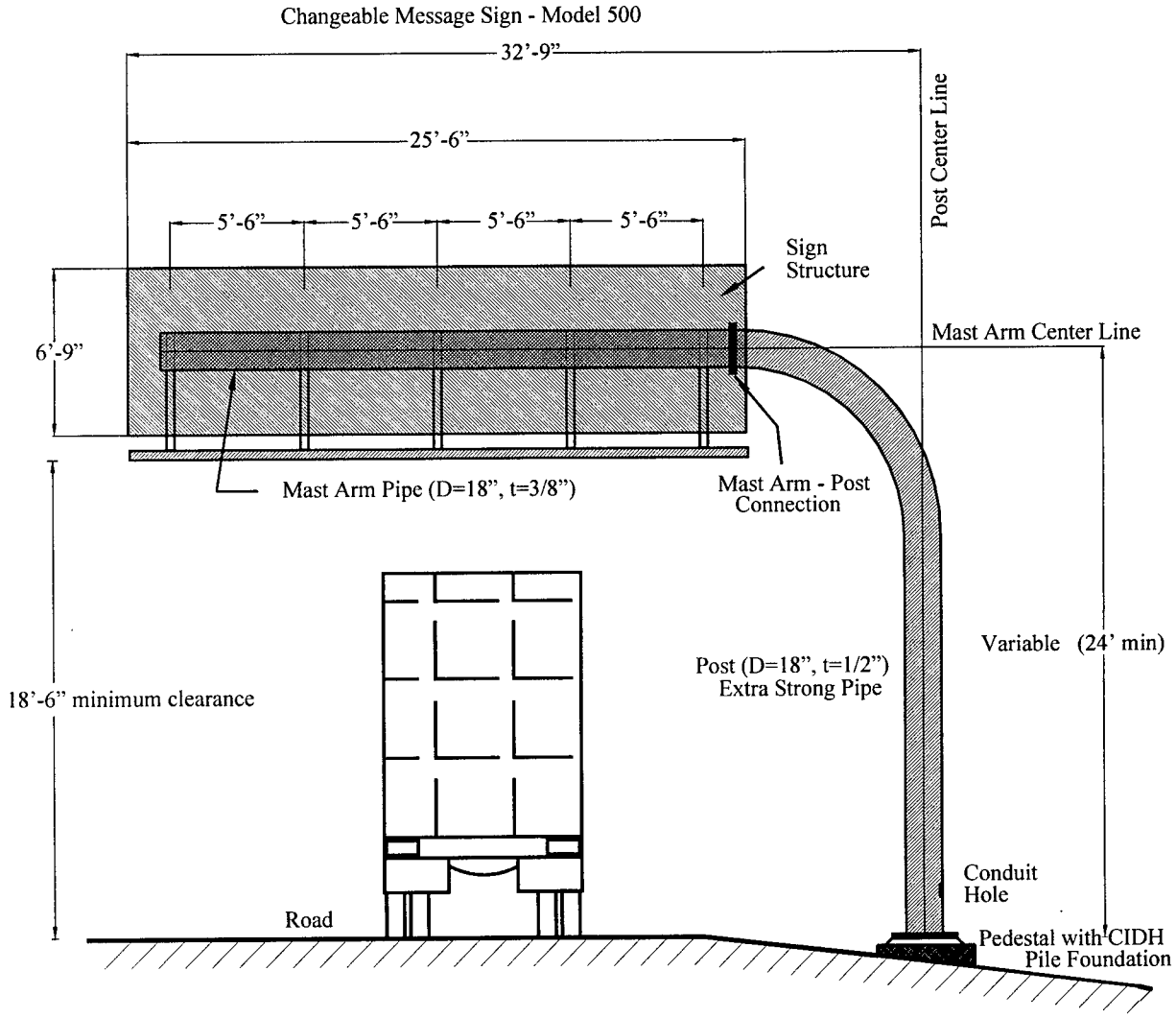


Figure 1.2: Dimensions of a CMS structure

# CHAPTER 2: BACKGROUND INFORMATION

## 2.1 General

Field observations have indicated that CMS structures are susceptible to wind-induced failure by fatigue. The study described in this report was funded by Caltrans with the purpose of 1) characterizing the reason(s) for the observed failures, and 2) developing procedures and details for new and retrofit CMS construction.

Prior to discussing the results of the research program, background information on fatigue and on the effects of wind on structures is presented. Current AASHTO procedures to design against failure due to fatigue are also presented. In Section 2.2, information regarding aerodynamic and aeroelastic wind effects is presented. This is followed in Section 2.3 by a brief review of the subject of fatigue. A review of the current AASHTO guidelines for CMS structures as related to design for wind effects is presented in Section 2.4. A more detailed treatment of these subjects is presented in Appendix A.

## 2.2 Wind Loading

### *2.2.1 General*

Wind effects on CMS structures can be classified as either aerodynamic or aeroelastic. Aerodynamic effects are due solely to external loading. Aeroelastic effects are due to the interaction of aerodynamic forces and structural motion, that is, the aeroelastic-induced forces acting on a structure are a result of the motion of the structure. Aeroelastic instability occurs when a structure deforms due to aerodynamic forces and this deformation produces oscillatory motions of increasing amplitudes. Two aerodynamic effects, natural and truck-induced wind gusts, and two aeroelastic effects, vortex shedding and galloping, can influence the response of CMS structures (see Appendix A1).

### *2.2.2 Natural Wind Gusts*

Wind gusts occur naturally from a change in the flow direction and/or amplitude of the wind. Due to wind turbulence, fluctuating pressures on a structure can cause it to vibrate. The resulting variable stresses introduced in a structure and its connections can contribute to fatigue-induced cracking.

### *2.2.3 Truck-Induced Wind Gusts*

The passage of trucks underneath a CMS structure induces wind pressure (horizontal and vertical) gradients on the CMS sign and its attachments connected to the mast arm.

The horizontal pressure acting on the faces of the sign introduce torsion and bending moment (about the $y$ axis) in the post. The stresses induced at the base of the post due to truck-induced wind loads are dependent on the length of the mast arm ($L$ in Figure 2.1), the height of the post ($h$ in Figure 2.1), and the projected frontal area and the exposed area of the underside of the sign ($b$ x $d$ in Figure 2.1). Field data suggests that the values of the these stresses are smaller than those due to natural wind gusts. The vertical gust pressures acting on the underside of the sign introduce bending moments (about the $x$ axis) in the post. The stresses induced at the base of the post are dependent on the length of the mast arm ($L$ in Figure 2.1) and the projected underside area of the sign ($b$ x $w$ in Figure 2.1). These stresses must be considered in the design of CMS structures.

### *2.2.4 Regular Vortex Shedding*

Regular Vortex shedding occurs when alternating regular vortices are shed in the wake of a structure. The frequency of these vortices is given by the Strouhal equation:

$$f_s = \frac{VS}{D} \tag{2.1}$$

where $D$ is the dimension of the structure perpendicular to the flow, $V$ is the mean wind velocity, and $S$ is the Strouhal number. The value of $S$ depends on the geometry of the structure and the Reynolds number. The Reynolds number is used to characterize the nature of wind flow as either laminar or turbulent. For a circular cross section, a Reynolds number of 5000 separates the laminar and turbulent flow regimes. When the frequency expressed by Equation 2.1 approaches one of the natural frequencies of a flexible and lightly damped structure, large motions may occur.

For a CMS structure with $D$ = 18 in. (457 mm), $f_s$ = 1 Hz (see Chapter 3), and $S$ = 0.18 (Simiu and Scanlan, 1996), the wind velocity required for regular shedding of vortices is 8.3 ft/sec (2.5 m/sec). This value is less than the wind velocity of 16.5 ft/sec (5 m/sec) required to initiate regular vortex shedding in most structures (Kaczinski, et al. 1996). Furthermore, the geometry of the sign is not conducive to the regular shedding of vortices. Thus, regular vortex shedding is not expected to be a problem for CMS structures such as those employed by Caltrans prior to the start of this research program.

### *2.2.5 Galloping*

Large amplitude motions in the direction normal to the wind flow, at frequencies smaller than $f_s$ in Equation 2.1, are defined as galloping motions. If a structure experiences motion in the across-wind direction, the flow around the structure can become unsymmetrical, generating a lift force in the across-wind direction. This force will increase the motion of the structure in the across-wind direction, and large amplitude motions may result.

For a prismatic, single-degree-of-freedom oscillator in a smooth wind flow and oscillating in the across-wind direction, the total system damping ($\xi_{total}$) may be expressed as:

$$\xi_{total} = \xi_{mech} + \xi_{aero} \quad (2.2)$$

where $\xi_{mech}$ is the mechanical or equivalent viscous damping of the oscillator (always positive), and $\xi_{aero}$ is the aerodynamic damping (often negative). Galloping instability (the Glauert-Den Hartog criterion) will occur when the total system damping is negative, that is, when the value of the aerodynamic damping, if negative, is larger than the mechanical damping. CMS structures possess small mechanical damping (see Chapter 3), and are susceptible to galloping instability. Wind load on the sign structure is the likely cause of galloping.

## 2.3 Fatigue Phenomenon

### *2.3.1 General*

Fatigue problems (see Appendix A2) occur in many kinds of structures, such as bridges, off-shore platforms, vehicle suspension systems, aircraft, ships, and sign support structures. Many of these structures utilize welded connections which are susceptible to failure due to fatigue (see Appendix A3).

Fatigue can be classified as either low-cycle or high-cycle. Low-cycle fatigue occurs when a connection or a component is subjected to strains exceeding the yield strain. The required number of loading cycles to failure is small (e.g., 10-100). High-cycle fatigue occurs when a connection or component is subjected to strain levels which are less, and often substantially less, than the yield strain. The number of cycles required to initiate failure is typically large (e.g., 1,000,000+). The failure of a CMS structure due to fatigue is associated with a large number of loading cycles at strain levels less than the yield strain. Accordingly, the focus of the remainder of this report is on high-cycle fatigue.

Geometry is one of the most dominant factors influencing fatigue life because variations in geometry influence stresses at critical locations where fatigue cracks can form. The metallurgical characteristics of the steel and the weld filler metal, and the presence of defects, also affect fatigue life. Material strength alone is not believed to be a significant factor in the fatigue life of a structure. However, the ratio of the applied stress to the yield stress has a significant effect on fatigue life.

### *2.3.2 Fatigue Life*

Although structures are typically subjected to complex loadings, constant amplitude sinusoidal loading is usually used to characterize the fatigue life of components and connections. As shown in Figure 2.2, the stress range is defined as the total stress amplitude in a given cycle. Using this definition, the

fatigue life of a specimen at different stress ranges can be represented by an S-N curve (where S is the stress range and N is the number of loading cycles to failure). A point on the S-N plot indicates the number of cycles a component or connection can sustain at a given stress range prior to failure. As shown in Figure 2.3, the S-N curve is typically plotted in logarithmic form, that is, the logarithm of the stress range is plotted versus the logarithm of the number of loading cycles to failure. The cycle count in the plot is the sum of the number of cycles required to initiate a crack and the number of cycles needed to propagate the crack to failure. Typical S-N curves consist of a descending branch and a constant value branch. In the descending branch, fatigue life is reduced as the stress range is increased. The fatigue limit is the stress level at which the number of cycles to failure is infinite. Theoretically, a component or connection loaded to stress ranges below the fatigue limit will have infinite fatigue life. A sample S-N relation is shown in Figure 2.3. For design, an S-N relation two standard deviations below the mean relation is typically used.

For structures subjected to a variable loading history, the fatigue damage caused by each loading cycle can be accumulated to determine the total fatigue life. A damage model known as the Palmgren-Miner rule (Miner, 1945) is typically used to sum damage ratios for each loading cycle.

### 2.3.3 *Fatigue-Related Research on Welded Structures*

The fatigue performance of welded civil engineering structures has been widely studied. The findings of some of these studies on cantilever light and sign structures, off-shore platforms, and bridges are summarized in Appendix A4.

Researchers at Lehigh University (Kaczinski, et al., 1996) have recently carried out wind tunnel tests of scaled components of sign structures and fatigue tests of anchor bolts. The objective of the Lehigh study was to evaluate the current AASHTO specifications (AASHTO, 1994) for design of cantilever sign structures for fatigue effects. The findings of this research have been presented as recommended changes to the AASHTO guidelines; the proposed changes are summarized in Appendix A5. The Lehigh researchers concluded that galloping-induced vibrations should be considered for design against fatigue failure, and recommended research in two areas: full-scale testing of CMS structures to characterize the fatigue life of the connection details (base-to-post, mast arm-to-post); and field testing of CMS structures to determine the wind pressure on a CMS sign as a function of wind speed and direction, and the dynamic properties of cantilever sign structures.

A related study (Mander, et al., 1992) was commissioned by the Erie County Department of Public Works to investigate the integrity of light pole bases at Rich Stadium in Buffalo, New York. Maintenance checks and ultrasonic tests indicated the presence of fatigue cracks in the anchor bolts at the location of the leveling nuts. As part of this investigation, Mander instrumented a light pole to measure the dynamic

response of the pole, and the stress distribution in the anchor bolts under wind loading. The anchor bolt stress distribution and acoustic emission tests confirmed the presence of fatigue cracks in the anchor bolts. The poles were retrofitted by adding post-tensioned high-strength threaded bars to the base plate connection. The installation of viscous dampers to reduce the dynamic response of the light poles was also recommended.

## 2.4 Design of CMS Structures for Fatigue

A summary of the AASHTO specifications for the design of cantilever sign post structures is presented in Appendix A5. The specifications use equivalent static methods of analysis and combine the stresses due to different sources of loading. A trial design for the vertical post of a CMS structure is presented in Appendix A6. Wind and vortex shedding effects are included in the stress check. New guidelines, based on the recommendations of Kaczinski, et al. (1996) will likely include provisions for galloping, natural wind gusts, and truck-induced gusts.

The design of sign structures for fatigue resistance is routinely based on criteria outlined in the AASHTO Standard Specifications for Highway Bridges (AASHTO, 1992). Welded connections are classified into eight categories ranging from A (longest fatigue life) through E' (shortest fatigue life). The full-penetration welded connections at the base of the CMS post and at the mast arm flanged connection are categorized as class E'. As such, they have a theoretically infinite fatigue life for stress ranges below 2.6 ksi (17.9 MPa), as shown in Figure 2.4. The E' classification is based on the difficulty associated with inspecting these welds due to the presence of the back-up ring inside the post immediately above the base plate.

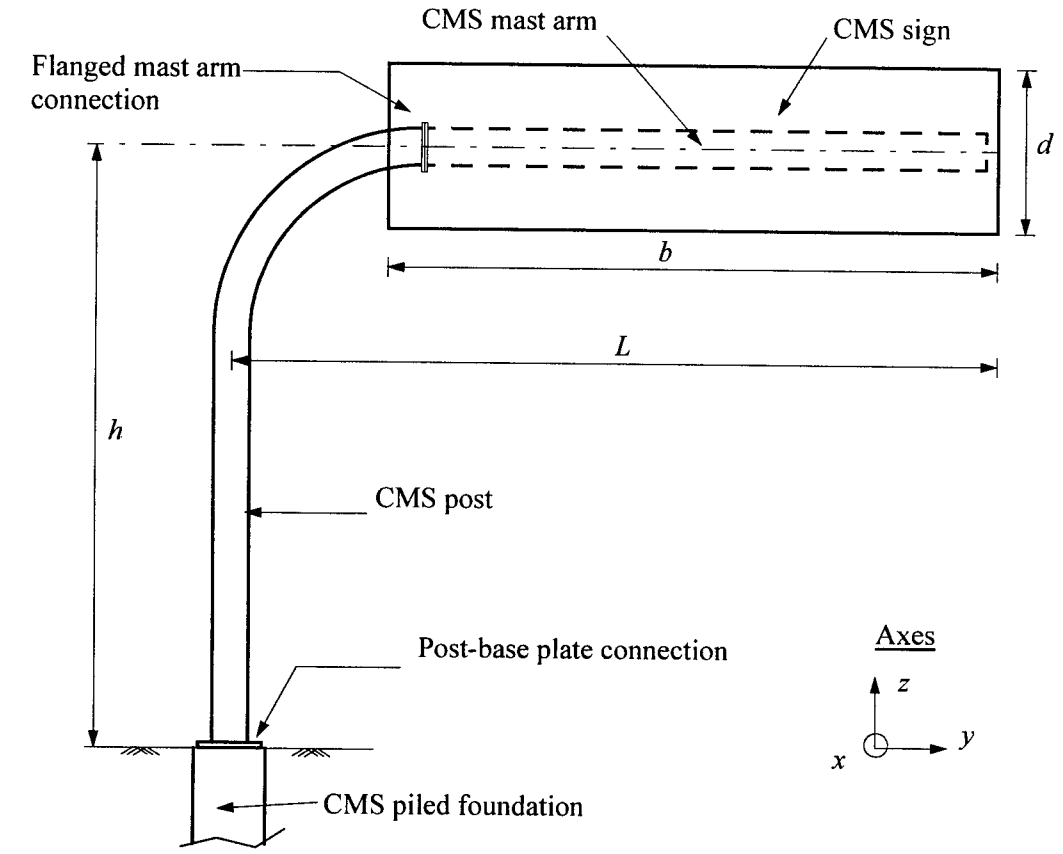


(a) Elevation

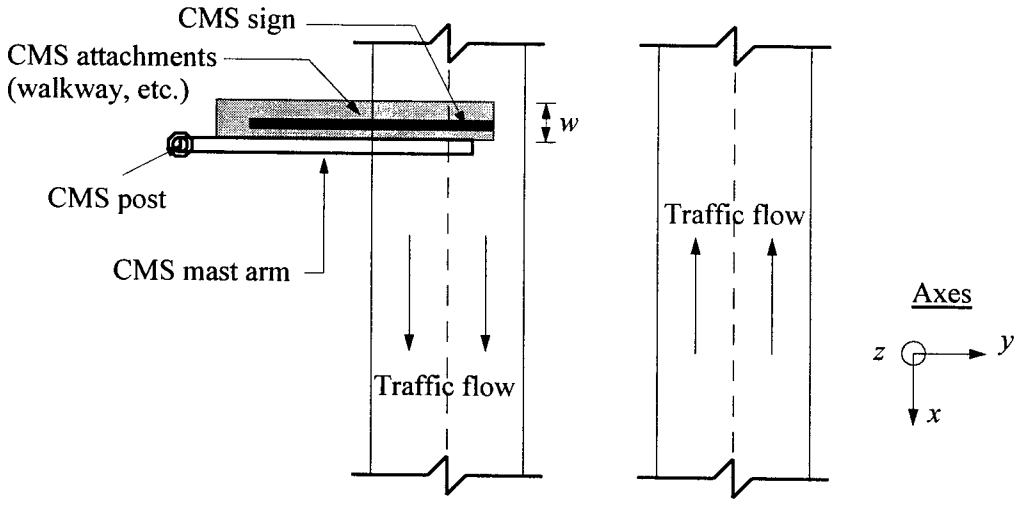


(b) Top view

Figure 2.1: Schematic views of a typical CMS structure

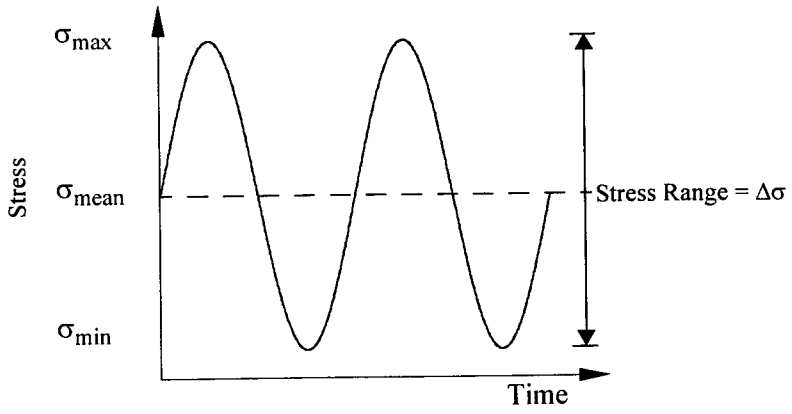


Figure 2.2: Constant amplitude loading

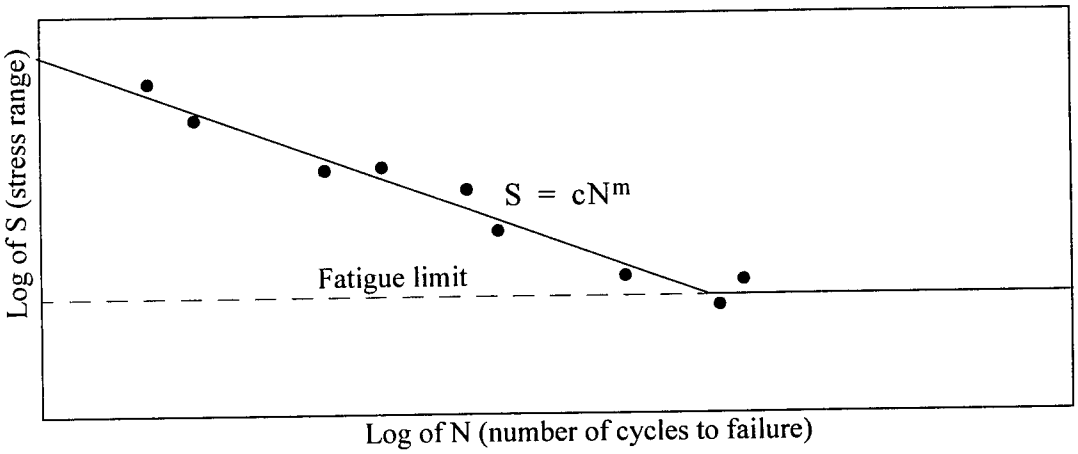


Figure 2.3: Experimental S-N curve

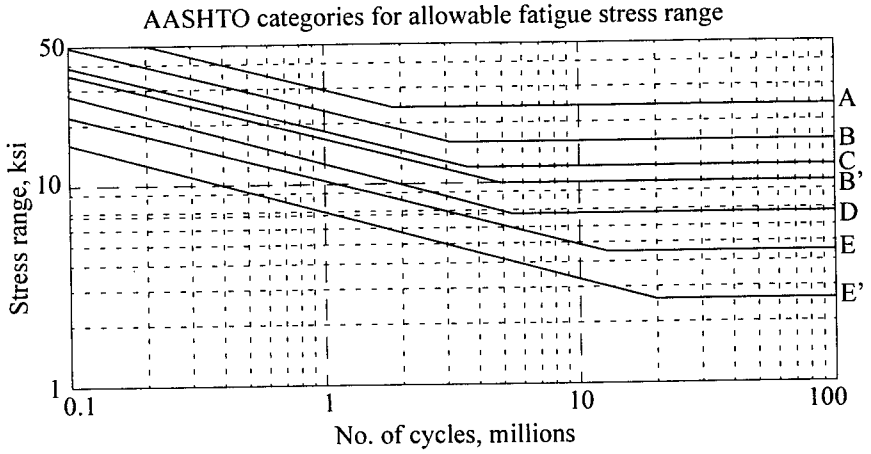


Figure 2.4: AASHTO design plots (AASHTO, 1994)

# CHAPTER 3: ANALYSIS OF FIELD EXPERIMENTAL DATA

## 3.1 General

Caltrans undertook an extensive field inspection of the response of CMS structures following the failure of a CMS structure in San Bernardino County (see Section 1.2). As part of this investigation, Caltrans instrumented several CMS structures situated in high-wind areas to ascertain the wind-induced response of these structures and to establish the dynamic characteristics of CMS structures. The data acquired from the wind-induced vibration and pull-back testing were used to determine selected dynamic properties of the CMS structures. This information is presented in this chapter. The two CMS structures described in this chapter are located on Interstate 15 (I-15) (see Figure 3.1) and California Highway 58 (R-58) (see Figure 3.2).

## 3.2 Field Measurements

A brief summary of test parameters and instrumentation to measure the response of the two CMS structures follows.

### *3.2.1 CMS Structure on Interstate 15*

The CMS designated for installation on southbound Interstate 15 at San Bernardino County post mile 4.65 was instrumented prior to erection. The response of this CMS was monitored at several stages: 1) throughout the assembly of the CMS structure; 2) during the application of both static vertical and horizontal loading; and 3) after installation. The reader is referred to Winter (1996) for a comprehensive discussion of the field testing procedures and the findings of these studies.

A total of eight uniaxial strain gages were used to monitor the response of the CMS structure. The gages were placed approximately 36 in. (914 mm) above the post-to-base plate connection. Gages 1 through 6 were placed longitudinally (i.e., parallel to axis of the post) and gages 7 and 8 were placed laterally. Figure 3.3 shows the layout of strain gages. The field data was gathered at a sampling rate of 100 Hz. The data was collected while the lane under the CMS was closed to traffic to minimize the effect of truck-induced gusts. The data acquired during the wind-induced response of the CMS is analyzed in this chapter.

### *3.2.2 CMS Structure on Highway 58*

A CMS structure located approximately six miles west of Mojave, westbound on Highway 58, was

instrumented on October 29, 1996. Pull-back free vibration tests were conducted on this CMS to gather data used to obtain the dynamic characteristics (i.e., vibration frequency and damping ratio) of a typical CMS structure.

The instrumentation of the CMS structure consisted of six strain gages: a triple rosette (sg1, sg2, and sg3) and three uniaxial gages. The rosette was placed approximately 48 in. (1219 mm) above the base plate on the tension face, that is on the side opposite to the rectangular conduit hole. A uniaxial gage (sg4) was placed on the opposite face of the post at the same height. Two uniaxial gages (sg5 and sg6) were placed 18 in. (457 mm) from the flanged mast arm-to-post connection on the tension side of the assembly: one on the post and one on the mast arm. The strain gages were calibrated so that 200 micro-strains corresponded to 1 volt. Figure 3.4 shows the strain gage configuration.

A load-rated nylon rope was attached near the tip of the mast arm (see Figure 3.5) approximately six feet from the free end of the mast arm. The other end of the rope was attached to a quick-release hook. Another rope was attached to the hook and to a turnbuckle which was attached to a stationary Caltrans truck. Using the turnbuckle, the tension in the rope was increased to approximately 2.5 kips. The applied tension was then suddenly released by disengaging the quick-release hook to produce free vibration in the structure.

Two free vibration tests were conducted. The test data was scanned at 100 Hz, amplified using Vishay signal conditioners, and recorded on a portable personal computer. In the first test, data for strain gages 4 through 6 were not recorded due to an equipment malfunction.

## 3.3 Analysis of Experimental Data

### *3.3.1 General*

The data processing package MATLAB (Matlab, 1996) and its signal processing utilities (Matlab, 1996) were used to process the experimental field response-history data. For each test, Fourier spectra were generated using Hanning windows of 8192 data points each. Samples had a duration of 81.92 seconds and overlapped by 1000 points. The frequency resolution was approximately 0.012 Hz.

Modal frequencies were estimated using the peaks of the Fourier spectra. Both the half-power and the log-decrement methods (Clough and Penzin, 1993) were used to estimate the modal damping. Due to the limited number of data channels, it was not possible to estimate the mode shapes of the CMS structure.

### *3.3.2 Wind-Induced Response of CMS on Interstate 15*

The frequency response of the eight strain gages is shown in Figure 3.6. For sg4 and sg6, placed in

the *x-z* plane (Figure 2.1), the peak amplitude occurs at a frequency of 1.04 Hz; for sg2 and sg5, placed in the *y-z* plane (Figure 2.1), the corresponding frequency is 1.10 Hz. Gages sg1 and sg3, placed between the *x-y* and *y-z* planes (Figure 2.1), show peak amplitudes at 1.04 and 1.10 Hz. These two frequencies correspond to the fundamental modal frequencies of a typical CMS structure. The first two modal frequencies are closely spaced. The proximity of the vibration modes is manifested as 'beating' in the response-history data.

Figure 3.7 shows the phase angle between sg2 and sg6, and between sg2 and sg4. The phase angles were obtained by computing the complex transfer function between the two channels in the frequency domain, and then calculating the phase angle of the complex function. At 1.04 Hz, the phase angle is zero, that is the response histories are in phase; at 1.10 Hz, the phase angle is 180 degrees and the response histories are out of phase.

To compute the damping ratios for the first two modes, the half-power method was used. The *n-th* modal damping ratio, $\xi_n$, was estimated from

$$\xi_n = \frac{(\omega_2 - \omega_1)}{2\omega_n} \tag{3.1}$$

where $\omega_n$ is the *n-th* modal frequency, and $\omega_2$ and $\omega_1$ are the half-power frequencies. Strictly speaking, this equation is valid only for a single-degree-of-freedom system. However due to the presence of single mode response in the strain response histories in each of principal planes (planes *x-z* and *y-z*), a reliable estimate of the damping ratio can be obtained. For the vibration mode of 1.04 Hz, the damping ratio is 0.7 percent of critical; for the vibration frequency of 1.10 Hz, the damping ratio is 0.5 percent of critical.

### *3.3.3 Free Vibration Response of CMS on Highway 58*

The response history of sg2 from the first free vibration test is shown in Figure 3.8. The initial portion of the response (between 0-3 minutes) corresponds to the static pull-back, the ensuing dynamic free vibration lasts approximately five minutes (between 3-8 minutes), and the response after eight minutes is a result of continuous wind-induced ambient vibrations.

Figure 3.9 shows the frequency response of sg2. The first vibration frequency is computed at 1.09 Hz. Since the pull-back testing was conducted in the *y-z* plane, and because no strain gages were placed in the *x-z* plane, only the modal damping in the *y-z* plane was computed. The damping ratio for this mode is computed by fitting a function of the form

$$y = A\sin(\omega t + \phi)e^{-\omega\xi t} \tag{3.2}$$

to the response-history data, as seen in Figure 3.10. The field data was low-pass filtered to identify only the

first mode response, prior to computing the coefficients of the analytic function. The damping ratio was then computed from the log decrement equation:

$$\xi = \frac{1}{2\pi(N)} \ln\left(\frac{y_2}{y_1}\right) \tag{3.3}$$

where $N$ is the number of cycles between the two amplitude readings, and $y_2$ and $y_1$ are the amplitudes of the analytic function. Using this technique, a modal damping ratio of 0.4 percent of critical was obtained. A similar damping value was obtained by half-power analysis of the frequency response. The modal frequency and damping ratios were consistent with the values obtained from the wind-induced response data.

### 3.4 Analytical Studies

The computer program Drain-3DX (Prakesh, et al., 1994) and its element library routines (Powell, et al., 1994) were used to develop a three-dimensional model of a CMS structure. Nominal section properties (geometric and material) were used to model the post and the mast arm. The mass of the sign and its attachments were modeled as lumped masses applied at the points of attachments to the mast arm. The masses of the post and the mast arm were lumped at the element nodes. The flanged connection between the mast arm and the post was assumed to be rigid. A two-dimensional torsional spring was attached to the base of the post to allow for rotation about the $x$ and $y$ axes (see Figure 2.1). The stiffness of this spring was computed from the stiffness and position of the anchor bolts. The analysis predicted that the first two vibration frequencies were 1.08 and 1.10 Hz. The first two mode shapes are shown in Figure 3.11.

### 3.5 Summary

Good agreement between the wind-induced, free vibration, and analytically computed modal frequencies was obtained. The first mode corresponds to the horizontal motion of the mast arm in the $x$-$y$ plane (as defined in Figure 2.1) while the second mode corresponds to the vertical motion of the mast arm and the post in $y$-$z$ plane (as defined in Figure 2.1). The first mode is excited by the application of horizontal loading, for example, along-wind components of wind loading, whereas the second mode is excited by application of vertical loading, for example, truck-induced gusting and across-wind galloping. A summary of the experimental and analytical mode shapes for a CMS structure is listed in Table 3.1.

Table 3.1: Modal properties of typical CMS structures

| Route Data | $f_1$ (Hz) | $\xi_1$ (%) | $f_2$ (Hz) | $\xi_2$ (%) |
|---|---|---|---|---|
| I-15, wind-induced | 1.04 | 0.7 | 1.10 | 0.5 |
| R-58, free-vibration | NA[a] | NA | 1.09 | 0.4 |
| Analytical | 1.08 | NA | 1.10 | NA |

a. Not Applicable

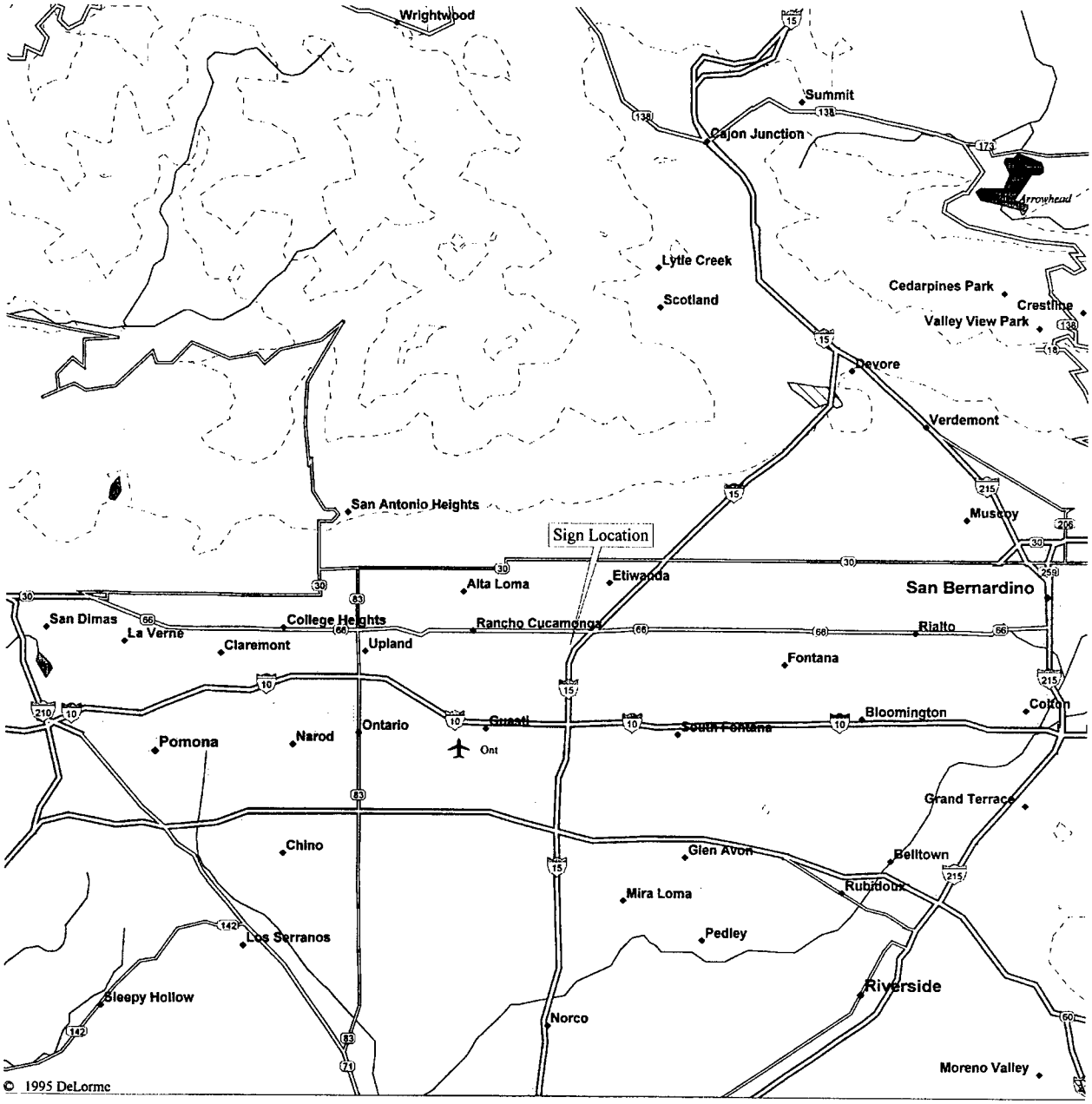


Figure 3.1: Map of the area for the CMS on I-15

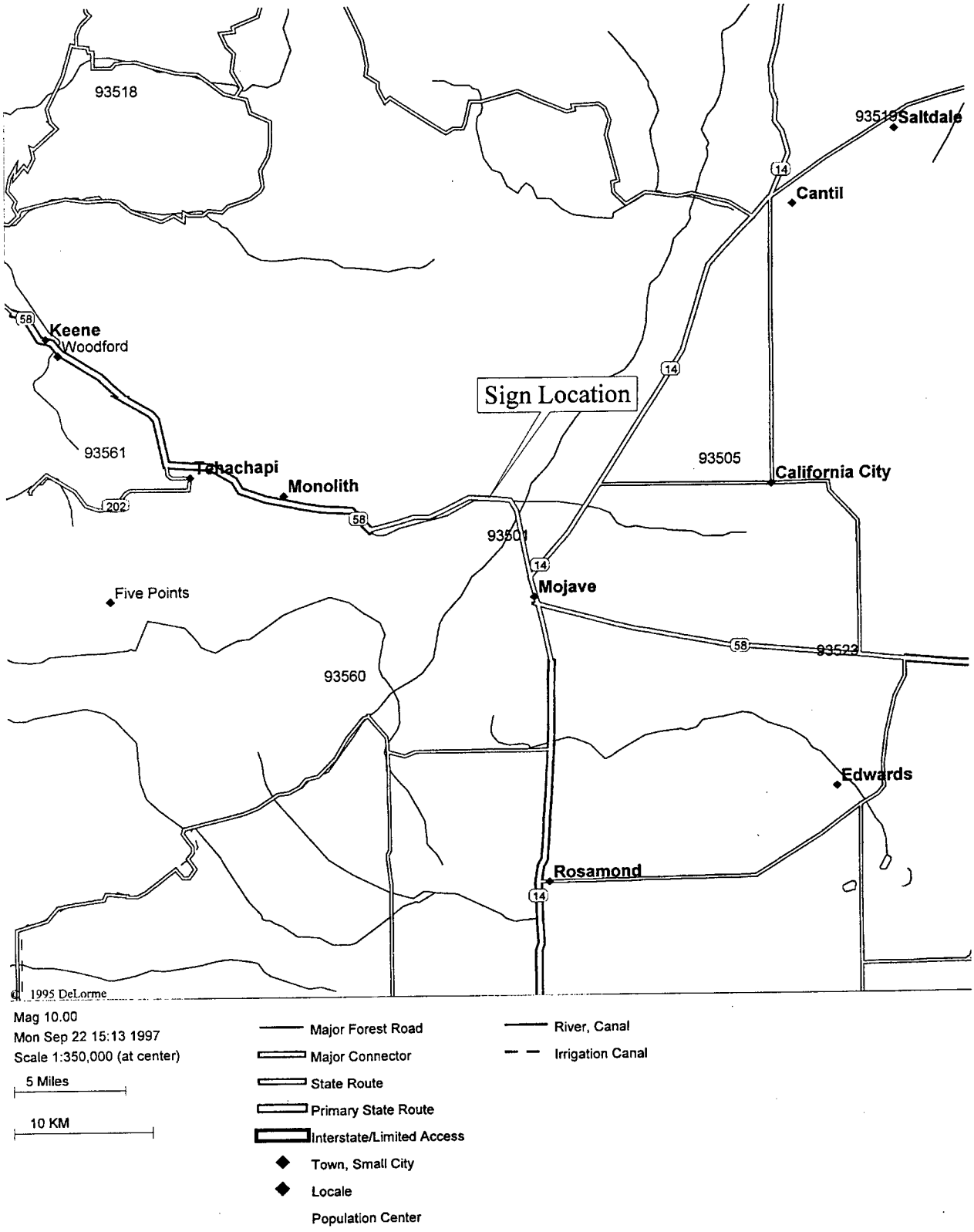


Figure 3.2: Map of the area for the CMS on R-58

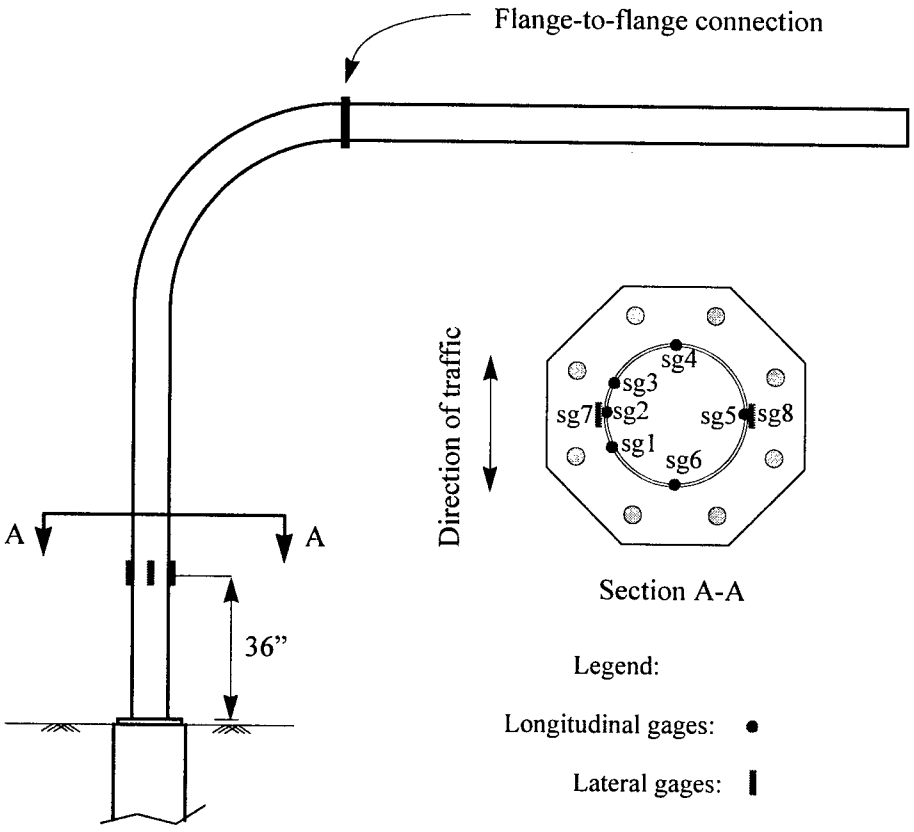


Note: The CMS sign and the sign attachments are not shown

Figure 3.3: Instrumentation for CMS on I-15

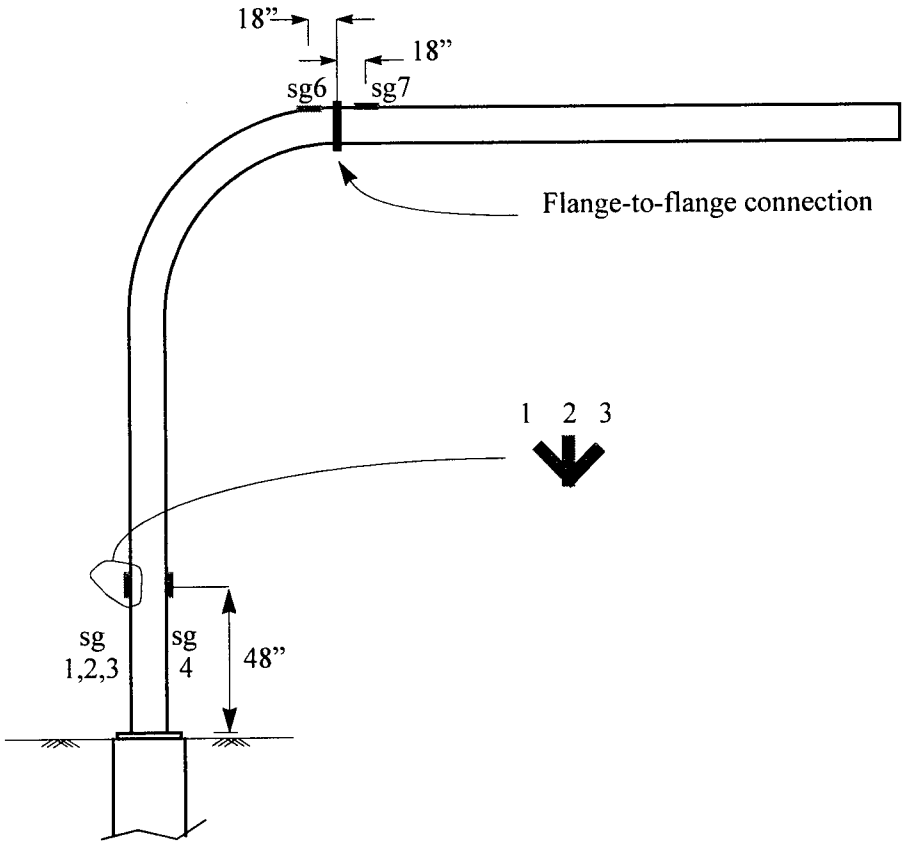


Note: The CMS sign and the sign attachments are not shown

Figure 3.4: Instrumentation for CMS on R-58

Figure 3.5: CMS on R-58 after the completion of the pull-back

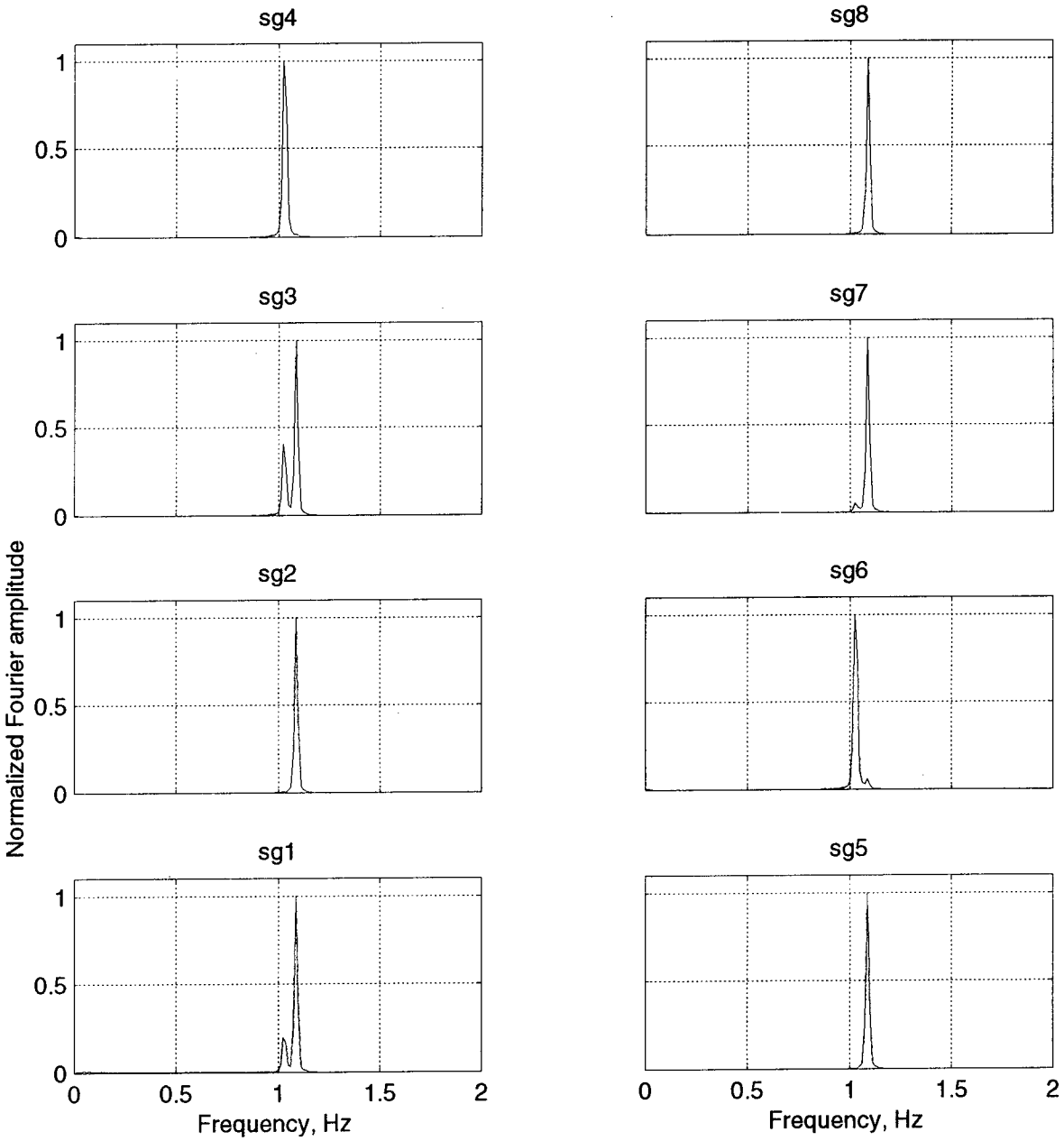


Figure 3.6: Strain gage frequency response for CMS structure on I-15

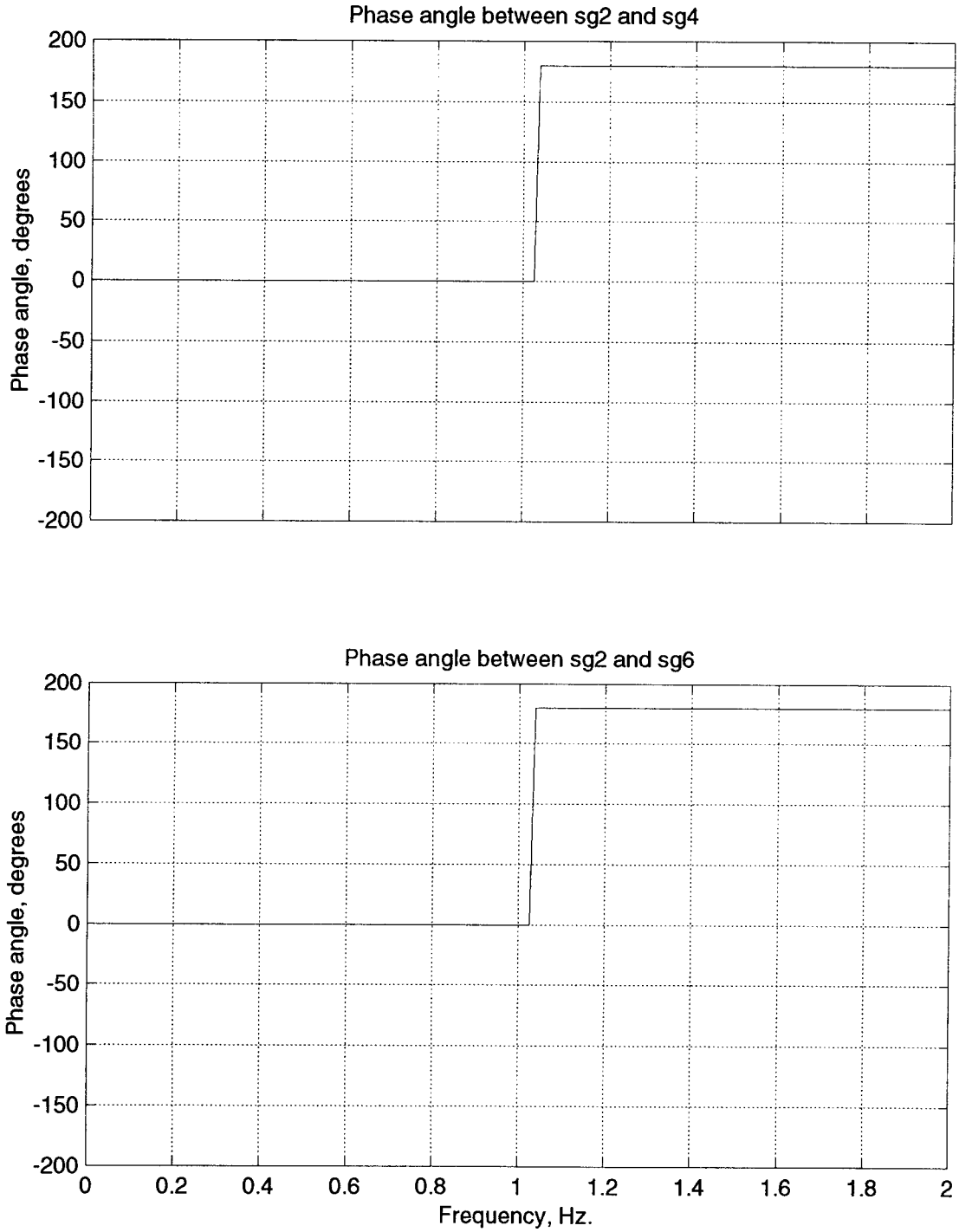


Figure 3.7: Phase angle between sg2 and sg4, and between sg2 and sg6, CMS structure on I-15

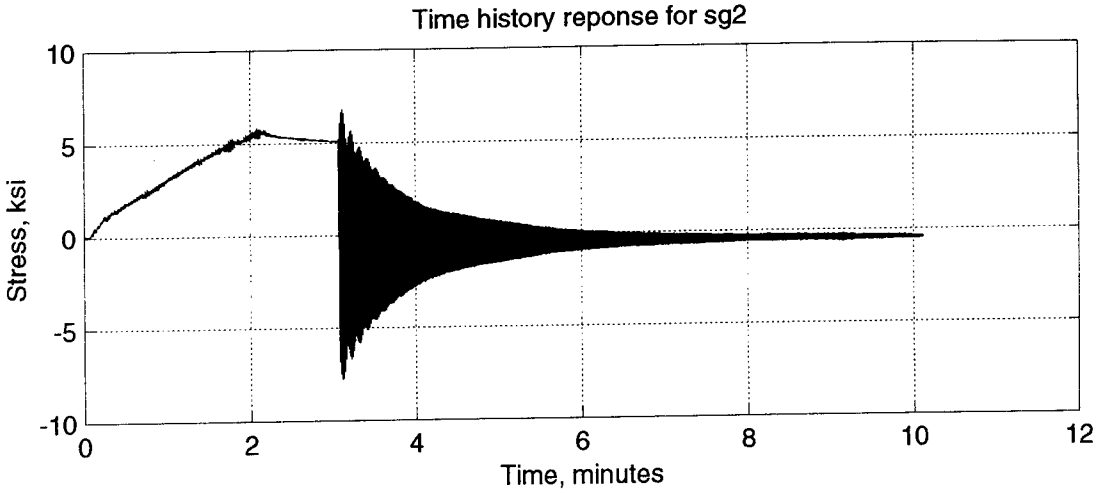


Figure 3.8: Longitudinal strain history response for sg2, CMS structure on R-58

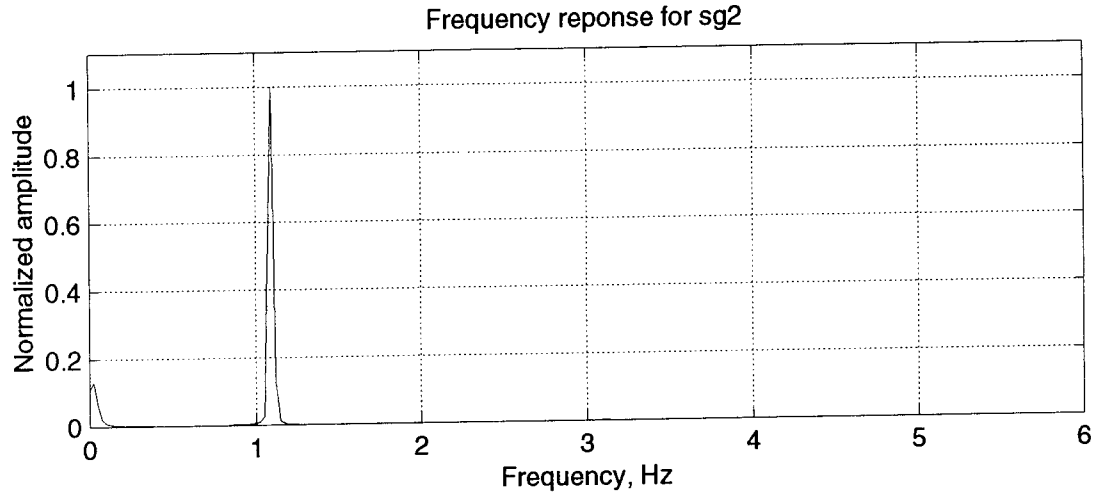


Figure 3.9: Frequency response for sg2, CMS structure on R-58

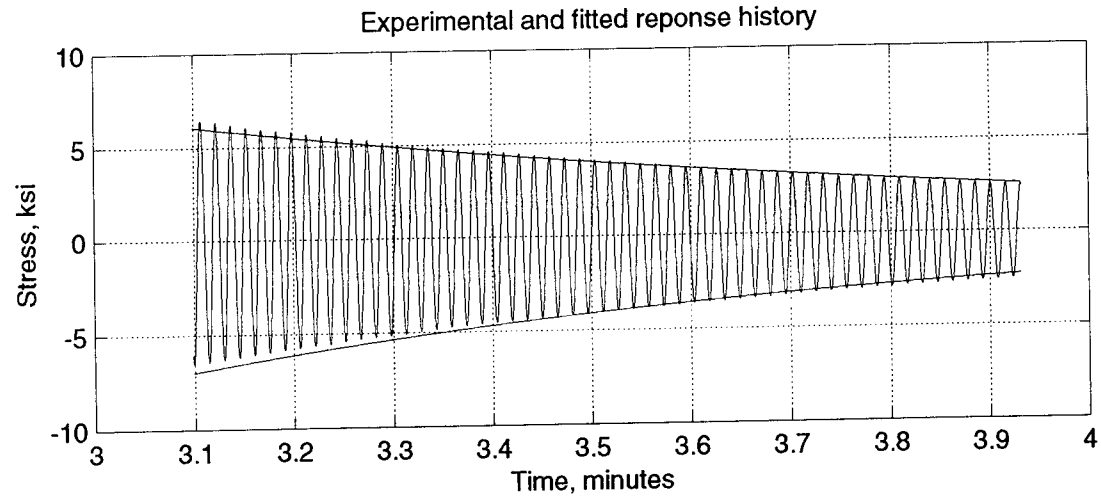


Figure 3.10: Analytical curve fit for sg2, CMS structure on R-58

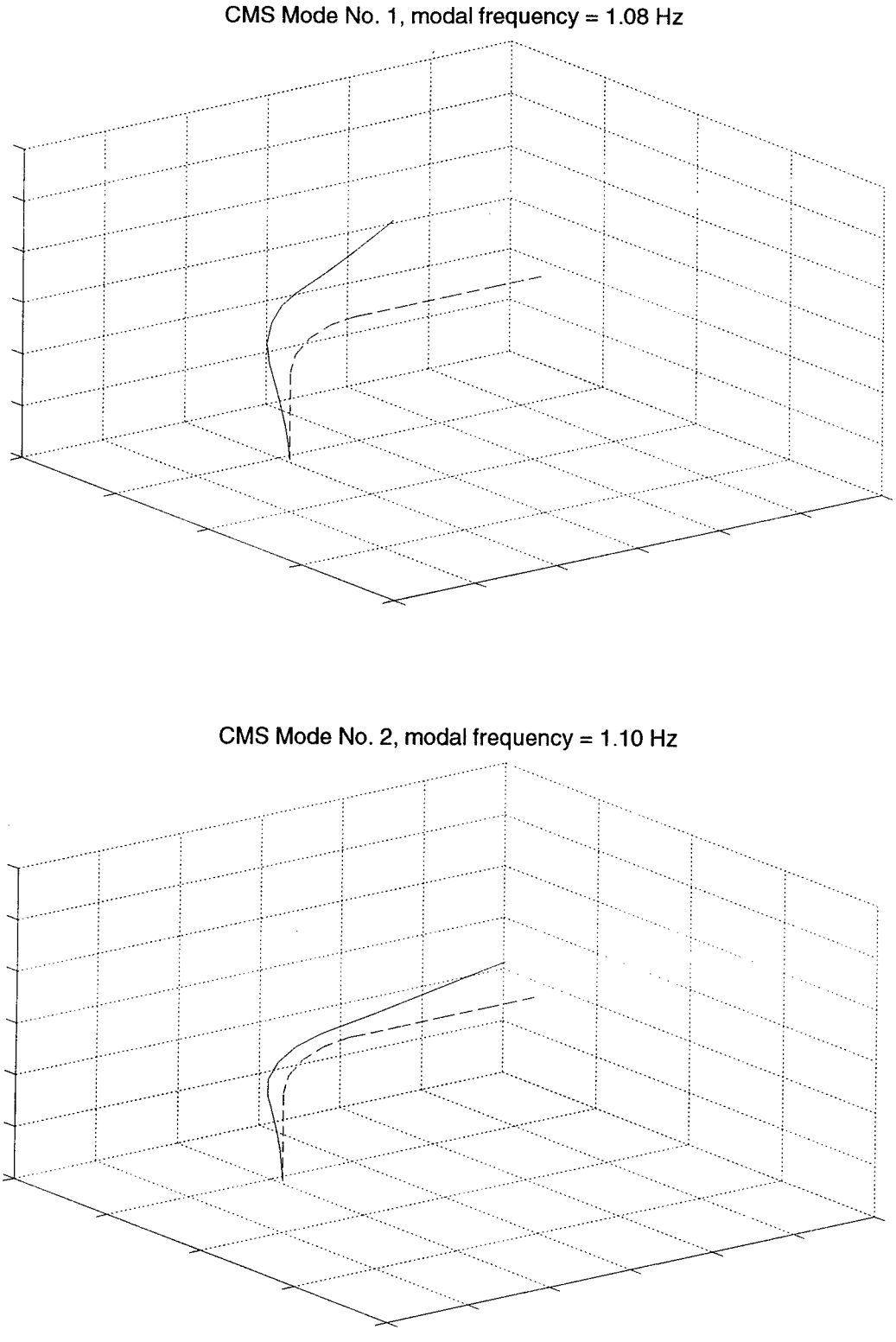


Figure 3.11: Modes of as-built CMS structures

# CHAPTER 4: ANALYSIS OF THE POST AND MAST ARM COMPONENTS

## 4.1 General

A CMS structure is composed of a cantilever post, a mast arm, and an electronic message sign. The structural components resisting the imposed loadings are the cantilever post and the mast arm. Wind-induced fatigue cracks have been observed in the welded connections of these components.

The purpose of this chapter is to report the results of preliminary finite element analyses of the CMS post and mast arm components that were conducted to: (a) support the experimental program, and (b) identify the areas of stress concentrations where potential cracks due to wind loadings are likely to occur. The post and the mast arm were both modeled as elastic cantilever elements subjected to horizontal loadings.

## 4.2 Modeling Techniques

The computer program SADSAP (Wilson, 1992) was used to perform the analysis. The vertical cantilever post and mast arm components (and the horizontal flange plates connecting the mast arm and the extension post) were modeled using a finite element mesh consisting of three-dimensional quadrilateral shell elements available in the SADSAP library. The SADSAP shell element has six degrees-of-freedom per node (three translation and three rotation). Membrane and bending behaviors are coupled within the element. Both membrane and bending effects contribute to the deformation of the vertical tubular post and mast arm sections. Bending effects are more important for the horizontal plate elements. Figure 4.1 shows a typical SADSAP shell element.

The horizontal loads were applied parallel to bolt lines AB and EF, as shown in Figure 4.2. It was assumed that the post and mast arm respond only in the elastic range. The program MATLAB (1996) was used to post-process the analysis data. Although a more refined analysis using fracture mechanics would be useful to study the influence of residual stresses, weld filler material, and crack propagation at the welded joints, such analysis was beyond the scope of the current study.

## 4.3 Modeling of the Cantilever Post

The cantilever post is composed of extra strong pipe with an outside diameter of 18 in. (457 mm) and a wall thickness of 1/2 in. (13 mm). The total height of the post in the field, including the $90°$ arc at its top, is 24 ft (7.3 m). A rectangular conduit hole 4 in. (102 mm) wide by 6 in. (152 mm) long is located 18 in. (457 mm) above the base of the post adjacent to side CD (see Figure 4.2) of the post. The cantilever

post is welded at the base to a 2-3/4 in. (70 mm) octagonal base plate which is attached to the foundation using eight high-strength 2-1/4 in. (57 mm) diameter anchor bolts. Only the vertical portion of the cantilever post, with a total length of 15 ft (4.6 m), was considered in the analysis. The properties of the post, base plate and anchor bolts are shown in Table 4.1.

A total of 1,914 quadrilateral shell elements were used to model the three-dimensional post-base structure shown in Figure 4.3(a). A fine mesh was used to model the lower portion of the post, and a mesh of larger elements was used near the top of the post. The element sizes varied from 3/4 in. by 1-3/4 in. (19 mm by 44 mm) at the base to 4 in. by 1-3/4 in. (102 mm by 44 mm) at the top. The base plate was modeled using 128 quadrilateral shell (plane) elements, as shown in Figure 4.3(b). The conduit hole was also considered in the modeling, as shown in Figure 4.3(c). The post-to-base plate connections were assumed to be rigid.

Equivalent springs were used to model the vertical axial stiffness of the bolts connecting the base plate to the foundation. Horizontal translational displacement of the joints at the location of the anchor bolts was prevented using springs of infinite stiffness. The top of the post was considered to deform freely. The assumed boundary conditions are indicated in Table 4.2.

A unit load acting in the direction parallel to bolt lines AB and EF was applied at the top of the post. The load, shown in Figure 4.3(d), was distributed among all the nodes at the top of the post to avoid undesirable local deformations associated with concentrated loads.

### 4.4 Analytical Response of the Cantilever Post

The post is similar to a cantilever structure, but more flexible due to the flexural rotation at the base of the post. The deformed configuration of the post is shown in Figure 4.4. The maximum displacement, due to the applied unit load, is 0.078 in. (2 mm), which results in a lateral stiffness of 12.8 kips/in. (2.2 MN/m). The computed stiffness of the post, assuming elementary beam theory and base fixity, is 16 kips/in. (2.8 MN/m).

The forces acting on the anchor bolts are shown in Table 4.3. In the direction of loading (longitudinal direction) the shear forces at the base of the post are uniformly distributed among the eight bolts. In the transverse direction the shear forces at bolts A, B, E, and F are more than twice the shear forces in bolts C, D, G, and H. The bolts located along the axis of loading (C, D, G, and H) resist about 80 percent of the overturning moment. The maximum axial stress in the bolts, due to the applied unit load at the top, is 0.5 ksi (3.4 MPa), which is about 1 percent of the bolt yield stress. As a result, the anchor bolts are not the critical elements for the cantilever post.

Figure 4.5 shows the longitudinal and horizontal stress contours on the lines perpendicular to the direction of the applied load; lines GH and CD. On line CD, there is a stress concentration around the conduit hole, and longitudinal stresses larger than 6 ksi (41.4 MPa) have developed. The stresses are more uniformly distributed away from the conduit hole. There is also a disturbance in the distribution of the horizontal stresses near the base. In line GH (opposite side to the conduit hole) where there are no geometric changes, the distribution of longitudinal stresses is linear along the height of the post, and the maximum stress at the base is about 1.5 ksi for a 1 kip load applied at the top of the post.

The distribution of the longitudinal stresses along the height of the post is shown in Figure 4.6. The conduit hole produces a stress concentration of about 6 ksi (41.4 MPa) at the bottom of the conduit hole. On the opposite side of the pipe, the stresses vary linearly along the height and increase slightly near the base. At about 27 in. (686 mm) above the base, the longitudinal stress at line GH is about 1.2 ksi (8.3 MPa); at the base the maximum stress is close to 1.5 ksi (10.3 MPa).

### 4.5 Modeling of the Mast Arm

Mast arms are composed of standard pipe steel with an outside diameter of 18 in. (457 mm) and a wall thickness of 3/8 in. (9.5 mm). An annular plate with an outside diameter of 24 in. (610 mm), an inside diameter of 16 in. (406 mm), and a thickness of 1-3/8 in. (35 mm) is welded to one side of the mast arm. In the field, a similar annular plate is also welded to the top of the cantilever post, and the two plates are connected using 26 high strength 1-3/4 in. (44 mm) diameter bolts uniformly distributed around the flange plates in a circular pattern 1-1/2 in. (38 mm) from the outside edge of the flange plates. A circular conduit hole 2-1/2 in. (63.5 mm) in diameter is located on the underside (compression) side of the mast arm 3-1/2 in. (90 mm) from the flange plate. The mast arm behaves like a cantilever structure suspended horizontally from the post. Table 4.4 shows the mast arm properties.

For the analysis, the mast arm was considered to have a length of 145-3/4 in. (3.7 m). To simulate the connection to the cantilever post, the mast arm was attached to a vertical extension piece with a length of 25-7/8 in. (657 mm) and a wall thickness of 1 in. (25 mm). The modeling of the connection between the mast arm and the extension piece was similar to the post-base plate connection described in the previous section. The total height of the mast arm-extension piece structure from the top of the mast arm to the top of the base plate was assumed to be 15 ft (4.6 m).

A total of 1804 elements were used to model the mast arm-extension piece structure, shown in Figure 4.7(a). A mesh of 338 elements of 2-1/4 in. by 2 in. (57 mm by 51 mm) was used to model the extension piece. The mast arm was modeled using 1200 shell elements of varying dimensions. A fine mesh was used at the lower portion of the mast arm and a more coarse mesh was employed at the top of the mast

arm. The base plate connection to the extension post was modeled using 152 shell (plate) elements, as shown in Figure 4.7(b). The circular plates used to connect the mast arm and the extension piece were modeled using quadrilateral shell (plate) elements, as shown in Figure 4.7(c). The circular conduit hole was also considered, as illustrated in Figure 4.7(d).

A continuous connection was assumed between the extension post and the lower flange plate, and between the mast arm and the upper flange plate. Contact between the flange plates was not considered, and all loads were transferred through the 1-3/4 in. diameter bolts. Therefore, the two flange plates were constrained to have the same translational and vertical displacements at the bolt locations. At the base, translational displacements were prevented (i.e., rigid restraint) and vertical springs were used to represent the anchor bolts. At its top, the mast arm was permitted to deform freely. The boundary conditions for the mast arm and the extension piece are listed in Table 4.5.

In the analysis, the mast arm was loaded using a unidirectional unit force applied uniformly to all the nodes at the top of the mast, as shown in Figure 4.7(e).

### 4.6 Analytical Response of the Mast Arm

The mast arm behaves like a cantilever structure attached to a relatively stiff support. The deformed configuration of the mast arm-extension piece system is shown in Figure 4.8. The maximum displacement due to an applied load of 1 kip is 0.084 in. (2 mm); this corresponds to a lateral stiffness of 11.9 kips/in. (2.1 MN/m). The same structure was also analyzed using the elementary beam theory assuming that the post was fixed at the base and assuming a rigid connection between the extension post and the mast arm. The computed stiffness of this simplified model is 13.2 kips/in. (2.3 MN/m).

The forces acting at the base of the extension piece are shown in Table 4.6. The shear forces at the base of the post are uniformly distributed among the eight bolts; the shear forces at the bolts in the direction of loading are close to twice the value of the applied load at the top of the base. In the transverse direction, the shear forces at the bolts are larger. The maximum forces in bolts A, B and E, F are close to four times the value of the applied unit load. The maximum axial forces in the bolts are approximately 3 kips (8.3 kN); this is equivalent to an axial stress in the bolts of 0.5 ksi (3.4 MPa) for the applied unit load, and 1.4 percent of the nominal yielding resistance of the bolts. At the connection between the mast arm and the extension piece, the maximum axial forces at the bolts are 1.5 kips (4.2 k N), or 5 percent of the yielding resistance of one of the bolts.

Figure 4.9 shows the longitudinal and horizontal stress contours on the sides perpendicular to the direction of the applied load: sides GH and CD. On the side CD, there is a localized stress concentration

around the conduit hole, and stresses larger than 2 ksi (13.6 MPa) are encountered there. The stresses are more uniformly distributed away from the conduit hole. On this side, there is also a disturbance in the distribution of horizontal stresses near the base. On the side GH, where there are no geometric changes, the longitudinal stresses are distributed linearly along the height of the post, and the maximum stress is about 1.5 ksi (10.2 MPa) at the base near the base of the mast arm.

The longitudinal stress profiles along different lines along the height of the mast arm-extension piece, are shown in Figure 4.10. The conduit hole produces stress concentrations of 2 ksi (13.6 MPa) at the bottom of the conduit hole. On the opposite side of the mast arm, the stresses vary linearly over the height and increase slightly near the base. At 27 in. (686 mm) above the base, the longitudinal stress at line GH is about 1.2 ksi (8.1 MPa); at the base the maximum stress is close to 2 ksi (13.6 MPa).

## 4.7 Summary

A preliminary analysis of the cantilever mast and the mast arm indicates that the conduit hole openings introduce significant localized increases in the longitudinal and horizontal stresses. The stresses around the rectangular opening in the cantilever post are 4 to 5 times larger than the stresses on the other side of the post. The smaller circular hole in the mast arm also produces stress concentrations near the conduit hole, but the increase in the stresses (about 50 percent) for the circular opening is smaller than that for the rectangular opening.

Table 4.1: Assumed properties of the cantilever post components

| Component | E (ksi) | Dimensions |
|---|---|---|
| Post | 30,000 | 18" OD, t = 1/2", H = 180" |
| Base plate | 30,000 | 32", t = 2-3/4" |
| Anchor bolts | 30,000 | 2-1/4" diameter |

Table 4.2: Boundary conditions for the cantilever post

| Location | Translational stiffness | | | Rotational stiffness | | |
|---|---|---|---|---|---|---|
| | X (kip/in.) | Y (kip/in.) | Z (kip/in.) | X (kip/rad) | Y (kip/rad) | Z (kip/rad) |
| Anchor bolts | ∞ | ∞ | 30, 000 | ∞ | 0 | ∞ |

Table 4.3: Forces on the anchor bolts of the cantilever post

| Bolt | $F_x$ (kips) | $F_y$ (kips) | $F_z$ (kips) |
|---|---|---|---|
| A | 1.83 | 4.07 | -1.50 |
| B | 1.68 | -3.84 | 1.90 |
| C | -1.96 | 1.64 | 2.58 |
| D | -1.96 | -1.64 | 2.58 |
| E | 1.68 | 3.84 | 1.90 |
| F | 1.83 | -4.07 | -1.50 |
| G | -2.05 | 1.69 | -2.97 |
| H | -2.05 | -1.69 | -2.97 |

Table 4.4: Assumed properties of the mast arm components

| Component | E (ksi) | Dimensions |
|---|---|---|
| Post | 30,000 | 18" OD, t = 3/8", H = 145-3/4" |
| Extension piece | 30,000 | 18" OD, t =1.0", H = 25-7/8" |
| Flange plates | 30,000 | 24" OD, 16" ID, t = 1-3/8" |
| Base plate | 30,000 | 32", t = 2-3/4" |
| Anchor bolts | 30,000 | 2-1/4" diameter |

Table 4.5: Boundary conditions for the mast arm

| Location | Translational stiffness | | | Rotational stiffness | | |
|---|---|---|---|---|---|---|
| | X (kip/in.) | Y (kip/in.) | Z (kip/in.) | X (kip/rad) | Y (kip/rad) | Z (kip/rad) |
| Anchor bolts | ∞ | ∞ | 30, 000 | ∞ | 0 | ∞ |
| Bolts connecting flange plates | ∞ | ∞ | | ∞ | | ∞ |

Table 4.6: Forces at the anchor bolts of the post-mast arm system

| Bolt | $F_x$ (kips) | $F_y$ (kips) | $F_z$ (kips) |
|---|---|---|---|
| A | 1.62 | 3.77 | -1.43 |
| B | 1.61 | -3.75 | 1.45 |
| C | -1.87 | 0.20 | 2.83 |
| D | -1.87 | -0.20 | 2.83 |
| E | 1.61 | 3.75 | 1.45 |
| F | 1.62 | -3.77 | -1.43 |
| G | -1.86 | 0.02 | -2.85 |
| H | -1.86 | -0.20 | -2.85 |
| Bolts at flange plates | | | 1.50 (max.) |

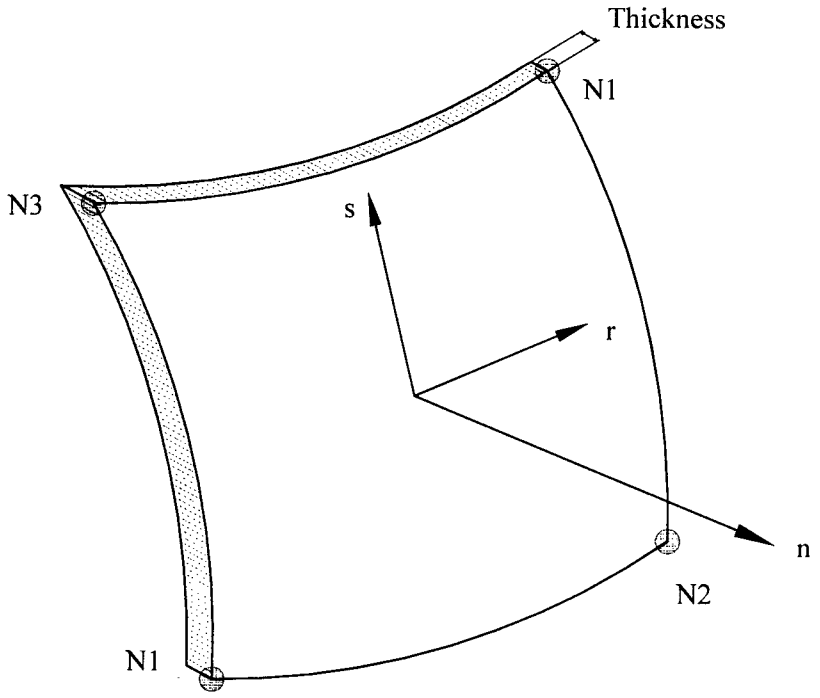


Figure 4.1: Typical shell element

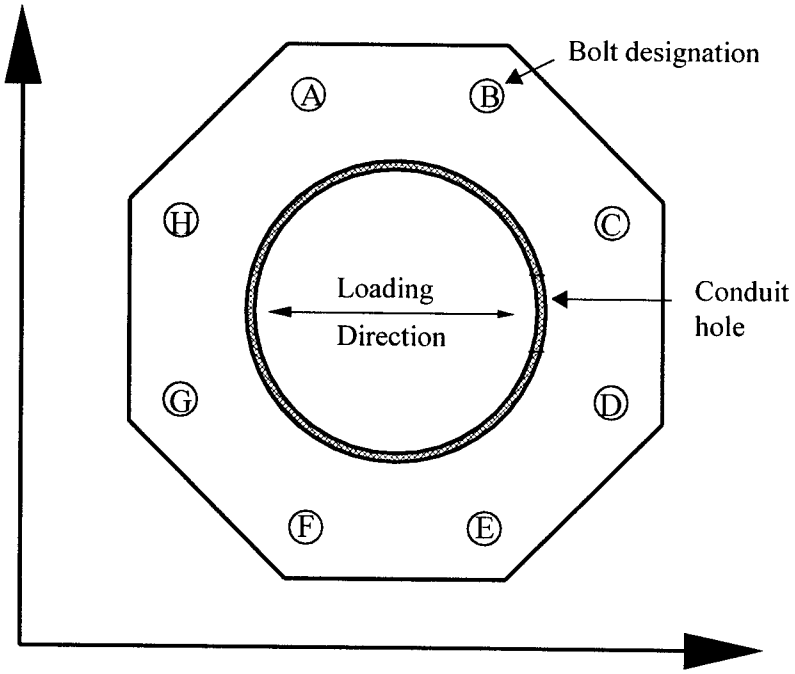


Figure 4.2: Base plate identification and direction of loading

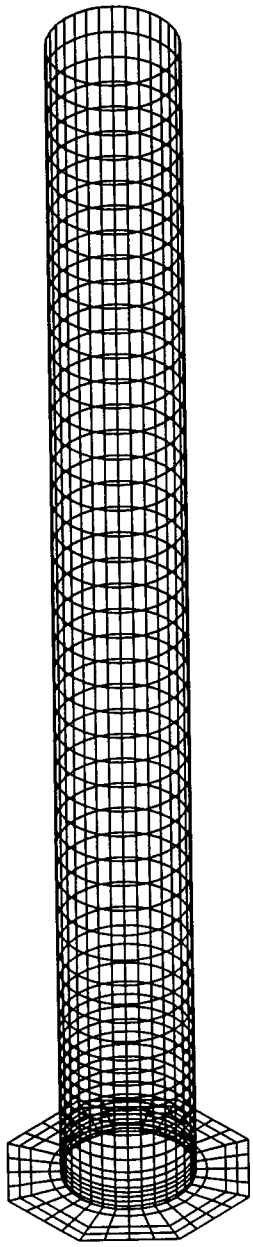

(a) FEM model


(e) Global coordinate system

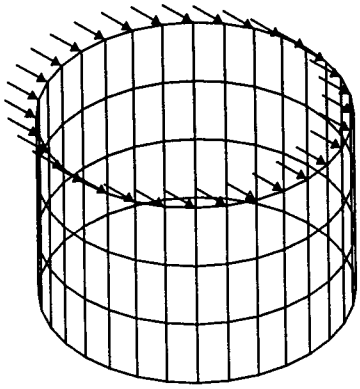

(d) Loading at top of the post

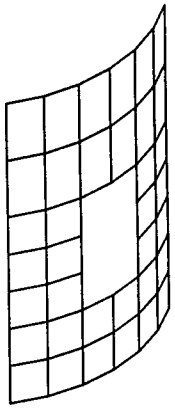

(c) Modeling of the conduit hole

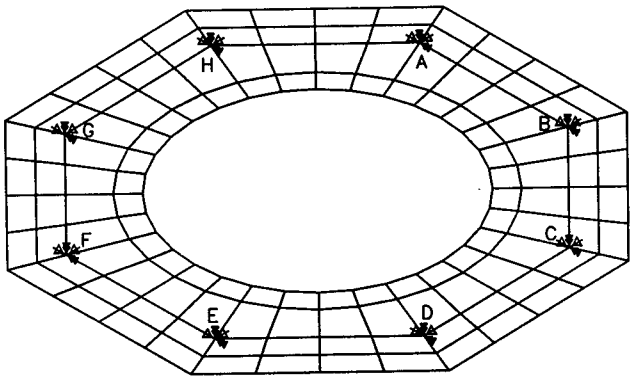


(b) Restraints at the base of the post

Figure 4.3: Modeling of the cantilever post

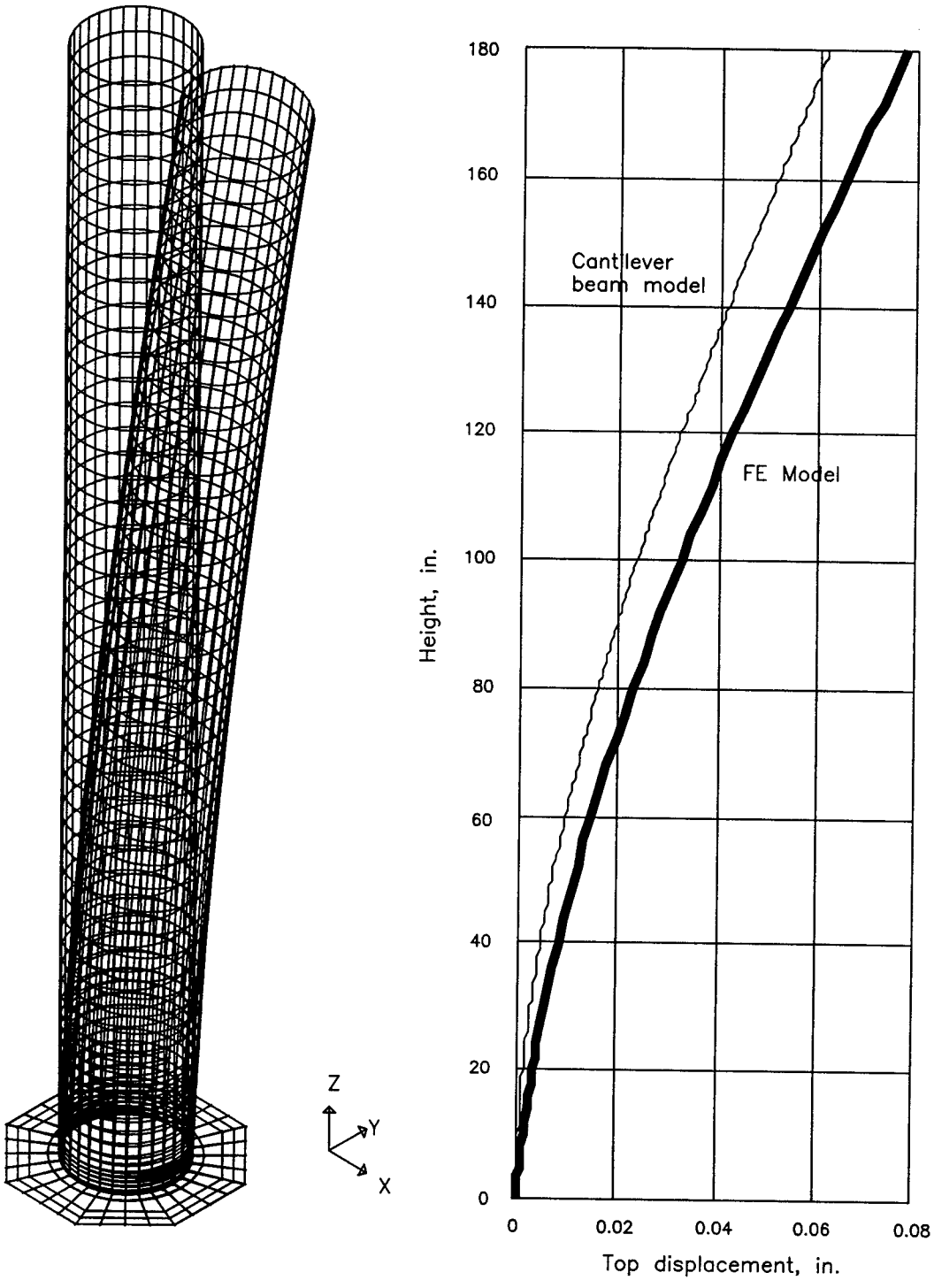


Figure 4.4: Deformed configuration of the cantilever post

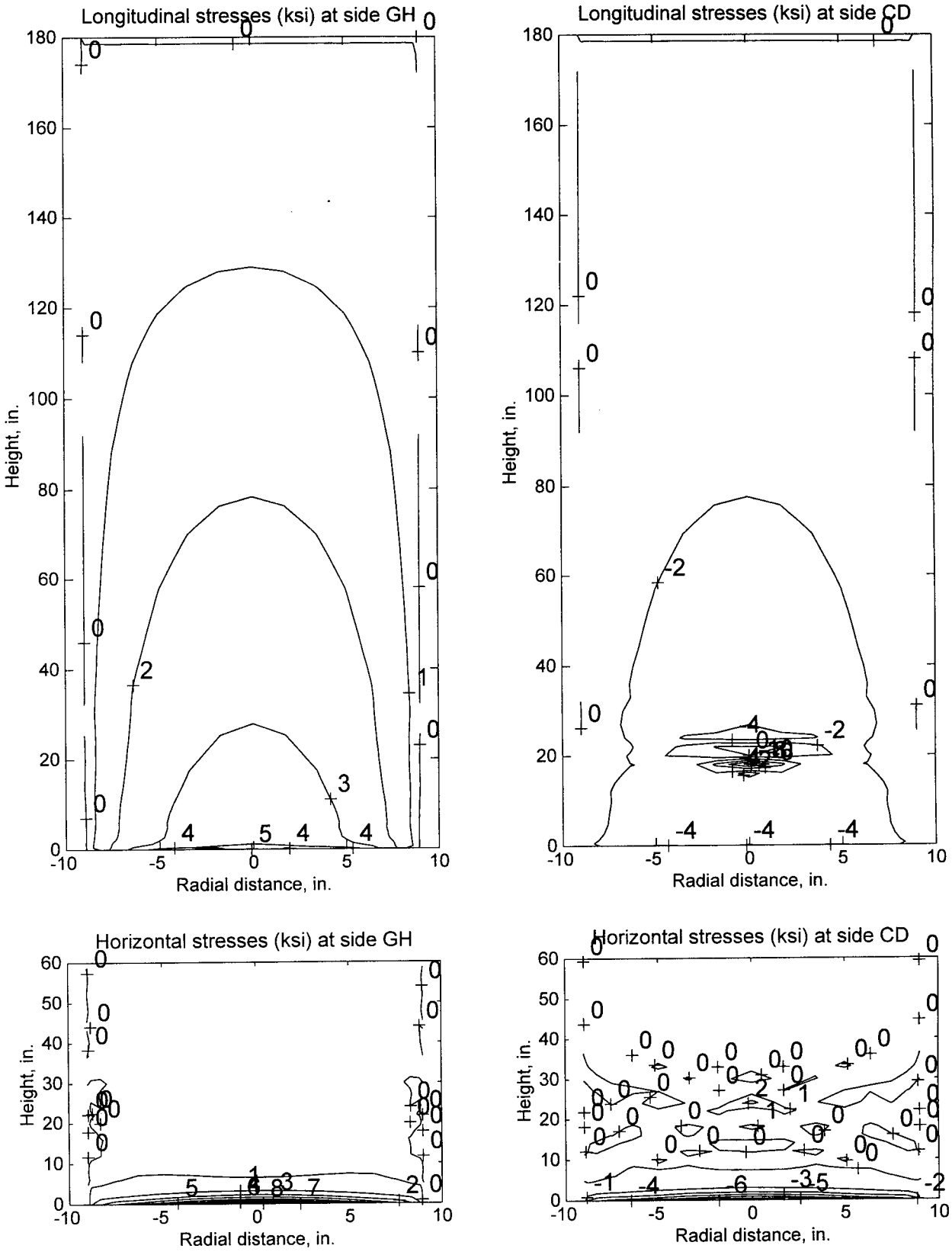


Figure 4.5: Stress contour for the cantilever post

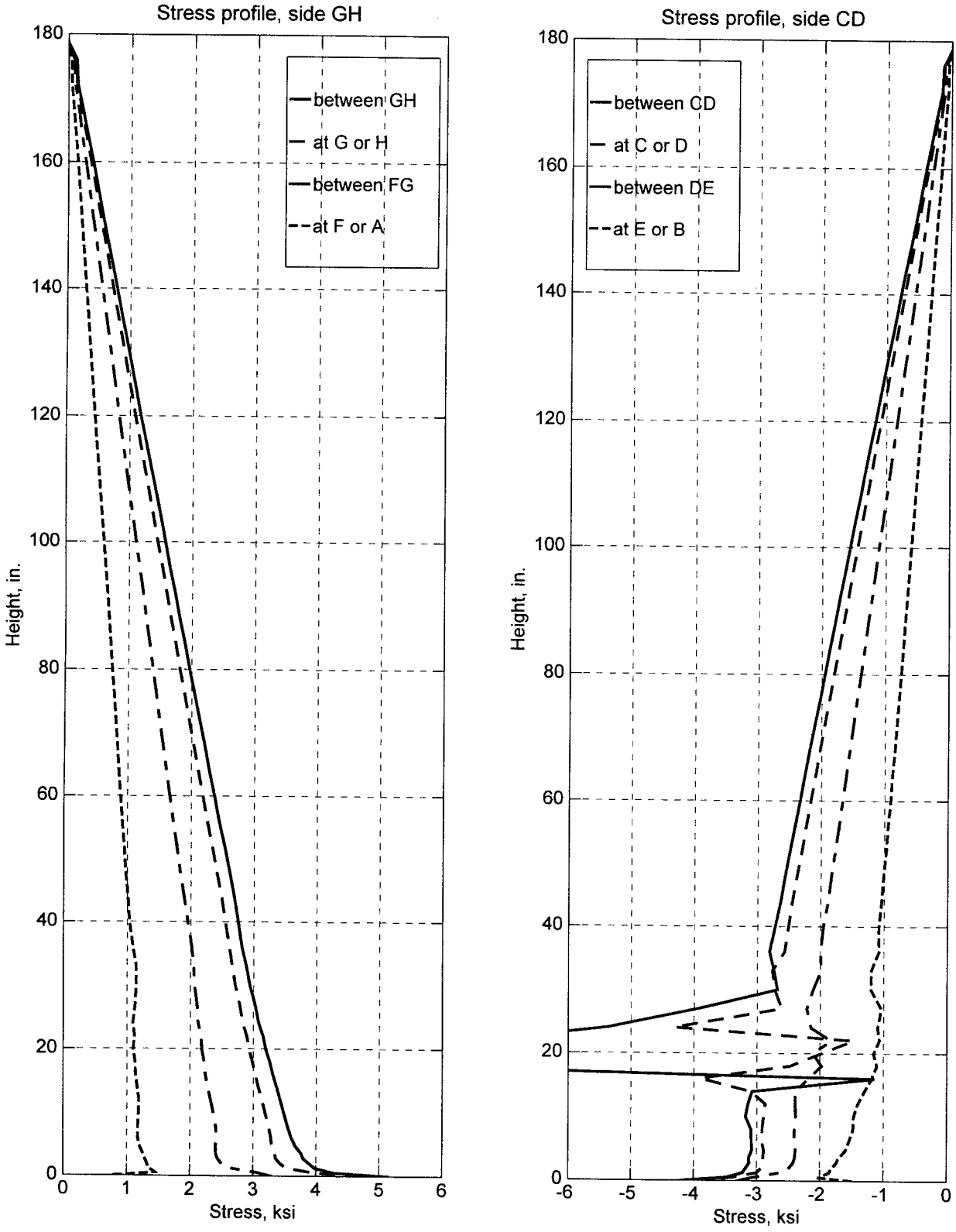


Figure 4.6: Stress distribution along the height of the cantilever post

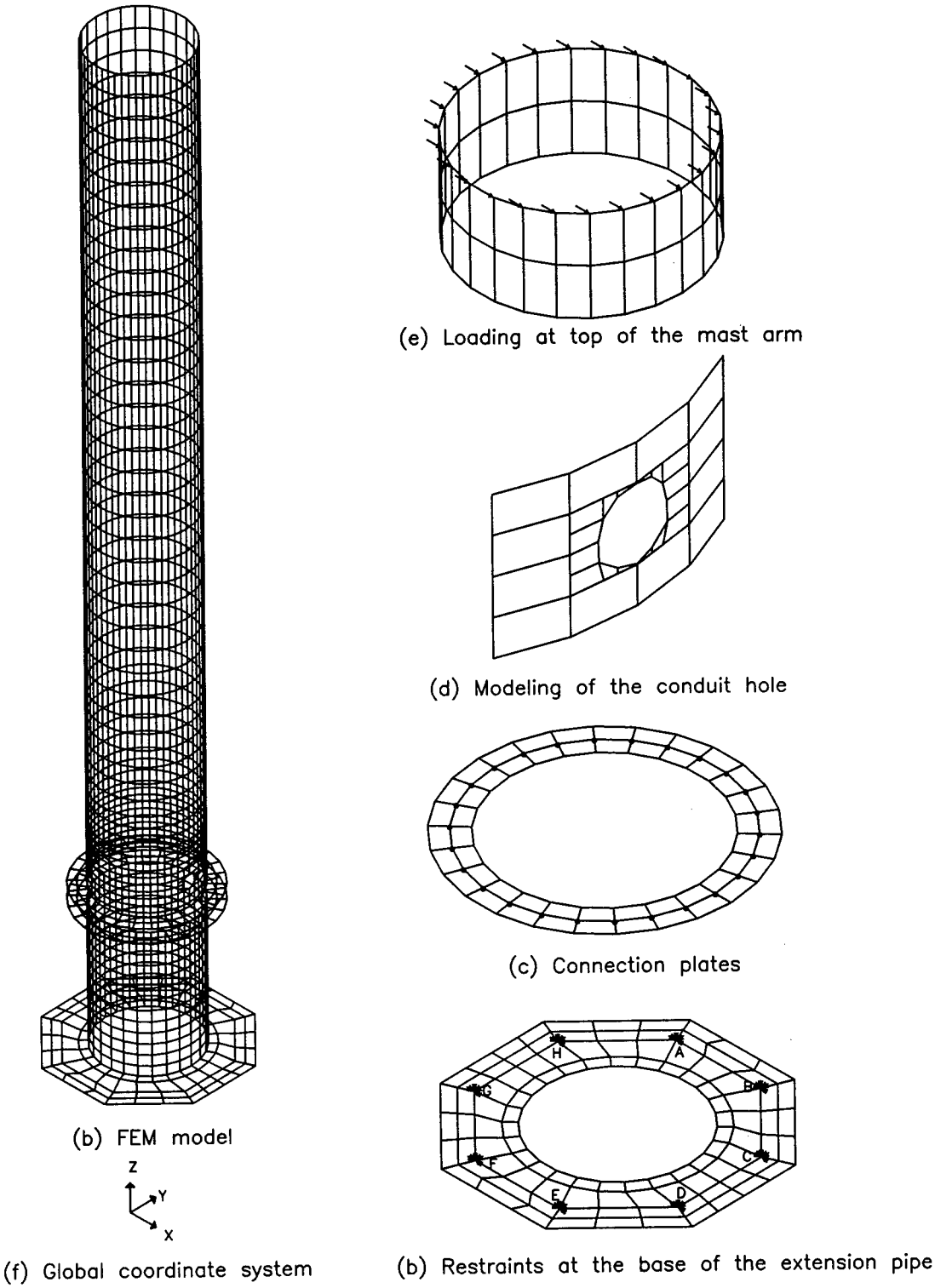


Figure 4.7: Modeling of the mast arm

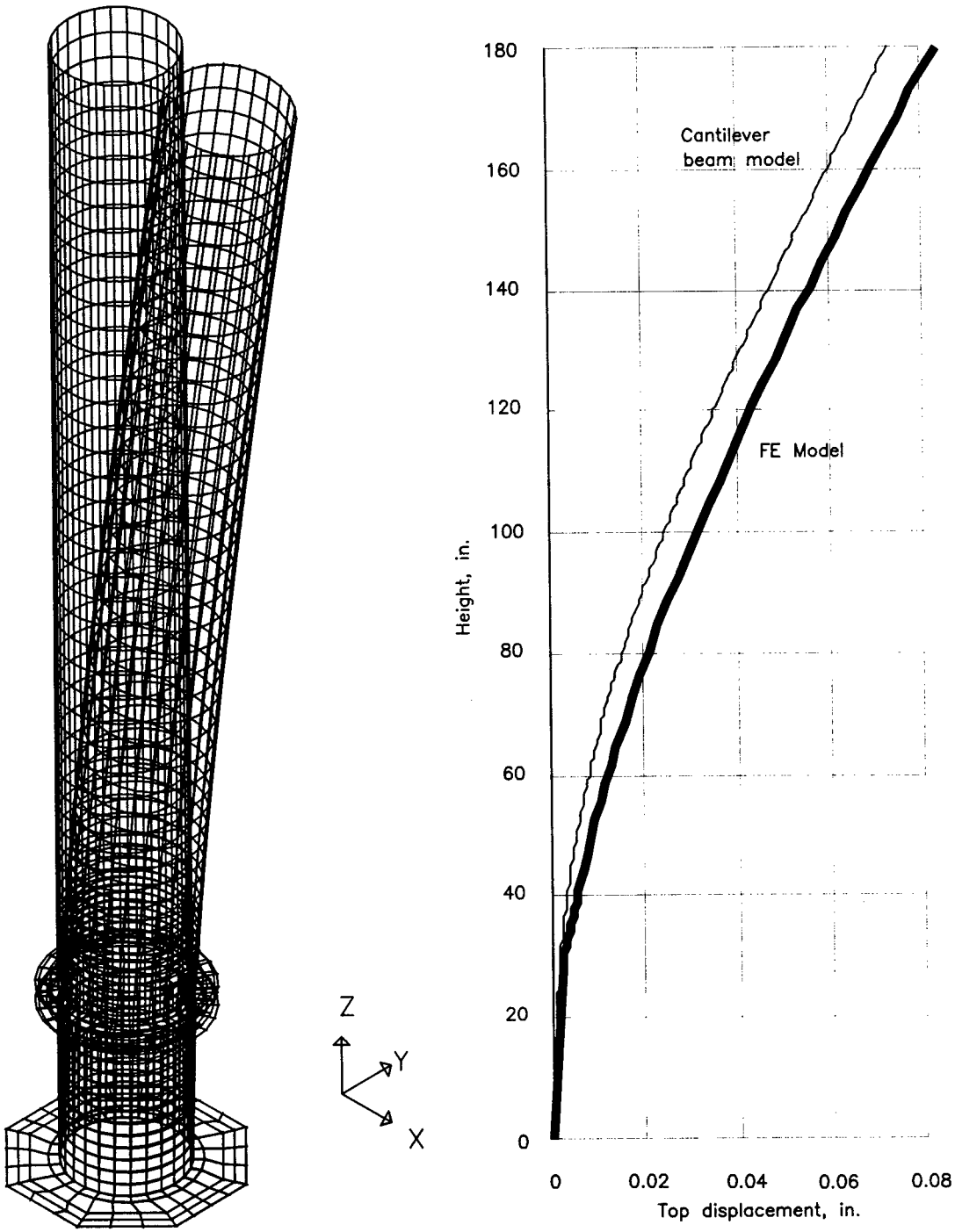


Figure 4.8: Deformed configuration of the mast arm

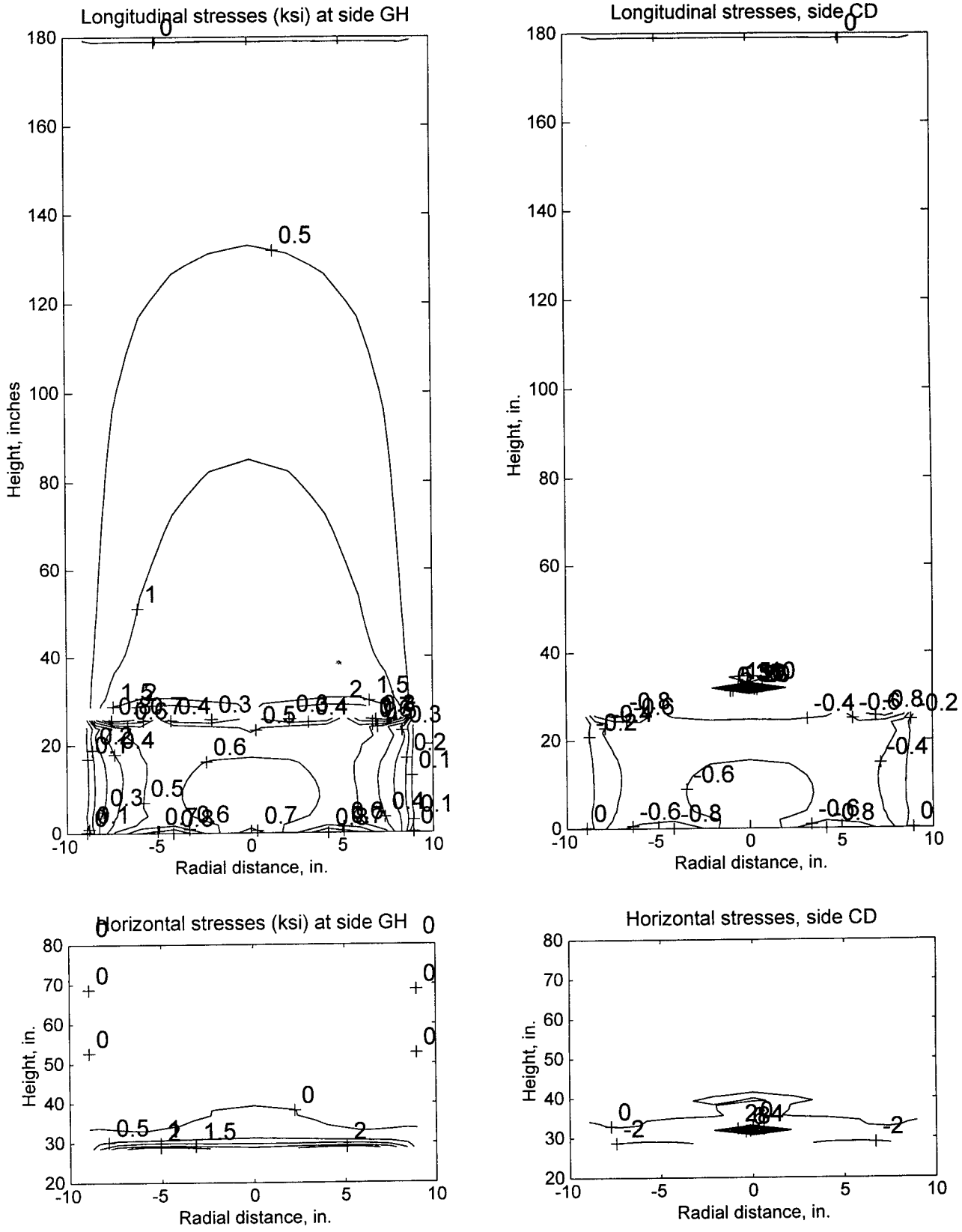


Figure 4.9: Stress contour for the mast arm

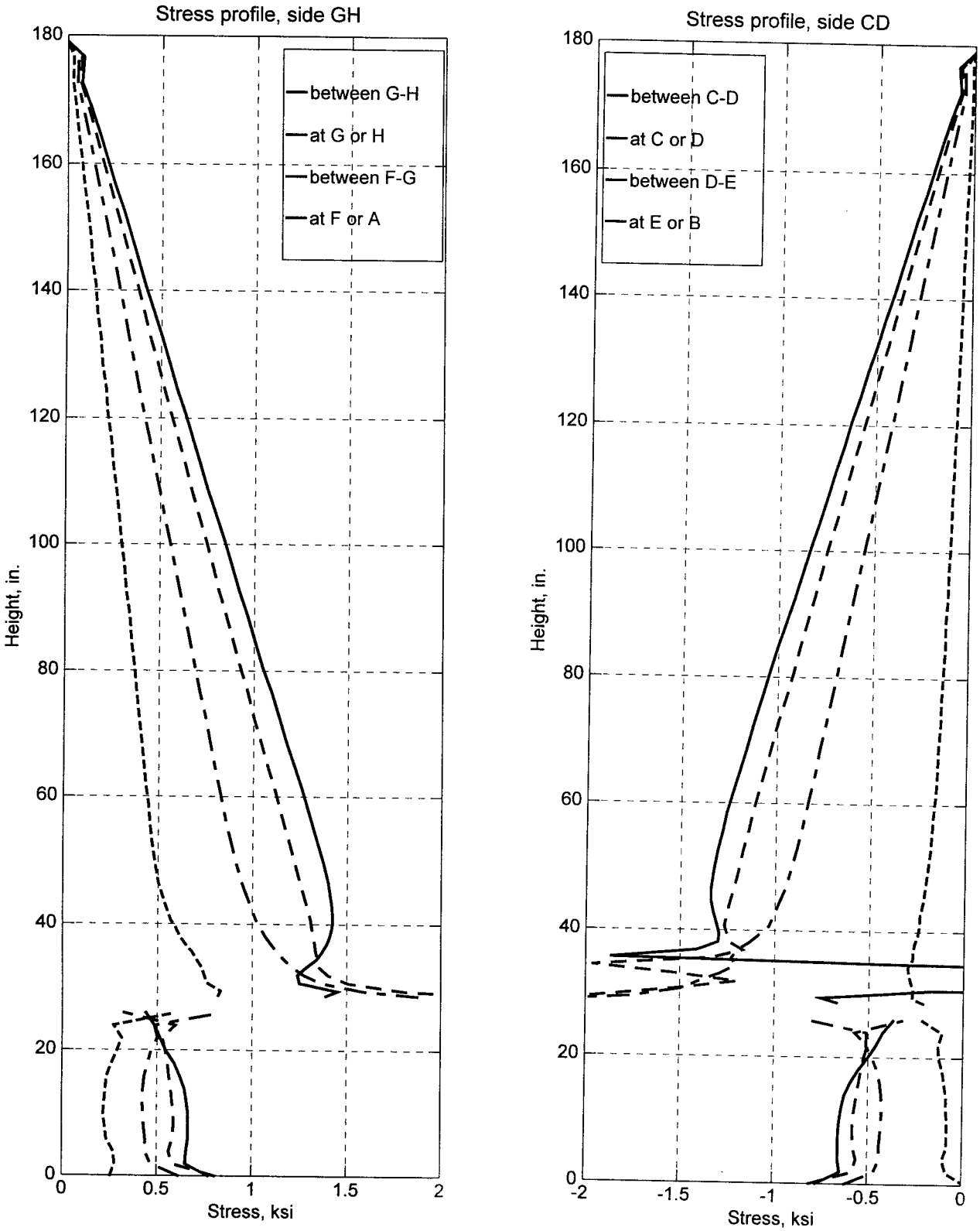


Figure 4.10: Stress distribution along the height of the mast arm

# CHAPTER 5: EXPERIMENTAL PROGRAM

## 5.1 General

The experimental program for the as-built specimens involved the full-scale testing of CMS cantilever post and mast arm components. Tests were conducted to estimate the fatigue life of the welded moment connections. Four specimens were tested; one cantilever post structure with a full-penetration connection (Specimen AB1) and three cantilever mast arms (Specimens MA1, MA2, and MA3). The sequence of testing of the as-built CMS structures is shown in Table 5.1.

This chapter describes the specimens (fabrication, material properties, welding procedure, and inspection) and the experimental program (test setup, test parameters, instrumentation, and data acquisition system).

## 5.2 Fabrication Procedure

### *5.2.1 Fabrication*

The cantilever post structure, specimen AB1, was fabricated by Sierra Nevada Steel Corp. of San Fernando, California (a Caltrans approved vendor) specifically for testing at the Earthquake Engineering Research Center (EERC). The mast arm specimens, (MA1, MA2, and MA3), were fabricated by Sierra Nevada Steel Corp. as part of three CMS structures designated for field installation. East Bay Steel Products, Inc., of Oakland, California (a local Caltrans approved vendor) modified the cantilever tip of the mast arms for connection to the horizontal actuator. An extension piece was fabricated by East Bay Steel Products, Inc. and fitted beneath the mast arm specimens to permit the use, without modification, of the test assembly developed for the Specimen AB1 (see Figure 5.4).

### *5.2.2 Material Properties*

Coupon testing of the anchor bolts and the pipe material was undertaken to determine the mechanical properties of the test specimens. Good agreement between the mill certificate and the coupon test data was obtained. A summary of material testing data for all test specimens is presented in Table 5.2.

### *5.2.3 Welding Procedure and Inspection*

All local fabrication and repair work was performed in accordance with Caltrans approved AWS procedures and monitored by Caltrans inspectors.

At the time the experimental work was conducted, standard Caltrans inspection practice consisted of visual inspection of the fabricated CMS structures prior to shipment to the field. Based on experience gained during the SAC testing program at EERC (Whittaker, et al. 1996), ultrasonic testing (UT) was also employed to detect weld imperfections for all specimens, except AB1. Comments on improving Caltrans inspection techniques are presented in Chapter 8.

## 5.3 Experimental Program

### *5.3.1 Test Setup*

To simulate field conditions, a reinforced concrete foundation block was cast and anchored to the strong floor in the Structures Research Laboratory at EERC. The concrete foundation block was intended to simulate the CIDH pipe typically used as the foundation for 18 in. (46 mm) diameter CMS structures. As shown in Figure 5.1, specially fabricated anchor bolts, identical to the bolts used in the field, were embedded in the foundation. The specimens were attached to the foundation using anchor bolts to Caltrans specifications. Each specimen was leveled using nuts underneath the base plate. The anchor bolts at the base plate were initially snug-tight and then tightened further using the 1/3-rd turn-of-nut method (AISC, 1995). The gap between the base plate and the foundation was grouted with cement mortar.

A support frame was designed and fabricated for attachment to an existing reaction frame in the Structures Research Laboratory at EERC. Two catwalks and a supporting framework were built to provide access to the top of the specimen at its connection to the servo-actuator. Figure 5.2 shows the test setup for Specimen AB1. Figure 5.3 and Figure 5.4 show schematics of the test setup for the post and mast arm specimens, respectively.

Each specimen was loaded at its top using a servo-hydraulic actuator attached to the reaction frame. The actuator consisted of a double acting ram with a capacity of 100 kips (445 kN), a stroke of 20 in. (508 mm), and a maximum flow rate of 200 g.p.m. (757 l.p.m.)

### *5.3.2 Test Parameters*

The specimens were tested vertically. An unidirectional displacement history was imposed at the top of the post. Axial load, to simulate the weight of the mast arm and the sign, was not imposed on any of the specimens. Other post and mast arm deformations observed in the field, such as those due to torsion and bidirectional displacements, were not accounted for.

A testing frequency of 5 Hz was selected for the test. This frequency is within the range of 1 to 13

Hz used in other studies (Fisher, et al., 1974; Schilling, et al., 1978; Fisher, et al., 1980), and is smaller than the specimen frequency (approximately 10 Hz) and the oil-column frequency of the servo-actuator. The tests were conducted at this frequency, and dynamic resonance effects were not observed. All tests were performed at room temperature.

The mean stress for Specimen AB1 was zero. Static dead-load stresses varying across the pipe diameter were imposed on the mast arm specimens, MA1, MA2, and MA3, to mimic the bending moment induced in the specimen due to the dead weight of the sign.

### *5.3.3 Instrumentation*

The instrumentation for the various specimens consisted of: a LVDT on the actuator center line measuring the imposed displacement; a load cell in line with the actuator measuring the axial force in the actuator; and longitudinal strain gages placed at strategic locations along the height of the specimens measuring the local stresses parallel to the vertical axis of the post. The layout of the strain gages varied from specimen to specimen. Chapters 6 and 7 detail the instrumentation layout for each specimen. Figure 5.5 shows specimen AB1 instrumented with strain gages.

### *5.3.4 Data Acquisition*

The test machine and data acquisition system are run by a PC Windows-based control and acquisition program called Automated Testing System (ATS) developed by SHRP Equipment Corporation of Walnut Creek, California. This program is capable of signal generation, four channel servo-actuator command, and sixteen-channel data acquisition. For the tests documented on herein, the ATS system was used to monitor and control the displacement and force-feedback signals.

Other data was monitored and recorded using an AutoNet data acquisition system with a capacity of 64 channels. Pacific signal conditioners were used to amplify the transducer signals and to remove frequencies above 100 Hz from the analog signal.

In order to limit the size of the data files, data was recorded for two seconds every 16 minutes. Each two-second data file records 10 cycles of response: 200 sample points for each recorded channel. The data was constantly monitored during the test. Part of the data acquisition system is shown in Figure 5.6.

### 5.4 Definition of Specimen Failure

For the purpose of these tests, failure was defined as the smaller number of the cycle count corresponding to either the resistance of the specimen dropping below 90 percent of the maximum resistance at maximum displacement (termed Type 1 failure in this report) or propagation of cracks in the post-base plate (or mast arm-flange plate) groove-welded connection (termed Type 2 failure in this report). Engineering judgement, and strain-gage data immediately above the groove-welded connection, were used to assign a cycle count to the point of crack propagation.

Table 5.1: List of test specimens

| Test No. | Specimen ID | Connection Details | | | |
|---|---|---|---|---|---|
| | | Type | Weld Type | Cut-off Hole | Conduit Hole |
| 1 | AB1 | as-built | full-penetration | no | rectangular, tension side |
| 3 | MA1 | as-built | full-penetration | no | circular, compression side |
| 4 | MA2 | as-built | full-penetration | no | circular, compression side |
| 5 | MA3 | as-built | full-penetration | no | circular, compression side |

Table 5.2: Material properties of test specimens

| Member | Size | Grade | Yield Stress (ksi) | | Ultimate Stress (ksi) | |
|---|---|---|---|---|---|---|
| | | | Mill Certificate | Coupon Test | Mill Certificate | Coupon Test |
| AB1 | | | | | | |
| Post | 18" OD, t = 1/2" | B/X42/A53 | 61 | 64 | 71 | 71 |
| Base plate | t = 2-3/4" | A36 | 42 | NT[a] | 70 | NT |
| Anchor bolts | d = 2-1/4", l = 39-3/4" | A36 | 46 | 41 | 70 | 69 |
| Patch plate | t = 5/8" | A572 Gr 50 | 50 | NT | 75 | NT |
| MA1, MA2, MA3 | | | | | | |
| Post | 18" OD, t = 3/8" | B/X42/A53 | 54 | 52 | 75 | 70 |
| Flange plate | t = 1-3/8" | A36 | 45 | NT | 74 | NT |
| Anchor bolts | d = 2-1/4", l = 39-3/4" | A36 | 46 | 41 | 70 | 69 |
| Base plate | t = 2-3/4" | A36 | 42 | NT | 70 | NT |
| Extension | 18" OD, t = 15/16" | A53 | 47 | NT | 80 | NT |

a. NT designates Not Tested

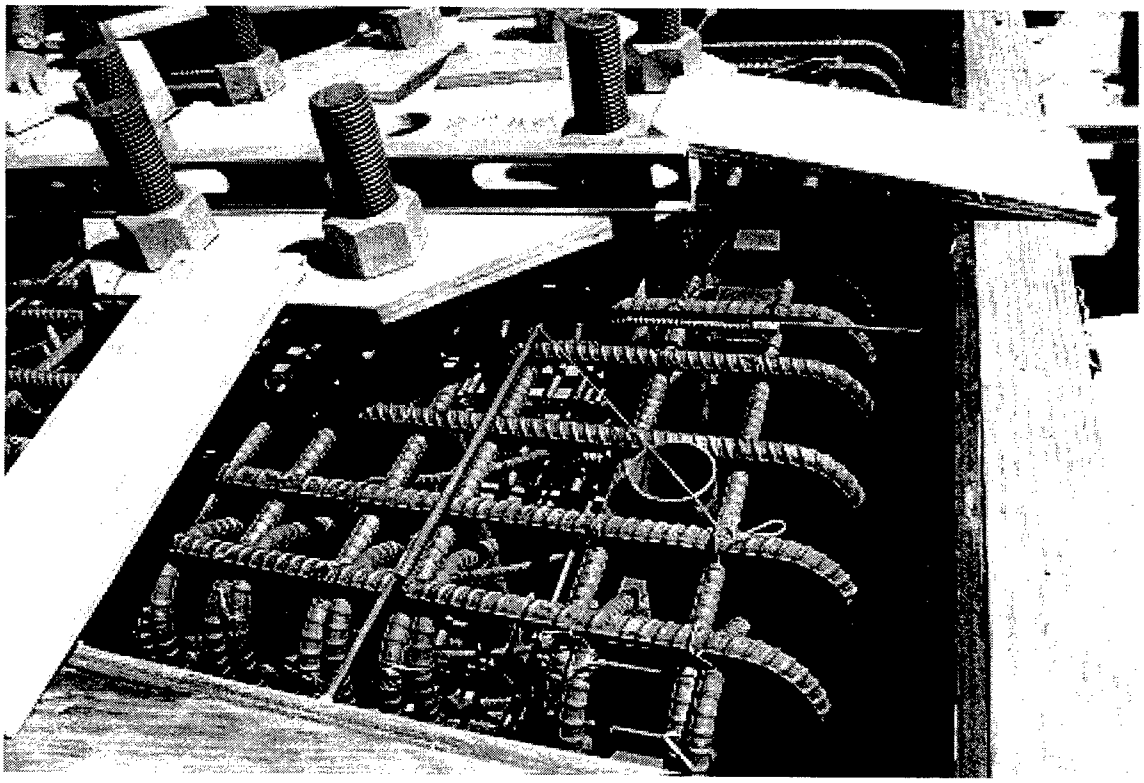

Figure 5.1: Foundation detail for Specimen AB1

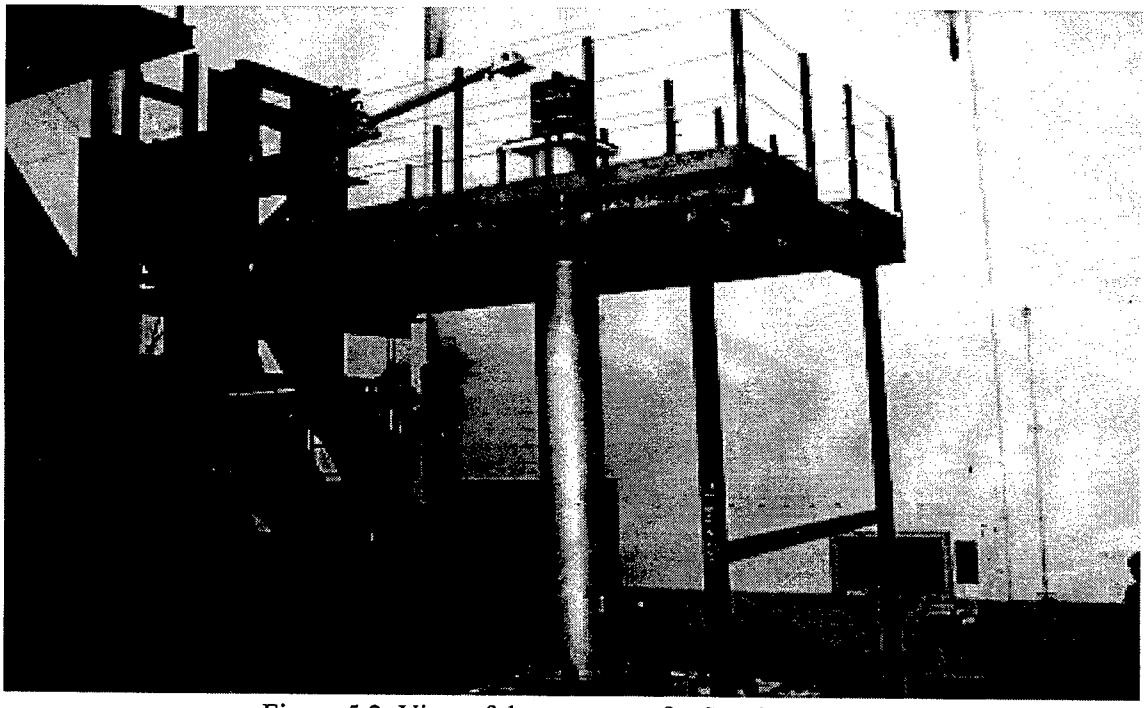

Figure 5.2: View of the test setup for Specimen AB1

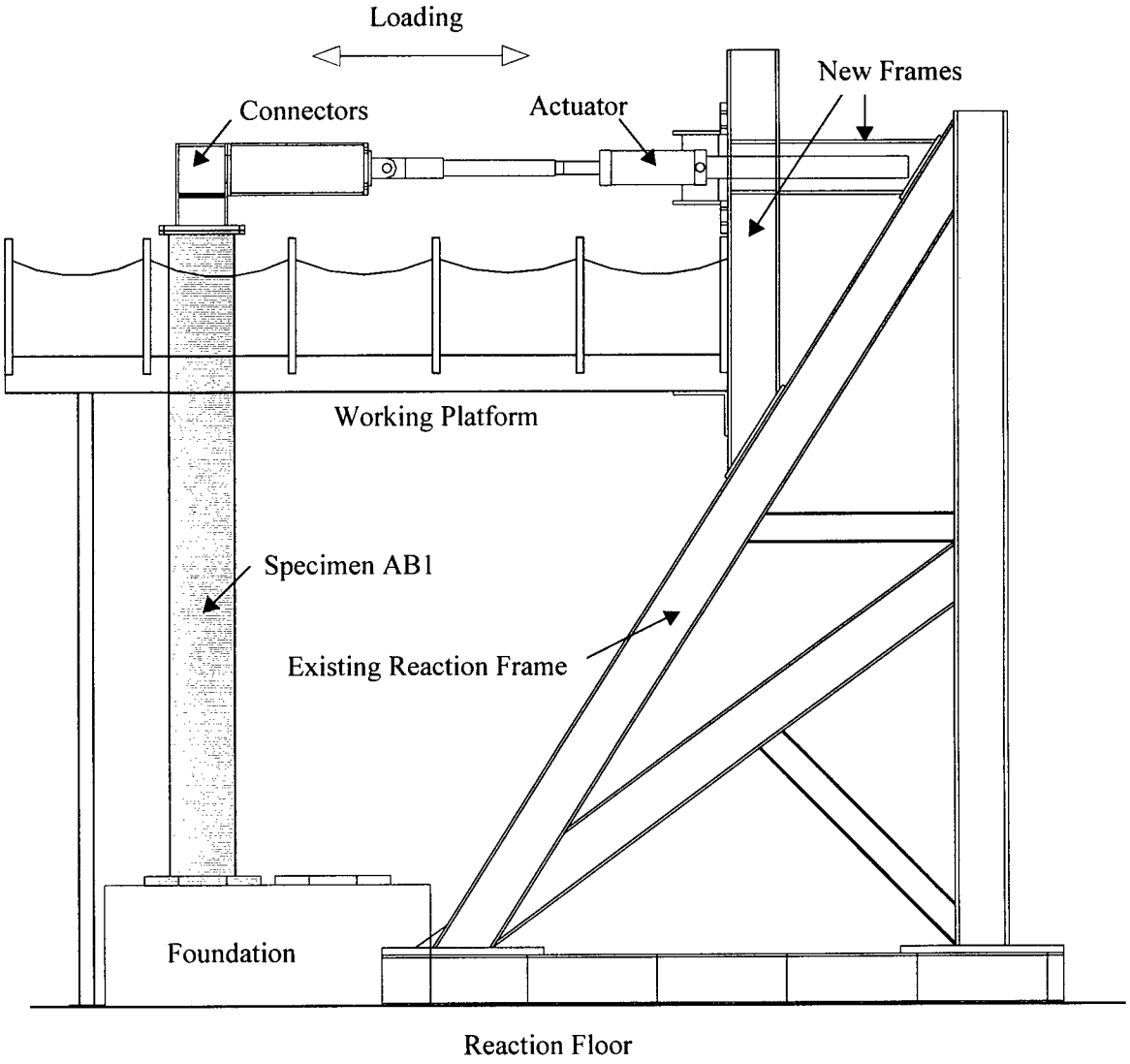


Figure 5.3: Main components of the test setup for Specimen AB1

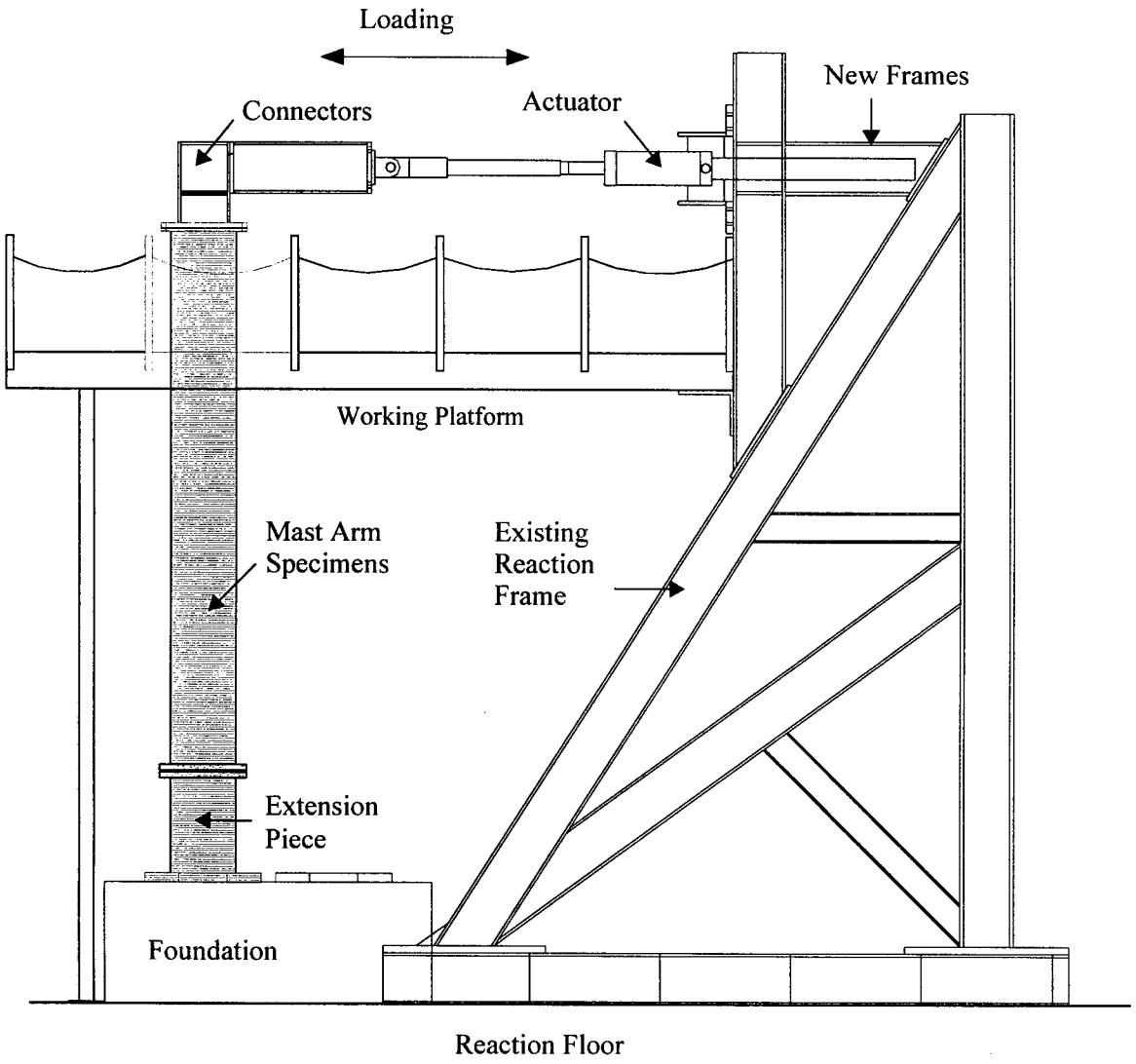


Figure 5.4: Main components of the setup for the mast arm specimens

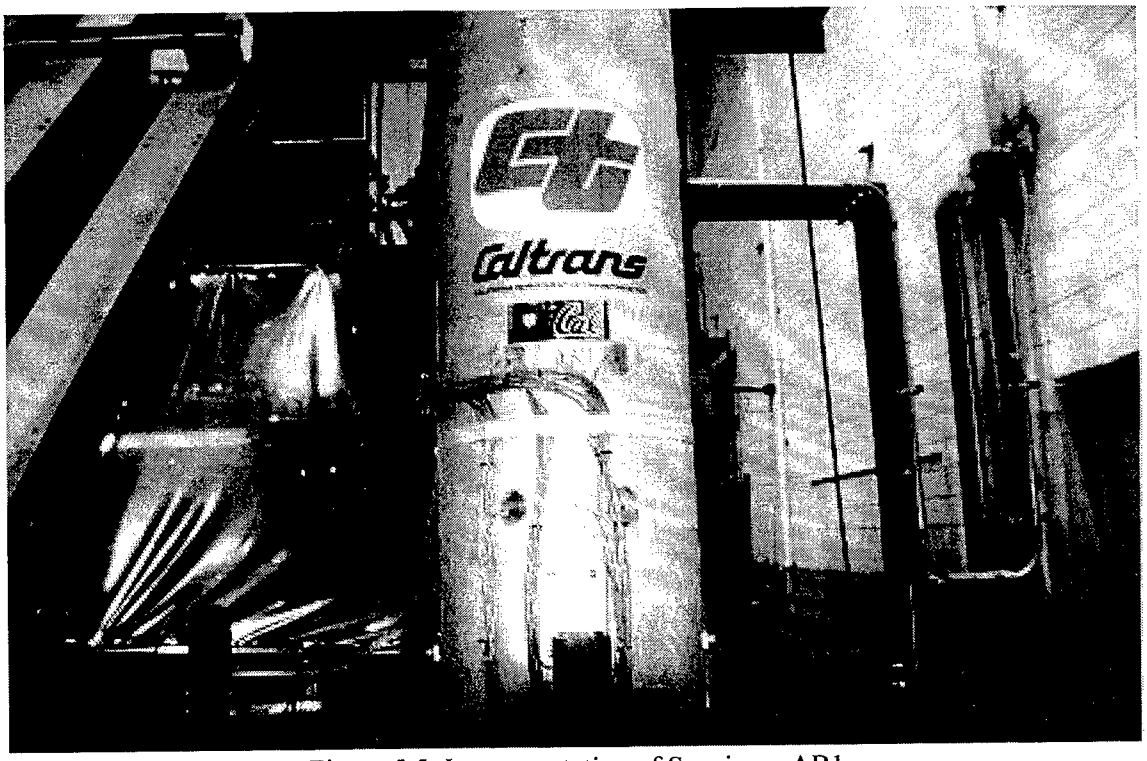


Figure 5.5: Instrumentation of Specimen AB1

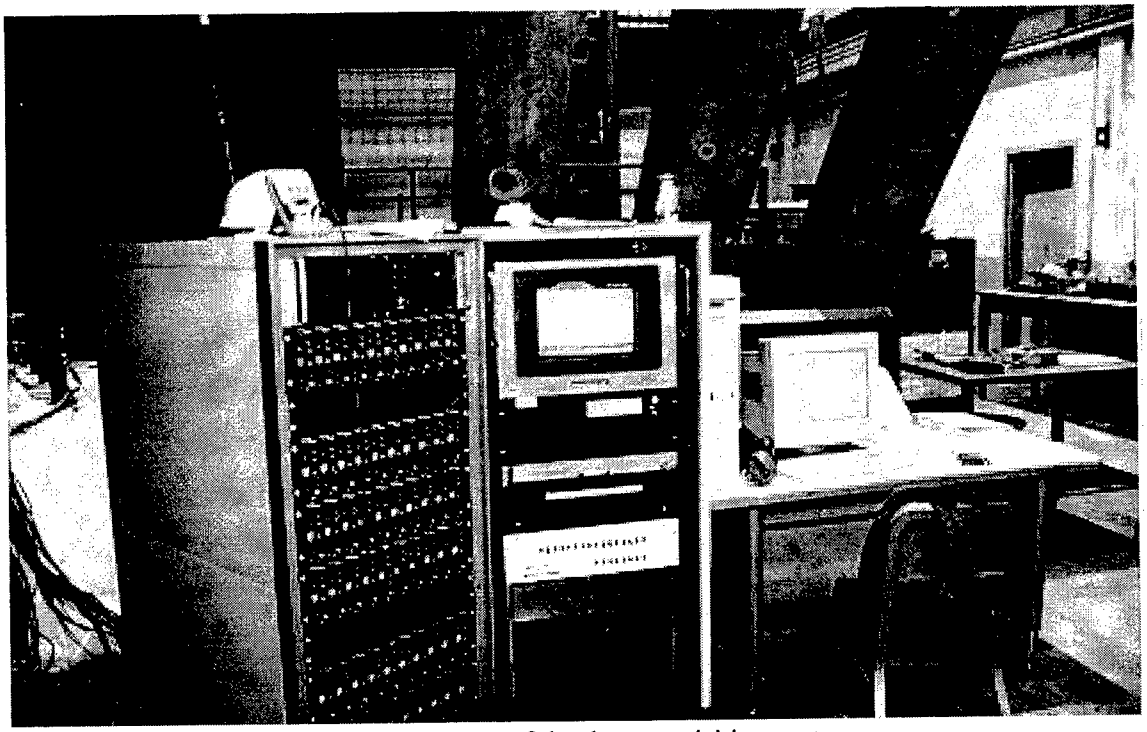

Figure 5.6: View of the data acquisition system

# CHAPTER 6: RESPONSE OF SPECIMEN AB1

## 6.1 General

Specimen AB1 is an as-built cantilever post with a full penetration post-to-base connection. The post has a rectangular, 4 in. by 6 in. (102 mm by 152 mm) conduit hole located 18 in. (457 mm) above the top of the base plate to permit wiring to be run up the inside of the post to the mast arm. In some field CMS structures a drainage hole is flame cut just above the post-to-base plate welded connection to facilitate the discharge of the galvanizing material. No drainage holes wee cut in the specimen AB1. The specimen was inspected and approved by Caltrans prior to shipment to EERC.

Figure 6.1 shows the details of a full penetration post-to-base connection designed to Caltrans specifications (Gugino and Woody, 1996). A 4 in. by 1 in. (102 mm by 25 mm) backing ring was placed inside the post (or mast arm) and tack welded to the base plate (or splice plate). This ring serves as a back-up bar for the groove weld of the post (or mast arm) to the base plate (or splice plate). The root pass of the groove weld cannot be visually inspected, and ultrasonic testing may not be reliable because wave reflections due to the presence of the backing ring may distort the ultrasonic readings. This lack of access for inspection is a major reason why this type of connection is rated E' in the AASHTO specifications (see Chapter 2). Figure 6.1 also shows a view of the section around the conduit hole. The conduit hole is flame cut, but its edges are not ground smooth nor are its corners cut to a radius; a stiffening tube is fillet welded to the post as shown in Figure 6.1.

## 6.2 Specimen Properties and Specimen Setup

Specimen AB1 was fabricated using extra strong steel pipe with a nominal yield stress of 60 ksi (414 MPa) and a modulus of elasticity of 30,000 ksi (207 GPa). Coupon testing of the pipe section produced values of yield stress equal to 64 ksi (441 MPa) and ultimate stress equal to 71 ksi (490 MPa), as indicated in Table 5.1. The pipe had an outside diameter of 18 in. (457 mm) and a wall thickness of 1/2 in. (13 mm). The height of the test specimen was 14 ft 4 in. (4.4 m). The post was groove welded at its base to a 2-3/4 in. (70 mm) thick octagonal ASTM A36 base plate. The plate was attached to the foundation using eight high-strength anchor bolts, following the Caltrans guidelines. A rectangular plate was welded to the top of the post to facilitate the connection of the post to the servo-actuator. The post was positioned such that the direction of loading was normal to the vertical face of the conduit hole. The identification and dimensions of the specimen are shown in Figure 6.2.

### 6.3 Test Parameters

Specimen AB1 was tested under displacement control with displacements applied at the tip of the post (see Figure 5.3). The unidirectional cyclic loading was applied at a frequency of 5 Hz. The displacement needed to achieve the target stress range was obtained by monitoring the stress range at 27 in. (686 mm) above the top of the base plate. This location was above the conduit hole at a point where the stresses in the post were likely not affected by the presence of the conduit hole.

The target stress range, $\Delta\sigma$ ($= \sigma_{max} - \sigma_{min}$), was determined using the strain data obtained from field testing (Winter, 1996). Specimen AB1 was tested at a stress range of 10 ksi (69 MPa) at 27 in. (686 mm) above the base plate. This corresponds to a nominal stress range of approximately 12 ksi (83 MPa) at the top of the base plate. The target number of cycles for Specimen AB1 was set at 4,000,000. The cycle count of 4,000,000 is twice the value of 2,000,000 used by AASHTO (1992) as the constant amplitude fatigue threshold.

Dead-load forces, simulating the effects of the weight of the mast arm, were not applied to Specimen AB1. The load was applied symmetrically with a mean stress equal to zero and a stress ratio, $R$ ($= \sigma_{max}/\sigma_{min}$) equal to -1. The face of the post adjacent to the conduit hole (North side) between bolts C and D, and the opposite face to the conduit hole (South side) between bolts G and H, were subjected to both tensile and compressive loadings (stresses).

### 6.4 Instrumentation

The instrumentation for Specimen AB1 consisted of:

- An LVDT on the servo-actuator center-line measuring the imposed displacement at the tip of the post.
- A load cell in-line with the servo-actuator measuring the imposed force.
- Forty-eight strain gages placed longitudinally along the height of the post at strategic locations. The gages were placed either at the extreme fibers (with respect to the imposed loading), or on the bolt lines adjacent to the extreme fibers. These gages measured axial strains parallel to the vertical axis of the post and were used to identify crack formation and propagation at the critical section along the height of the post.
- Three groups of four displacement transducers (DCDTs) were placed at three levels adjacent to the base of the post to monitor ovaling (out-of-shape) deformations of the post near its base. The DCDTs in each group were oriented at $90°$ to the face of the pipe.

The instrumentation list and a schematic diagram of the strain gage and DCDT locations are shown in Table 6.1 and Figure 6.3, respectively.

## 6.5 Crack Detection and Monitoring

Crack detection gages were developed at EERC for Specimen AB1 and placed across the post-to-base connection to monitor the initiation of cracking at the base of the post. The presence of cracks was also monitored by a combination of visual observation and liquid dye penetrant, and then confirmed by analysis of the variation in the strain-history response (shifts or changes in the amplitude) near the base of the post and adjacent to the conduit hole. The latter techniques proved to be more useful in determining the presence and growth of cracks than the crack detection gages; the use of these gages was discontinued following testing of Specimen AB1.

## 6.6 Experimental Results

### *6.6.1 General*

The accumulated number of loading cycles for Specimen AB1 was nearly 2.7 million. A total of 585 records (each containing 10 cycles) were recorded during the test. Substantial fatigue-induced cracking was observed initially around the rectangular conduit hole and later in the weld in the post-to-base plate connection. Table 6.2 summarizes the crack history for Specimen AB1. The test was terminated when the resistance of the post at the target displacement dropped to 90 percent of its initial value.

### *6.6.2 Cracks Around the Conduit Hole*

After approximately 1,000,000 cycles, the specimen developed small fatigue cracks around the corners of the conduit hole. These cracks were not easily visible at that time. After another 200,000 cycles of loading, the axial strains at locations near the conduit hole (see Figure 6.3) lost their symmetry and only compression stresses were developed, clearly indicating the presence of a through-thickness crack. Visual observation confirmed the presence of three, 2 in. (51 mm) to 8 in. (103 mm) long cracks, as shown in Figure 6.4. The cracks propagated from the corners of the flame-cut conduit hole in the pipe.

### *6.6.3 Repair of Cracks at the Conduit Hole*

To gage the efficacy of a simple repair scheme, Caltrans and EERC decided to repair the specimen prior to additional testing. During the repair process, a liquid penetrant was used to determine the extent of cracking after 1,200,000 cycles of loading (see Figure 6.4).

The cracks extended through the wall thickness of the post. A repair procedure was developed by EERC and approved by Caltrans. The repair procedure included the following work:

- Removal of the stiffener tube at the conduit hole; rounding the corners of the conduit hole; grinding the edges of the conduit hole.

- Drilling 1/4 in. (6 mm) holes at the end of cracks to arrest further crack growth.
- Removal of the base metal at the crack locations in the shape of a 45° V with a 1/4 in. (6 mm) minimum opening on the inside face of the post.
- Tack welding of backup bars behind the cracks (and inside the post) and replacement of the base metal previously removed with weld filler material, as shown in Figure 6.5.
- Grinding the welds flush with the face of the post.
- Welding a 12 in. x 24 in. x 5/8 in. (305 mm x 610 mm x 16 mm) patch plate over the conduit hole with a continuous fillet weld. The patch plate was bent to an inside diameter equal to the outside diameter of the post.

Figure 6.6 shows the specimen at the completion of the repair. The repair was performed by a Caltrans-approved contractor and monitored by a Caltrans inspector.

### *6.6.4 Post-Repair Cracking at the Base and Conduit Hole*

The testing of Specimen AB1 resumed following repair of the cracks and the addition of the patch plate. New cracks appeared at the bottom of patch plate-to-post weld at 1,700,000 cycles and at different locations at 2,000,000 cycles. In both instances, the failed weld material was ground out and replaced.

### *6.6.5 Cracking at the Post-Base Plate Connection*

After 2,100,000 cycles of loading, cracks were observed at the top of the weld at the post-base plate connection. The cracks became clearly visible at 2,400,000 cycles. At this time, no tensile stresses were being developed at the base of the plate on the side of the conduit hole; the location of the neutral axis at the base of the post had shifted from its initial position and the strains had redistributed. The test was terminated at approximately 2,700,000 cycles when the resistance of the post at the target displacement dropped to 90 percent of its initial value. Figure 6.7 shows the crack patterns in the welds at the post-to-base connection at the end of the test.

## 6.7 Typical Test Data

Typical test data (top displacement, lateral force, and stresses at selected heights) are shown in Figures 6.8 and 6.9. The data in these plots represent response at approximately 700,000 cycles, and are representative of the specimen behavior before cracking. The stresses were obtained by multiplying the strain gage data values by the elastic modulus. Figure 6.8 and Figure 6.9 show the stresses, after removal of the drift from the data, along the line between bolts CD (side of the conduit hole), and along the line between bolts GH (opposite side of the conduit hole), respectively.

## 6.8 Response Maxima

The minimum and maximum peak responses were computed for each data channel and each test. The computed stress range was used to determine the stress profile along the height of the post and to detect the presence of cracks.

The results of the 585 test records were obtained and plotted. Figure 6.10 shows the response history of the average stress range at the extreme fibers at the side of the conduit hole (between bolts C and D). The stresses are approximately constant for cycles 1 through 1,000,000. After 1,000,000 cycles, the stresses dropped noticeably as cracks around the conduit hole developed. At 1,200,000 cycles, the specimen was repaired, and for the next 800,000 cycles (to a total of 2,000,000 cycles) stresses remained constant, beyond which point the stresses dropped due the formation of to new cracks. The stress immediately above the base plate dropped to near zero at a cycle count of 2,400,000 after the new cracks propagated. Figure 6.11 shows the response history of the average stress range at the extreme fibers on the opposite side of the post to the conduit hole (between bolts G and H). The stresses were almost constant during the entire test. However, the cracks at the post-to-base plate caused the stresses on the cross-section to redistribute and increased the axial stress range near the end of the test (see bottom plot in Figure 6.11).

## 6.9 Strain Gage History

Figure 6.12 shows the stresses at 27 in. (686 mm) above the base plate on the side of the conduit hole between 800,000 and 1,200,000 cycles and prior to the development of cracks around the conduit hole. At 800,000 cycles the response was symmetric. At 1,000,000 cycles the stresses decreased due to cracking adjacent to the conduit hole. At 1,100,000 cycles the stresses lost their symmetry and the gages were responding only to compression strains indicating that the cracks had propagated through the thickness of the pipe wall.

Figure 6.13 shows the stress history at 1.25 in. (32 mm) above the base plate. Between 1,200,000 and 2,200,000 cycles and immediately following the addition of the patch plate, the stresses are symmetric; the load remained constant until the cycle count reached 2,200,000. By 2,300,000 cycles the stresses had decreased slightly, but after the following 100,000 cycles, the stresses dropped to nearly zero, indicating cracking at the post-to-base welded connection. These conclusions are verified by visual observation.

## 6.10 Stress-Range Distribution

The absolute value of the stress range along the height of the post was obtained from strain gage data maxima. Figure 6.14 shows the stress profiles along lines GH and CD at different stages (from the beginning to the end of the test). The stress distribution is linear at heights more than 6 in. (152 mm) above

the base. However, within 6 in. (152 mm) of the base plate the distribution is nonlinear along lines GH and CD. This may be attributed to the backing ring near the base and excess weld filler metal observed in the interior of the post (after the completion of the test). The drop in the stress range along line CD, at 27 in. above the base plate, is a result of the stress redistribution around the conduit hole.

### 6.11 Ovaling

The displacements transducers (DCDTs 1 through 12 in Figure 6.3) placed normal to the face of the pipe were used to investigate ovaling of the post close to its base. The transducer responses were negligible and no ovaling effect was identified. These transducers were not used for the testing of the mast-arm specimens.

### 6.12 Comparison with AASHTO Guidelines

Figure 6.15 presents the relationship between allowable stress range and number of cycles to failure (S-N curve) as adopted in the AASHTO specifications (AASHTO, 1994). The AASHTO design plots incorporate a two standard deviation factor of safety. The response of Specimen AB1 is shown in this figure. The marker '**o**' indicates the maximum stress and cycle number corresponding to crack initiation at the conduit hole. The marker '**x**' indicates the maximum stress and cycle number corresponding to the time when the crack propagated at the post-base plate connection.

### 6.13 Elastic Analysis of Specimen AB1

The experimentally determined stiffness of the post prior to cracking is 12.0 kips/in (2100 kN/m), and close to the analytical stiffness of 12.8 kips/in (2240 kN/m) obtained from the finite element analysis described in Chapter 4. The good correlation between these values is attributed to the inclusion of the conduit hole and base plate flexibility in the mathematical model, and the simplicity of the specimen.

### 6.14 Summary

The focus of the testing program is the fatigue-life evaluation of the groove-welded post-base plate connection. As such, failure of the post-base plate connection should not be linked to the failure of the post adjacent to the conduit hole. Nonetheless, the initial cracking of the specimen at the conduit hole identified this location as a point of potential failure (cracking) in other as-built CMS structures.

The cycle counts corresponding to the Type 1 and Type 2 failures (see Section 5.4) were 2,700,000 and 2,100,000 respectively. Accordingly, the cycle count of the point of failure in Specimen AB1 is 2,100,000.

Quality of workmanship likely contributed to the poor performance of Specimen AB1. To improve

the fatigue life of post specimens, the following recommendations are made:

1. *Relocate and reconfigure the conduit hole.* Moving the conduit hole further away from the baseplate will reduce the nominal stresses at this reduced cross section. Changing the conduit hole from rectangular to circular, and drilling rather than frame cutting the conduit hole, will reduce stress concentrations and minimize the residual strains.

2. *Develop a prequalified Welding Procedure Specification (WPS) for the groove-welded post-base plate connection.* Standardized WPSs are commonly used for joining steel components in the building, bridge, and off-shore oil industries. In the past, it has been the contractors' responsibility to develop and implement a WPS (Shepard, 1997) for Caltrans sign structures. To maintain high standards of construction, Caltrans should prepare a WPS for groove-welded post-base plate connections. A WPS for the subject connection should include, but not be limited to, information on welding type (i.e., shielded metal arc welding, flux core-arc welding), end preparation, fit-up and root opening, maximum electrode diameter, electrode type, maximum current, maximum root-pass thickness, and pre-heat and cool-down requirements. The use of toughness-rated weld filler metal is recommended. Improved weld profiles, such as those shown in Figure 3.10 of AWS D1.1 (AWS, 1996), should be investigated for possible use. It is recommended that a welding consultant be engaged by Caltrans to develop the WPS.

3. *Develop improved quality control and inspection (quality assurance) procedures.* Current Caltrans standards for quality control and inspection of welded components should be reviewed. Minimum standards for quality control should be proposed by Caltrans and imposed on contractors building CMS structures. Visual inspection alone of non-redundant welded connections is likely inappropriate. As a minimum, all groove-welded connections should be ultrasonically tested (UT) by an approved testing agency as part of the quality control program. Good quality control and inspection are key to high-quality construction: all defects identified by UT should be gouged out and replaced prior to shipment of the post to the field. Standard procedures for repairing such defects must be developed. A Caltrans inspector should be present during the fit-up and welding of the post-base plate connections to ensure that the WPS is followed exactly. It is recommended that a welding consultant be engaged by Caltrans to develop new quality control and inspection procedures.

Table 6.1: Instrumentation for Specimen AB1

| Ch. No. | Inst. ID. | Instrument | Location |
|---|---|---|---|
| Global transducers | | | |
| 1 | lc | load cell | actuator center line; top of the post |
| 2 | lvdt | displ. transducer | actuator center line; top of the post |
| Longitudinal strain gages placed on the post, and lateral displacement transducers orthogonal to the post | | | |
| 3 | sg1 | strain gage | above bolt-line C; 36" above base plate |
| 4 | sg2 | strain gage | between bolt-lines C & D; 36" above base plate |
| 5 | sg3 | strain gage | above bolt-line D; 36" above base plate |
| 6 | sg4 | strain gage | above bolt-line G; 36" above base plate |
| 7 | sg5 | strain gage | between bolt-lines G & H; 36" above base plate |
| 8 | sg6 | strain gage | above bolt-line H; 36" above base plate |
| 9 | sg7 | strain gage | between bolt-lines C & D; 27" above base plate |
| 10 | sg8 | strain gage | between bolt-lines G & H; 27" above base plate |
| 11 | dcdt1 | displ. sensor | between bolt-lines A & B; 9" above the base |
| 12 | dcdt2 | displ. sensor | between bolt-lines C & D; 9" above the base |
| 13 | dcdt3 | displ. sensor | between bolt-lines E & F; 9" above the base |
| 14 | dcdt4 | displ. sensor | between bolt-lines G & H; 9" above the base |
| 15 | sg9 | strain gage | between bolt-lines C & D; 12" above base plate |
| 16 | sg10 | strain gage | between bolt-lines G & H; 12" above base plate |
| 17 | dcdt5 | displ. sensor | between bolt-lines A & B; 4.5" above base plate |
| 18 | dcdt6 | displ. sensor | between bolt-lines C & D; 4.5" above base plate |
| 19 | dcdt7 | displ. sensor | between bolt-lines E & F; 4.5" above base plate |
| 20 | dcdt8 | displ. sensor | between bolt-lines G & H; 4.5" above base plate |
| 21 | sg11 | strain gage | above bolt-line C; 6" above base plate |
| 22 | sg12 | strain gage | between bolt-lines C & D; 6" above base plate |
| 23 | sg13 | strain gage | above bolt-line D; 6" above base plate |
| 24 | sg14 | strain gage | above bolt-line G; 6" above base plate |
| 25 | sg15 | strain gage | between bolt-lines G & H; 6" above base plate |
| 26 | sg16 | strain gage | above bolt-line H; 6" above base plate |
| 27 | dcdt9 | displ. sensor | between bolt-lines A & B; 1.5" above base plate |
| 28 | dcdt10 | displ. sensor | between bolt-lines C & D; 1.5" above base plate |
| 29 | dcdt11 | displ. sensor | between bolt-lines E & F; 1.5" above base plate |
| 30 | dcdt12 | displ. sensor | between bolt-lines G & H; 1.5" above base plate |

Table 6.1: Instrumentation for Specimen AB1

| Ch. No. | Inst. ID. | Instrument | Location |
|---|---|---|---|
| 31 | sg36 | strain gage | between bolt-lines C & D; 1.25" above base plate |
| 32 | sg38 | strain gage | above bolt-line G; 1.25" above base plate |
| 33 | sg17 | strain gage | above bolt-line C; 3.5" above base plate |
| 34 | sg18 | strain gage | between bolt-lines C & D; 3.5" above base plate |
| 35 | sg19 | strain gage | above bolt-line D; 3.5" above base plate |
| 36 | sg20 | strain gage | above bolt-line G; 3.5" above base plate |
| 37 | sg21 | strain gage | between bolt-lines G & H; 3.5" above base plate |
| 38 | sg22 | strain gage | above bolt-line H; 3.5" above base plate |
| 39 | sg23 | strain gage | above bolt-line C; 2.75" above base plate |
| 40 | sg24 | strain gage | between bolt-lines C & D; 2.75" above base |
| 41 | sg25 | strain gage | above bolt-line D; 2.75" above base plate |
| 42 | sg26 | strain gage | above bolt-line G; 2.75" above base plate |
| 43 | sg27 | strain gage | between bolt-lines G & H; 2.75" above base plate |
| 44 | sg28 | strain gage | above bolt-line H; 2.75" above base plate |
| 45 | sg29 | strain gage | above bolt-line C; 2.0" above base plate |
| 46 | sg30 | strain gage | between bolt-lines C & D; 2.0" above base plate |
| 47 | sg31 | strain gage | above bolt-line D; 2.0" above base plate |
| 48 | sg32 | strain gage | above bolt-line G; 2.0" above base plate |
| 49 | sg33 | strain gage | between bolt-lines G & H; 2.0" above base plate |
| 50 | sg34 | strain gage | above bolt-line H; 2.0" above base plate |
| 51 | sg35 | strain gage | above bolt-line C; 1.25" above base plate |
| 52 | sg37 | strain gage | above bolt-line D; 1.25" above base plate |
| 53 | sg39 | strain gage | between bolt-lines G & H, 1.25" above base plate |
| 54 | sg40 | strain gage | above bolt-line H; 1.25" above base plate |
| 55 | crack gage | | base plate-connection |
| not used | sg41 | strain gage | above bolt-line C; 27" above base plate |
| 56 | sg42 | strain gage | above bolt-line D; 27" above base plate |
| 57 | sg43 | strain gage | above bolt-line G; 27" above base plate |
| not used | sg44 | strain gage | above bolt-line H; 27" above base plate |
| Internal data acquisition channels | | | |
| 58 | counter | | |
| 59 | timer | | |

Table 6.2: Crack log for Specimen AB1

| Cycle Count (millions) | Event |
|---|---|
| 1.00 | Cracks developed around the conduit hole. |
| 1.20 | The base metal around the test conduit hole was repaired; patch plate added over the conduit hole. |
| 1.70 | Cracks appeared in the patch plate-to-post weld; cracks repaired. |
| 1.75 | Crack gage at the post-to-base plate connection failed. |
| 2.00 | New cracks in the patch plate-to-post weld observed; cracks were repaired. |
| 2.10 | Cracks observed at the post-to-base plate connection immediately above the groove welded connection. |
| 2.30 | Additional cracks identified at the patch plate-to-post weld. |
| 2.40 | Cracks immediately adjacent to the post-to-base plate propagated. |
| 2.70 | Test terminated. |

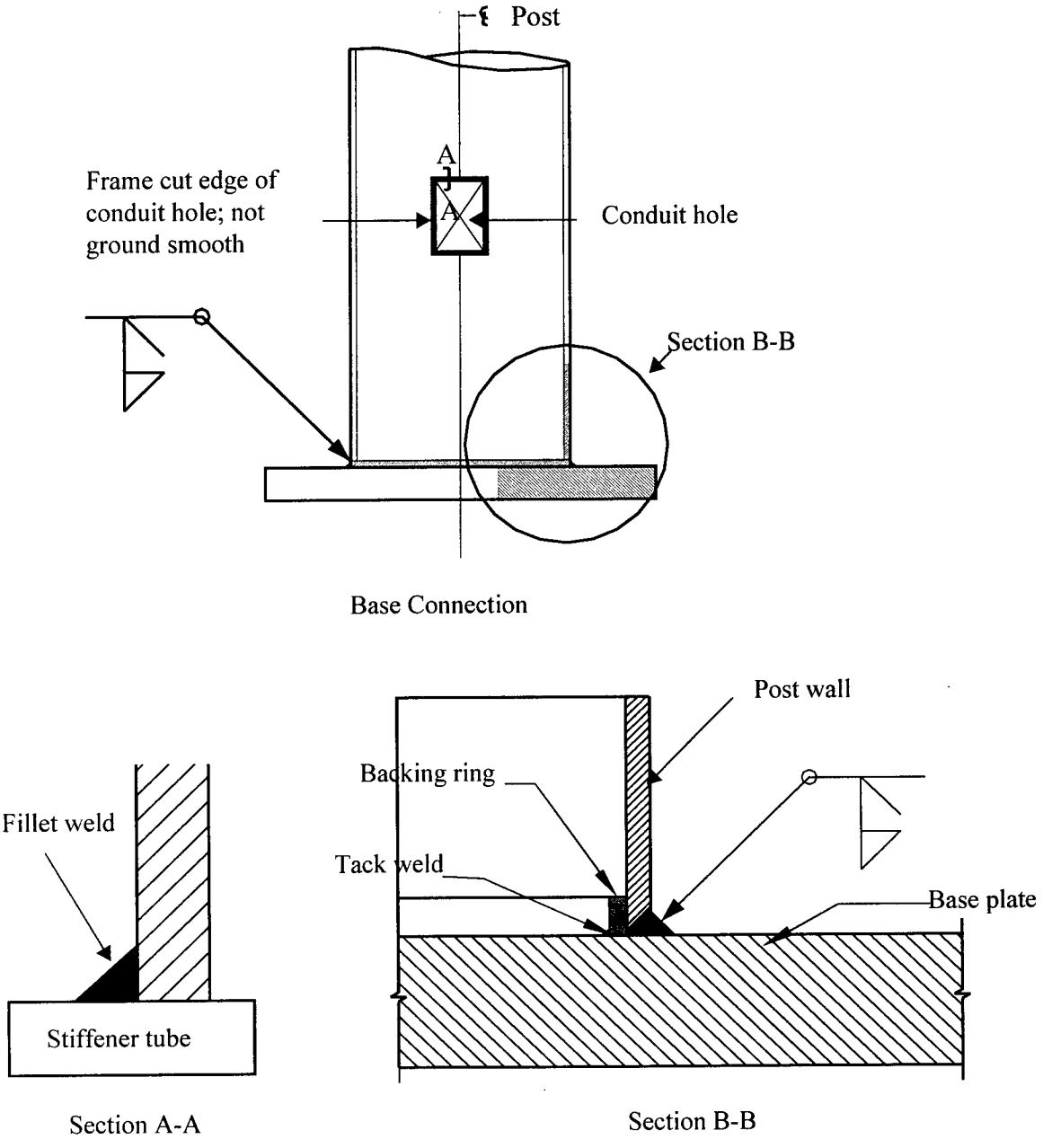


Figure 6.1: Connection details for Specimen AB1 (adopted from Gugino and Woody, 1996)

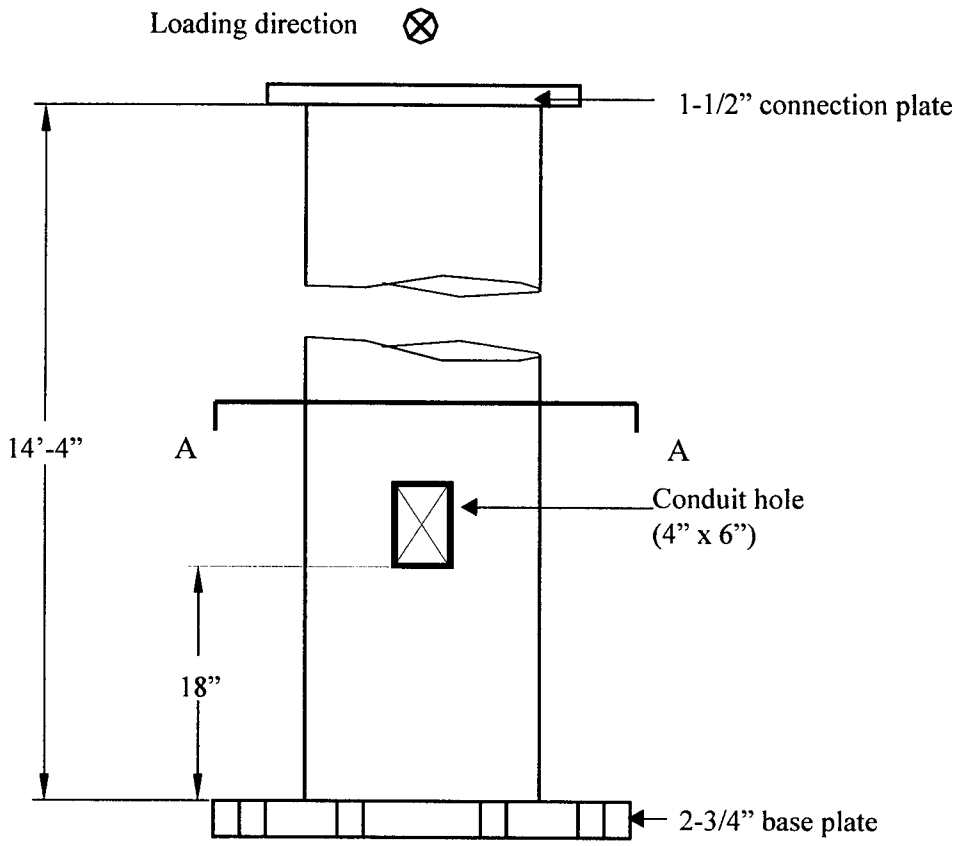


(a) Elevation of post

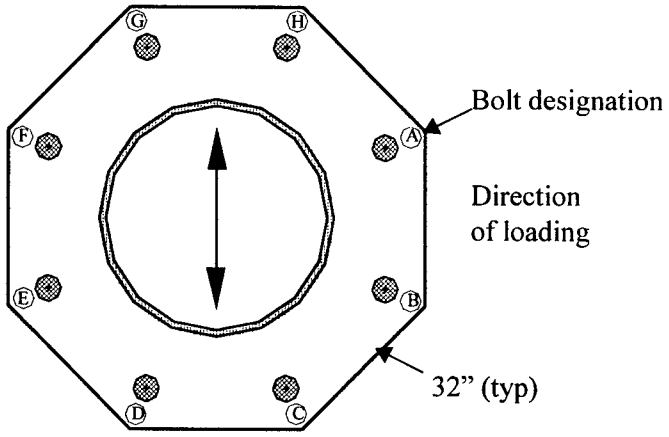


(b) Section A-A (Plan)

Figure 6.2: Setup for Specimen AB1

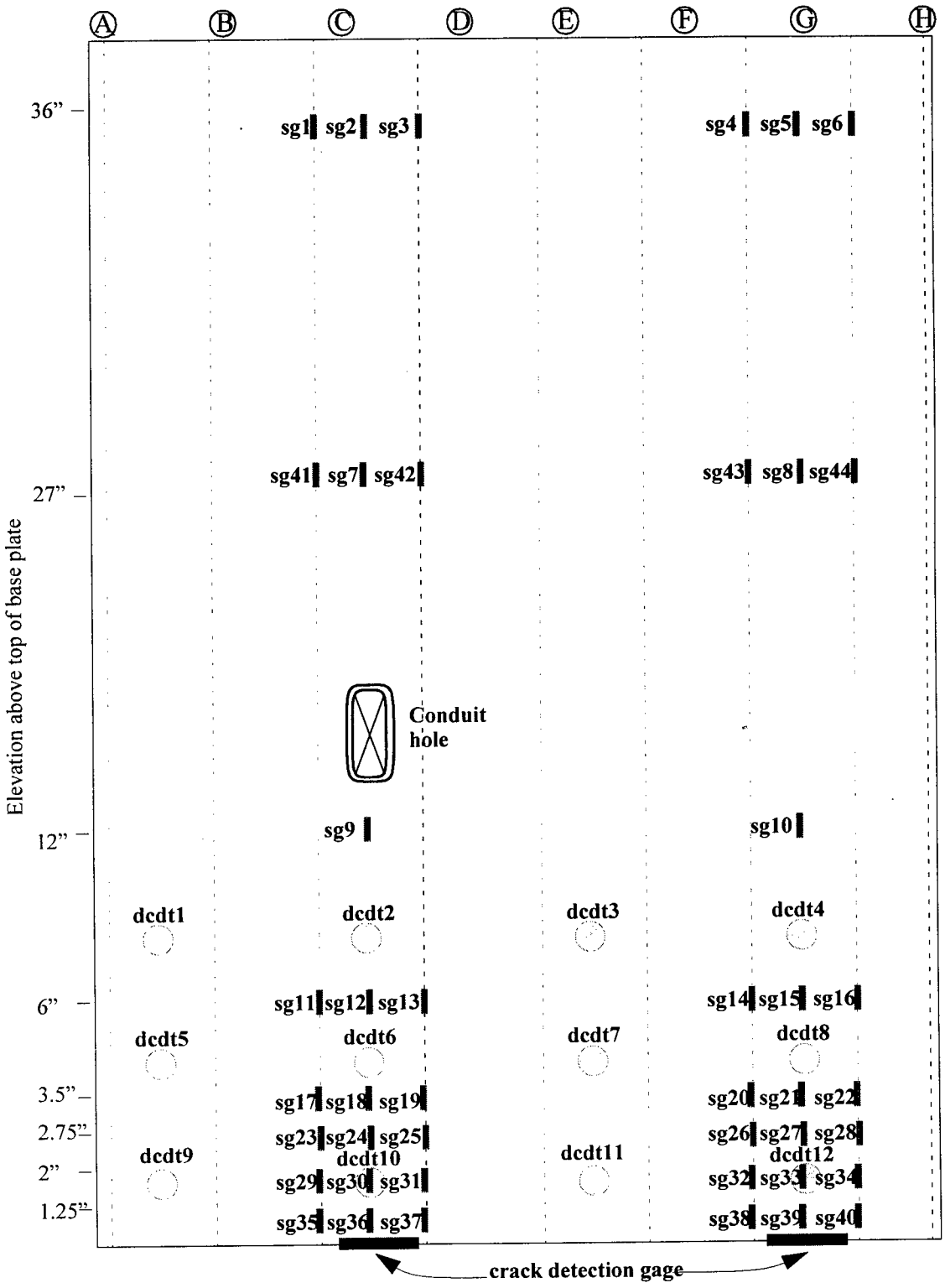


Figure 6.3: Exploded view of the instrumentation for Specimen AB1

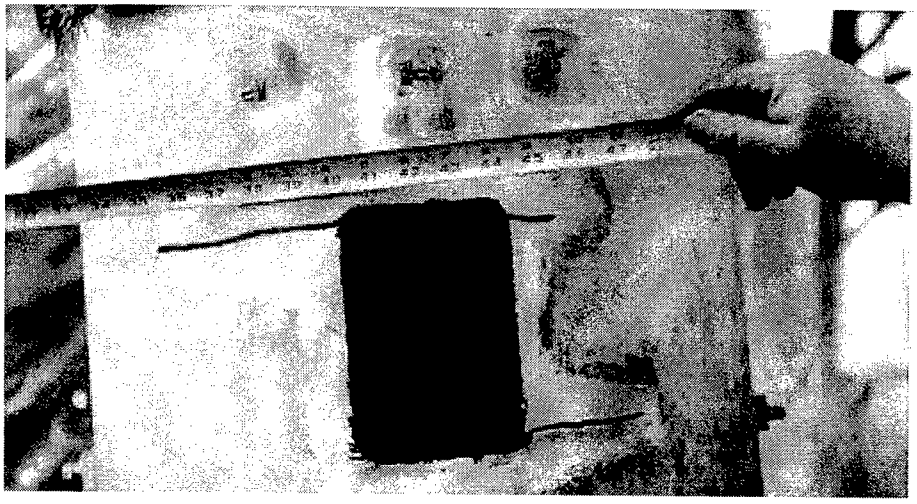

Figure 6.4: Location of cracks at the conduit hole for Specimen AB1

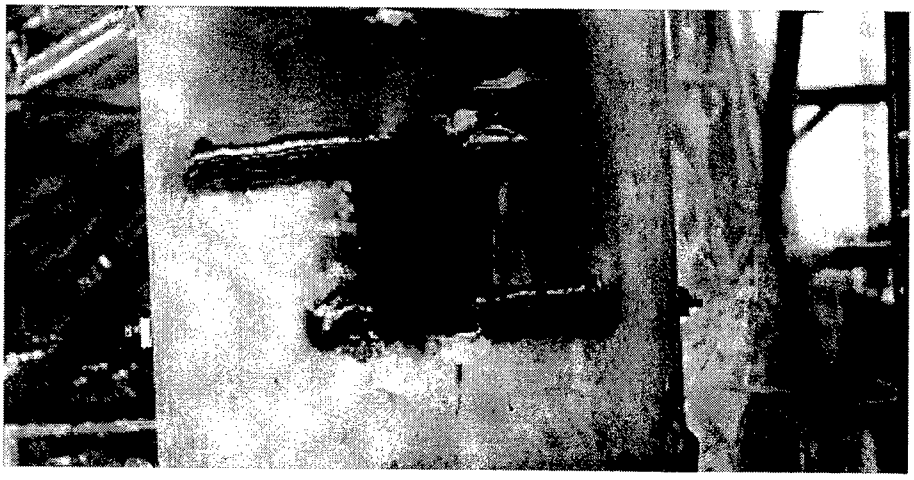

Figure 6.5: Repair of cracks at the conduit hole for Specimen AB1

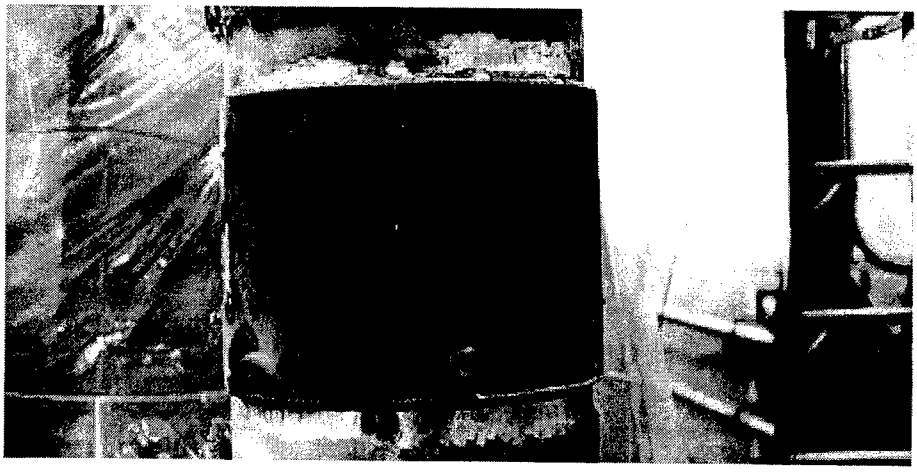

Figure 6.6: Specimen AB1 after repair showing patch plate

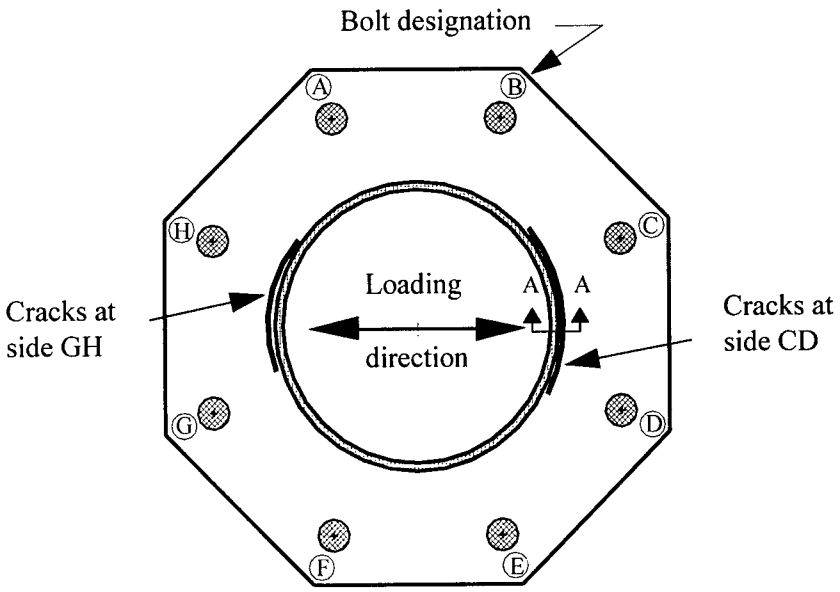


(a) Plan view of post at the base

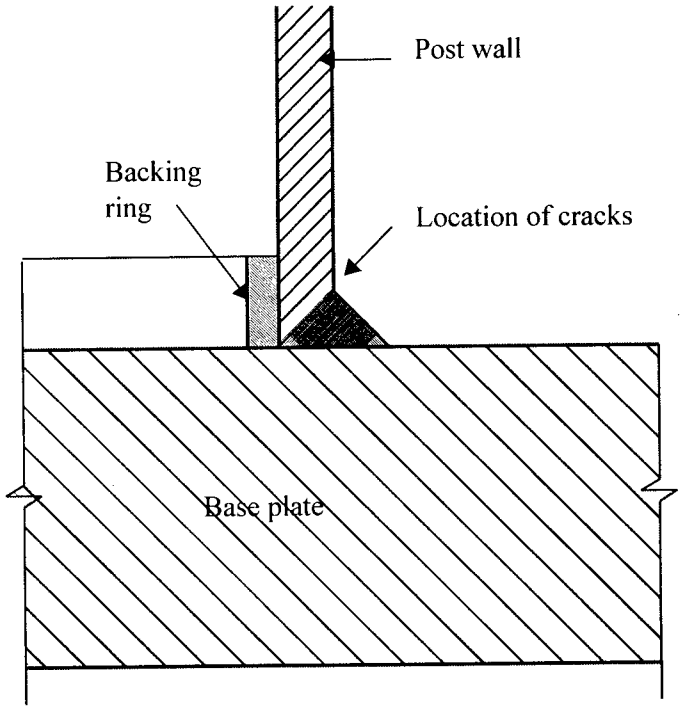


(b) Section A-A showing crack location

Figure 6.7: Cracks at the post-base plate connection of Specimen AB1

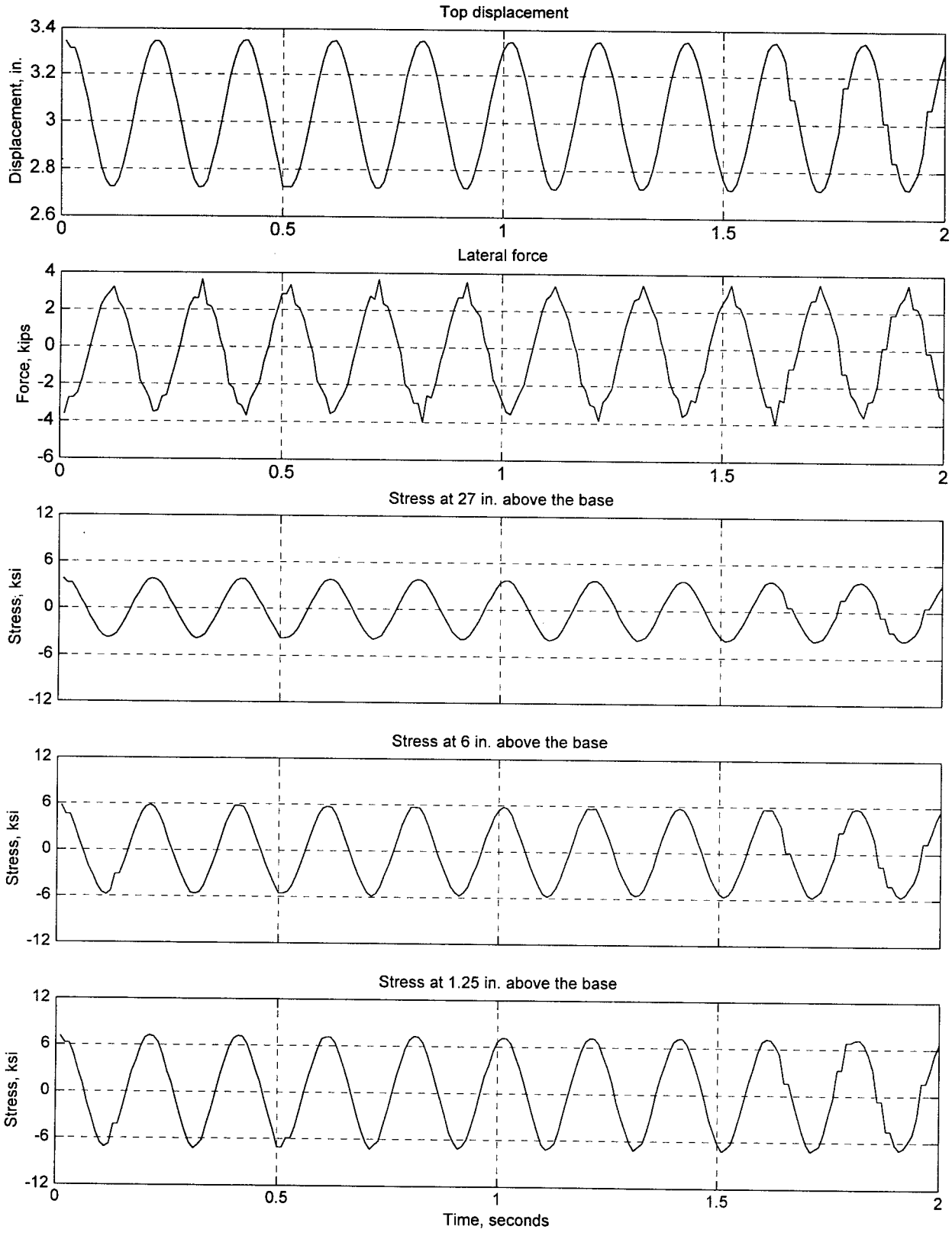


Figure 6.8: Typical response history for specimen AB1 at the side of the conduit hole

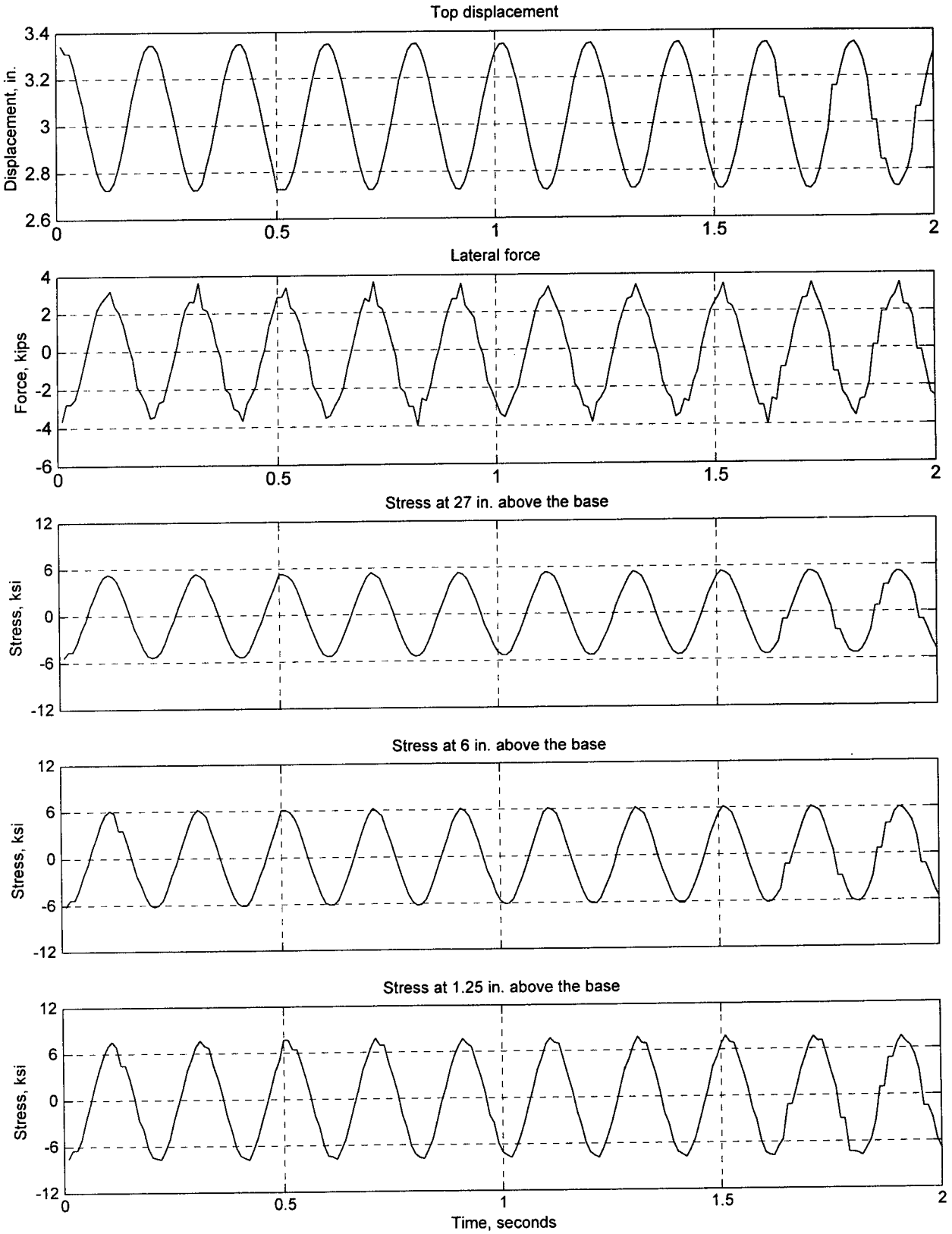


Figure 6.9: Typical response history for specimen AB1 at the opposite side of the conduit hole

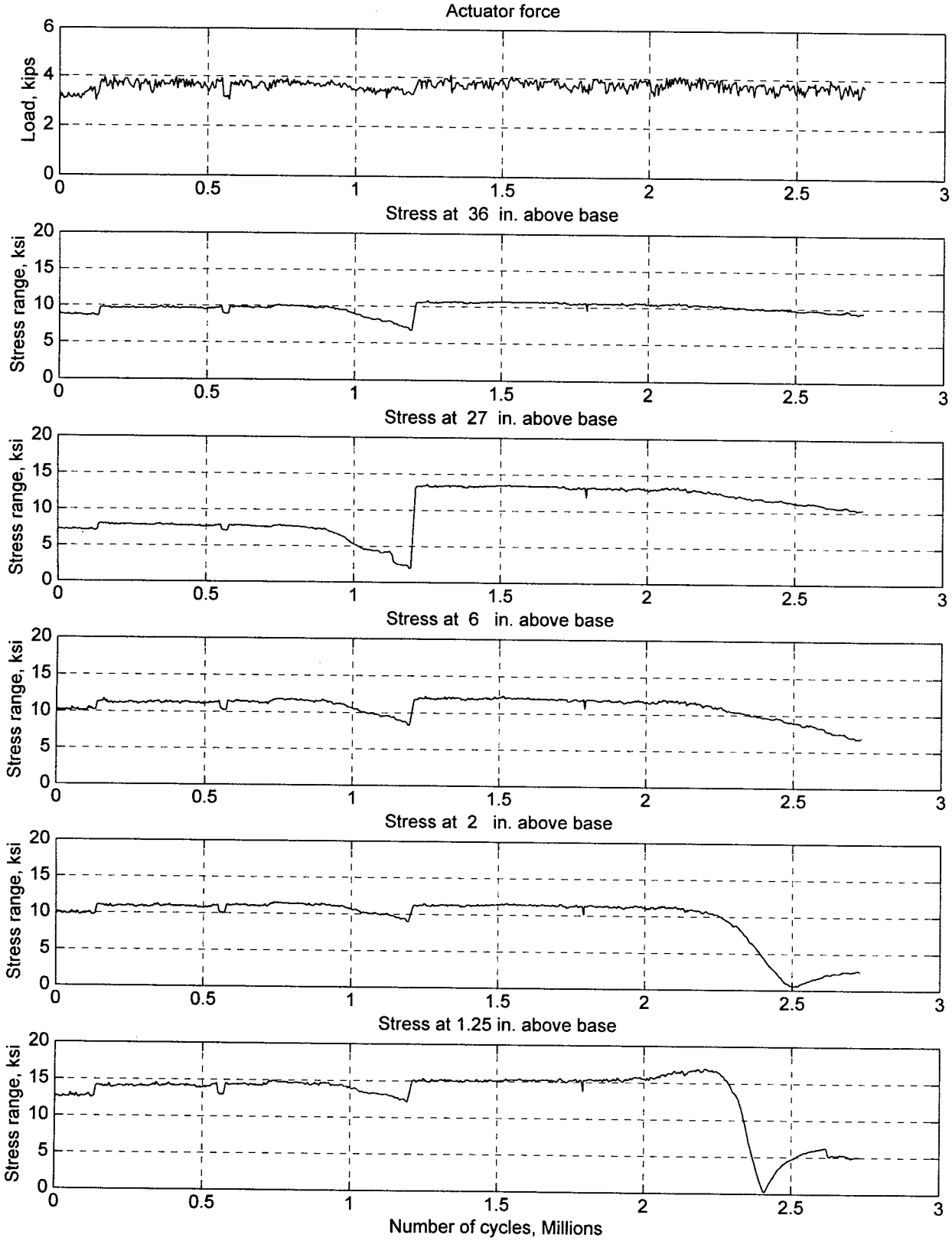


Figure 6.10: Stress history at the side the conduit hole (between bolts C and D) for Specimen AB1

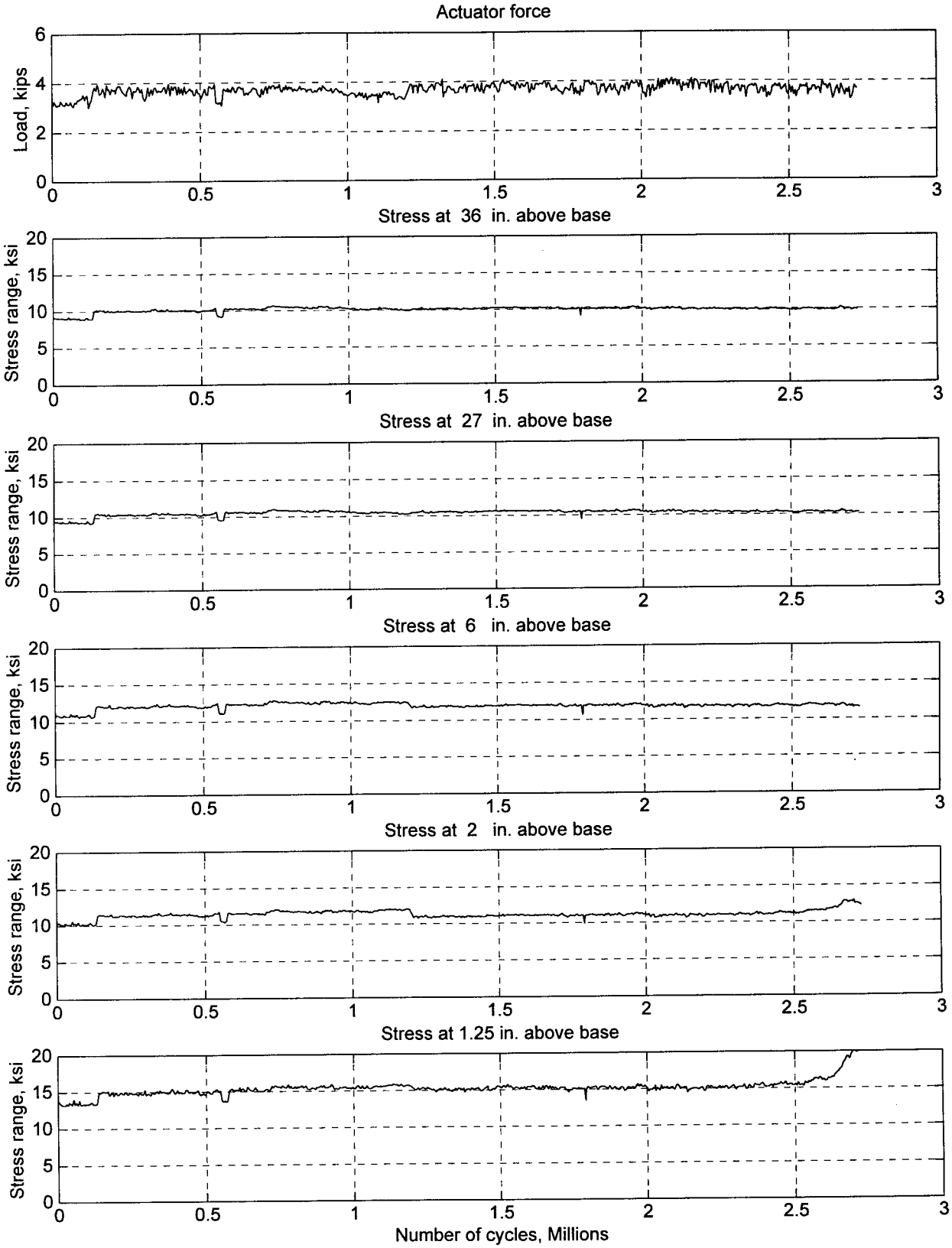


Figure 6.11: Stress history at the opposite side of the conduit hole (between bolts G and H) for Specimen AB1

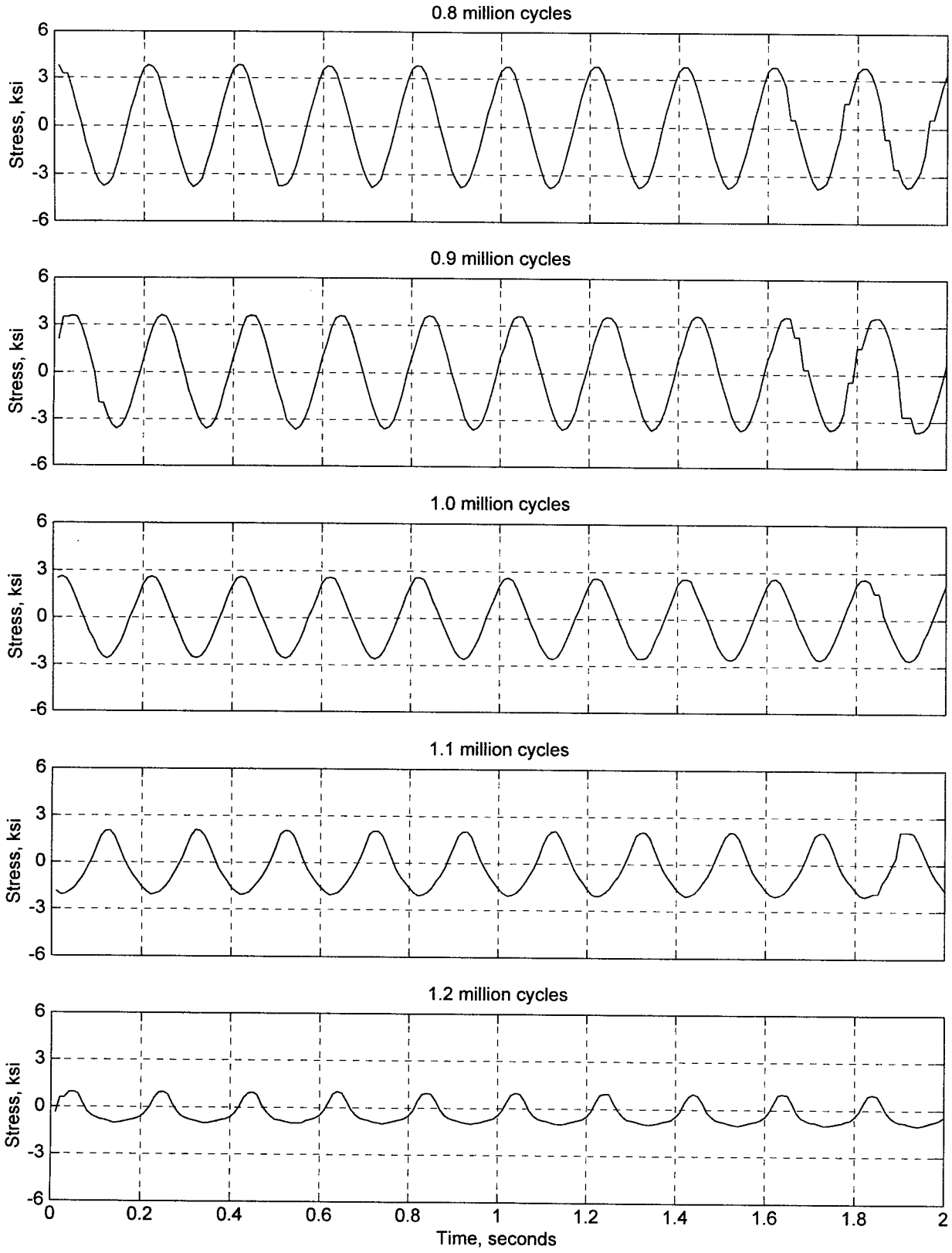


Figure 6.12: Stress history at 27 in. above the base plate on the side of the conduit hole for Specimen AB1

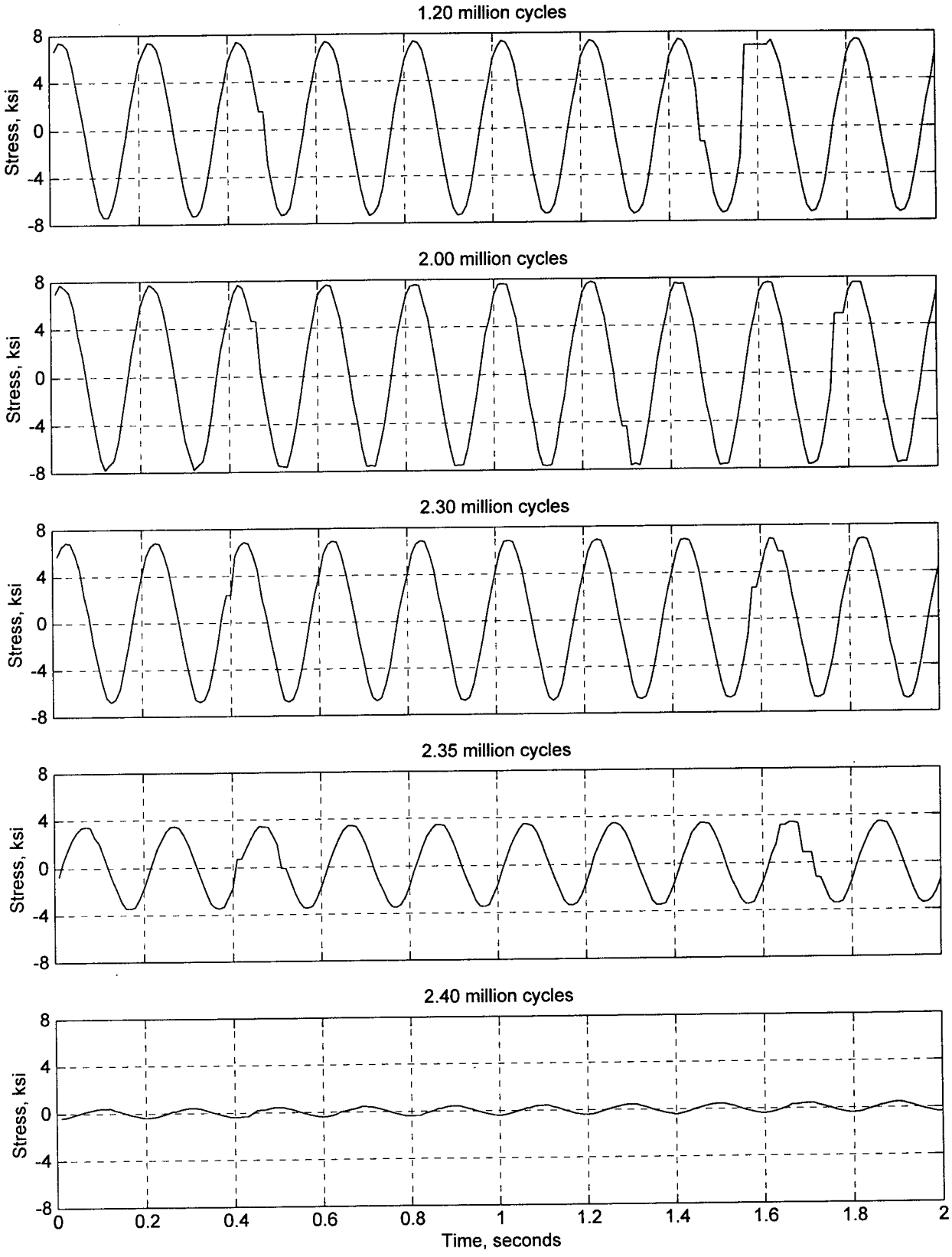


Figure 6.13: Stress history at 1.25 in. above the base plate on the CD side, after repair, for Specimen AB1

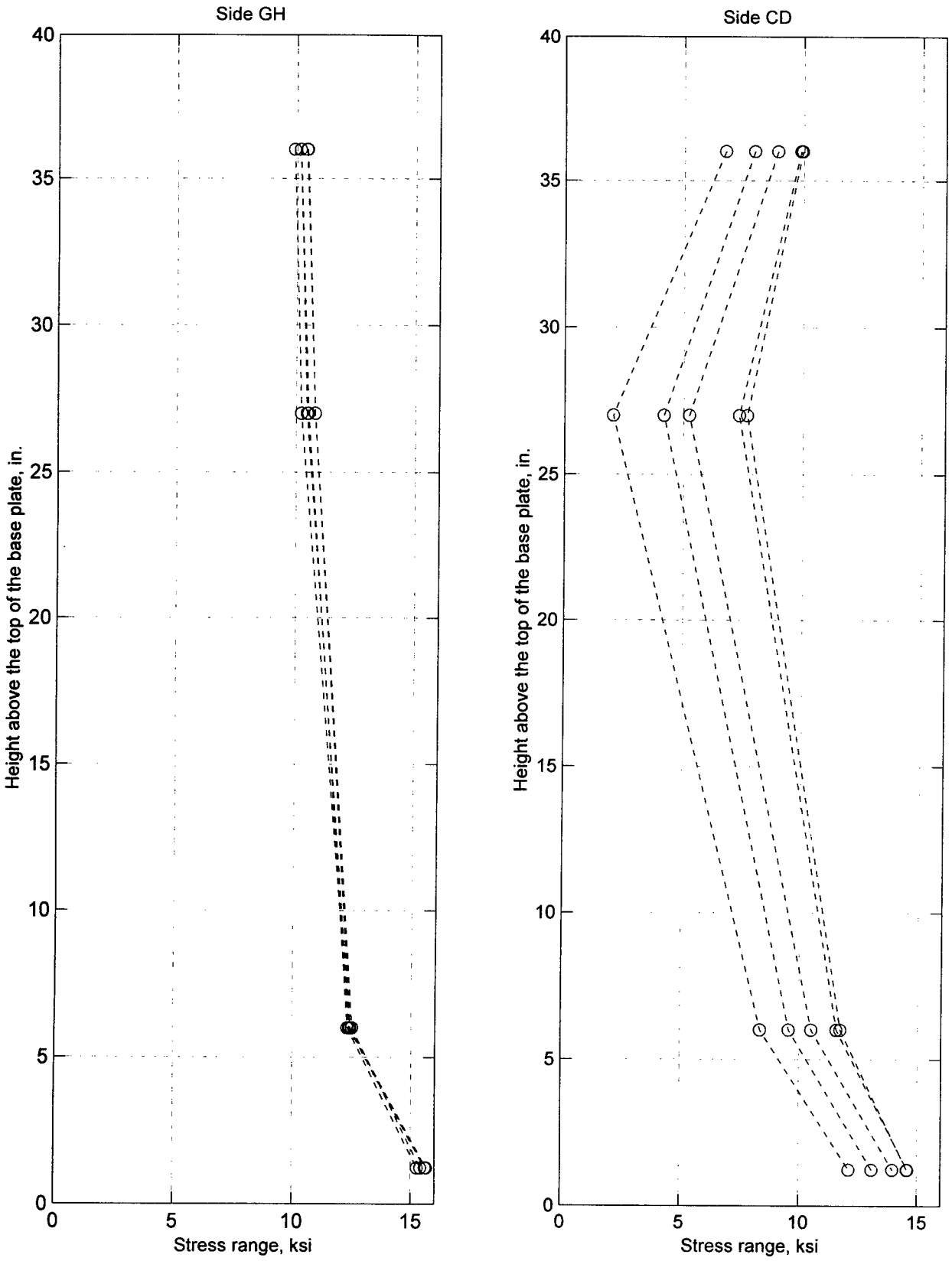


Figure 6.14: Absolute values of stress range at maximum response for Specimen AB1

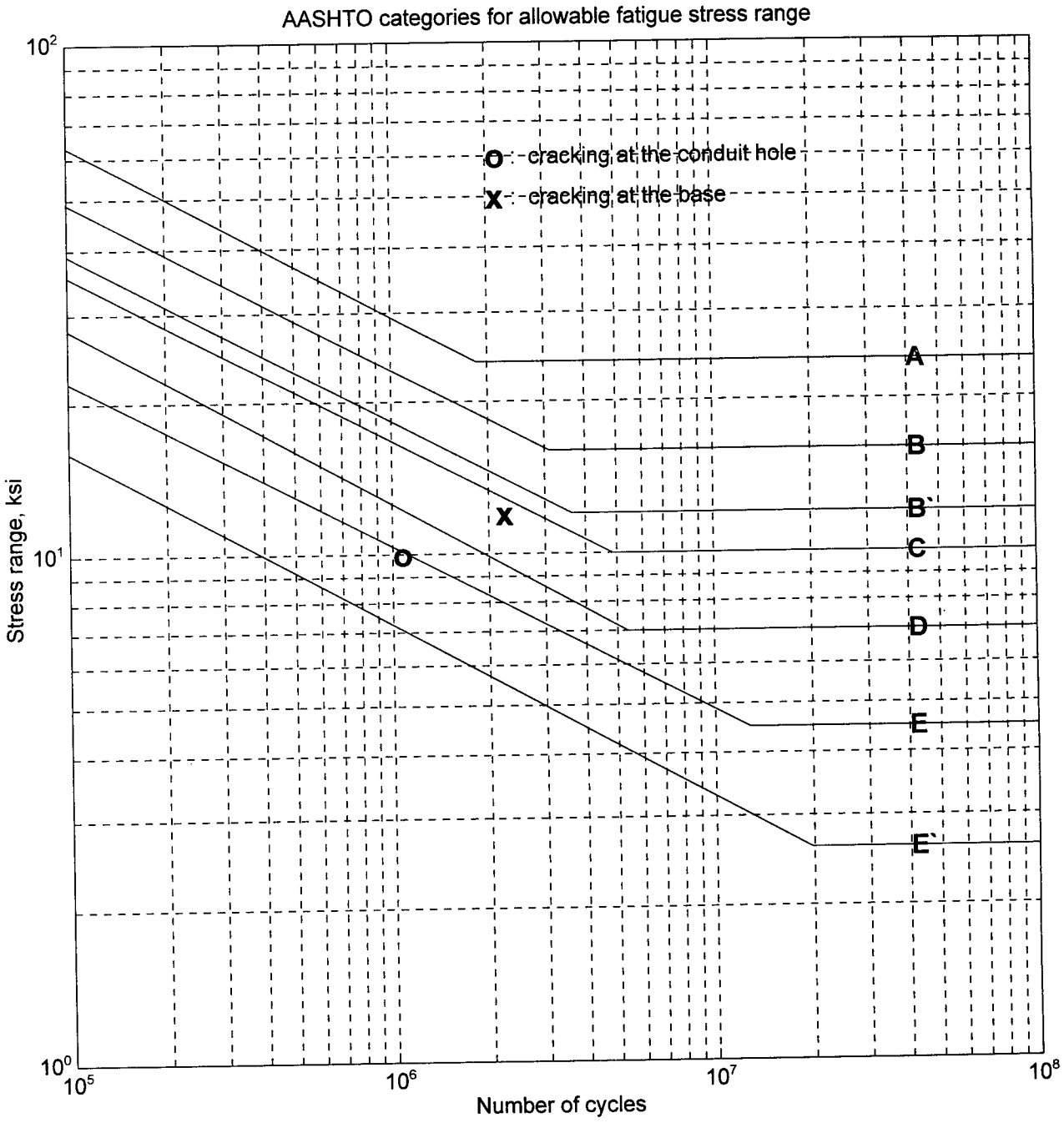


Figure 6.15: Comparison of Specimen AB1 experimental data and AASHTO fatigue design curves

# CHAPTER 7: RESPONSE OF MAST ARM SPECIMENS MA1, MA2, MA3

## 7.1 General

This chapter presents the results of the experimental studies on the response of mast arm segments of CMS structures (see Figure 1.2). Mast arms from three complete CMS structures, initially designated for field installation, were used as test specimens. As such, the quality of these specimens is expected to be representative of those CMS mast arms currently in service.

The mast arms (herein referred to as Specimens MA1, MA2, and MA3) were fabricated from 18 in. (457 mm) diameter pipe with a wall thickness of 3/8 in. (9.5 mm). The mast arm-to-flange plate connection consists of a full-penetration groove weld with the backup ring left in place, and is conceptually identical to the post-to-base plate connection. A circular conduit hole, 2.5 in. (63.5 mm) in diameter, is located on the underside of the mast arm, approximately 4.5 in. (114 mm) from the flange plate. Figure 7.1 shows connection details of a typical mast arm.

## 7.2 Test Configuration

The test specimens were fabricated by cutting the CMS mast arms to a length of 12 ft (3.7 m) to accommodate the existing test setup. An extension piece, 26 in. (660 mm) in height, was fabricated from an 18 in. (457 mm) diameter pipe with a wall thickness of 15/16 in. (24 mm) so that the test assembly built for specimen AB1 could be reused. A 2-3/4 in. (70 mm) thick octagonal base plate was welded to the bottom of the extension piece facilitating the use of previously cast concrete foundation blocks. An annular mating flange plate was welded to the top of the extension piece, and the extension piece was bolted to the mast arm test specimens using 26 No. 3/4 in. (19 mm) A325 galvanized bolts in the flange plate connection. This type of connection was used to simulate the field attachment. During the testing of the mast arm specimens, the extension piece was also subjected to constant amplitude cyclic loading. As such, the full-penetration groove-welded connections at the top and bottom of the mast arm provide additional data points for evaluating the fatigue life of this type of connection.

Figure 7.2 shows the test setup for the mast arms. The extension piece was connected to the foundation using eight 2-1/4 in. (57 mm) diameter anchor bolts. The 2-3/4 in. (70 mm) thick base plate was leveled using the nuts beneath the plate. The nuts above the base plate were first snug tightened and then further tightened by the turn-of-the-nut method (AISC, 1995). Load-rated washers were used in the mast arm-to-extension piece flange plate connection. Each bolt was pretensioned to 28 kips (124 kN) axial force, per the Caltrans specification (Gugino and Woody, 1996).

The out-of-flatness of the flange plates for the three mast arm specimens and the extension piece was measured; data are reported in Figure 7.3. The distortions, which likely occur due to welding of the flange plates to the mast arm and the extension piece, were largest for Specimen MA1. The values of measured out-of-flatness are considered to be representative of field conditions. As the flange plate bolts were tightened, substantial strains in the gages placed near the flange plates were recorded as a result of reducing the non-uniform gap between the distorted flange plates. Further, following bolt tightening, micro-cracking in the groove-welded mast arm-to-flange plate connection was observed. The strain values are shown in Table 7.1. For the strain gages placed just above the flange plate-to-mast arm connection in Specimen MA3, the strains due to bolt tightening were of the order of twice the yield strain.

## 7.3 Material Properties, Welding Procedures, and Inspections

The three CMS structures (mast arms and posts) were fabricated from Grade A53 steel (API, 1995; ASTM, 1991) by a Caltrans-approved vendor (Sierra Nevada Steel Corp.) and were inspected by Caltrans inspectors prior to shipment to a local Caltrans-approved fabricator (East Bay Steel Products Inc.) for modifications to suit the testing setup at EERC. The extension piece was also made of Grade A53 steel and was fabricated locally under the supervision of a local Caltrans inspector. All welding followed the current AWS D1.1 standards (AWS, 1996).

Ultrasonic testing (UT) was used to establish the integrity of the welded connections. The tests identified three flaws in the mast arm-to-flange plate connection in Specimen MA1. Specimens MA2, MA3, and the extension piece passed the ultrasonic testing.

## 7.4 Test Parameters

The mast arm specimens were tested with non-zero mean stress corresponding to the dead-load stresses at the mast arm-to-post connection. Cyclic testing was then carried out symmetrically with respect to this non-zero mean stress.

The available strain gage data from the field measurements (Gugino and Woody, 1996) were used to calculate the stress range for the mast arm specimens. Field measurements indicated a static stress range of 9 ksi (62 MPa) and a cyclic stress range of 10 ksi (69 MPa) measured near the mast arm-to-flange plate connection. Due to the presence of the circular conduit hole close to the base of the test specimen, the strain gages close to the flange plate were not used to monitor the stress level. Instead, the strain gage located 36 in. (914 mm) above the flange plate, on the side of the mast arm without the conduit hole, was used to monitor the stresses. The nominal static and cyclic stresses at this point were approximately 7 ksi (48 MPa) and +/-4 ksi (27.6 MPa), respectively.

In summary, the mast arm specimens were tested at stress levels varying between -3 ksi and -11 ksi (-21 to -76 MPa) (compression) on the side of the conduit hole, and +3 ksi to +11 ksi (21 to 76 MPa) (tension) on the side opposite the conduit hole, all at 36 in. (914 mm) above the flange plate. This corresponds to a cyclic stress range of approximately 10 ksi (69 MPa) at the groove-welded flange plate connection. The nominal stresses at the top and bottom of the extension-piece base plates were approximately 4.5 and 5.4 ksi (31 and 37 MPa), respectively.

The target number of cycles for the mast arm tests was set at 4,000,000, that is, twice the value of 2,000,000 used by AASHTO (AASHTO, 1992) as the constant amplitude threshold.

### 7.5 Crack Detection and Propagation

For the mast arm specimens, cracks were monitored by a combination of visual observation and dye liquid penetrant, and confirmed by real-time analysis of strain-gage data. Dye liquid penetrant was used to check for cracks in the extension piece.

### 7.6 Instrumentation

The instrumentation for the mast arm specimens consisted of: an LVDT on the servo-actuator center-line measuring the applied displacement; a load cell in-line with the servo-actuator measuring the actuator force; and strain gages placed at strategic locations recording axial strain histories. For specimens MA1 and MA2, a total of ten strain gages were placed along the height of the post at its extreme fibers, measured with respect to the plane of loading, to assess the strain distribution.

Additional gages were attached to specimen MA3 as follows. A strain gage (sg11) was attached to the inside wall of specimen MA3 opposite sg6 at 1.25" (32 mm) above the flange plate. This gage was used to detect local bending effects. Three strain gages (sg12, sg13, and sg14) were placed immediately above the welded flange plate-to-mast arm connection. These gages were used to determine the local strain effects due to tightening of the flange plate bolts. The instrumentation for the mast arm specimens is listed in Table 7.2 and shown on an exploded elevation of the mast arm in Figure 7.4.

### 7.7 Data Analysis Procedure

The computer program Matlab and its signal processing toolbox (Matlab, 1996) were used to process the experimental data. The reduction of the experimental data consisted of three steps. In the first step, the raw data was read, the file header was removed, and a test log was created. Next, the drift in the data was removed, the resulting data were low-pass filtered with a cut-off frequency of 10 Hz; the first and the last ten data points were disregarded, and the peak-to-peak extreme values of response were extracted. Stress ranges were obtained by multiplying the peak-to-peak strains by the Young's modulus of the mast

arm equal to 30,000 ksi (208 GPa). Response histories were plotted in the third step.

## 7.8 Experimental Results for Mast Arm Specimens and the Extension Piece

### *7.8.1 General*

A summary of significant experimental observations is presented in the following section. The extension piece was not instrumented, and no experimental data is available. Cracking in the extension piece was monitored over the course of the testing program using dye liquid penetrant.

### *7.8.2 Test Summary*

To provide the reader with information on the type of data collected throughout the testing program, selected force, displacement, and stress history data after approximately 20,000 cycles of loading are shown in Figures 7.5, 7.6, and 7.7 for Specimens MA1, MA2, and MA3, respectively. Summary information on the response of each of the three mast arm specimens follows.

*Specimen MA1* Figure 7.8(a) shows the Specimen MA1 during the testing program. Figure 7.8(b) shows the specimen at the conclusion of the program. The crack that formed on the tension-side of the mast arm can be seen in this figure at the juncture of the mast arm and the groove-weld. A total of 834 individual tests, each of 16 minutes duration, were recorded. At 1,500,000 cycles, the maximum values of axial strains on the tension side close to the flanged connection (sg6, sg7, and sg8 in Figure 7.4) declined noticeably. The cycle counts corresponding to the Type 1 and Type 2 failures (see Section 5.4) were 2,800,000 and 1,500,000, respectively. Accordingly, the cycle count at the point of failure of Specimen MA1 is 1,500,000. Table 7.3 provides a summary of the test for Specimen MA1.

*Specimen MA2* Figure 7.9(a) shows Specimen MA2 during the testing program. Figure 7.9(b) shows the specimen at the conclusion of the program. A total of 829 individual tests, each of 16 minutes duration, were recorded. At the conclusion of the testing, there was no reduction in the resistance of this specimen. After approximately 3,000,000 cycles, the maximum values of axial strains on the tension side close to the flanged connection (sg6 in Figure 7.4) dropped gradually. However, no cracks in the mast arm-flange plate were identified by visual inspection, the use of liquid dye penetrant, or ultrasonic testing. The cycle counts corresponding to the Type 1 and Type 2 failures (see Section 5.4) were 4,000,000+ and 4,000,000+, respectively. Accordingly, the cycle count at the point of failure of Specimen MA2 exceeds 4,000,000. Table 7.4 provides a summary of the test for Specimen MA2.

*Specimen MA3* Figure 7.10(a) Shows the specimen MA3 during the testing program. Figure 7.10(b) shows the specimen at the conclusion of the program. A total of 806 individual tests, each of 16 minutes duration, were recorded. After 2,000,000 cycles, the maximum values of axial strain on the

compression side close to the flanged connection and close to the conduit hole (sg1, sg2, and sg3 in Figure 7.4) gradually declined. The cracks adjacent to the conduit hole are identified in this figure by one arrow on each side of the hole. However, no cracks in the post-base plate were identified by visual inspection, the use of liquid dye penetrant, or ultrasonic testing. The drop in the strain readings for gages sg1, sg2, and sg3 is attributed to cracking around the conduit hole and not the cracking at the mast arm-flange plate connection. The cycle counts corresponding to the Type 1 and Type 2 failures (see Section 5.4) were 4,000,000+ and 4,000,000+, respectively. Accordingly, the cycle count at the point of failure of Specimen MA3 exceeds 4,000,000. Table 7.5 summarizes testing for specimen MA3.

Extension Piece. The extension piece placed beneath the mast arm specimens (see Figure 5.4) sustained approximately 7,500,000 cycles of loading before cracks were identified in the groove-welded connection of the pipe to the 2-3/4 in. (70 mm) thick base plate. Although the extension piece was not instrumented, it is appropriate to assign a Type 2 failure to the extension piece at 7,000,000 cycles at a stress range of 5.4 ksi (37 MPa). Note that a cycle count for a Type 1 failure can not be assigned to the extension piece because the Specimen MA2 actuator force at maximum displacement did not drop below 90 percent of the average maximum value, approximately 2.5 kips (11 kN); see Figure 7.15 for information.

### *7.8.3 Mast Arm Specimen Cracks*

Liquid dye penetrant was used to determine the presence of micro-cracking at the welded connection prior to testing and after the flange plate bolts were tightened.

*Specimen MA1* Micro-cracking in the flange plate-to-mast arm connection was noted prior to testing. During testing, evidence of further cracking in the welded connection was noted. In particular, a crack at the weld-to-mast arm interface (near the extreme fiber of the specimen on the tension side) propagated during the testing program. Figure 7.11(a) shows the schematics of this crack at the conclusion of testing and the flaws detected during the ultrasonic testing conducted prior to testing. At the conclusion of testing, this crack had propagated through both the wall of the mast arm and the thickness of the back-up ring, and was clearly visible on the inner wall of the specimen, and propagated through the thickness of the mast arm as seen in Figure 7.12(a).

*Specimen MA2* A micro-crack formed on the flange plate-to-mast arm weld at approximately 500,000 cycles and propagated slowly for the remainder of the test. Ultrasonic testing at the conclusion of the test did not identify any cracking. At the test conclusion, a section of the mast arm around the extreme fiber on the tension side was cut and polished. A cross section of the connection is shown in Figure 7.12(b); no evidence of cracking in the weld or parent mast arm material was found.

*Specimen MA3* Micro-cracking in the flange plate-to-mast arm was noted prior to testing. During testing, additional cracks were identified. Two significant cracks initiated at the conduit hole (on the compression side) at 2,300,000 cycles and propagated slowly into the mast arm. Figure 7.11(b) shows the extent of these cracks at the conclusion of the test. Ultrasonic tests at the conclusion of the test did not reveal any cracks at the flange plate-to-mast arm connection. After testing, a section of the specimen containing the conduit hole was cut out for further inspection. As seen in Figure 7.12(b), the cracks initiated at points on the conduit hole where the weld connecting the reinforcing pipe to the mast arm was abruptly terminated.

*Extension Piece* After approximately 7,500,000 cycles of loading (close to the finish of the tests on Specimen MA2), a small crack measuring less than two inches in length was detected in the groove weld connecting the extension piece to the 2-3/4 in. thick octagonal base plate on the tension side, close to the extreme fiber. Ultrasonic tests of the extension piece at the conclusion of the testing of Specimen MA2 indicated that this crack was approximately four inches long and that two other cracks existed on the opposite face, with one of these cracks measuring nearly five inches in length; see Figure 7.11(c). The extension piece was repaired prior to testing Specimen MA3 and passed ultrasonic testing both prior to and after the testing of Specimen MA3. No defects were identified in the groove-welded flange plate connection at the top of the extension piece.

### *7.8.4 Response Maxima*

The maximum peak-to-peak response for each data channel was obtained for each individual test for each mast arm specimen. Selected results are presented here.

*Specimen MA1* Figure 7.13 shows response maxima histories for the servo-actuator force and displacement. Evidence of significant cracking is clearly seen in Figure 7.13(a), starting at a cycle count of 2,500,000, wherein the resistance (actuator force) for a given tip displacement (actuator displacement) starts to drop. Figure 7.14 shows stress-range maxima histories for all locations on the mast arm. The stress range at 2.5 in. (63.5 mm) above the flange plate drops after approximately 2,000,000 cycles due to cracking at the flange plate welded connection. The stress range at 1.25 in. (32 mm) above the flange plate suggests that the stresses began to drop after approximately 1,500,000 cycles. At 2,200,000 cycles, the crack was sufficiently large enough so that the tensile stress at this location was equal to zero.

*Specimen MA2* Figure 7.14 shows response maxima histories for the servo-actuator force and displacement. The maxima remain essentially constant over the course of the testing program. Figure 7.15 shows the stress-range maxima histories for all locations on the mast arm. The stress range responses show very little deterioration over the course of the testing program.

*Specimen MA3* Figure 7.17 shows response maxima histories for the servo-actuator force and displacement. Figure 7.18 shows the stress-range maxima histories for selected locations on the mast arm. The stress ranges close to both the flange plate (sg1) and the conduit hole (sg2 and sg3) drop after approximately 1,500,000 cycles. At the conclusion of testing, the values of the stress range within 7 in. of the flange plate on the compression side are substantially smaller than those recorded at the start of testing due to cracking around the conduit hole.

### *7.8.5 Strain-Gage Histories*

Selected stress-range data were used to study the change in response as a function of the number of accumulated cycles. To account for drifting in the transducers in data observed due to signal conditioner response, the data is adjusted by removing the error which is assumed to be linearly increasing (from zero) over the course of the test. To illustrate the change in the stress range, the data are presented in the corrected form.

*Specimen MA1* Figure 7.19 shows the stress-response history (sg6) at 1.25 in. (32 mm) above the flange plate on the tension side of the specimen. At the beginning of the test, the stress history is sinusoidal. At 2,000,000 cycles of loading, the stress amplitude is significantly reduced due to cracking at the flange plate connection (see Figure 7.11a). At 4,000,000 cycles of loading, the stress range is extremely small.

*Specimen MA2* Figure 7.20 shows the stress-response history (sg6) at 1.25 in. (32 mm) above the flange plate on the tension side of the specimen. At the end of the test, the stress response is smaller than that at the start, due primarily to the smaller imposed displacement: see Figure 7.17 between cycles 3,200,000 and 4,000,000.

*Specimen MA3* Figure 7.21 shows the stress response history (sg6) at 1.25 in. (32 mm) above the flange plate on the compression side of the specimen. At the beginning of the test, the stress response is sinusoidal. At 3,000,000 cycles of loading, the value of stress response reduces because of extreme cracking around the conduit hole (see Figure 7.11b).

### *7.8.6 Selected Results for Specimen MA3*

Figure 7.22 shows the variation in lateral stiffness of specimen MA3 during testing. The stiffness increased from 10.0 kips/in (1.8 MN/m) to approximately 11.9 kips/in. (2.1 MN/m) after tightening the 2-1/4 in. (57 mm) anchor bolts using the turn-of-nut method, at a cycle count of approximately 100,000.

Figure 7.23 shows the ratio of axial strain readings at 1.25 in. (32 mm) above the flange plate on the tension side on the exterior (sg1) and interior (sg11) walls of the mast arm. The measured ratio is very

close to the theoretical value of 0.96 (obtained from simple flexural analysis with no in-plane bending effects) after the tightening of the nuts. However, prior to retightening of the bolts, the ratio differs significantly from the theoretical value, and this discrepancy is likely due to in-plane bending. The deviation of the ratio from the theoretical value at approximately 1,500,000 cycles is due to transducer malfunction.

### 7.9 Comparison with AASHTO Specifications

The AASHTO Specifications (AASHTO, 1994) classify the full-penetration welded connection used in the fabrication of the mast arm specimens and the extension piece into category E' for the purpose of characterizing fatigue life. For this category, a connection will have theoretically infinite fatigue life at stress ranges below 2.6 ksi (18 MPa).

A target stress range of 8 ksi (55 MPa) at a point 36 in. above the flange plate was used to determine nominal stress ranges at other points over the height of the mast arm and the extension piece. The corresponding stress ranges at key locations are as follows.

| Component | Height above base | Stress range, ksi (MPa) |
|---|---|---|
| Mast arm[1] | 36 in. (914 mm) | 8 (55) |
| Mast arm | 0 | 10 (69) |
| Extension piece | 26 in. (660 mm) | 4.5 (31) |
| Extension piece | 0 | 5.4 (37) |

1. See Figure 7.2

Specimen MA1 sustained approximately 1,800,000 cycles at a stress range of 10 ksi (69 MPa) at its base before cracks propagated in the groove-welded mast arm-to-flange plate connection. This cycle count is substantially higher than the fatigue limit of 400,000 cycles at 10 ksi (69 MPa) assigned to category E' construction by AASHTO. Specimen MA2 sustained more than 4,000,000 cycles at a stress range of 10 ksi (69 MPa) at its base with no signs of significant deterioration. Specimen MA3 sustained 4,000,000 cycles at a stress range of 10 ksi (69 MPa) at its base. The groove-welded connection of the extension piece to the 2-3/4 in. (70 mm) thick base plate sustained 7,500,000 cycles of loading at a stress range of 5.4 ksi (37 MPa) before any cracking in the connection was identified. The groove-welded connection of the extension piece to the 1-3/8 in. thick (35 mm) flange plate sustained more than 8,000,000 cycles at a stress range of 4.5 ksi (31 MPa) with no signs of significant deterioration.

These data points (MA1, MA2, MA3, Extension piece) are shown together with the AASHTO *design* curves classes in Figure 7.24. The AASHTO design curves are set two standard deviations below the mean response curve to provide a margin of safety against failure, and should not be directly compared with the actual data points.

### 7.10 Summary

Three mast arm specimens with nominally identical geometry were tested using one protocol to a maximum of 4,000,000 cycles of loading. As such, data collected from these tests provide only a small population of samples. Although it is difficult to draw conclusions about the general performance of this type of connection with such a small population, the following general observations are made.

The response of Specimen MA2 was superior to that of Specimens MA3 and MA1, although the cracking in Specimen MA3 cannot be attributed to the groove-welded mast arm-to-flange plate connection. The quality of workmanship was likely the key factor leading to the superior response of Specimen MA2. To maximize the fatigue life of the mast arm specimens, the following recommendations are made:

1. *Relocate the conduit hole*: Moving the conduit hole away from the flange plate will reduce the nominal stresses at this reduced cross section.

2. *Drill the circular conduit hole*: Drilling rather than flame cutting the conduit hole will likely reduce the magnitude of the stress concentrations at this reduced cross section.

3. *Develop a prequalified Welding Procedure Specification (WPS) for the groove-welded mast arm-to flange plate connection.* Standardized WPSs are commonly used for joining steel components in the building, bridge, and off-shore oil industries. In the past, it has been the contractors' responsibility to develop and implement a WPS (Shepard, 1997) for Caltrans sign structures. To maintain high standards of construction, Caltrans should prepare a WPS for groove-welded mast arm-to-flange plate connections. A WPS for the subject connection should include, but not be limited to, information on welding type (i.e., shielded metal arc welding, flux core-arc welding), end preparation, fit-up and root opening, maximum electrode diameter, electrode type, maximum current, maximum root-pass thickness, and pre-heat and cool-down requirements. The use of toughness-rated weld filler metal is recommended. Improved weld profiles, such as those shown in Figure 3.10 of AWS D1.1 (AWS, 1996), should be investigated for possible use. It is recommended that a welding consultant be engaged by Caltrans to develop the WPS.

4. *Develop improved quality control and inspection (quality assurance) procedures.* Current Caltrans standards for quality control and inspection of welded components should be reviewed. Minimum standards for quality control should be proposed by Caltrans and imposed on contractors building CMS structures. Visual inspection alone of non-redundant welded connections is likely inappropriate. As a minimum, all groove-welded connections should be ultrasonically tested (UT) by an approved testing agency as part of the quality control program. Good quality control and inspection are key to high-quality construction: all defects identified by UT should be gouged out and replaced prior to shipment of the post to the field. Standard procedures for repairing such defects must be developed. A Caltrans inspector should be present during the fit-up and welding of the mast arm-to-flange plate connections to ensure that the WPS is followed exactly. It is recommended that a welding consultant be engaged by Caltrans to develop new quality control and inspection procedures.
5. *Specify a maximum out-of-flatness for the flange plates, following welding, and a flange plate bolt-tightening sequence:* The substantial out-of-flatness of the flange plates led to the development of high local strains in the walls of the mast arms upon tightening of the flange plate bolts. A maximum out-of-flatness of the flange plates and a bolt-tightening sequence should be established such that the local strains in the walls of the mast arm are limited to a relatively small value, for example, 25 percent of yield strain.

Cracks initiated and propagated around the conduit hole located on the compression side of Specimen MA3. That is, cracks initiated and propagated in a zone subjected to nominal compressive stresses. Recognizing that crack propagation requires a net tensile stress at the crack tip, it is clear that high residual tensile strains were present in the mast arm adjacent to the conduit hole. Relocation of the conduit hole (see item 1 above) and drilling, as opposed to flame cutting, the conduit hole are recommended as methods of reducing the strains adjacent to the conduit hole.

Table 7.1: Strain distribution due to the tightening of flange plates for mast arm specimens (as a percent of yield strain)

| Strain gage | Specimen | | |
|---|---|---|---|
| | MA1 | MA2 | MA3 |
| sg1 | 88 | 64 | 60 |
| sg2 | 62 | 56 | 24 |
| sg3 | 16 | 7 | 13 |
| sg4 | 10 | 8 | 7 |
| sg5 | 3 | 4 | 1 |
| sg6 | 54 | 50 | 55 |
| sg7 | 96 | 79 | 63 |
| sg8 | 12 | 19 | NU[1] |
| sg9 | 11 | 10 | 7 |
| sg10 | 4 | 2 | 3 |
| sg12 | NU | NU | 215 |
| sg13 | NU | NU | 260 |
| sg14 | NU | NU | 160 |

1. NU designates Not Used.

Table 7.2: Instrumentation list for mast arm specimens

| Ch. | Inst. ID. | Placement | Location | Specimen |
|---|---|---|---|---|
| 1 | lc[1] | -------- | top of post | all |
| 2 | lvdt[2] | -------- | top of post | all |
| 3 | sg1[3] | exterior | compression side; 1.25" above flange | all |
| 4 | sg2 | exterior | compression side; 2.5" above flange plate (just below conduit hole) | all |
| 5 | sg3 | exterior | compression side; 7" above flange plate (just above conduit hole) | all |
| 6 | sg4 | exterior | compression side; 21" above flange plate | all |
| 7 | sg5 | exterior | compression side; 36" above flange plate | all |
| 8 | sg6 | exterior | tension side; 1.25" above flange plate | all |
| 9 | sg7 | exterior | tension side; 2.5" above flange plate | all |
| 10 | sg8 | exterior | tension side; 7" above flange plate | all |
| 11 | sg9 | exterior | tension side; 21" above flange plate | all |
| 12 | sg10 | exterior | tension side; 36" above flange plate | all |
| 13 | sg11 | interior | tension side; 1.25" above flange plate | MA3 |
| 14[4] | sg12 | exterior | compression side; just above the weld line | MA3 |
| 15 | sg13 | exterior | tension side; just above the weld line | MA3 |
| 16 | sg14 | exterior | neutral axis; just above the weld line | MA3 |

1. lc designates load cell.
2. lvdt designates displacement transducer.
3. sg designates strain gage.
4. designates the channels used to measure the effect of tightening of the flange plate bolts (not used in cyclic tests).

Table 7.3: Test summary for Specimen MA1

| Cycle Count (millions) | Event |
|---|---|
| 0 | Ultrasonic testing reveals several flaws in the welded connection of the flange plate; flaws not repaired. |
| 0 | Micro-cracking of the welded connection during tightening of the flange bolts. |
| 1.0 | Circumferential crack on the tension side of the welded flange plate connection is observed. |
| 2.3 | The crack propagates into the groove weld at the location of a flaw detected by ultrasonic testing. |
| 2.5 | The crack propagates through the thickness of mast arm wall. |
| 4.0 | Test terminated; post-test inspection reveals the crack on the tension side has propagated through the thickness of the mast arm and the back-up ring, and is visible from inside the mast arm; see Figure 7.12(a). |

Table 7.4: Test summary for Specimen MA2

| Cycle Count (millions) | Event |
|---|---|
| 0 | Specimen passes ultrasonic testing. |
| 1 | No cracking of the welded connection during tightening of the flange bolts. |
| 0.3 | Small crack in the weld around the conduit hole is observed. |
| 0.5 | Small crack in the mast arm-to-flange plate weld (tension side) is observed. |
| 1.2 | Small crack in the mast arm-to-flange plate weld (compression side) is observed. |
| 2.5 | Small growth in the crack on the tension side of the mast arm-to-flange plate weld. |
| 4.0 | Test terminated; specimen passes ultrasonic testing. |

Table 7.5: Test summary for Specimen MA3

| Cycle Count (millions) | Event |
|---|---|
| 0 | Specimen passes ultrasonic testing. |
| 1 | No cracking of the welded connection during tightening of the flange bolts. |
| 2.0 | Strains on the compression side drop. |
| 2.3 | A crack at the conduit hole weld (compression side) is observed. |
| 2.4 | A second crack at the conduit hole, opposite side to the other crack, is observed. |
| 3.4 | Substantial propagation of cracks around the conduit hole. |
| 3.8 | Crack lengths around the conduit hole exceed 0.5 in. |
| 4.0 | Test terminated; post-test inspection reveals the crack length exceeds 2.5 in. and propagates through the thickness of the mast arm, see Figure 7.12(c). |

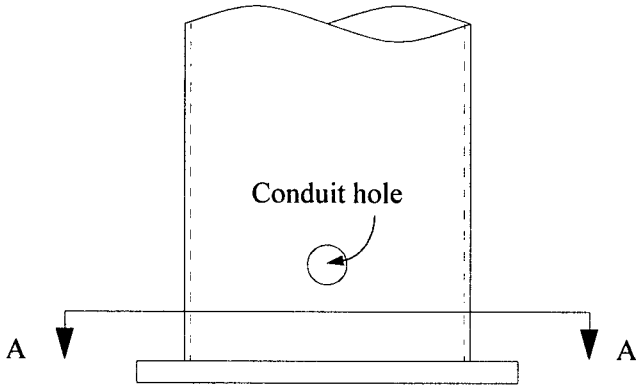


(a) Elevation at base of mast arm

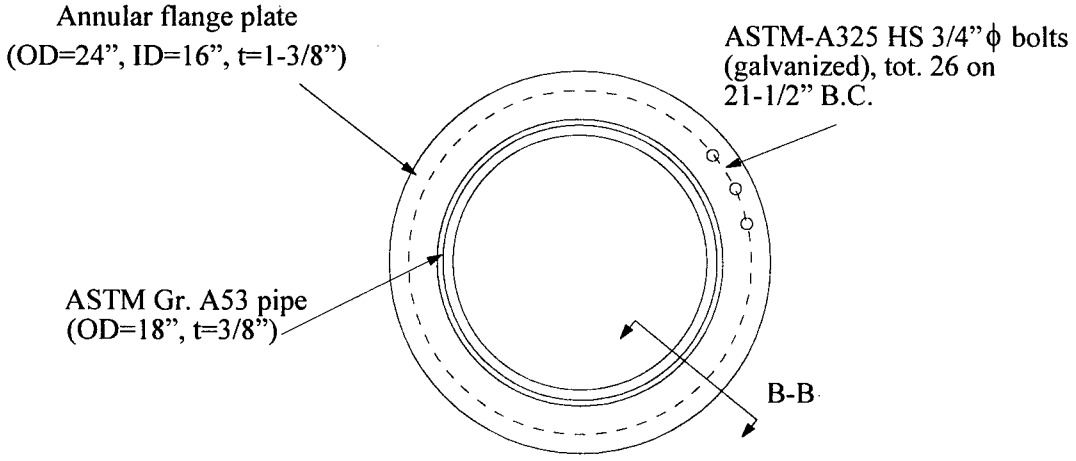


(b) Section A-A (plan view)

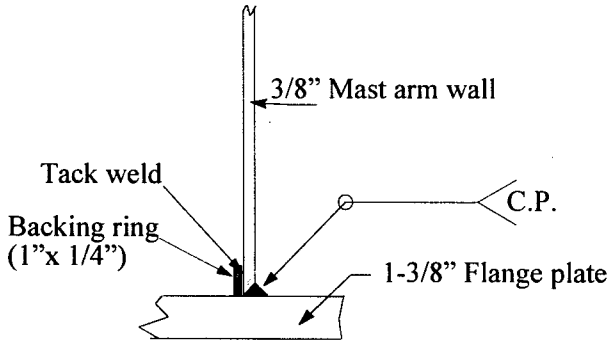


(c) Section B-B (connection details)

Figure 7.1: Connection details for mast arm specimens

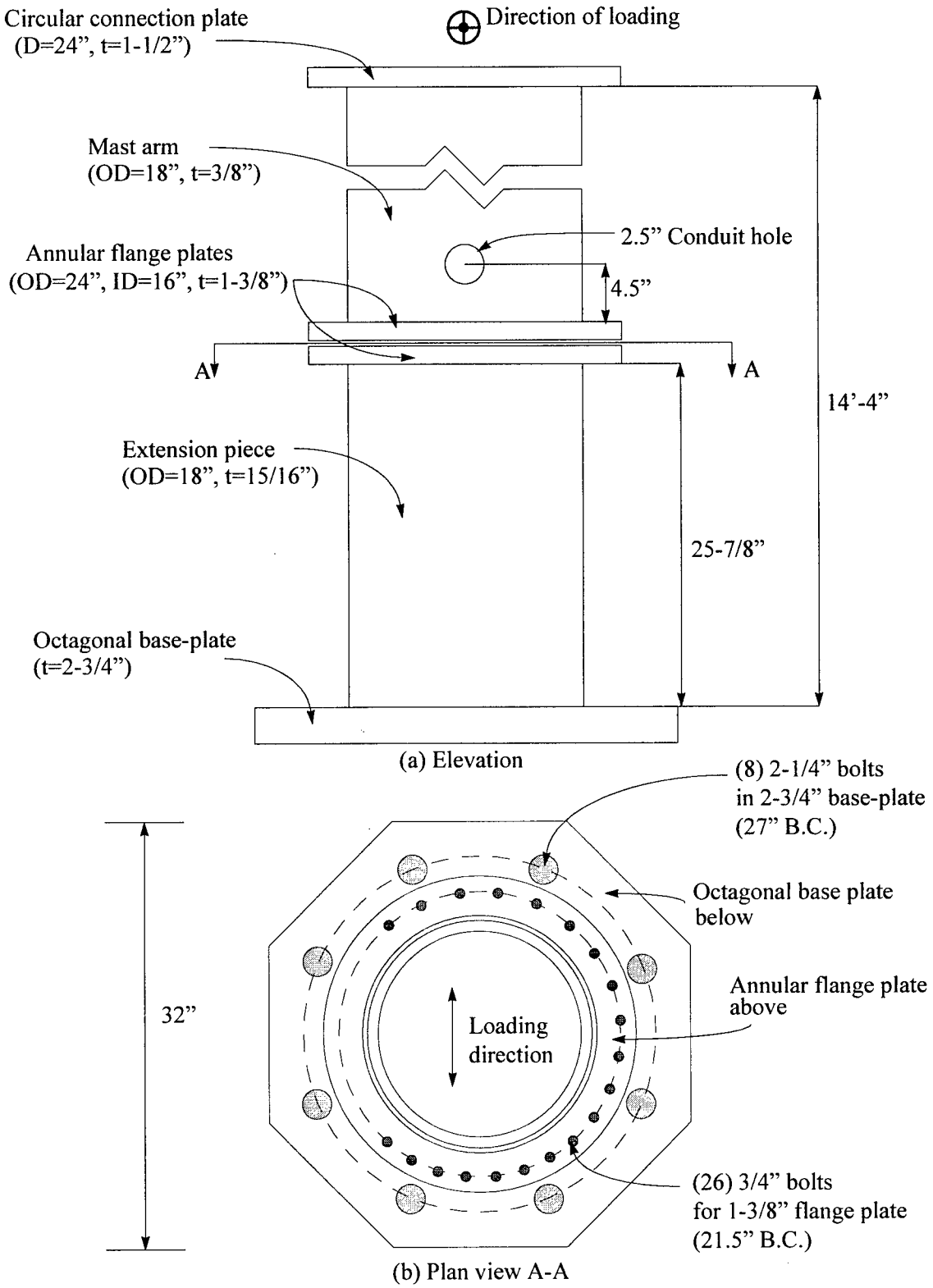


Figure 7.2: Schematic views of mast arm specimens

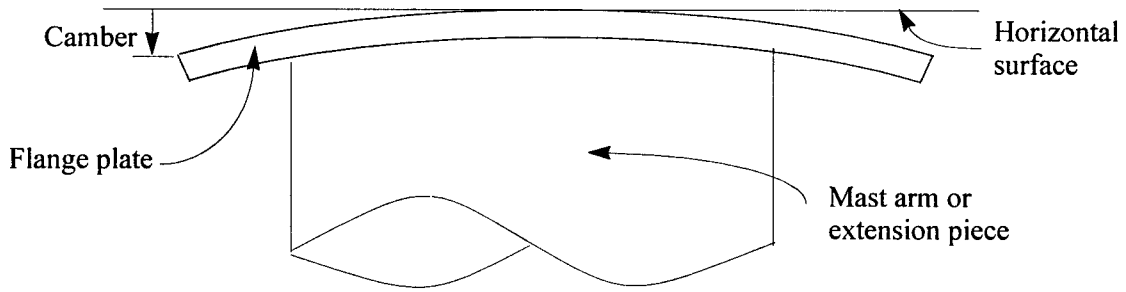


(a) Measurement of camber (out-of-flatness)

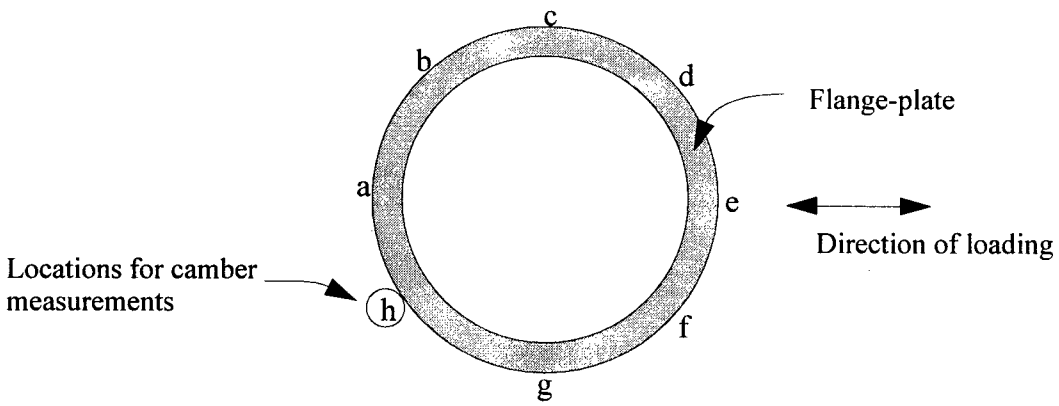


(b) Plan view of flange plate

| Location | MA1 | MA2 | MA3 | Extension Piece |
|---|---|---|---|---|
| a | 60 | 20 | 32 | 130 |
| b | 65 | 35 | 31 | 65 |
| c | 70 | 45 | 28 | 70 |
| d | 65 | 47 | 42 | 80 |
| e | 45 | 52 | 51 | 80 |
| f | 60 | 60 | 46 | 95 |
| g | 65 | 72 | 52 | 95 |
| h | 55 | 40 | 40 | 140 |

(c) Camber values measured prior to testing of mast arms (x1000 inch)

Figure 7.3: Camber measurements for mast arm specimens and the extension piece

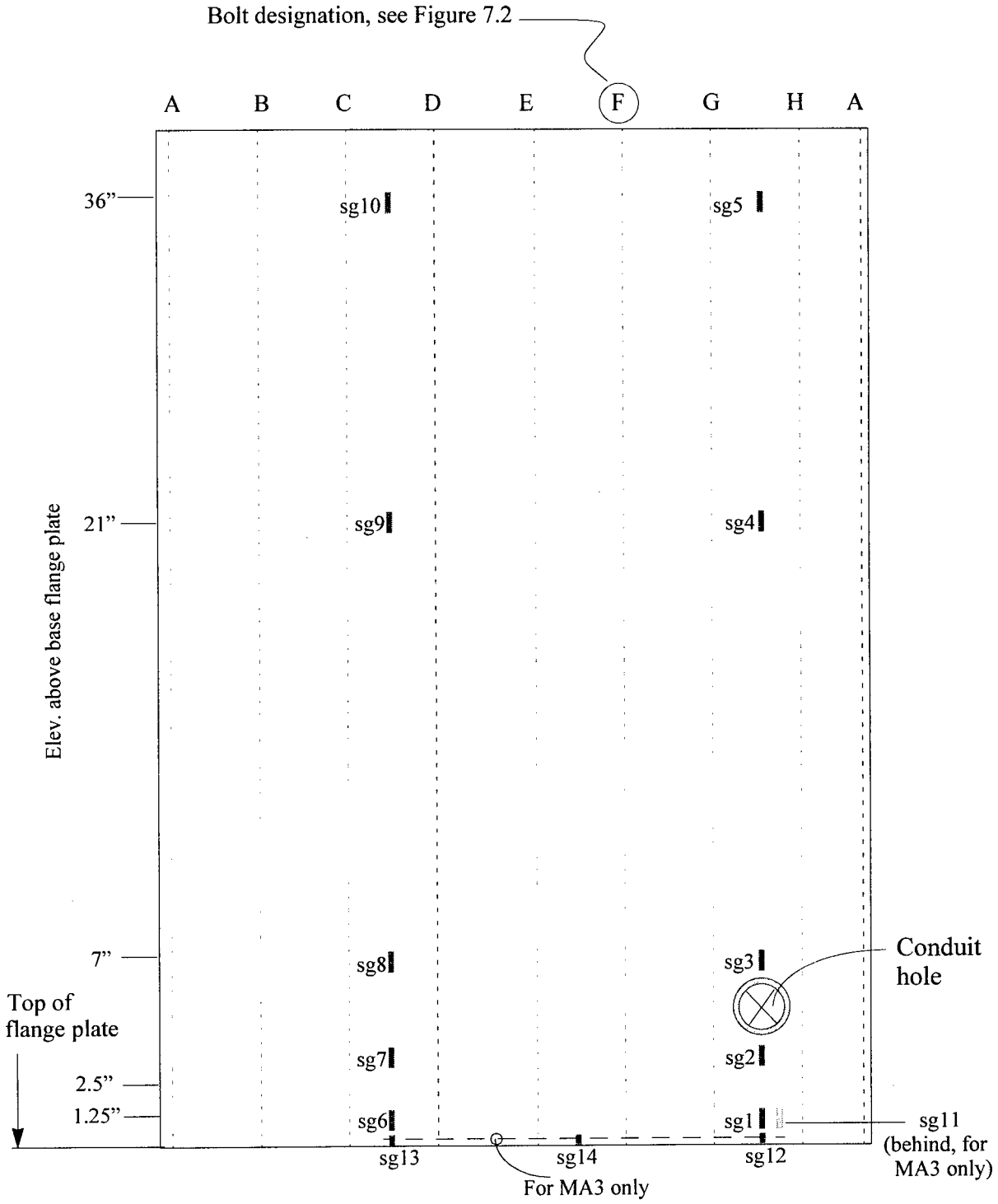


Figure 7.4: Exploded view of instrumentation for mast arm Specimens MA1, MA2, and MA3

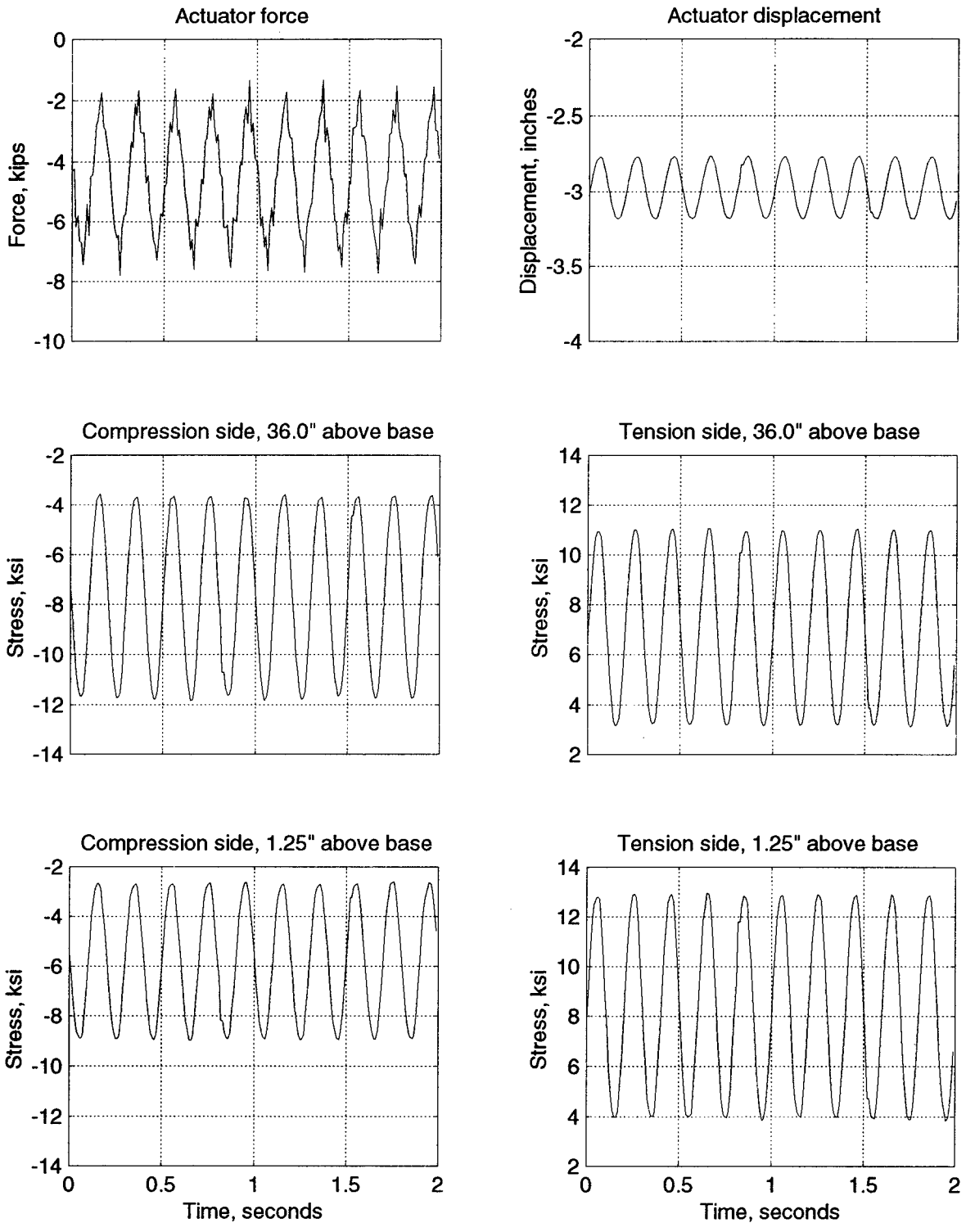


Figure 7.5: Response histories after 20,000 cycles for Specimen MA1

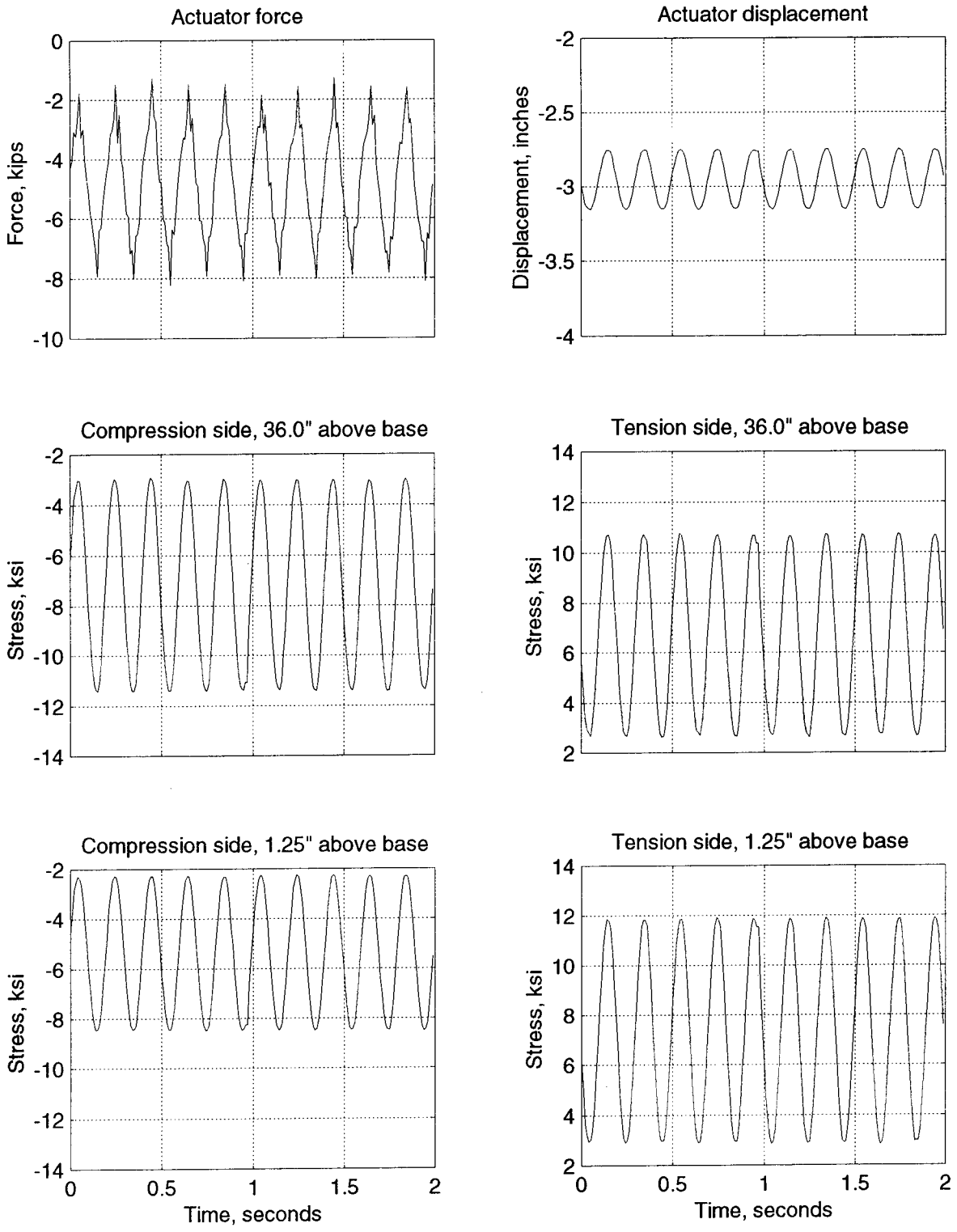


Figure 7.6: Response histories after 20,000 cycles for Specimen MA2

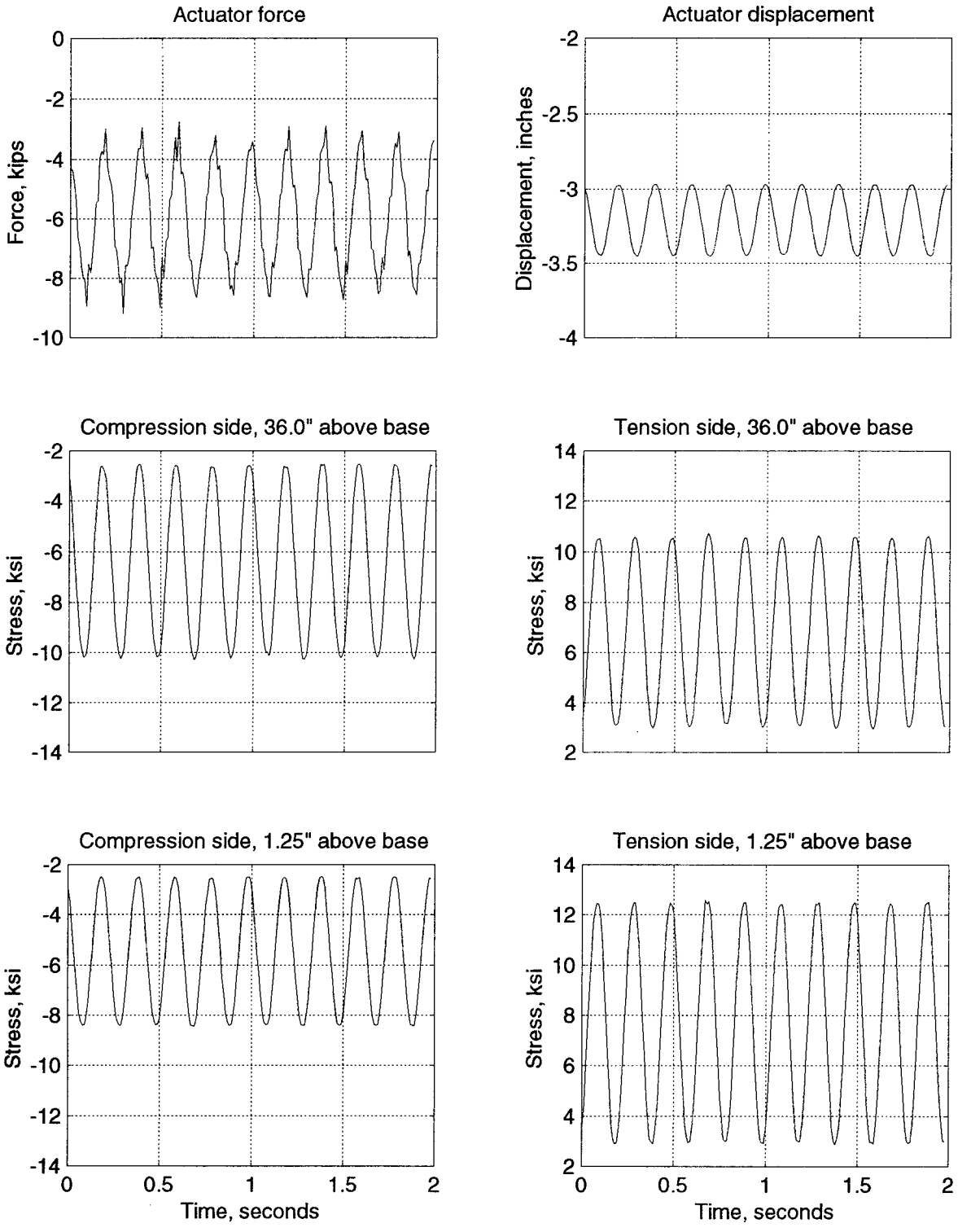


Figure 7.7: Response histories after 20,000 cycles for Specimen MA3

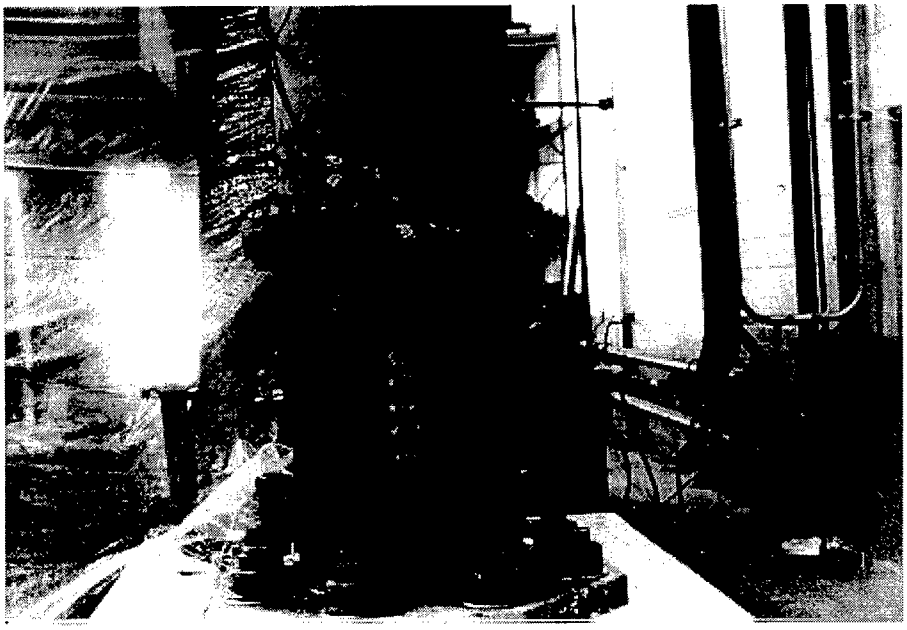

(a) During testing

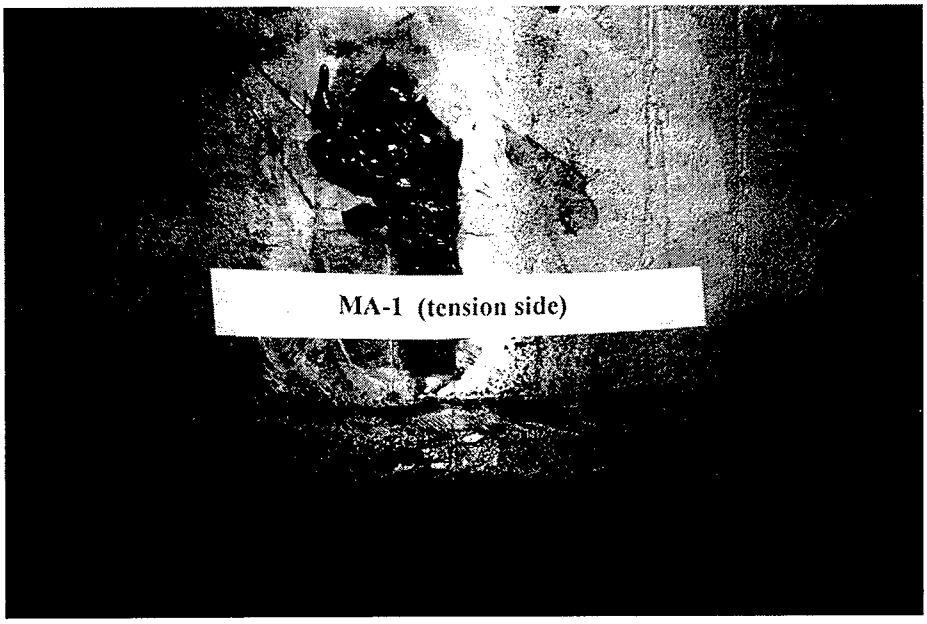


(b) At the conclusion of testing

Figure 7.8: Photographs of Specimen MA1

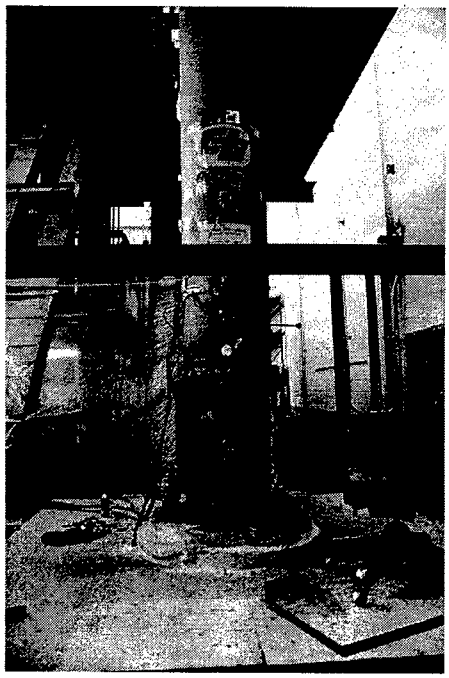

(a) During testing

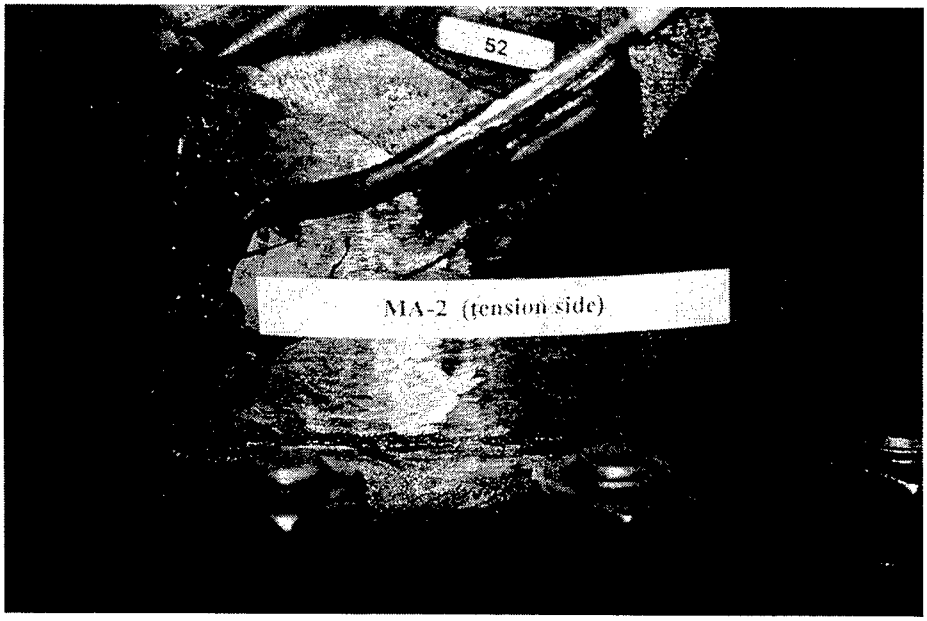


(b) At the conclusion of testing

Figure 7.9: Photographs of Specimen MA2

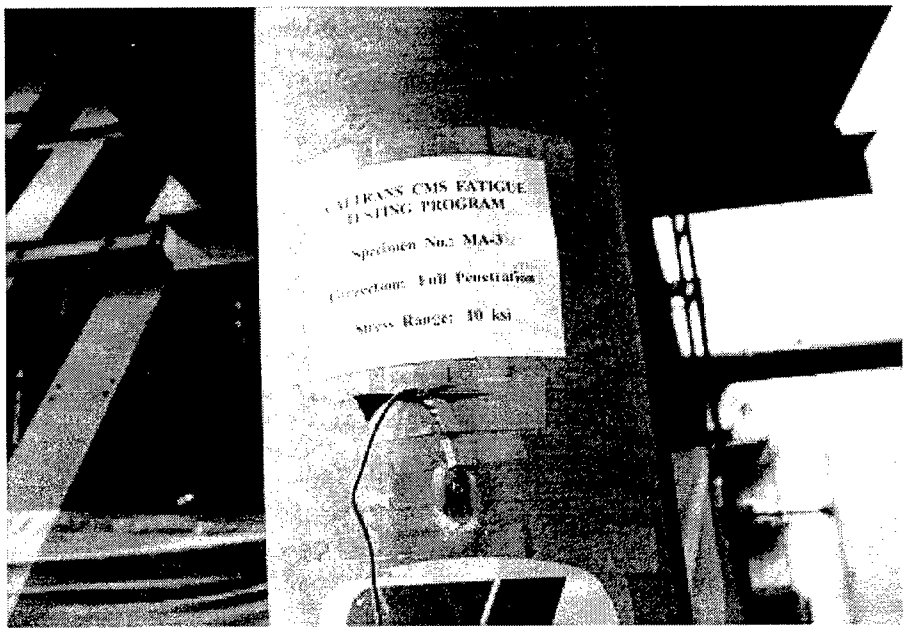


(a) During testing

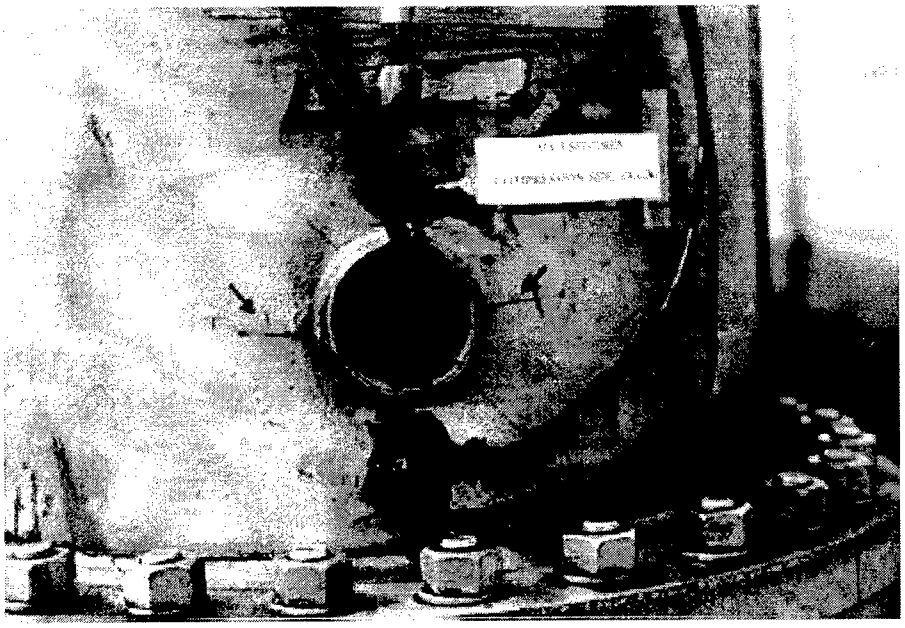

(b) At the conclusion of testing

Figure 7.10: Photographs of Specimen MA3

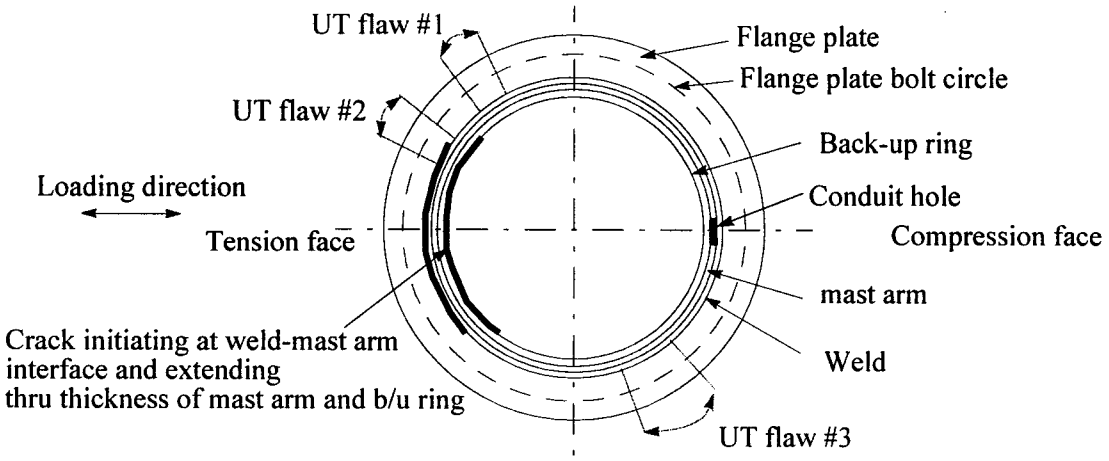


(a) Pre-testing flaws and final crack configuration at the base of Specimen MA1

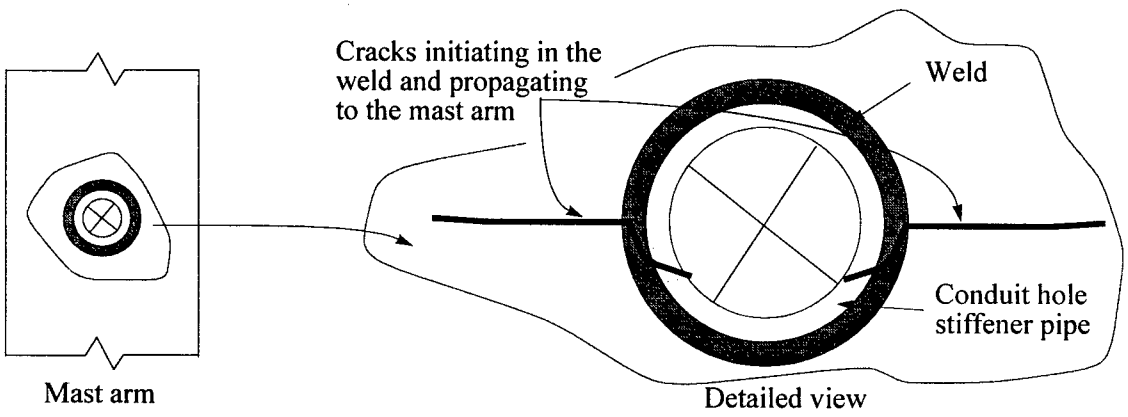


(b) Final crack configuration, Specimen MA3

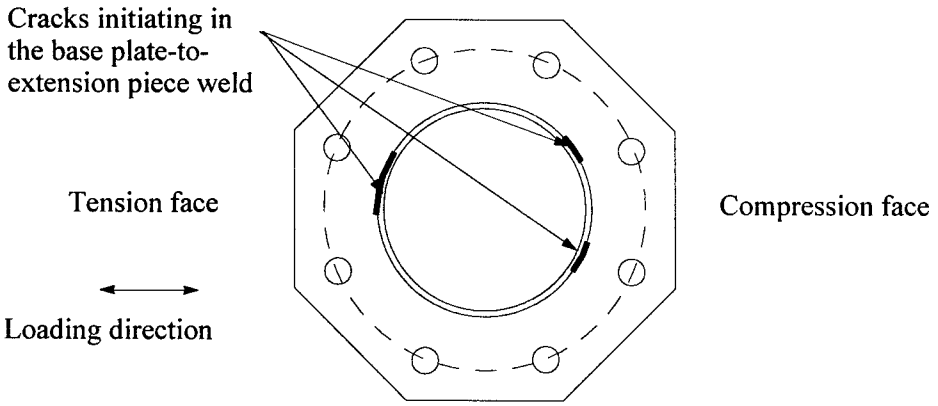


(c) Cracking of the extension piece at the conclusion of Specimen MA2 tests

Figure 7.11: Cracking of welded connections in test specimens

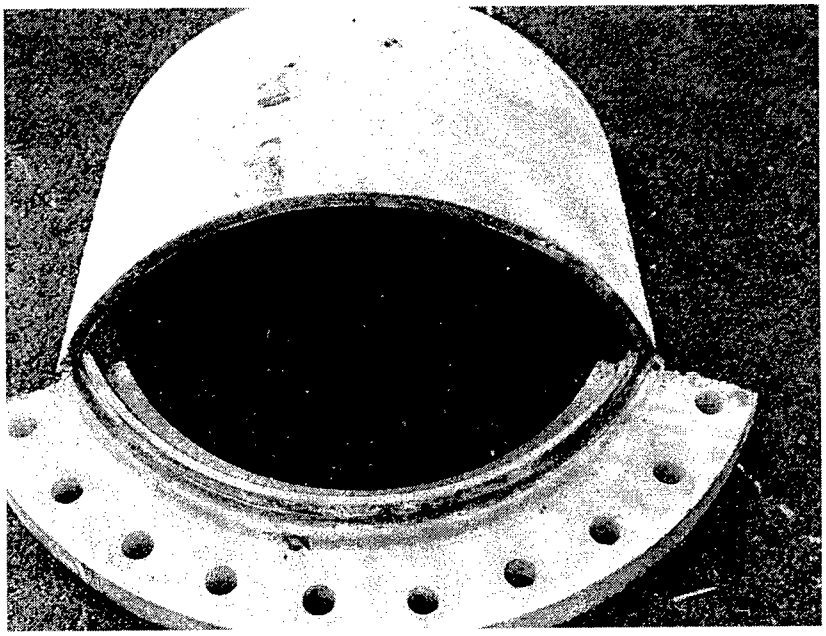

(a) Cracking of the post-to-base plate connection for Specimen MA1

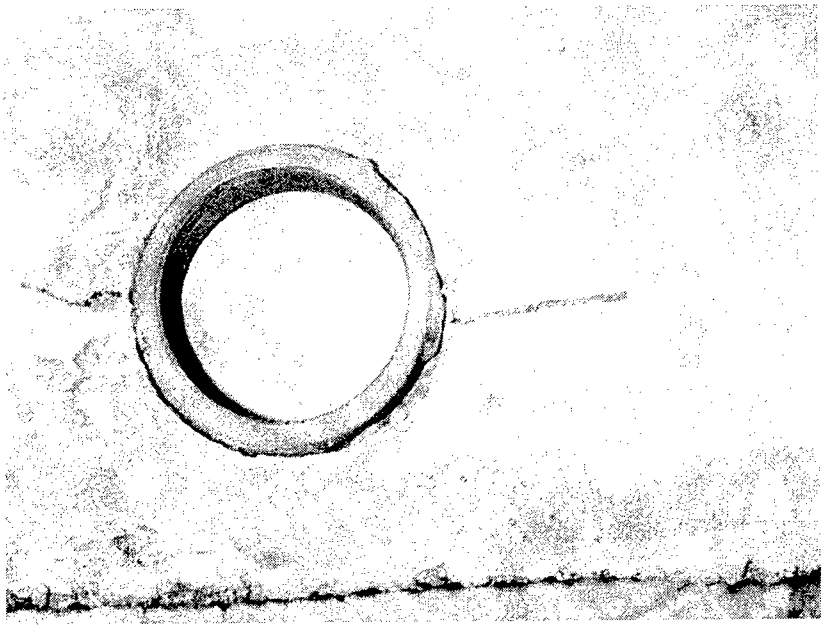

(b) Cracks around the circular conduit hole for Specimen MA3

Figure 7.12: Photos of inside of specimens MA1 and MA3

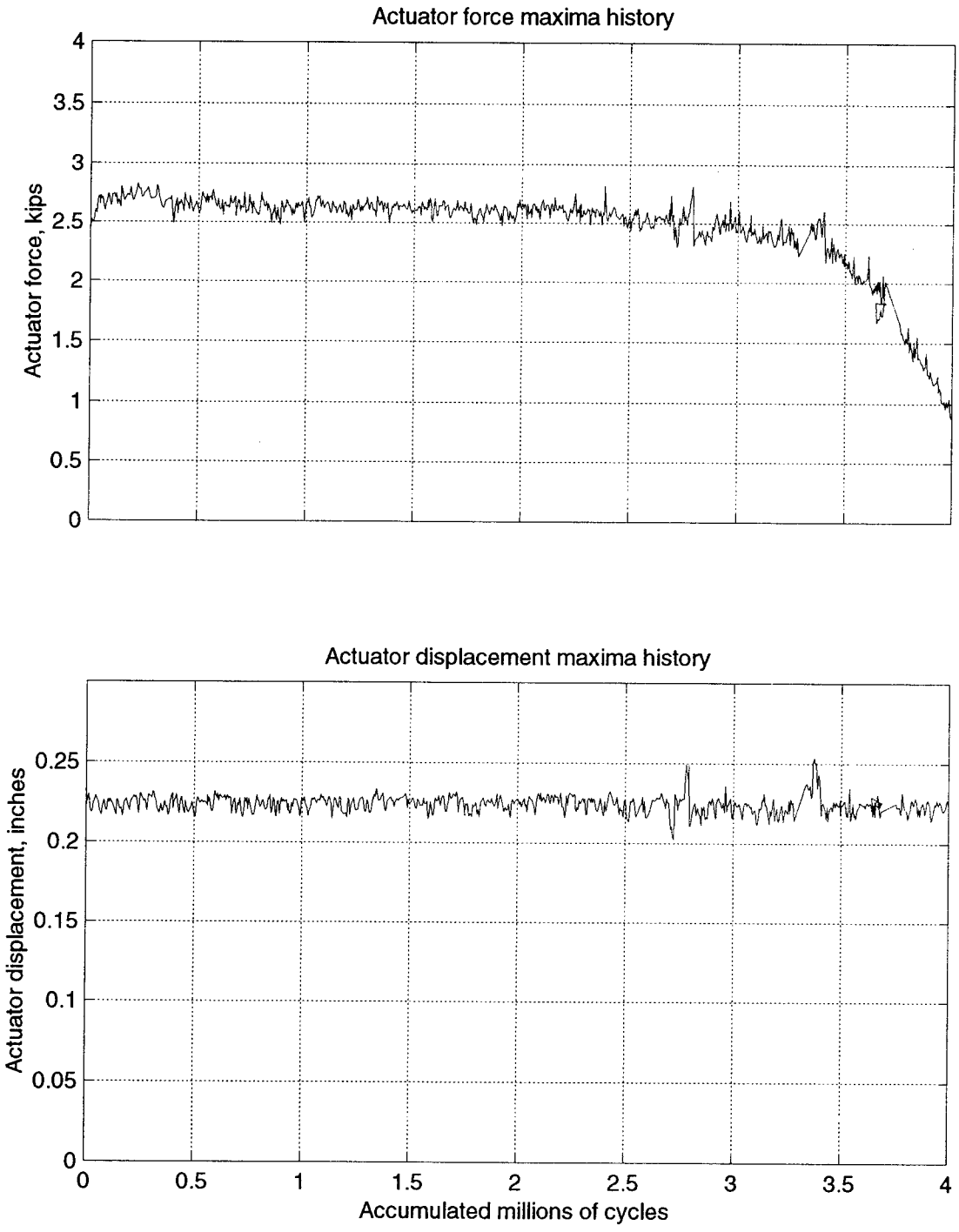


Figure 7.13: Actuator force and displacement maxima history for Specimen MA1

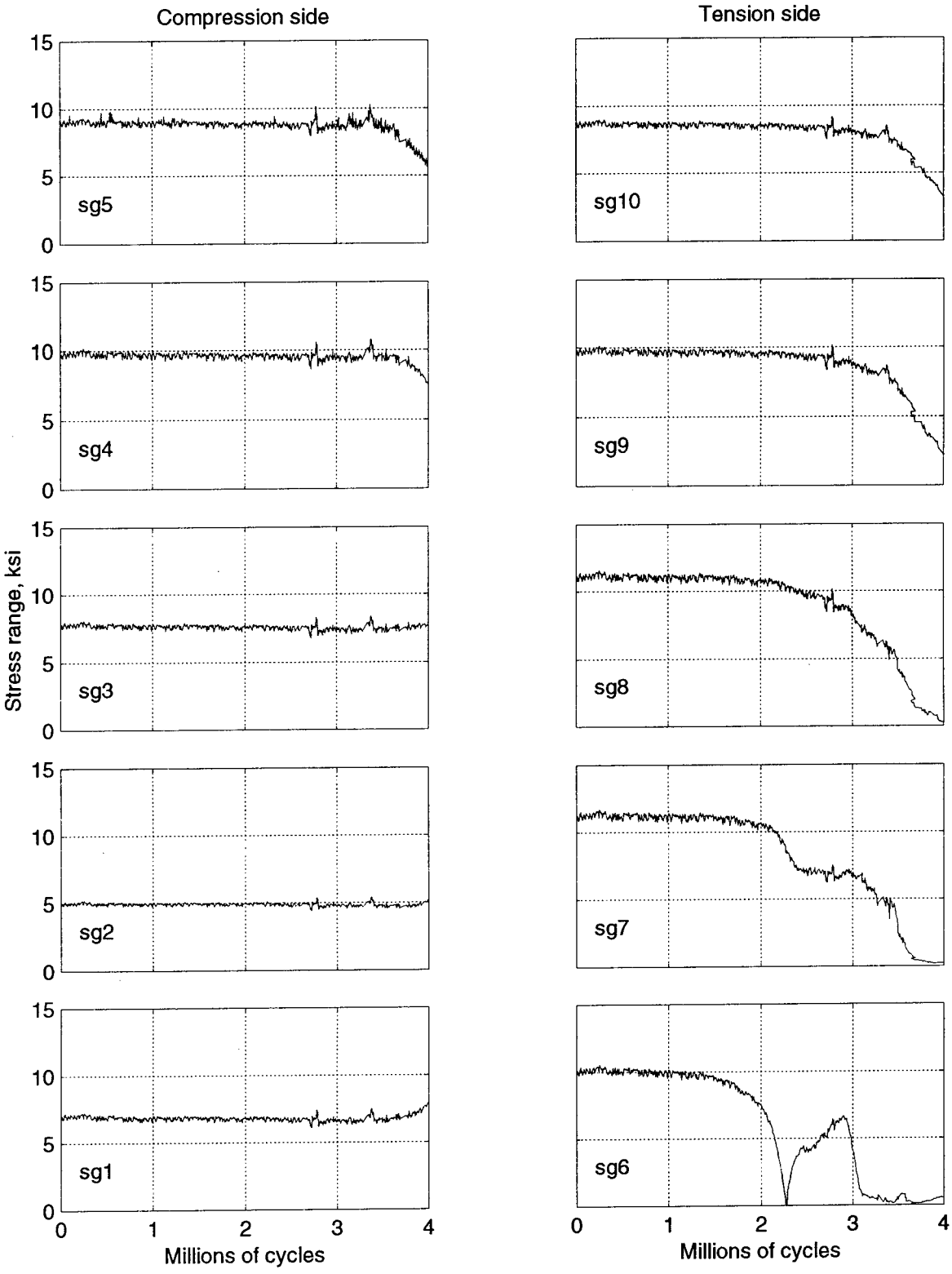


Figure 7.14: Stress range maxima during the testing for Specimen MA1

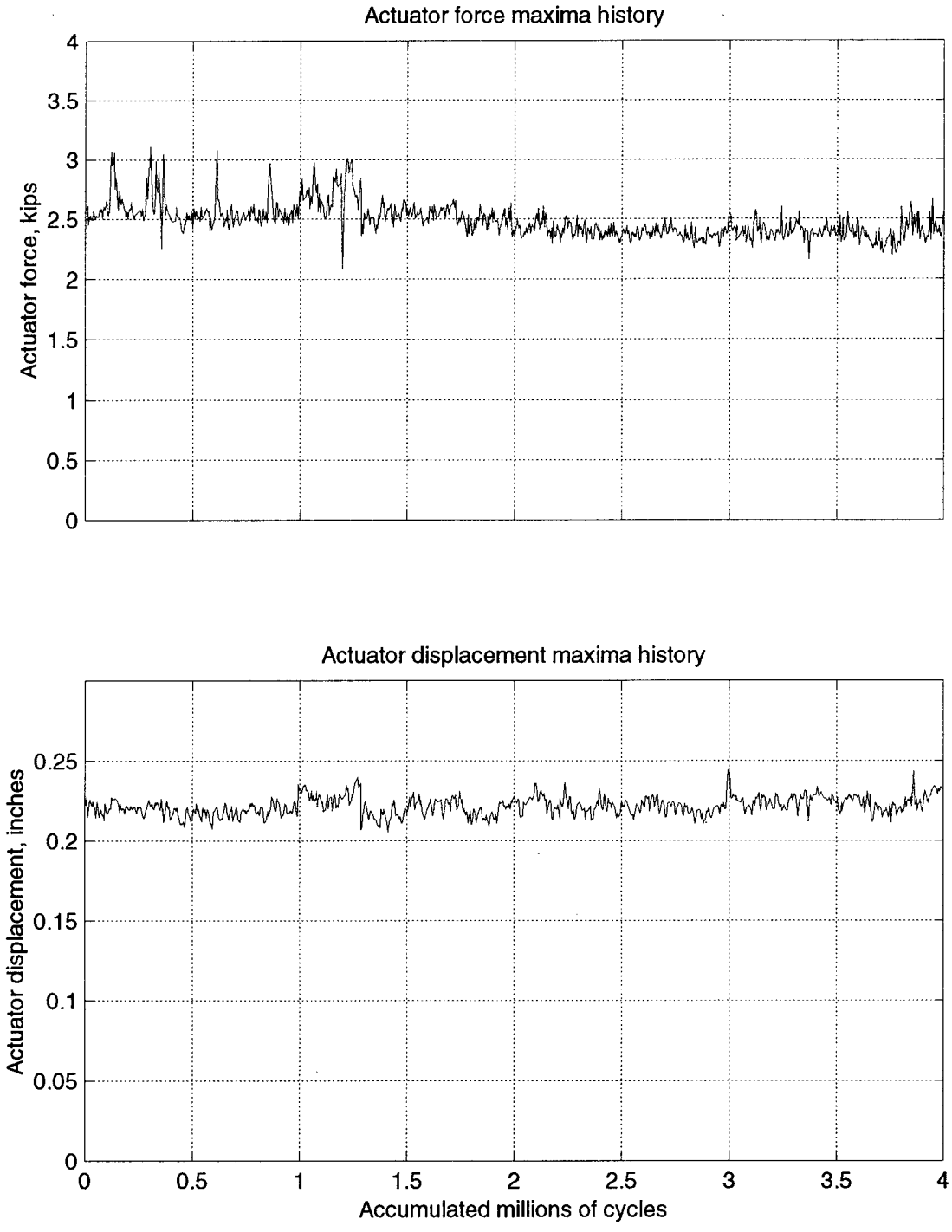


Figure 7.15: Actuator force and displacement maxima history for Specimen MA2

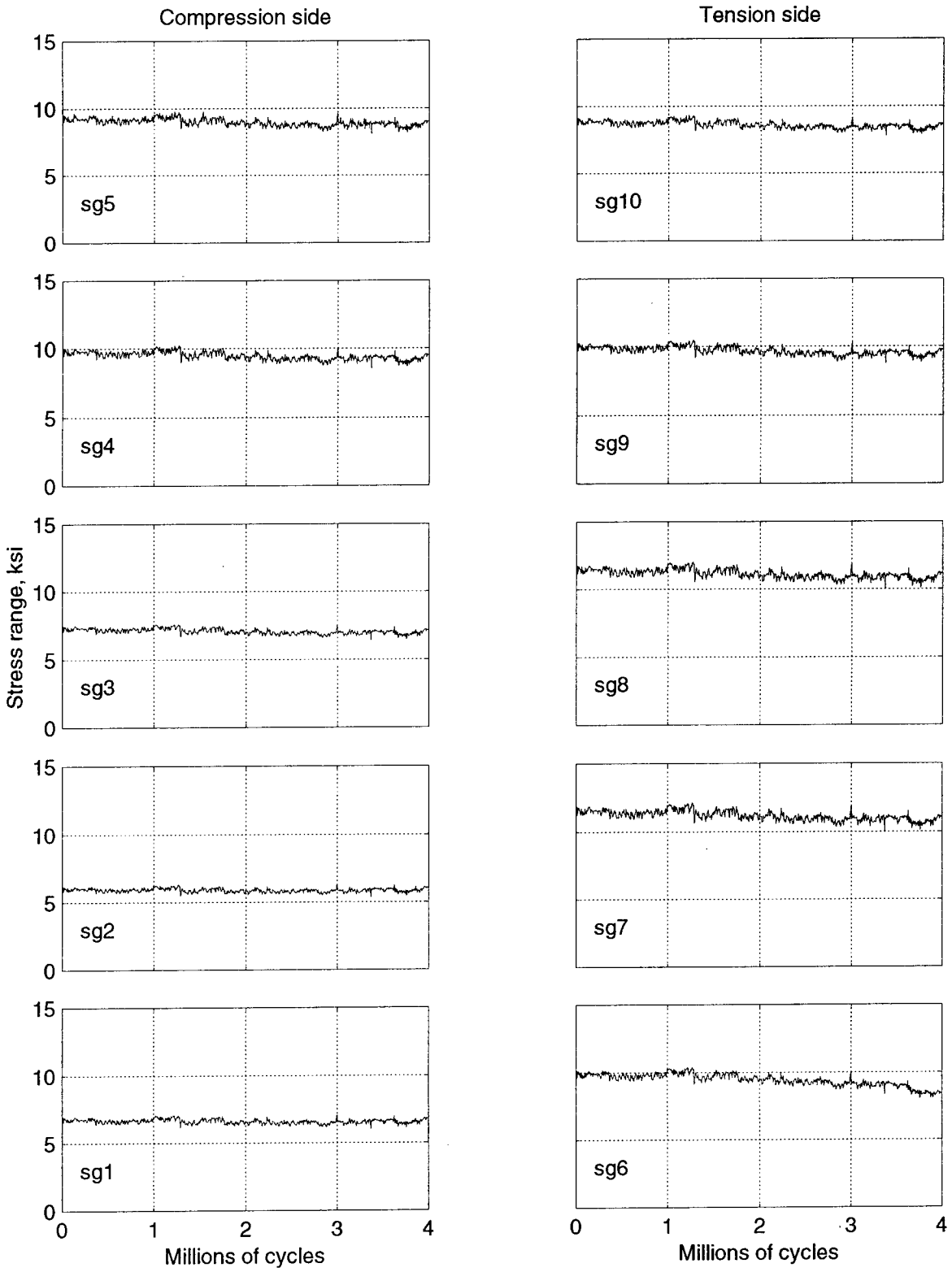


Figure 7.16: Stress range maxima during the testing for Specimen MA2

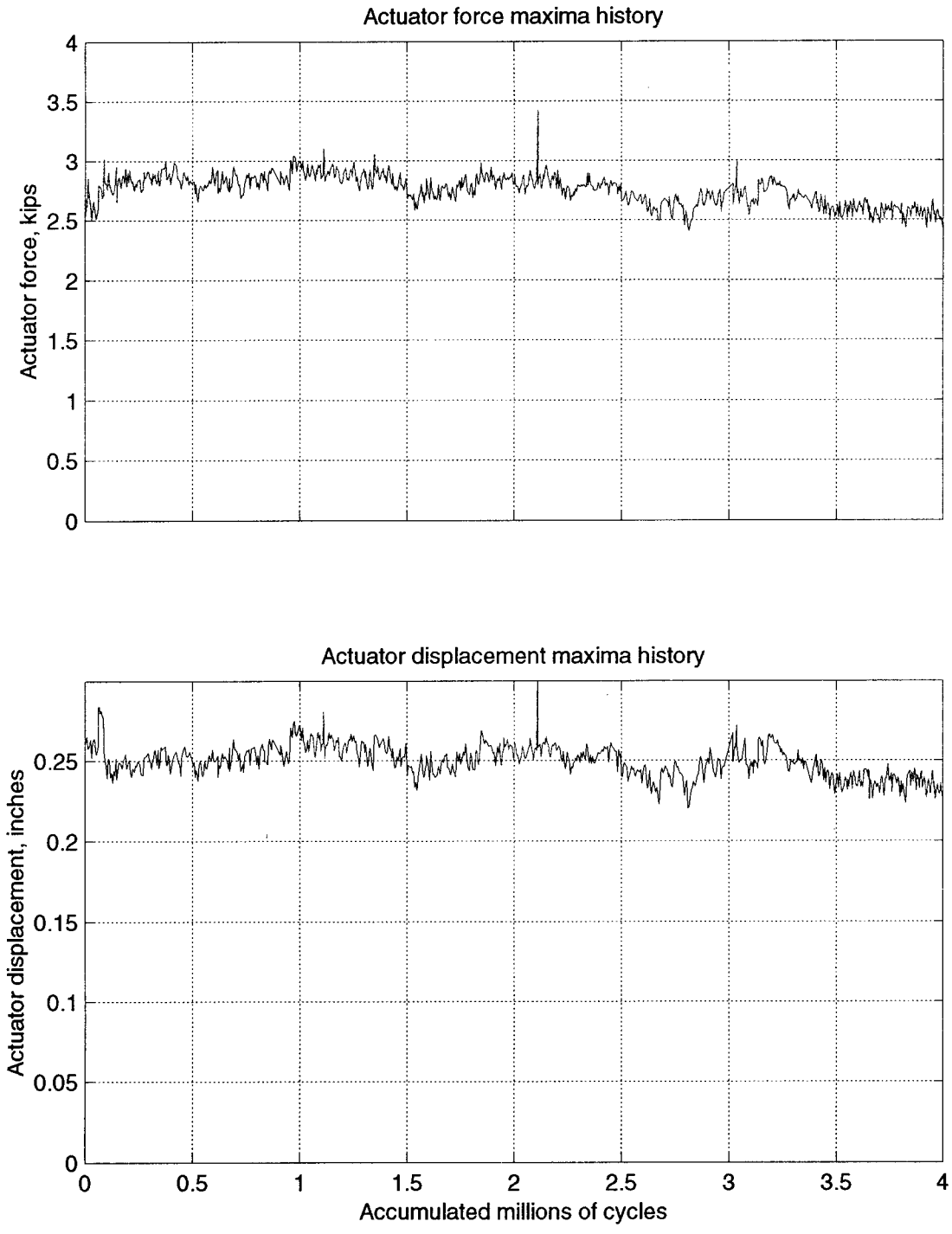


Figure 7.17: Actuator force and displacement maxima history for Specimen MA3

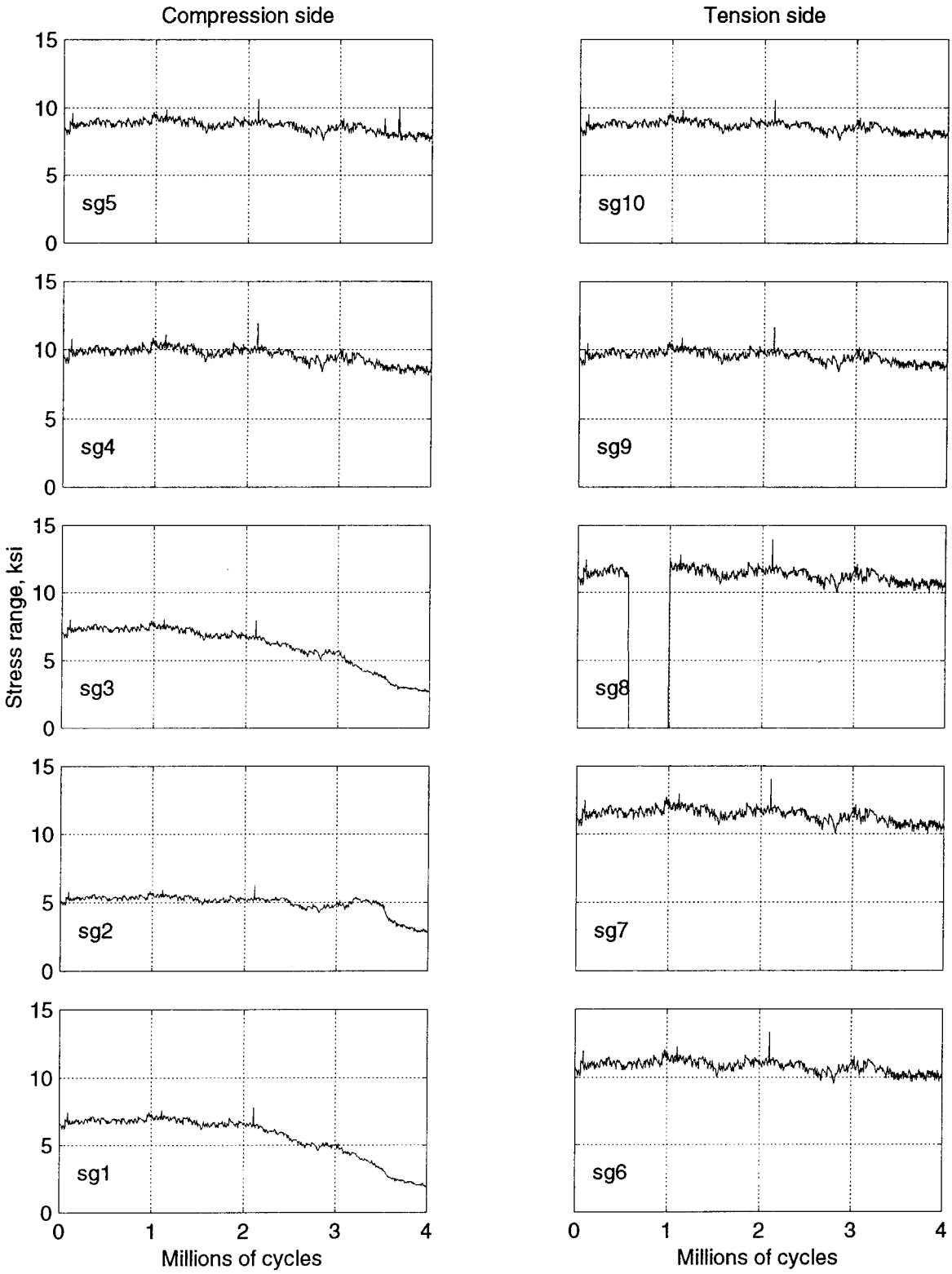


Figure 7.18: Stress range maxima during the testing for Specimen MA3

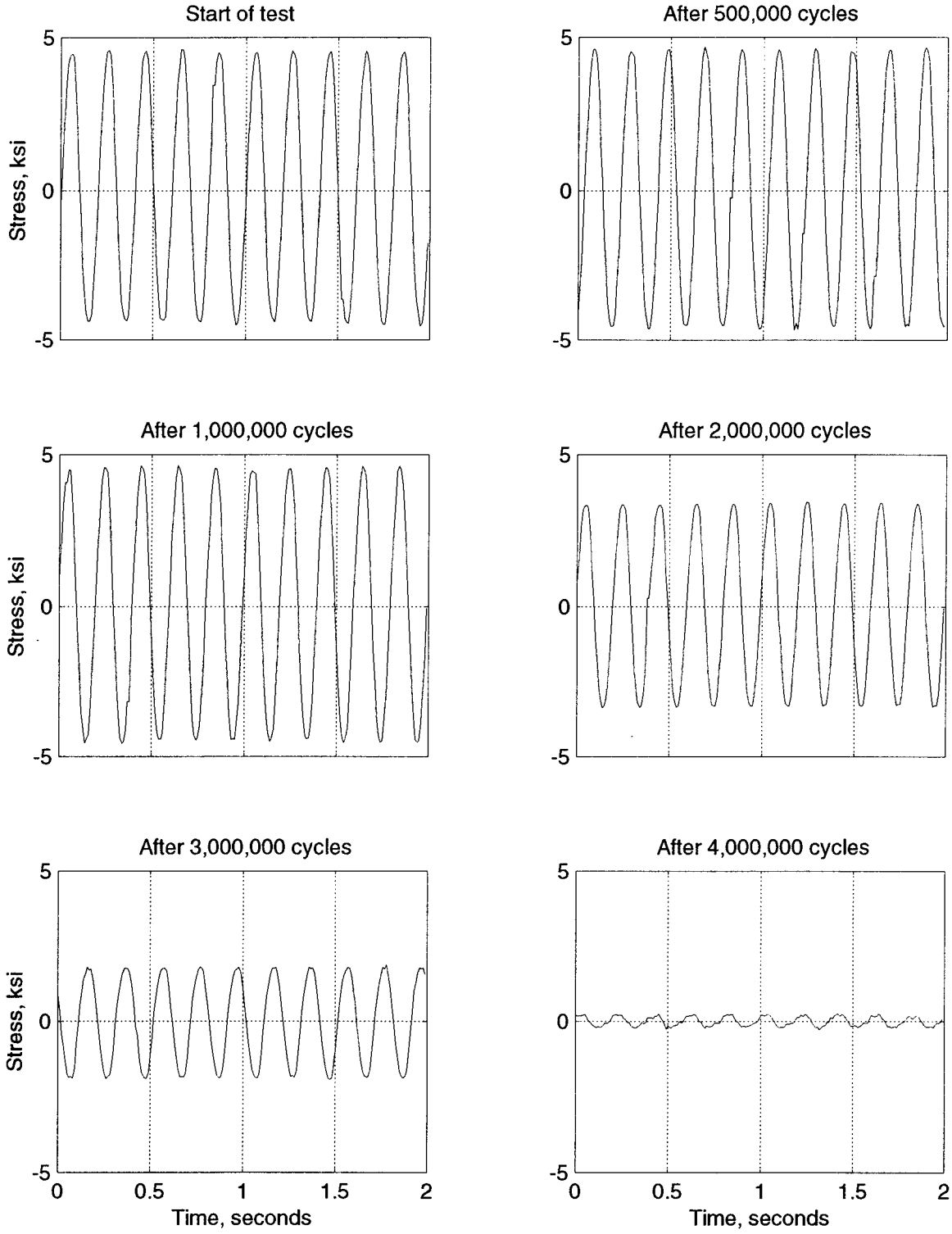


Figure 7.19: Tensile stress history at 1.25 in. above the flange plate (sg6) for Specimen MA1

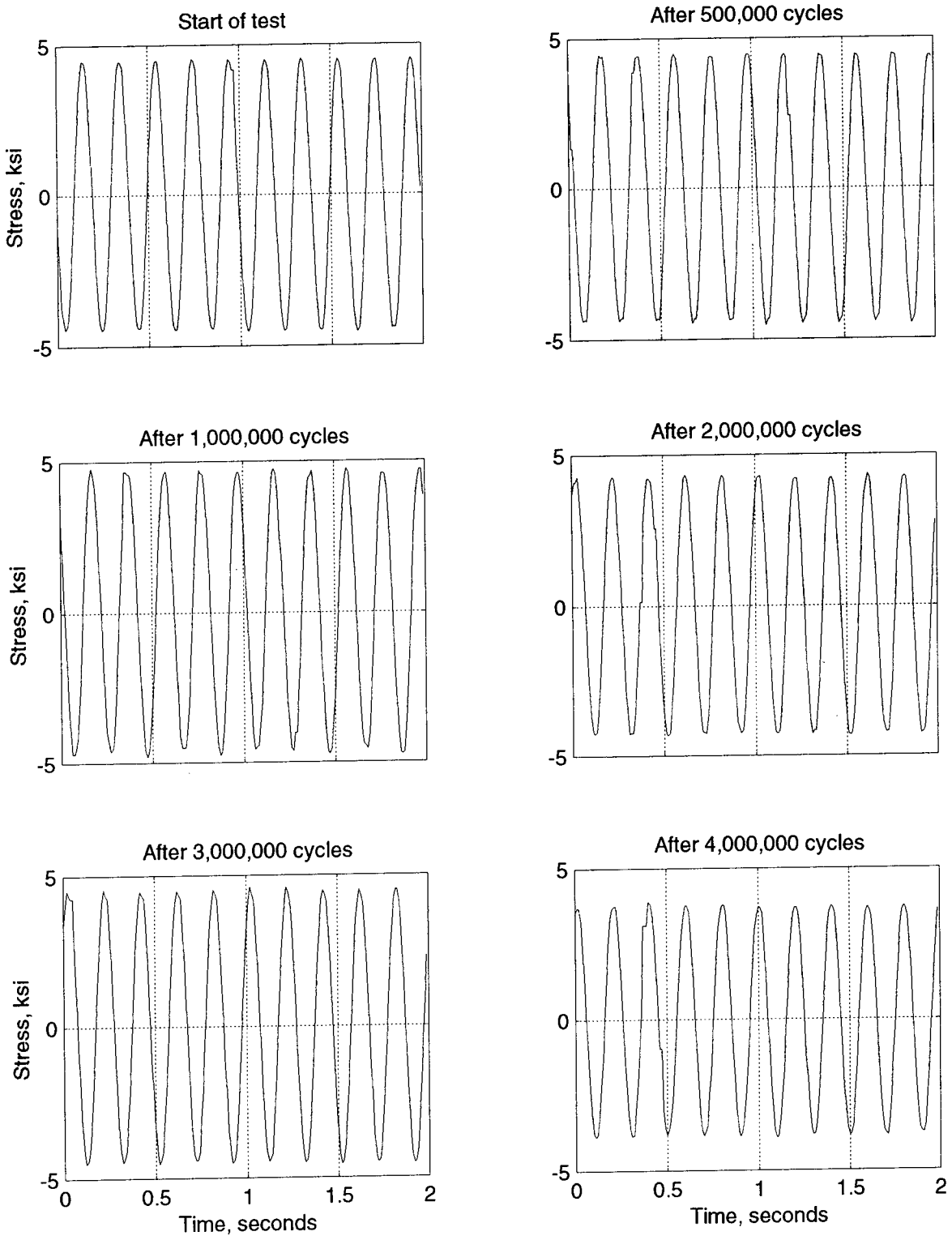


Figure 7.20: Tensile stress history at 1.25 in. above the flange plate (sg6) for Specimen MA2

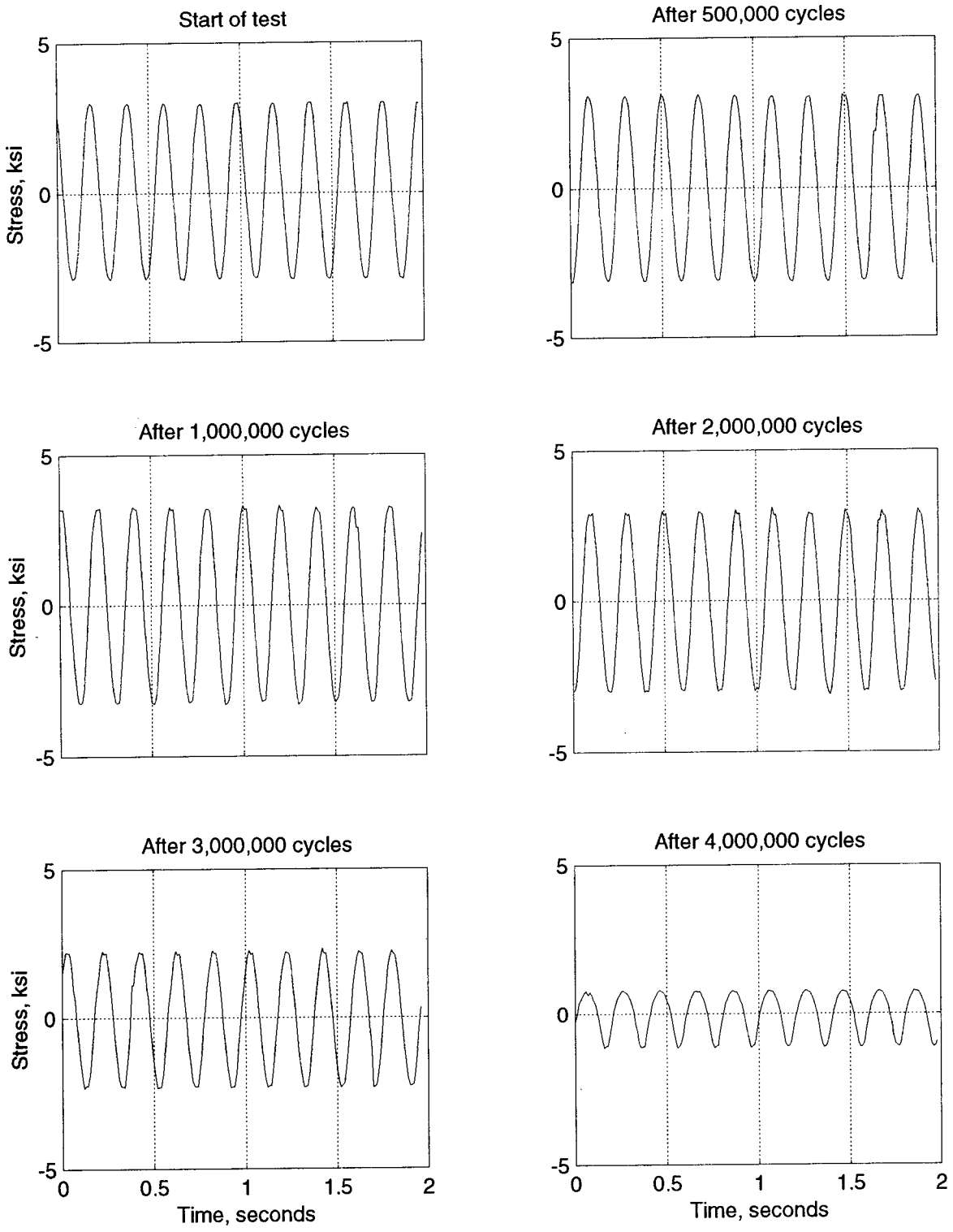


Figure 7.21: Compressive stress history at 1.25 in. above the flange plate (sg1) for Specimen MA3

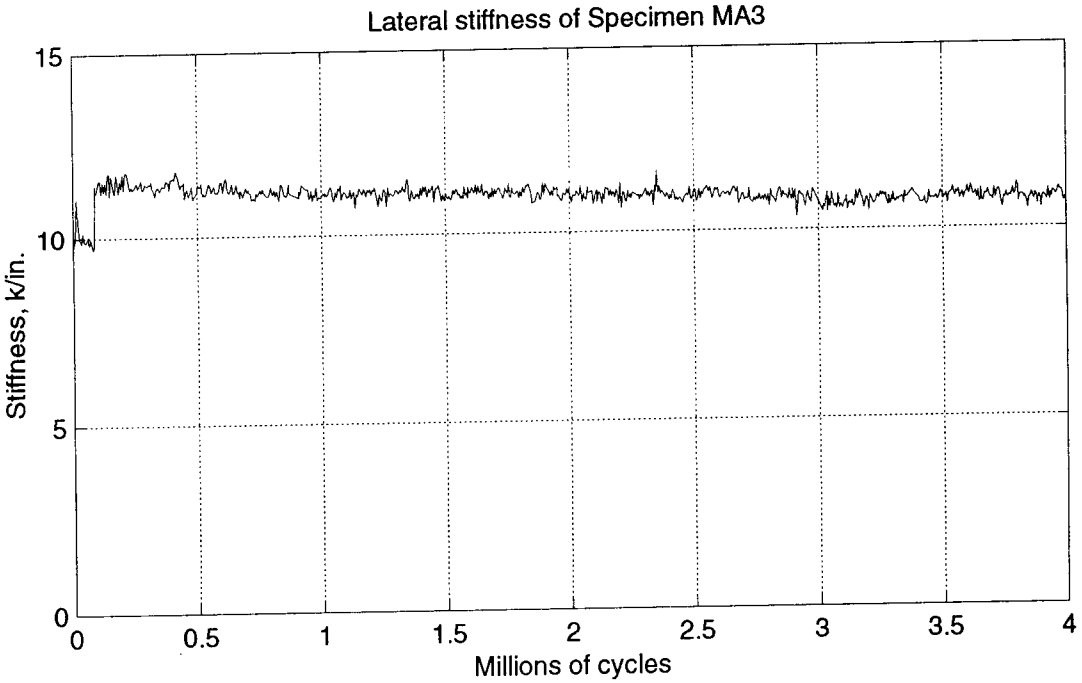


Figure 7.22: Lateral stiffness maxima history for Specimen MA3

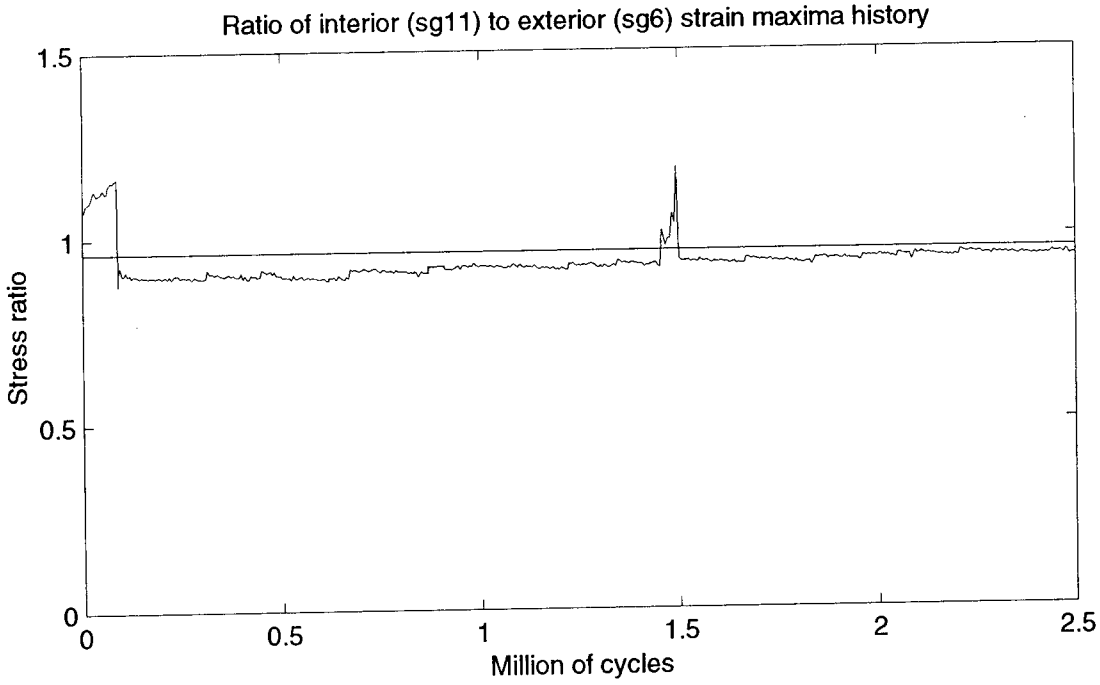


Figure 7.23: Stress-ratio maxima history for Specimen MA3

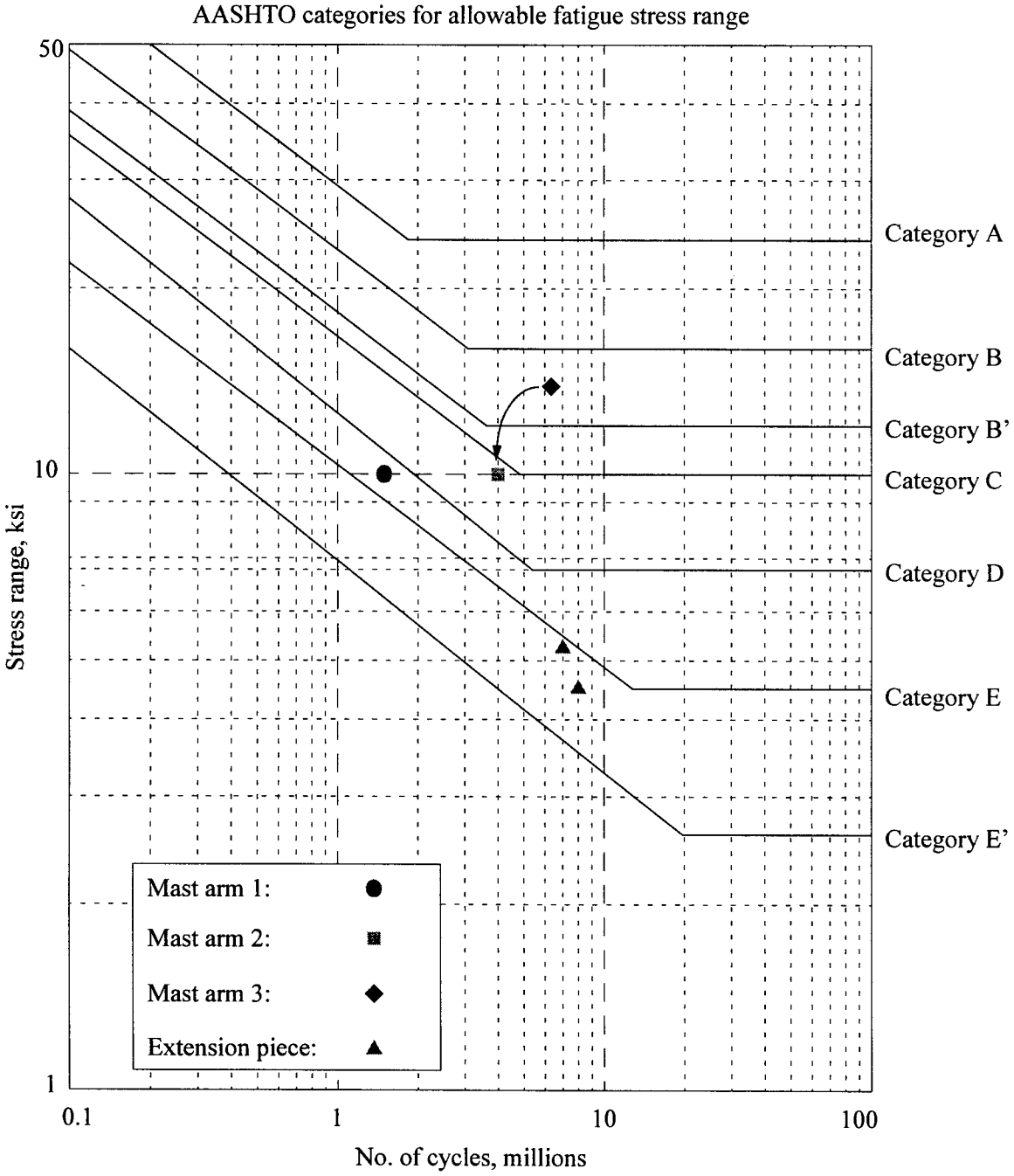


Figure 7.24: Comparison of mast arm experimental data and AASHTO fatigue design curves

# CHAPTER 8: SUMMARY AND CONCLUSIONS

## 8.1 Summary

### *8.1.1 Introduction*

Changeable Message Sign (CMS) structures are widely used in California by the California Department of Transportation (Caltrans) to deliver information to freeway motorists in a timely manner regarding road and weather conditions. These structures are inverted L-shaped cantilever structures composed of a vertical post and a horizontal mast arm. Both the post and the mast arm are fabricated from pipe sections. The post is anchored to a concrete foundation (typically a CIDH pile) by a thick baseplate; the post is groove-welded to a 2-3/4 in. (70 mm) thick baseplate, and the baseplate is attached to the foundation by 8 No. 2-1/4 in. (57 mm) diameter anchor bolts. The top of the post is bent 90° to make the connection to the mast arm. The mast arm is connected to the post by a flanged connection: annular plates are groove-welded to the post and the mast arm, and the flange plates are bolted together with 26 No. 3/4-in. (19 mm) diameter high-strength bolts. A 4 in. by 6 in. (101 mm by 152 mm) rectangular hole is flame-cut in the post, approximately 18 in. (457 mm) above the base plate, to enable electricians to run wiring up into the mast arm. A 2-1/2 in. (63 mm) diameter circular hole is flame-cut in mast arm, approximately 6 in. (152 mm) from the flange plate, to permit the electrical wiring in the post to be connected to the changeable message sign.

The failure of a CMS structure in a high-wind area in Southern California prompted Caltrans to undertake widespread field investigations of CMS structures in California. These investigations revealed wind-induced fatigue cracks in both the failed CMS structure and other CMS structures. Two welded connections were found to be vulnerable to fatigue cracking: the groove-welded post-to-base plate connection, and the groove-welded connections to the annular flange plates.

Caltrans contracted with the Earthquake Engineering Research Center (EERC) at the University of California at Berkeley to undertake integrated experimental and analytical studies to investigate the fatigue life of the vulnerable welded connections. The five key objectives of the study were:

1. Conduct full-scale laboratory experimental studies to develop an understanding of the fatigue life of the welded connection details currently in use by Caltrans.
2. Prepare mathematical models of CMS structures for the purposes of a) estimating their dynamic characteristics, and b) estimating the increases is stress adjacent to the conduit holes in the post and the mast arm.

3. Analyze field data collected by Caltrans engineers and EERC researchers to establish the dynamic characteristics of CMS structures.
4. Prepare draft recommendations for improving the fatigue-life of CMS structures through improved fabrication, construction, and installation practices.
5. Develop retrofit schemes for the vulnerable welded connections in conjunction with Caltrans engineers.

This report addresses the first four objectives. Information on the fifth objective will be available in a soon-to-be-published companion EERC report.

### *8.1.2 Summary of Laboratory Experimental Data*

A customized reaction frame was designed and built at EERC to facilitate high-cycle fatigue testing of full-scale post and mast arm specimens. Each specimen was loaded at its free end by a fatigue-rated servo-actuator. One post and three mast arm specimens were tested. A specimen was assumed to have failed once either its resistance at a given displacement dropped below 90 percent of the maximum resistance at that displacement (termed Type 1 failure) or cracks propagated in the groove-welded post-base plate connection (termed Type 2 failure). The response of the four specimens is summarized in Table 8.1 below. The stress range is the difference between the maximum and minimum stress at any point in the specimen.

Table 8.1: Summary data for post and mast arm specimens

| Specimen | EERC designation | Stress range | Cycles to failure[1] or maximum cycles[2] | Comments |
|---|---|---|---|---|
| Post | AB1 | 12 ksi | 2,100,000[3] | Test terminated after 2,700,000 cycles; Type 2 failure |
| Mast Arm | MA1 | 10 ksi | 1,500,000 | Test terminated after 4,000,000 cycles; Type 2 failure |
| Mast Arm | MA2 | 10 ksi | 4,000,000 | Specimen did not fail; fatigue life will exceed 4,000,000 |
| Mast Arm | MA3 | 10 ksi | 4,000,000 | Specimen did not fail; fatigue life will exceed 4,000,000 |
| Extension Piece | - | 5.4 ksi | 7,000,000 | Extension piece used for testing mast arm Specimens MA1 and MA2; Type 2 failure. |

1. Failure defined as either start of crack propagation at post-base plate connection or resistance drops below 90 percent of the maximum resistance at the maximum displacement; cycle count rounded down to nearest 100,000.

2. Maximum number of cycles set at 4,000,000 for AB1, MA1, MA2, and MA3.

3. Crack formation at the rectangular conduit hole after 1,200,000 cycles

The testing of Specimen AB1 was halted at 1.2 million cycles following the formation of fatigue-induced cracks at the edges of the rectangular conduit hole. This hole was flame-cut in the pipe section, and the four corners of the hole were neither ground smooth nor drilled out to reduce stress concentrations. A short piece of rectangular stiffener tube was inserted into the rectangular hole and fillet welded to the outside of the pipe section to frame the conduit hole. Both the rough flame cutting of the hole and the residual strains introduced by the fillet welding of the stiffener tube to the post likely contributed to the initiation of the crack. The cracks appeared to form in the region of the fillet weld and then propagated into the post proper. An attempt was made to repair the cracked pipe section by gouging out the parent metal on each side of the crack, replacing the parent metal with weld filler metal, and adding a rectangular patch plate (rolled to an internal diameter equal to the outside diameter of the pipe) that was fillet welded to the pipe section. Despite close attention to the repair work by both the fabricator and the Caltrans inspector, the repaired pipe performed poorly, and fatigue cracks appeared in the patch plate-to-pipe fillet welds within 500,000 additional cycles of loading. These cracks were repaired, and the test was continued. Cracks formed at the post-to-base plate connection after 2,100,000 cycles of loading.

Cracks formed in the groove-welded mast arm-flange plate connection in Specimen MA1 after approximately 1,500,000 cycles of loading. These cracks propagated over the course of the remainder of the test. After 2,800,000 cycles, the resistance of the specimen at the maximum displacement dropped below 90 percent of the maximum resistance at the maximum displacement.

Specimen MA2 developed no detectable (visual, dye penetrant, UT) cracks in the groove-welded mast arm-flange plate connection, although the maximum strain readings immediately above the flange plate on the tension side of the mast arm started to drop in value after approximately 3,000,000 cycles.

No cracks were identified in the mast arm-flange plate groove-welded connection of Specimen MA3. The drop in the strain readings on the compression side of the mast arm after 2,300,000 cycles, between the circular conduit hole and the flange plate, was a result of localized cracking in the mast arm adjacent to the conduit hole. Because such cracking was not associated with the groove-welded mast arm-plate connection, the testing was continued to approximately 4,000,000 cycles.

The extension piece was placed beneath the mast arm specimens to facilitate the use of the setup developed for testing the mast arm specimens. Only one extension piece was fabricated. The extension piece was subjected to approximately 7,500,000 cycles of loading before cracks were identified in the groove-welded connection of the pipe to the 2-3/4 in. (70 mm) thick base plate. Because the extension piece was monitored less frequently than the mast arm specimens, the cycle count at failure was reduced, somewhat arbitrarily, to 7,000,000.

### *8.1.3 Modeling of CMS Structures*

The post and mast arm specimens were modeled separately as cantilever structures, using the computer code SADSAP, to support the experimental program and to provide information on the distribution of stresses around the conduit holes and adjacent to the post-base plate and mast arm-flange plate connections. The extension piece was included in the mathematical model of the mast arm specimens. Quadrilateral shell elements were used to model both the post (mast arm) and base plate (flange plate). Linear springs were used to model the axial stiffness of the 2-1/4 in. (57 mm) diameter anchor bolts.

The rectangular conduit hole in the post locally produced a five-fold increase in stress range with respect to the stress range on the other side of the post. The maximum stress range adjacent to the conduit hole, corresponding to a stress range of 10 ksi (69 MPa) at the base of the post, was 15 ksi (104 MPa). The circular conduit hole in the mast arm locally produced a nearly two-fold increase in stress range with respect to the stress range on the other side of the mast arm. The maximum stress range adjacent to the conduit hole, corresponding to a stress range of 10 ksi (69 MPa) at the base of the mast arm, was 6 ksi (42 MPa). These estimates of the magnitude of the stress range adjacent to the conduit hole are likely lower bounds to the true values because the edges of the conduit holes in the field specimens are ragged because they are typically prepared by flame cutting and not smooth as assumed in the analysis.

### *8.1.4 Analysis of Field Experimental Data*

Response data was acquired from field testing of two CMS structures in Southern California for the purpose of measuring key dynamic characteristics of in-place CMS structures. A review of the field data suggests that the fundamental modal frequency of a CMS structure ranges between 1.0 and 1.1 Hz, and that the lowest two modal frequencies of CMS structures are closely spaced. The modal damping ratios in the lowest two modes are likely less than 0.7 percent of critical. Analysis of a mathematical model of a CMS structure using the computer code Drain-3DX predicted the lowest two vibrational frequencies to be 1.08 and 1.10 Hz, respectively, and in good agreement with the results calculated by analysis of the field data.

## 8.2 Conclusions

### *8.2.1 Fatigue Life of Components of CMS Structures*

AASHTO (1994) assigns the groove-welded connections of the post-base plate and the mast arm-flange plate to Category E' with a infinite fatigue life associated with a stress range of 2.6 ksi (18 MPa). The groove-welded connections of AB1 and the three mast arm specimens were tested at a stress range of 10+ ksi (69+ MPa). For such a stress range and Category E', the AASHTO *design* number of cycles to

failure is approximately 400,000. Note that the AASHTO S-N relations are conservative, that is, the relations presented in AASHTO (1994) are set two standard deviations below the mean relations. The smallest cycle count to failure was 1,500,000 for Specimen MA1. Although this substantially exceeds the AASHTO design value of 400,000, AASHTO requires CMS structures to be designed for an infinite fatigue life—a cycle count arguably substantially greater than 1,500,000.

In the absence of additional information and much additional testing, it is appropriate to continue designing components of CMS structures assuming an infinite fatigue life and Category E', that is, a maximum stress range of 2.6 ksi (18 MPa). Although some could argue that this recommendation is too conservative given the experimental data presented earlier, the number of specimens tested as part of this research program is too small a sample space from which to develop quantitative guidelines for the design of CMS structures.

### *8.2.2 Mathematical Modeling of CMS Structures*

Relatively simple mathematical models can be used to establish the modal frequencies and shapes of typical CMS structures. The flexibility of the baseplate assembly should be included in the mathematical model. The first and second modes of response of a typical CMS structure are closely spaced and the first two modal frequencies lie in the range between 1.0 Hz and 1.1 Hz.

Preliminary finite element analysis of the post and mast arm specimens show that the conduit holes introduce significant local increases in the horizontal and longitudinal stresses. The rectangular conduit hole produces larger local stresses in the post than does the circular conduit hole in the mast arm.

### *8.2.3 Analysis of Field Experimental Data*

CMS structures are characterized by substantial flexibility and low damping. From analysis of the field data collected following the testing of a CMS structure on Interstate 15, it is estimated that $f_1 = 1.04$ Hz, $f_2 = 1.10$ Hz, $\xi_1 = 0.7$, and $\xi_2 = 0.5$ percent of critical. The modal frequency data are very similar to the values predicted by eigen analysis of simple mathematical models of CMS structures (see Section 8.2.2).

The first mode of response corresponds to horizontal motion of the mast arm in the *x-y* plane, and the second mode of response corresponds to vertical motion of the mast arm in the *y-z* plane (see Figure 2.1). As such, the first mode will be excited by along-wind components of wind loading, and the second mode will be excited by across-wind galloping. Truck-induced gusting is not expected to constitute a severe loading environment for CMS structures.

### *8.2.4 Draft Recommendations for Improving the Fatigue Life of CMS Structures*

On the basis of the experimental studies conducted at EERC, recommendations can be made regarding how Caltrans could improve the fatigue life of CMS structures. These recommendations are listed below:

1. *Relocate and reconfigure the conduit holes in the post and mast arm*: The conduit holes should be moved as far away from the base plates as possible in order to reduce the nominal stresses at these reduced cross-sections. The rectangular conduit hole in the post should be replaced by a circular conduit hole to reduce the magnitude of the stress concentrations. The conduit holes should be drilled in the post (mast arm) rather than flame cut in order to minimize the residual strains around the conduit hole. Relocating the conduit hole and drilling, as opposed to flame cutting, the conduit hole are recommended as methods of reducing the strains adjacent to the conduit hole. If stiffening rings are to be welded to the post (mast arm), seal welds should be used if possible and the pipe should be pre-heated and cooled per AWS standards.
2. *Develop a prequalified Welding Procedure Specification (WPS) for the groove-welded connections.* Standardized WPSs are commonly used for joining steel components in the building, bridge, and off-shore oil industries. In the past, it has been the contractors' responsibility to develop and implement a WPS (Shepard, 1997) for Caltrans sign structures. To maintain high standards of construction, Caltrans should prepare a WPS for groove-welded post-base plate and mast arm-flange plate connections. A WPS for the subject connections should include, but not be limited to, information on welding type (i.e., shielded metal arc welding, flux core-arc welding), end preparation, fit-up and root opening, maximum electrode diameter, electrode type, maximum current, maximum root-pass thickness, and pre-heat and cool-down requirements. The use of toughness-rated weld filler metal is recommended. Improved weld profiles, such as those shown in Figure 3.10 of AWS D1.1 (AWS, 1996), should be investigated for possible use. It is recommended that a welding consultant be engaged by Caltrans to develop the WPS.
3. *Develop improved quality control and inspection (quality assurance) procedures.* Current Caltrans standards for quality control and inspection of welded components should be reviewed. Minimum standards for quality control should be proposed by Caltrans and imposed on contractors building CMS structures. Visual inspection alone of non-redundant welded connections is likely inappropriate. As a minimum, all groove-welded connections should be ultrasonically tested (UT) by an approved testing agency as part of the quality control program. Good quality control and inspection are key to high-quality construction: all defects identified by UT should be gouged out and replaced prior to shipment of the post to the field. Standard procedures for repairing such defects must be developed. A

Caltrans inspector should be present during the fit-up and welding of the post-base plate connections to ensure that the WPS is followed exactly. It is recommended that a welding consultant be engaged by Caltrans to develop new quality control and inspection procedures.

4. *Specify a minimum out-of-flatness for the flange plates and a flange-plate bolt-tightening sequence*: The substantial out-of-flatness of the flange plates contributed to the high local strains in the walls of the mast arm upon tightening of the flange-plate bolts. A maximum out-of-flatness of the flange plates and a bolt-tightening sequence should be established such that the local strains in the walls of the mast arm and the post are limited to relatively small values, for example, 25 percent of the yield strain.

### 8.3 Recommendations for Future Studies

The work conducted to date, and described both in this report and the companion report (Chavez, et al., 1997), has focused on the first five of the seven topics identified by Caltrans for urgent study. No effort has been made at the time of this writing to a) estimate the wind load demands on CMS structures as a function of wind speed and wind direction, or b) develop vibration mitigation strategies suitable for CMS structures. To complete the research program in a comprehensive manner, the following studies are recommended:

1. *Continue laboratory testing of components of CMS structures*: It is difficult to develop new guidelines for the design of CMS structures on the basis of a limited number of data points. Additional high-cycle fatigue testing of components of CMS structures is needed to develop new design guidelines.
2. *Undertake additional field testing of CMS structures*: Field testing of CMS structures in high-wind areas could provide, at a substantially reduced cost with respect to wind-tunnel testing, valuable new information on the dynamic characteristics of CMS structures and data relating wind speed and direction to both pressures on components of CMS structures and design forces on posts and mast arms. Further, field testing of proposed vibration mitigation techniques would provide a full-scale assessment of their efficacy.
3. *Develop vibration mitigation strategies*: Stresses in components of CMS structures can be reduced by either increasing the size of the structural components (e.g., increasing the diameter of the post and mast arms) or reducing the effects of the dynamic component of the wind loads using damping technologies. Although attention to date has focused on increasing the diameter of the post and mast arm, it may be more cost-effective to reduce the wind-load demands than to increase the strength of components of the CMS structure. It is likely that existing vibration mitigation strategies developed for wind and oil pipeline applications could be readily adapted to reduce the effects of wind loads on CMS structures.

# CHAPTER 9 : REFERENCES

AISC (1994). *Load and Resistance Factor Design Specification*, American Institute of Steel Construction, 2nd Edition, Chicago, Illinois.

API (1995). *Specifications for Line Pipe,* American Petroleum Institute, 41st Ed., Washington D.C.

ASTM (1995). *Standard Specifications for Pipe, Steel, Black and Hot-Dipped, Zinc-coated Welded and Seamless,* ASTM Standards in Buildings and Codes, 28th Ed., Volume 1, A1-B 210M, Philadelphia, PA.

AASHTO (1992). *Standard Specifications for Highway Bridges,* 15th Edition, American Association of State Highway and Transportation Officials, Washington D. C.

AASHTO (1994). *Standard Specifications for Structural Supports for Highway Signs, Luminaries and Traffic Signals,* American Association of State Highway and Transportation Officials, Washington, D. C.

ASCE (1987). *Wind Loading and Wind-Induced Structural Response,* Committee on Winds Effects of the Committee on Dynamic Effects of the Structural Division of the ASCE, American Society of Civil Engineers, New York, New York.

AWS (1996). *Structural Welding Code, AWS D1.1*, 15th Edition, American Welding Society, Miami, Florida.

Balendra, T. (1993). *Vibration of Buildings to Wind and Earthquake Loads,* Springer-Verlag, London, U.K.

Blom, A. F. (1989). "Modeling of Fatigue Crack Growth," *Advances in Fatigue Science and Technology*, Kluwer Academic Publishers, pp. 77-110, Edited by M. Branco and L. Guerra Rosa.

Branco, C. M., Radon, J. C. and Culver, L. E. (1976). "Growth of Fatigue Cracks in Steels," *Met. Sci.*, Vol. 10, pp. 149-155.

Chavez, J. W., Gilani, A. S. and Whittaker, A. S. (1997). *Fatigue Life Evaluation of Changeable Message Sign Structures, Volume 2: Retrofit Specimens,* In Progress, Report UCB/EERC-**/**, Earthquake Engineering Research Center, University of California at Berkeley, Berkeley, California.

Clough, R. W. and Penzien, J. (1993). *Dynamics of Structures,* McGraw-Hill, Inc., 2nd Edition, New York, New York.

Dijkstra, O. D. and deBack, J. (1980). "Fatigue Strength of Tubular T- and X- Joints," *Offshore Technology Conference Proceedings*, Vol. 1, pp. 177-186, Houston, Texas.

Dou, R. F., Li, H. M., Sun, C. G. and Wang, P. Y. (1991). "Static and Fatigue Tests on Large-Sized Welded Tubular T-Joints for Offshore Structures," *Proceedings of the International Symposium on Marine Structures*, pp. 311-316, Shangai, China.

Ewins, D. J. (1989). *Modal Testing: Theory and Practice,* Research Studies Press Ltd., Taunton, Somerset, U.K.

Fisher, J. W., Frank, K. H., Hirt, M. A. and McNamee, B. M. (1970). *Effect of Weldments on the Fatigue Strength of Steel Beams,* NCHRP Report 102, Transportation Research Board, Washington, D. C.

Fisher, J. A., Albrecht, P. A., Yen, B. T., Klingerman, D. J. and Mcnamee, B. M. (1974). *Fatigue Strength of Steel Beams with Welded Stiffeners and Attachments,* NCHRP Report 147, Transportation Research Board, Washington, D. C.

Fisher, J. W., Hausammann, H., Sullivan, M. D. and Pense, A. W. (1979). *Detection and Repair of Fatigue Damage in Welded Highway Bridges,* NCHRP Report 206, Transportation Research Board, Washington, D. C.

Fisher, J. W., Mertz, D. R. and Zhong, A. (1983). *Steel Bridge Members Under Variable Amplitude Long Life Fatigue Loading,* NCHRP Report 267, Transportation Research Board, Washington, D. C.

Fisher, J. W. (1984). *Fatigue and Fracture in Steel Bridges - Case Studies*, John Wiley & Sons, New York, New York.

Fisher, J. W., Yen, B. T. and Wang, D. (1990). *Fatigue Cracking of Steel Bridge Structures,* Report FHWA-RD-89-167, Federal Highway Administration, McLean, Virginia.

Forman, J. K., Kearney, V. E. and Engle, R. M. (1967). "Numerical Analysis of Crack Propagation in Cyclic Loaded Structures," *Journal of Basic Engineering*, ASME, Vol. 89, pp. 459-464, New York, New York.

Gowda, S. S. (1985). "Effect of Layers on Fatigue Crack Propagation in Tubular Steels of Offshore Structures," *Offshore Technology Conference Proceedings*, Vol. 4, pp. 41-50, Houston, Texas.

Gugino, A. and Woody, J. (1996). Personal Communication, California Department of Transportation,

Caltrans, Sacramento, California

Kaczinski, M. R., Dexter, R. J. and Van Dien, J. P. (1996). *Fatigue-Resistant Design of Cantilevered Signal, Sign, and Light Supports,* Report to NCHRP, ATLSS Engineering Research Center, Lehigh University, Bethlehem, Pennsylvania.

Kwok, K. (1991). *Wind Induced Vibrations of Structures, Structures Subjected to Dynamic Loading - Stability and Strength,* Elsevier Applied Science, Edited by R. Narayanan and T.M. Roberts, London, U.K.

Liu, H. (1991). *Wind Engineering - A Handbook for Structural Engineers,* Prentice Hall, Englewood Cliffs, New Jersey.

Luna, R. L. and Sunder, S. S. (1982). *Cyclic Behavior of Structural Steel with Applications to Offshore Platforms,* Research Report R82-38, Massachusetts Institute of Technology, Department of Civil Engineering, Cambridge, Massachusetts.

Maddox, S. J. (1989). "Fatigue Behavior of Welded Joints," *Advances in Fatigue Science and Technology*, pp. 539-550, Edited by M. Branco and L. Guerra Rosa.

Mander, J. B., Chen, S. S., Shah, K. M. and Madan, A. (1992). *Investigation of Light Pole Base Integrity,* Report to Erie County Department of Public Works, Department of Civil Engineering, State University of New York at Buffalo, Buffalo, New York.

Matlab (1996). *MATLAB The Language of Technical Computing,* The Mathworks, Inc., Natick, Massachusetts.

Miner, M. A. (1945). "Cumulative Damage in Fatigue," *Journal of Applied Mechanics*, ASME, Vol. 67, pp. 159-164.

McDonald, J. R., Mehta, K. C., Oler, W. W. and Pulipaka, N. (1995). *Wind Load Effects on Signs, Luminaires and Traffic Signal Structures,* Report No. 1303-1F, Wind Engineering Research Center, Texas Tech University, Lubbock, Texas.

Paris, P. C. and Erdogan, F. (1965). "A Critical Analysis of Crack-Propagation Laws," *Journal of Basic Engineering*, ASME, Vol. 85, pp. 528-534, New York, New York.

Powell, G. H. and Campbell, S. (1994). *DRAIN-3DX Element Description and User Guide,* Report No. UCB/SEMM-94/08, Department of Civil Engineering, University of California at Berkeley, Berkeley, California.

Prakash, V., Powell, G. H. and Campbell, S. (1994). *DRAIN-3DX Base Program Description and User Guide,* Report No. UCB/SEMM-94/07, Department of Civil Engineering, University of California at Berkeley, Berkeley, California.

Radon, J. C. and Guerra Rosa, L. (1989). "Fatigue Threshold Behavior, Part I: Modeling of FCG Near Threshold," *Advances in Fatigue Science and Technology*, pp. 129-139, Edited by M. Branco and L. Guerra Rosa.

Schilling, C. G., Klippstein, K. H., Barsom, J. M. and Blake, G. T. (1978). *Fatigue of Welded Steel Bridge Members Under Variable Amplitude Loadings,* NCHRP Report 188, Transportation Research Board, Washington, D. C.

Shepard, R. (1997). Private Communication, California Department of Transportation, Caltrans, Sacramento, California

Sih, G. C. (1973). *Handbook of Stress Intensity Factors,* Institute of Fracture and Solid Mechanics, Lehigh University, Bethlehem, Pennsylvania.

Simiu, E. and Scanlan, R. H. (1996). *Wind Effects on Structures - Fundamentals and Applications to Design,* John Wiley and Sons, Third Edition, New York, New York.

Tada, H., Paris, P. C. and Irwin, G. R. (1973). *The Stress Analysis of Cracks Handbook,* Del Research Corporation, Hellertown, Pennsylvania.

Tolloczko, J. J. A. (1991). "Fatigue of Tubular Joints in Offshore Structures," *Structures Subjected to Repeated Loading - Stability and Strength*, Edited by R. Narayanan and T. M. Roberts, Elsevier Applied Science, London, U.K.

Whittaker, A. S., Gilani, A. S. and Bertero V. V. (1997). *Seismic Testing of Full-Scale beam-Column Assemblies,* In Progress, Report UCB/EERC-**/**, Earthquake Engineering Research Center, University of California at Berkeley, Berkeley, California.

Winter, W. (1996). "Instrumentation Activity Report," California Department of Transportation, Caltrans, Sacramento, California.

Wilson, E. L. (1992). *SADSAP Static and Dynamic Structural Analysis Program,* Structural Analysis Programs, Inc. Berkeley, California.

Woody, J. and Gugino, A. (1997). Personal Communication, California Department of Transportation, Caltrans, Sacramento, California

Wylde, J. C. and McDonald, A. (1979). "The Influence of Joints Dimensions on the Fatigue Strength of Welded Tubular Joints," *Proceedings of the Second International Conference on Behavior of Offshore Structures*, Vol. 1, London, U.K.

Zwerneman, F. J. (1991). "Fatigue Damage Accumulation Under Varying-Amplitude Loads," *Structures Subjected to Repeated Loading - Stability and Strength*, Edited by R. Narayanan and T. M. Roberts, Elsevier Applied Science, London, U.K.

# APPENDIX A1: AN INTRODUCTION TO WIND ENGINEERING

## A1.1 General

Wind is the motion of the air with respect to the surface of the earth, fundamentally caused by differences of pressure between points of equal elevation due to the unequal solar heating of the earth's surface. Strong winds are associated with large storm systems (extratropical cyclones) and local storms (tornadoes, thunderstorms, downbursts, jet effect winds).

As the air flows, it strikes engineered structures in its path, generating forces in those structures. The wind-induced forces can be resolved into a drag (along-wind) component acting in the direction of the mean wind velocity and a lift (across-wind) component acting transverse to that direction. The term lift does not mean, as its name may suggest, an upward force. It can be upward, downward, sideways, or in any direction perpendicular to the wind (Liu, 1991). A schematic of the wind force decomposition is shown in Figure A1.1.

Adequate understanding of wind loads and their effects is essential to the safety and economy of many engineered structures. Failure to understand the impacts of high sustained winds and the response of engineered construction to those winds can result in structural failures, loss of life, and significant economic losses.

## A1.2 Wind Characteristics

### *A1.2.1 Components of Wind Velocity*

Wind is characterized by random fluctuations of velocity with time. In general, for a three-dimensional wind, the velocity of the wind, $V_{tot}$, at a location ($x$ and $y$), is a time, $t$, dependent function of the elevation of the point above ground, $z$ (Balendra, 1993), and may be represented as:

$$V_{tot}(z,t) = \begin{bmatrix} \tilde{V}_x \\ \tilde{V}_y \\ \tilde{V}_z \end{bmatrix} = \begin{bmatrix} V_x \\ V_y \\ V_z \end{bmatrix} + \begin{bmatrix} v_{xx} & v_{xy} & v_{xz} \\ v_{yx} & v_{yy} & v_{yz} \\ v_{zx} & v_{zy} & v_{zz} \end{bmatrix} \begin{bmatrix} V_x \\ V_y \\ V_z \end{bmatrix} \tag{A1.1}$$

where $V_a$ $(a = x, y, z)$ are the components of the wind velocity; $\tilde{V}_a$ $(a = x, y, z)$ denotes the components of the mean wind velocity; and $v_{ab}$ $(a = x, y, z;\ b = x, y, z)$ designates the time varying fluctuating gust coefficients. For one-directional flow in the $x$ direction, this equation may be simplified as:

$$V_{tot}(z,t) = \begin{bmatrix} V \\ 0 \\ 0 \end{bmatrix} + \begin{bmatrix} v_{xx} & 0 & 0 \\ v_{yx} & 0 & 0 \\ v_{zx} & 0 & 0 \end{bmatrix} \begin{bmatrix} V \\ 0 \\ 0 \end{bmatrix} = \begin{bmatrix} V \\ 0 \\ 0 \end{bmatrix} + \begin{bmatrix} v_x \\ v_y \\ v_z \end{bmatrix} \tag{A1.2}$$

where $V$ is the height-dependent mean wind velocity along the $x$ direction; $v_x$, $v_y$, and $v_z$ are the time-varying fluctuating components of the gust in the $x$, $y$, and $z$ (herein referred to as longitudinal, lateral and vertical) directions, respectively.

For tall structures that are flexible in the along-wind direction (e.g. a CMS structure) subjected to one-dimensional wind flow in the $x$ direction, the fluctuating component $v_x$ is the largest and most important of the three, and the gust components in the other two directions can be ignored. Thus, as shown in Figure A1.2, the longitudinal wind velocity, $V_{x_{tot}}$, can be expressed as:

$$V_{x_{tot}}(z,t) = V(z) + v_x(z,t) \tag{A1.3}$$

### *A1.2.2 Mean Wind Speed*

The mean wind speed must be estimated prior to calculating the forces acting on a structure in the direction of the wind. The mean wind speed depends on the sample time interval used to compute the mean value and varies principally with the height above the ground and the terrain roughness, as the earth's surface exerts a horizontal drag force that retards the motion of the air. The effect of this drag force, also termed a boundary layer effect, decreases as the height above the ground increases. The wind velocity is zero at the ground surface. The wind velocity increases with height above the ground and reaches a constant value at a height $\delta$, known as the atmospheric boundary layer thickness. Above this layer, the effect of the surface roughness becomes negligible, and the wind speed does not vary with height, as shown in Figure A1.3.

The wind speed profile within the atmospheric layer can be approximated by either a logarithmic equation or by a simpler power-law as follows:

Logarithmic law: $$V(z) = \frac{1}{\kappa} \cdot v \cdot \ln\left(\frac{z}{z_o}\right) \tag{A1.4}$$

Power law: $$V(z) = V(z_{ref}) \cdot \left(\frac{z}{z_{ref}}\right)^{\beta} \tag{A1.5}$$

In these equations, $V(z)$ is the velocity (mean wind speed) at height $z$ above ground; $V(z_{ref})$ is the wind velocity at a reference height, $z_{ref}$; $v = \sqrt{\tau_o/\rho}$ is the shear velocity, where $\tau_o$ is the surface shear and $\rho$ is the air density; $\kappa$ is the Von Karman constant assumed equal to 0.4 (Simiu and Scanlan, 1996); $z_o$ is

the roughness length; and $\beta$ is the terrain roughness parameter. For open terrains, which are typical for most CMS structures, the roughness length is 0.23 ft (70 mm), and the terrain roughness parameter is 0.14 (ASCE, 1987).

### A1.3 Wind Forces

A stream of air moving at velocity $V$ exerts a force $q$ per unit area. This force $q$ is the dynamic head of air and is defined as:

$$q = \frac{1}{2}\rho V^2 \tag{A1.6}$$

For a closed stream of air, the total pressure remains constant at all points, and by the Bernoulli equation:

$$p + \frac{1}{2}\rho V^2 = const \tag{A1.7}$$

where $p$ is the static pressure at a given point in the air stream.

When a body is immersed in a two-dimensional flow field, it is subjected to a net force in the direction of the flow (drag force) and a force transverse to the flow (lift force). Furthermore, when the resultant of the net force is eccentric to the body's center of rigidity, the body will be subjected to a torsional moment (Kwok, 1991). The drag force, $F_D$, and the lift force, $F_L$, may be computed as follows:

$$F_D = \frac{1}{2}\rho C_D D V^2 \tag{A1.8}$$

$$F_L = \frac{1}{2}\rho C_L D V^2 \tag{A1.9}$$

where $V$ is the mean wind velocity; $C_D$ and $C_L$ are the drag and lift coefficients, respectively; and $D$ is the projected length of the body normal to the flow. For a cylindrical body with a smooth surface in such a flow, the drag and lift coefficients depend on the Reynolds number (see Section A1.7).

### A1.4 Wind Effects on Structures

Wind-induced loading has to be accounted for in the design of a wide variety of structures. For example, tall buildings, chimeneys, towers, cable-suspended bridges, cable-suspended roofs, light poles, traffic light fixtures (CMS structures), and sheet metal roofs are all sensitive to wind-induced vibrations. The degree and the type of wind-induced vibrations depend to a large extent on the geometric and dynamic characteristics (shape, flexibility, and damping) of the structure and on the features of the wind.

In general, wind-induced vibrations and wind effects on structures can be classified as either *aerodynamic* or *aeroelastic*. Aerodynamic effects are due solely to external wind loading. For sign structures, natural wind gusts and truck-induced wind gusts provide the primary aerodynamic effects.

Aeroelastic effects are due to the interaction of aerodynamic forces and structural motion. Aeroelastic instability occurs when aerodynamic forces deform a structure, and the deformation from the initial position gives rise to oscillatory motions of increasing amplitude. That is, the forces acting on the structure are amplified as the result of the motion of the structure. Regular vortex shedding and galloping are aeroelastic effects that may affect sign structures.

### A1.5 Natural Wind Gusts

Wind gusts occur naturally from a change in flow direction and amplitude. Due to wind turbulence, fluctuating pressures on the structure cause the structure to vibrate.

### A1.6 Truck-Induced Wind Gusts

Consider a CMS structure as depicted in Figure 2.1. A local coordinate system is defined such that the direction of traffic, the mast arm direction, and the axis of the cantilever post correspond to the $x$, $y$, and $z$ directions, respectively. The passage of trucks underneath a CMS structures (in the x direction) induces horizontal ($x$) and vertical ($z$) pressure components acting on the mast arm sign attachment.

The horizontal pressure gradient (acting in the $x$ direction) acts perpendicular to the frontal face of the sign attachment ($y$-$z$ plane). This component introduces torsional moment (about the $z$ axis) and bending moment (about the $y$ axis) in the post. The torsional moment generates uniform shear stresses in the post that depend on the length of the mast arm (along the $y$ axis) and the projected frontal vertical area (in the $y$-$z$ plane) of the sign. The bending moment produces linearly varying normal stresses in the post which reach a maximum at the base. The amplitude of these normal stresses depends on the length of the post (in the $z$ direction) and the projected frontal area (in the $y$-$z$ plane). Typically, the values of these truck-induced gust stresses are much smaller than those resulting from natural wind gusts.

The vertical pressure gradient (acting in the $z$ direction) acts on the bottom of the mast arm sign attachment ($x$-$y$ plane), inducing bending moments in the post (about the $x$ axis). The bending moment induces uniform normal stresses in the post. The amplitude of these normal stresses is dependent on the projected horizontal area of the sign bottom (in the $x$-$y$ plane) and the length of the mast arm (in the $y$ direction). This component of truck-induced gust stresses may be large.

### A1.7 Regular Vortex Shedding

Response amplification occurs when alternating regular vortices are shed in the wake of a structure. The shedding of the vortices is correlated with the Reynolds number, $R_e$, which characterizes the flow. The Reynolds number is a measure of the ratio of inertial to viscous forces within the flow, and is defined as:

$$R_e = \frac{VD}{\upsilon} \tag{A1.10}$$

Where $V$ is the wind speed, $D$ is a characteristic body dimension, and $\upsilon$ is the kinematic viscosity of air, approximately $1.6 \times 10^{-5}$ $ft^2/sec$ (1.5 $mm^2/sec$). For low values of the Reynolds number (e.g., $R_e$ =1), the flow is considered laminar. For Reynolds numbers in the range of $30<R_e<5000$, alternating vortices are shed from a body and form a vortex trail downstream, as shown in Figure A1.5. For Reynolds numbers exceeding 5000, a transition from laminar to turbulent flow will occur (Simiu and Scanlan, 1996).

Shedding of regular vortices (hereafter termed *vortex shedding*) creates periodic lateral forces and causes slender structures such as stacks, masts, towers, and CMS structures to vibrate. The frequency (in Hz) of the vortex shedding, $f_s$, is given by the Strouhal equation:

$$f_s = \frac{VS}{D} \tag{A1.11}$$

where $S$ is the Strouhal number, which depends on the geometry of the structure and the Reynolds number.

The Strouhal number can be related to the Reynolds number by combining Equations A1.10 and A1.11 to obtain:

$$S = \left(\frac{f_s \upsilon}{V^2}\right) R_e \tag{A1.12}$$

When the frequency expressed by Equation A1.11 approaches one of the natural frequencies of a flexible and lightly damped structure, large motions may occur. Once vortex shedding commences, it will be *locked-in,* and even a slight change to the input frequency will not arrest the shedding of vortices. The effect of *lock-in* is represented in Figure A1.6. In the lock-in region, shedding is controlled by the natural frequency of the structure and not by the wind. If the wind speed is increased above or below that causing lock-in, the frequency of shedding will again be controlled by the wind.

For a typical CMS structure, $D$=1.5 Hz, $f_s$=1 Hz (see Chapter 3), and $S$=0.18 for circular sections (Simiu and Scanlan, 1996). As a result, a wind velocity of 8.3 ft/sec (2.5 m/sec) is required to initiate the regular shedding of vortices. This wind velocity is less than the velocity of 16.5 ft/sec (5 m/sec) required to initiate vibration in most structures (Kaczinski, et al., 1996). Therefore, for CMS structures, vortex shedding is typically not considered to be a problem.

### A1.8 Galloping

Galloping is defined as the large amplitude motions occurring in the direction normal to the wind flow at frequencies smaller than the vortex shedding frequency, $f_s$, (see Equation A1.11). Consider a body moving with a velocity, $\dot{y}$, in a direction, $y$, normal to the wind flow of velocity, $V$, in the $x$ direction. As

indicated in Figure A1.4, the resultant aerodynamic force acting on the body is a function of relative wind velocity, $V_{rel}$. As a result, the flow becomes asymmetric, and a lift force is generated in the $y$ direction. This force will augment the motion of the body in the $y$ direction, and large amplitude motions may result in the across-wind direction.

For a prismatic single-degree-of-freedom oscillator in a smooth wind flow, the total system damping, $\xi_{total}$, in the across-wind direction (Simiu and Scanlan, 1996) may be expressed as:

$$\xi_{total} = \xi + k\left(\frac{dC_L}{d\alpha} + C_D\right) \tag{A1.13}$$

On the right hand side of this equation, the term $\xi$ represents the mechanical damping of the structure and is always positive. The second term represents the aerodynamic damping and it is often negative. The constant $k$ depends on the wind mean velocity, the geometry of the structure, and the structure's vibration frequency. The angle of wind attack is denoted by $\alpha$.

Galloping instability (Glauert-Den Hartog criterion) will occur when the total system damping is negative. Galloping from the equilibrium position can only occur if the value of the negative aerodynamic damping is larger than the mechanical damping of the system.

CMS structures possess minimal mechanical damping (see Chapter 3) and are susceptible to galloping instability. This has been verified by field observations of the sudden onset of large amplitude across-wind oscillations (Winter, 1996).

The post and the mast arm of CMS structures are made of circular cross sections. Because of symmetry, circular cylinders cannot gallop, since $\frac{dC_L(\alpha)}{d\alpha} = 0$. Therefore, the overhead sign is the likely cause of galloping for CMS structures. Wind tunnel tests conducted by Kaczinski, et al. (1996), support with this observation.

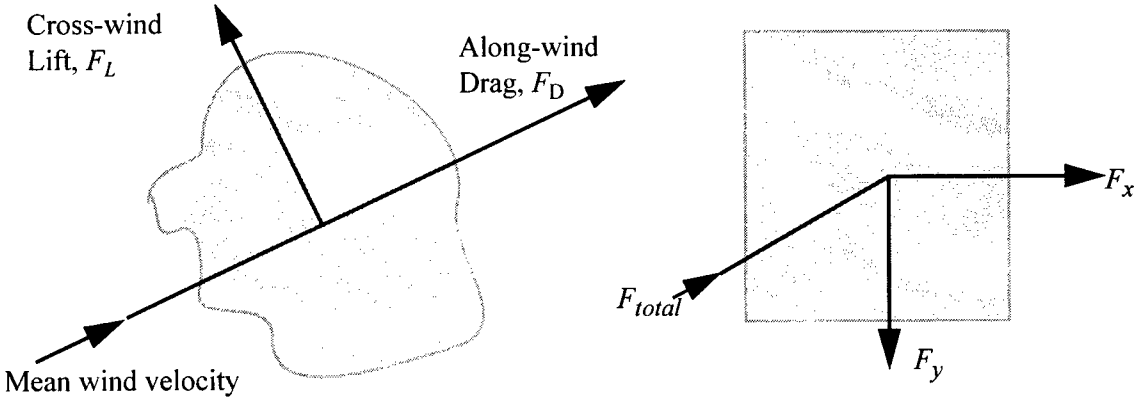


(a) Wind axes (b) Body axes

Figure A1.1: Components of wind-induced forces and responses

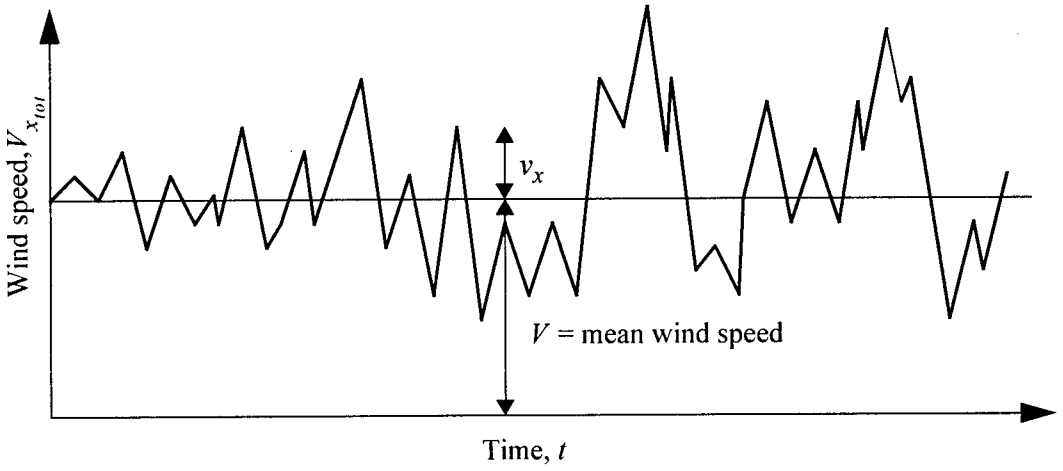


Figure A1.2: Typical variation of longitudinal wind speed

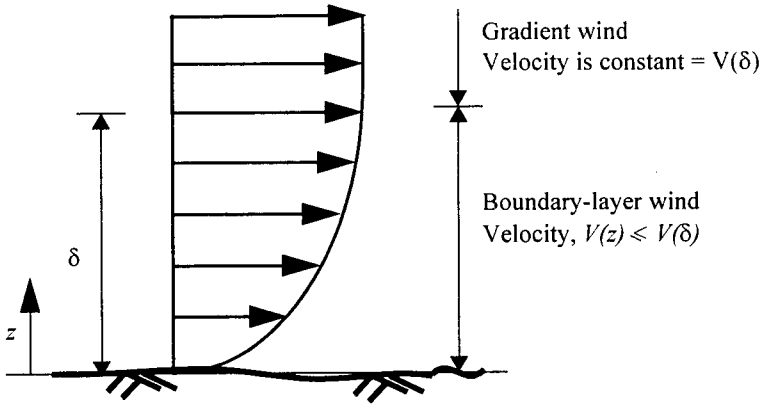


Figure A1.3: Variation of mean wind speed

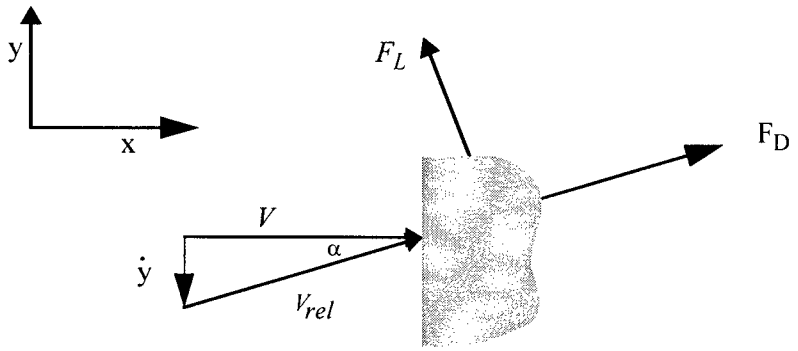


Figure A1.4: Galloping phenomenon

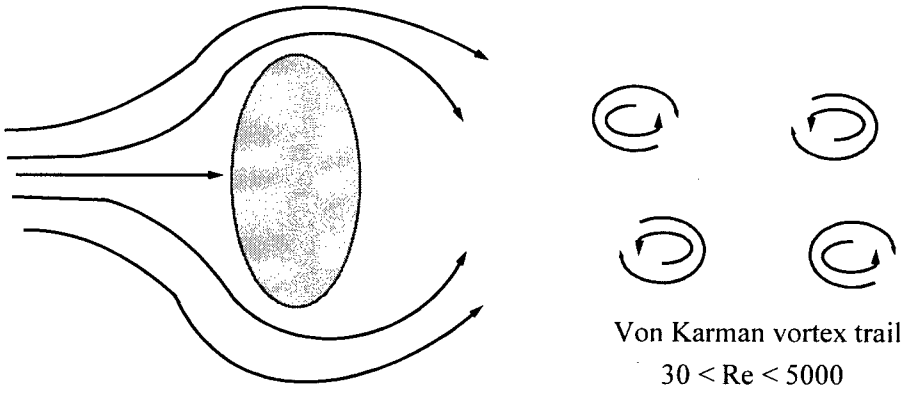


Figure A1.5: Regular vortex shedding

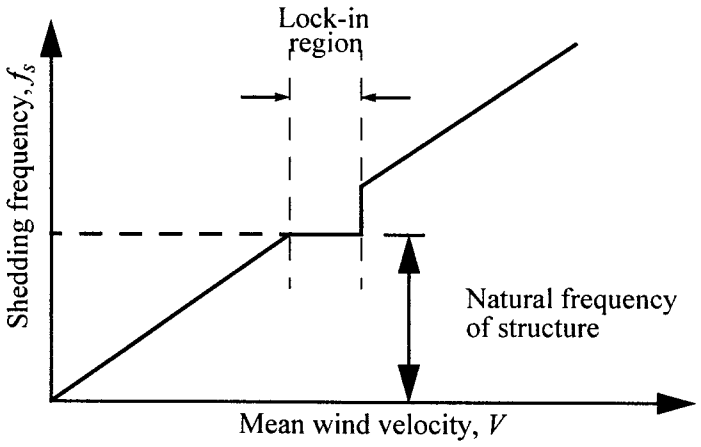


Figure A1.6: Conceptual description of lock-in

# APPENDIX A2: AN INTRODUCTION TO FATIGUE

## A2.1 General

Fatigue failure is a problem that occurs in many kind of structures, such as bridges, off-shore platforms, vehicle suspension systems, aircraft, ships, and sign support structures. Cracks form and grow under the repeated action of applied cyclic forces, which are generally lower than those required to yield the material under unidirectional static loading. This appendix introduces the subject of fatigue and describes the factors affecting the fatigue life of structures, crack propagation, S-N curves, and the prediction of fatigue life under variable loadings.

## A2.2 Fatigue Phenomenon

Fatigue may be defined as the process of initiation and propagation of a localized microscopic crack into a macroscopic crack by the repeated application of cyclic stresses. If unchecked, fatigue cracks may grow and result in the failure of connections or components. A crack can only grow if tensile strains normal to the crack exist at the crack tip. The total useful life (herein referred to as fatigue life) of a structure can be measured by the sum of the number of cycles required to initiate a crack and the number of cycles needed to propagate the crack to failure.

The fatigue life of a steel structure is affected principally by:

- *Structure geometry*: Variations in geometry influence the stresses at critical locations (stress concentration) where fatigue cracks often initiate. Changes in geometry are found at connections and around openings.
- *Cyclic loading amplitudes and states of stress:* The stress range, mean stress, residual stresses, and load sequence, are important factors.
- *Material properties*: Stress-strain behavior, grain size and shape, hardness, chemical composition, homogeneity, and microstructural discontinuities are key material properties. These properties influence how a component or connection responds to cyclic loading. Material strength is likely not a significant factor in calculation of fatigue life, because the design stress range is generally much lower than the yield stress.
- *Metallurgical characteristic of the steel and weld materials:* Fatigue life is influenced by the surface integrity in the form of surface roughness, material composition, and material hardness.
- *Environmental factors*: Corrosion and temperature can influence the fatigue life of a structure.

### A2.3 Fatigue Loading

Engineered structures are typically subjected to time-varying loading environments. As such, the fatigue study of a structure should address different loading patterns.

A simple cyclic loading pattern is a constant-amplitude sinusoidally varying loading at a given frequency. In each cycle, the maximum and minimum stresses are defined as $\sigma_{max}$ and $\sigma_{min}$, respectively. As shown in Figure A2.1, this type of loading can be represented by a mean stress, $\sigma_{mean}$, and a fluctuating stress range, $\Delta\sigma$:

Mean stress: $$\sigma_{mean} = (\sigma_{max} + \sigma_{min})/2 \quad \text{(A2.1)}$$

Stress range: $$\Delta\sigma = \sigma_{max} - \sigma_{min} \quad \text{(A2.2)}$$

A stress ratio, $R$, is defined as: $$R = \sigma_{min}/\sigma_{max} \quad \text{(A2.3)}$$

For zero-to-tension loadings, $R$ is equal to zero. For fully reversed loadings, $R$ is equal to -1.

A sinusoidal, variable-amplitude loading, shown in Figure A2.2, may be used to represent a more complex loading environment such as the random stress history shown in Figure A2.3.

### A2.4 Crack Propagation

Metal fatigue failures arise from the propagation of small cracks resulting from material or manufacturing defects. Tensile strains normal to the crack at the tip of the crack are necessary for the crack to propagate.

For uniaxial loading, crack propagation is usually divided into three stages (Blom, 1989), as shown in Figure A2.4.

Stage I corresponds to the early growth of fatigue cracks and is heavily influenced by the microstructural surface roughness. Damage is generally crystallographic, associated with the formation of slip planes. Cracks develop by reversed shear deformation in the slip planes. Stage I is essentially a shear-controlled slip process.

Stage II is characterized by the growth of the cracks in the direction normal to the applied maximum principal tensile stresses, producing a fracture surface known as a striation. Under a constant applied cyclic stress, the width of a striation in the direction of crack advance is proportional to the current crack size. The larger the striation, the faster the rate of crack growth.

Stage III is reached towards the end of the fatigue life of a component or when tearing takes place.

For low toughness materials, crack growth is very rapid just prior to crack growth instability, but for ductile materials, it can represent a significant part of the total crack growth rate.

### A2.5 Models for Crack Propagation

For constant-amplitude load fluctuations, the rate of fatigue crack propagation in a material, $da/dN$, may be expressed as a function of several variables (Radon and Guerra, 1989):

$$\frac{da}{dN} = f(\Delta K, R, F, T, \eta) \tag{A2.4}$$

where $a$ is the crack length, $N$ is the accumulated number of cycles, $\Delta K$ is the range of the stress intensity factor applied in the loading cycle, $R$ is the stress ratio, $F$ is the loading frequency, $T$ is the temperature, and $\eta$ is an environmental constant. Figure A2.5 represents the stages (regimens) of crack propagation.

There have been many attempts to characterize Equation A.2.4. Although many relationships have been developed (Forman, et al., 1967; Branco, et al., 1976), the fatigue crack growth rate is usually represented by the Paris-Ergodan equation (Paris and Ergodan, 1965), which was derived by fitting a curve to experimental data. The Paris-Ergodan equation is:

$$\frac{da}{dN} = c(\Delta K)^m \tag{A2.5}$$

In this equation, $c$ and $m$ are experimentally determined constants. The value of the exponent $m$ is between 2 and 5, and, for most steels, is approximately equal to 3. This equation is valid only for the intermediate segment of Figure A2.5 (regime B), and corresponds to a stable crack growth.

At low values of $\Delta K$, the value of $da/dN$ decreases to zero at a threshold value, $\Delta K_{th}$. Behavior in the near-threshold region (regime A) is extremely sensitive to variations in microstructure, mean stress, and environment. For most materials, an operational, although arbitrary, threshold value is defined as the value of $\Delta K$ corresponding to a fatigue crack rate of $4 \times 10^{-9}$ in./cycle ($10^{-10}$ m/cycle).

At high values of $\Delta K$, the rate of crack growth increases because monotonic or static modes of fracture are produced by the applied loading cycles. In this region (regime C), behavior is influenced by the applied mean stress.

### A2.6 Stress Intensity Factor

The expression of the stress intensity factor, $\Delta K$, for the case of a infinite plate of constant thickness subjected to a uniaxial stress range, $\Delta\sigma$, is:

$$\Delta K = (F_s F_w F_e F_g)\Delta\sigma\sqrt{\pi a} \tag{A2.6}$$

where $a$ is half of the crack length, $F_s$ is the correction factor associated with a free surface at the crack

origin (the front of the free surface), $F_w$ accounts for the free surface at the same finite length of crack growth, $F_e$ adjusts for the shape of the crack front (often assumed to be elliptic), and $F_g$ is a factor which accounts for either a nonuniform stress field (such as bending) or a stress concentration caused by the geometry. Values of the correction factors are dependent on the overall geometry of the specimen, the crack shape, and the distribution of the applied stresses. Solutions for the correction factors for selected idealized problems are available (Sih, 1973; Tada, 1973).

For a rectangular plate (see Figure A2.6) containing a central through-thickness crack of length *2a,* where the length $2a$ is small in comparison with the width of the plate, the expression for the stress intensity factor is:

$$\Delta K = \Delta\sigma\sqrt{\pi a} \tag{A2.7}$$

**A2.7 Number of Cycles to Failure**

The total fatigue life (initiation plus propagation) of a specimen can be represented by a simple diagram known as an S-N curve. As shown in Figure A2.7, the logarithm of the stress range is plotted against the logarithm of the number of loading cycles to failure. The relation is obtained by fitting sets of experimental data from specimens subjected to constant-amplitude stress range cyclic tests until failure occurs. The relation consists of an inclined descending branch and a flat branch. The stress level at which the relation becomes independent of the cycle count is called the fatigue limit. A component or connection loaded to a stress range lower than the fatigue limit will theoretically have an infinite fatigue life.

S-N curves for many metals can be found in the literature. Design specifications often use a lower bound curve that is approximately two standard deviations below the mean curve.

The following empirical equation is used to calculate the number of cycles to failure, $N$:

$$N = A \cdot (\Delta\sigma)^{-m} \tag{A2.8}$$

where $A$ and $m$ are constants. This equation can be related to the Paris-Ergodan equation. Equation A2.5 can be re-written as:

$$dN = \frac{1}{c}(\Delta K)^{-m} da \tag{A2.9}$$

Integrating the right side of the equation between the initial crack width, $a_i$, and the final crack width, $a_f$, and multiplying the numerator and denominator by $(\Delta\sigma)^{-m}$ gives:

$$N = \left[\frac{1}{c}\int_{a_i}^{a_f} \frac{1}{(\Delta K/\Delta\sigma)^m} da\right](\Delta\sigma)^{-m} = A(\Delta\sigma)^{-m} \tag{A2.10}$$

### A2.8 Fatigue Under Variable Amplitude Loading

The increment in crack growth per cycle of variable loading is not equal to the crack growth rate for an equivalent constant amplitude load cycle (Fisher, et al., 1983). Crack advance under variable amplitude loading is dependent upon the loading history. Information on the fatigue life of specimens subjected to a variable amplitude loading can be found in the literature (e.g., Fisher, et al., 1983; Zwerneman, 1991).

### A2.9 Accumulated Fatigue Life

For a component subjected to a variable loading history, the fatigue damage caused by each loading can be accumulated to determine the total fatigue life. Damage produced by individual cycles is summed to estimate fatigue life. Linear, nonlinear, and interaction damage models can be used (Zwerneman, 1991).

The best-known and most widely used fatigue-damage model is the linear Palmgren-Miner (Miner, 1945) damage model. According to this model, failure occurs when:

$$\sum \frac{n_i}{N_i} = 1 \tag{A2.11}$$

where $n_i$ is the number of cycles of loading applied at the stress range $\Delta\sigma_i$, and $N_i$ is the number of cycles of loading required to cause failure for continuous loading at the stress range $\Delta\sigma_i$.

### A2.10 Effective Stress Range

The effective stress range is the stress range of a constant-amplitude load history which will produce the same degree of damage as a variable-amplitude load history for the same number of cycles.

From Equation A2.5, and substituting $N_t = A \cdot (\Delta\sigma_{ref})^{-m}$, where $\Delta\sigma_{ref}$ is the effective stress range:

$$1 = \sum \frac{n_i}{N_t} = \sum \frac{n_i}{N_i} \cdot \frac{N_t}{N_t} = \sum \frac{n_i}{A(\Delta\sigma)^{-m}} \cdot \frac{A(\Delta\sigma_{ref})^{-m}}{N_t} = \sum \frac{n_i}{N_t} \cdot \frac{(\Delta\sigma_{ref})^{-m}}{(\Delta\sigma_i)^{-m}} \tag{A2.12}$$

and thus the effective stress range, $\Delta\sigma_{ref}$, is given by:

$$\Delta\sigma_{ref} = \left[\sum (n_i/N_t) \cdot (\Delta\sigma_i)^m\right]^{1/m} \tag{A2.13}$$

If the slope of the S-N curve, $m$, is equal to 2, the model is referred to as the root mean square (RMS) model. If $m$ is equal to 3, the model is referred to as the root mean cube (RMC) model. A value of $m$ equal to 3 provides a reasonable fit to experimental data for steel components and structures (Schiling, et al., 1978).

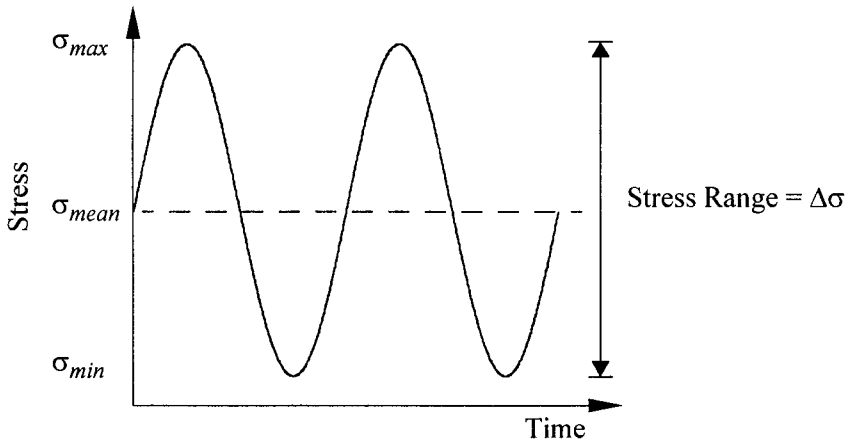


Figure A2.1: Constant sinusoidal loading history

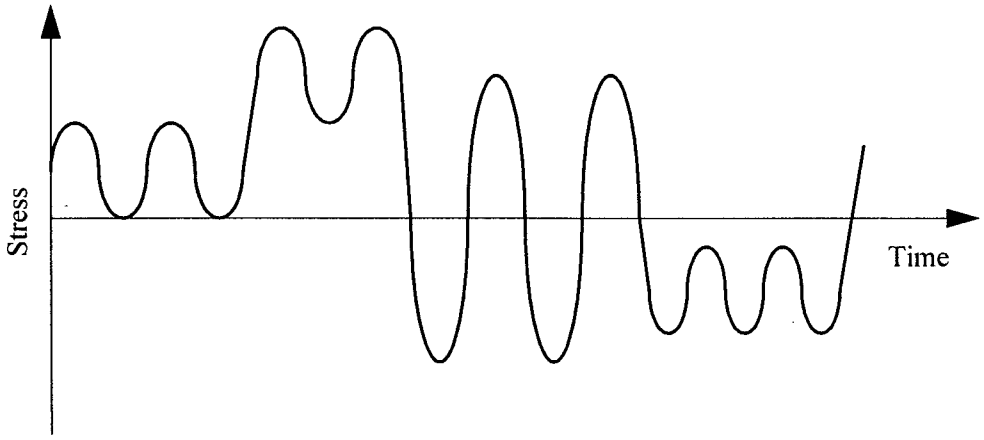


Figure A2.2: Variable-amplitude sinusoidal loading history

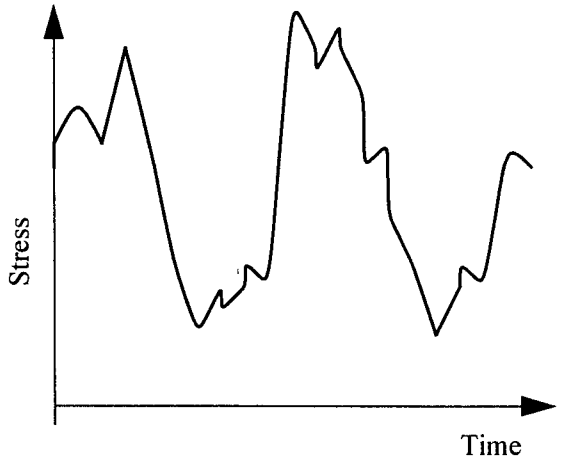


Figure A2.3: Random loading history

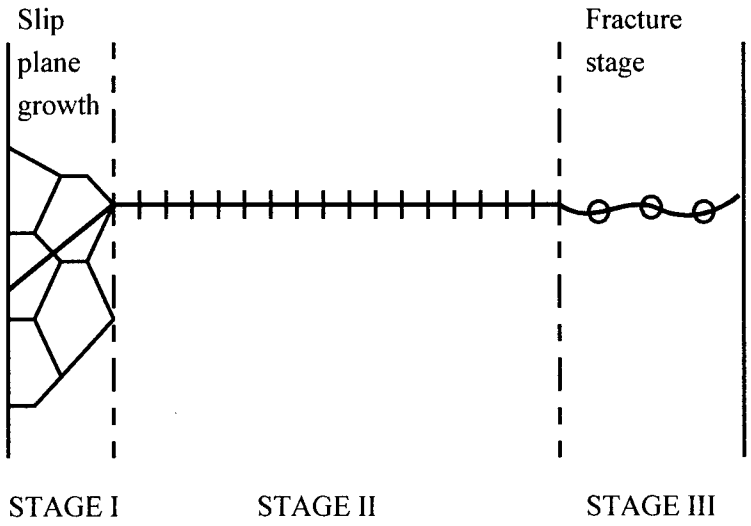


Figure A2.4: Stages of fatigue crack propagation

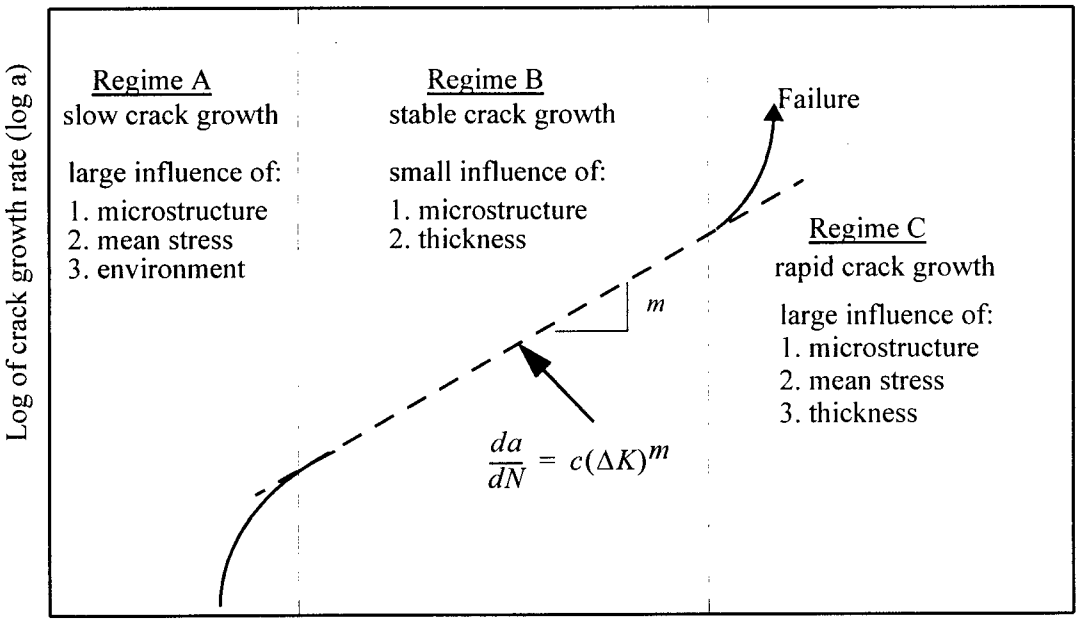


Figure A2.5: Fatigue crack growth rate

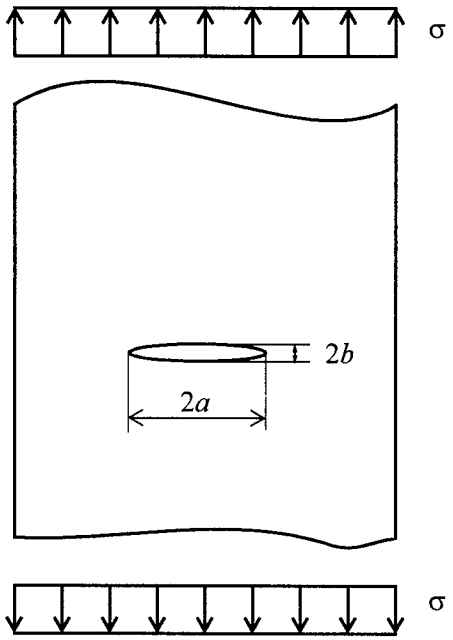


Figure A2.6: Stress intensity factor

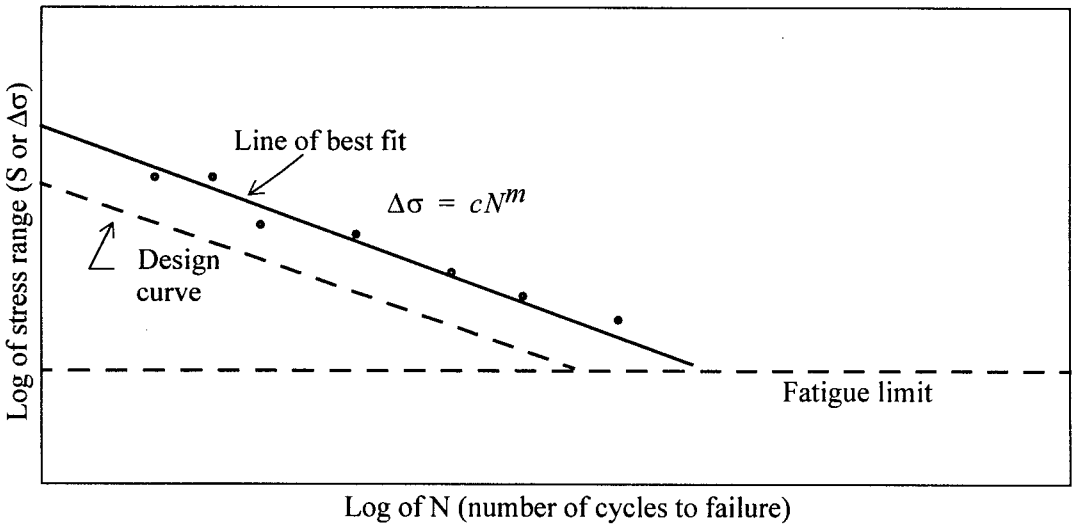


Figure A2.7: Typical S-N curve

# APPENDIX A3: FATIGUE BEHAVIOR OF WELDED CONNECTIONS

## A3.1 General

Welding is the process of joining materials (usually metals) by heating their surfaces to a plastic or fluid state, with or without pressure, and allowing the parts to flow together and join (with or without the addition of other molten materials). Welding includes many different processes. The American Welding Society (AWS) prequalifies four welding processes: shielded metal arc welding (SMAW), submerged arc welding (SAW), gas metal arc welding (GMAW), and flux cored arc welding (FCAW).

### *A3.1.1 Categories of Welded Connections (Joints)*

For the purpose of design, connections are often parsed into categories. A joint category depends on factors such as the size and shape of the members framing into the joint, the type of loading, and the amount of joint area available for welding. There are five basic types of welded joints; many variations and combinations of these basic types are used. The five basic types of welded joints (shown in Figure A3.1) are the butt, lap, tee, corner, and edge joints.

### *A3.1.2 Types of Welded Connections*

There are four types of welded connections (also termed weldments): fillet, groove, slot, and plug welds. These welds are shown in Figure A3.2. Most structural connections (about 80 percent) are fillet welds. Groove welds represent about 15 percent of welded connections, and they are common for column splices and beam-to-column moment connections. Slot and plug welds are rarely used.

## A3.2 Fatigue Behavior of Weldments

### *A3.2.1 General*

Welding a cyclically loaded structural member can reduce the performance of that member significantly (Maddox, 1989). As shown in Figure A3.3, the allowable stress range of a welded connection is substantially lower than that of the base metals being welded. As such, the design stresses in structures subjected to cyclic loadings are often limited by the fatigue strength of the welded connection.

### *A3.2.2 Stress Concentrations due to Weld Shape and Joint Geometry*

A welded joint alters the local cross-section dimensions of the parent metal at the point of welding. This change in geometry will lead to a concentration of stresses at locations close to the welded zone. The precise location and the magnitude of the stress and strain concentrations in a welded joint depend on the

design of the joint, the direction of the applied load, and the welding procedure used. For example, if the weld throat of a fillet weld is insufficient, the root area can become a region of high stress that can result in initiation of a fatigue crack at the root of the weld.

The geometry of a weld, and hence its propensity to act as a stress riser, has a large influence on the fatigue resistance of weldments. The fatigue strength of a welded joint decreases with increasing plate thickness, increasing weld angle, decreasing toe radius, and misalignment.

### *A3.2.3 Stress Concentrations due to Weld Imperfections*

All welded connections contain imperfections. The welding imperfections fall into three broad categories: planar imperfections (lamellar tears, lack of fusion, reheat cracks, and weld toe intrusions), volumetric imperfections (porosity and slag inclusions), and geometrical imperfections (misalignment, overfill, stop/starts, undercuts, and weld ripples). Figure A3.4 shows sample imperfections. The imperfections have differing effects on the fatigue life of welded connections. Imperfections (e.g., lack of side wall fusion) reduce the fatigue life. Volumetric imperfections (e.g., slag inclusion or porosity) can be tolerated to some extent, because the notch effect of these imperfections is minor. Geometric imperfections further increase the level of stress concentration.

### *A3.2.4 Effect of Residual Stresses*

Local tensile and compressive residual stresses and strains are normally present in the weldment area. Residual strains can exceed the yield strain of a material. Such strains occur as a result of the thermal expansion and contraction during welding due to geometric constraints.

Residual strains have a significant effect on the fatigue response of welded connections. When such a connection is subjected to cyclic loading, the residual strains (and stresses) have the effect of modifying the mean local stress.

### *A3.2.5 Effect of Material Properties*

The fatigue life of a welded connection is generally dominated by crack *growth,* whereas the fatigue life of an unwelded component is normally dominated by crack *initiation*. As a result, the fatigue life of a component excluding the connections normally increases with an increase in material tensile strength. For a welded connection, the fatigue strength is not influenced by the strength of the base metal, although the use of a more ductile base metal material will increase the fatigue life of a welded connection by preventing sudden, brittle failure.

## A3.3 Increasing Fatigue Life

The three key factors that influence the fatigue life of a welded joint are: 1) stress concentrations due to joint and weld geometry, 2) stress concentrations due to localized effects, and 3) residual stresses. The fatigue life can be improved by mitigating these factors.

The Structural Welding Code, AWS D1.1 (AWS, 1996), outlines some mitigation techniques. Section 8.4 of the AWS D1.1 specifies different methods of reworking a weld detail to improve fatigue life, including:

- *Profile improvement*: Reshaping the weld face by grinding the weld with a carbide burr to obtain a concave profile with a smooth transition from the base material to the weld material.
- *Toe grinding*: Reshaping only the weld toe by grinding with a burr or pencil grinder.
- *Peening*: Shot peening of the weld surface, or hammer peening of the weld toe.
- *TIG dressing*: Reshaping of the weld toe by remelting the existing weld metal with heat from a Gas Tungsten Arc Weld.

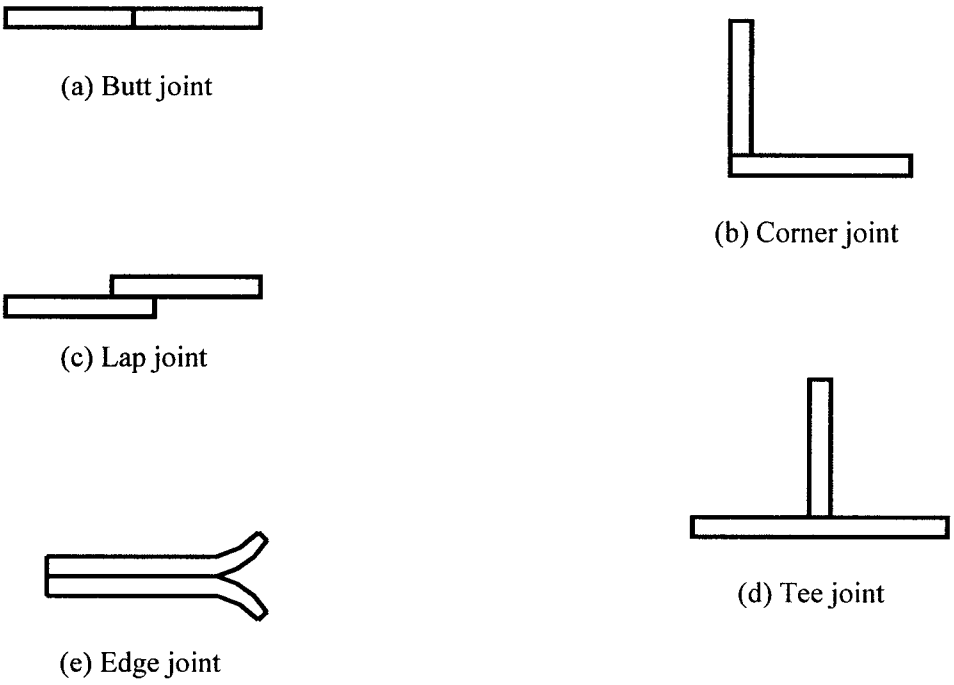


Figure A3.1: Types of joints

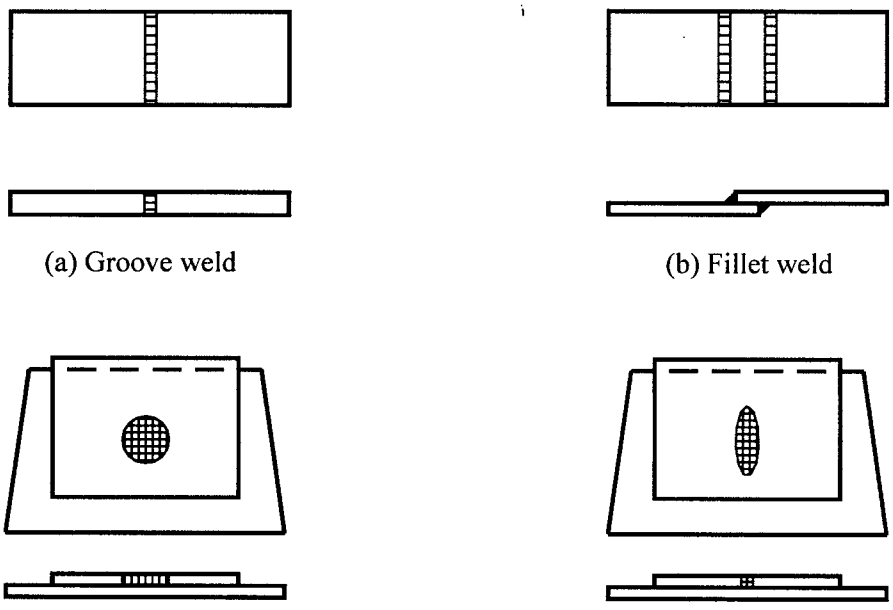


Figure A3.2: Types of welds

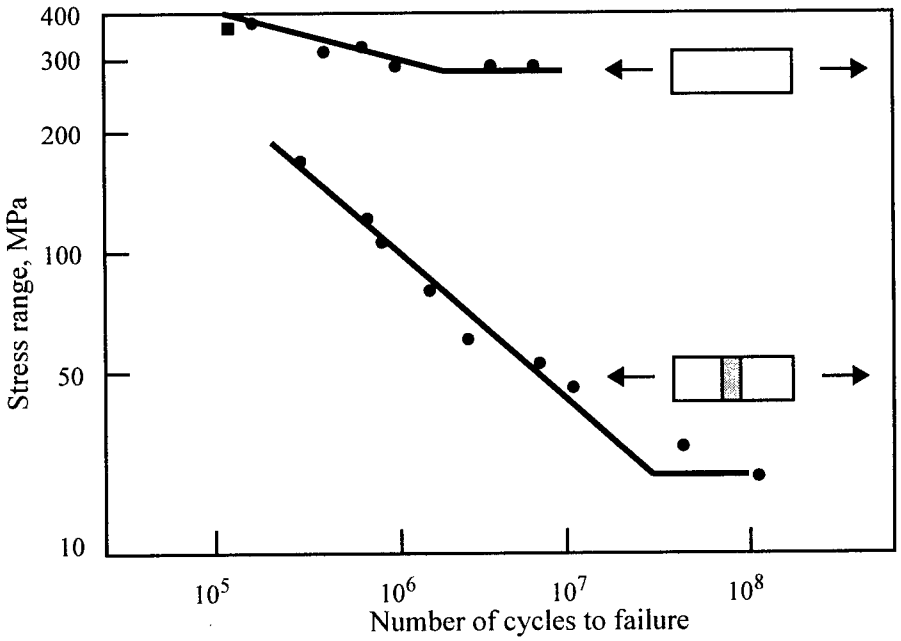


Figure A3.3: S-N curves for base metals and welded joints

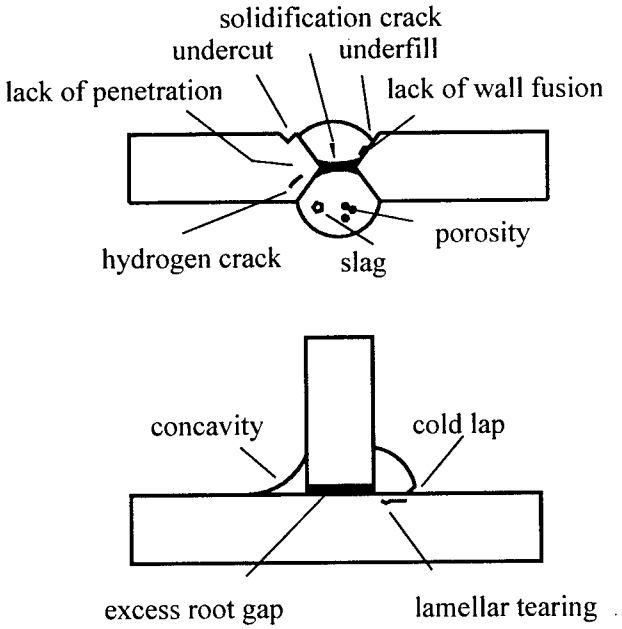


Figure A3.4: Welding imperfections

# APPENDIX A4: PREVIOUS RESEARCH ON FATIGUE

## A4.1 General

The fatigue life of a variety of welded civil engineering structures has been studied and reported. These structures include sign structures, cantilever light structures, off-shore platforms, and steel bridges. A brief description of the fatigue life characteristic of these structures, and findings from selected studies, follows.

## A4.2 Cantilever Sign and Luminary Structures

### *A4.2.1 General Description*

Sign and light structures typically consist of a vertical post, a horizontal arm, and signs or top attachments. These structures are generally fabricated from uniform or tapered pipe sections. The cantilever posts are welded to a base plate, which is attached to concrete pedestals by a set of anchor bolts. Sign and luminary structures are often tall, 30 ft (9 m) or more; the height of the sign is necessary to avoid obstructing the motorist's view or distracting his/her attention. The support structures can be classified into several groups: 1) overhead and roadside structures used to furnish support for highway traffic signs; 2) poles and towers used to illuminate large areas; 3) traffic signal support structures used for traffic control; and 4) combinations of the above. Figure A4.1 shows the schematics of typical sign and luminary structures.

Sign and luminary structures are usually very flexible and possess small structural (mechanical) damping. In their lifetime, they experience many repeated cycles of variable loading due to passage of traffic and environmental loading (e.g., wind forces). As such, the components and connections of these structures may be susceptible to fatigue cracking and failure.

### *A4.2.2 Fatigue Behavior of Sign Structures*

An analytical and experimental study of scaled components of sign structures (Kaczinski, et al., 1996) has recently been completed. The objective of that study was to evaluate the current AASHTO provisions (AASHTO, 1994) for design of cantilever sign structures to prevent fatigue failure.

Aerodynamic and aeroelastic wind tunnel testing of scale models was carried out. A typical model used for the wind tunnel tests is shown in Figure A4.2(a). The experimental work indicated that sign structures were most susceptible to galloping but not susceptible to vortex shedding.

Dynamic finite element analyses of the wind tunnel test specimens were undertaken to determine the magnitude of the across-wind pressures that would need to be applied to the sign structure to produce a similar response to that of the wind tunnel tests. Static finite element analysis procedures were used to determine the magnitude of the static lift pressures. Good agreement with AASHTO guidelines was obtained in most cases.

Dynamic tests on the anchor bolts were undertaken, and the effects of tightening techniques, thread forming methods, anchor bolt yield strength, misalignment, and bolt preload were investigated. Figure A4.2(b) shows the test setup for the anchor bolt tests. Experimental results indicate that the fatigue life can be improved by tightening of the anchor bolts to 1/3 turn beyond snug, using adequately thick base plates to prevent prying action, and limiting the anchor bolt misalignment to less than 1:40 to the vertical.

The findings of this research have been proposed as changes to the AASHTO guidelines.

## A4.3 Light Structures

### *A4.3.1 General Description*

Light poles are tall cantilever structures and behave much like luminary structures that are very flexible and are lightly damped.

### *A4.3.2 Fatigue Behavior of a Light Pole at Rich Stadium, Buffalo*

A study was performed by Mander, et al. (1992) to investigate the integrity of a flood light pole at Rich Stadium in Buffalo, New York. The tapered rectangular tubular steel light pole studied by Mander is 162 feet (49 m) in height. The plan dimensions vary from 43-1/8 in. x 57-7/16 in. (1.10 m x 1.46 m) at the base to 15-3/4 in. x 21 in. (0.40 m x 0.53 m) at the top. Figure 4.4 (a) shows the schematic of the light pole. Fatigue cracks were identified by ultrasonic testing in the anchor bolts at the location of leveling nuts. No fatigue cracks at the pole-to-base plate connection were reported.

As part of the Mander study, the light poles were instrumented using accelerometers, anemometers, strain gages, and acoustic devices. The instruments were used to measure the wind speed and the dynamic loading on the pole, and the reaction forces in the bolts. The experimental anchor bolt stress distribution and acoustic emission tests confirmed the presence of fatigue cracks in the bolts. The poles were retrofitted using high-strength post-tensioned threaded bars to relieve the load on the existing anchor bolts. Figure A4.3(b) shows the as-built and the retrofitted base details. Mander also recommended the installation of viscous dampers to reduce the wind-induced dynamic response of the pole.

## A4.4 Steel Offshore Structures

### *A4.4.1 General Description*

These structures consist of a prefabricated steel support structure (jacket), which extends from the seabed to above the water surface, and a prefabricated steel platform located on top of the support structure (topside), as shown in Figure A4.4 (Tollozco, 1991). The structure is typically fixed to the seabed by piles for shallow water applications. The steel jackets are commonly fabricated from thin tubular members due to the buoyancy and high torsional rigidity of these sections. The number, size, and orientation of members meeting at a joint varies significantly according to the configuration and size of the structure. Joints are parsed into four categories for design: simple welded joints, complex welded joints, cast steel joints, and composite joints. Figure A4.5 shows a typical simple welded joint and a complex welded joint. An offshore structure is exposed throughout its life to environmental cyclic loadings (waves, wind, currents, mechanical vibrations caused by machinery, and earthquakes) which produce stress variations in the structural members that can result in fatigue-induced cracking.

For offshore structures, the fatigue problem differs from that in other types of structures in two ways. First, the loading is generally introduced by ocean waves with a relatively long period (typically 6-7 seconds), and most of the damage is caused by many cycles loading at small stress ranges (Luna and Sunder, 1982). Second, offshore structures are placed in the corrosive environment of sea water, and the adverse effects of corrosion and fatigue are combined. For offshore structures, there does not seem to be a fatigue limit. That is, regardless of the applied stress range, infinite fatigue life of a connection may not be assumed (Luna and Sunder, 1982).

### *A4.4.2 Fatigue Behavior of Steel Offshore Rigs*

There has been a considerable amount study of the fatigue life of joints of tubular members (herein referred to as tubular joints). Early studies (Wylde and McDonald, 1979; Dijkstra and deBack, 1980) concentrated on fatigue testing of small-size tubular welded joints and compared their fatigue behavior with those of large-size tubular welded joints. Although a reduction in the fatigue strength with increase in tubular joint size was noted, the significance of size alone on fatigue life seemed small.

Gowda (1985) studied the characteristics of fatigue crack growth in tubular steel offshore components. The experimental work was carried out on specimens fabricated from large-size tubular joints. In the laboratory tests, the fatigue cracks initiated in the toe of the welds of brace or chord members, and typically propagated along the weld toe, perpendicular to the surface. However, the cracks did not always follow a regular path. Figure A4.6 shows an irregular crack which did not propagate along the

circumferential direction. Residual stresses and grain size distribution influenced the growth of the fatigue crack. The authors concluded that: 1) crack orientation had a significant effect on the crack growth rate, and 2) in the case of welded specimens, stress relief enhanced the fatigue life of welded specimens by increasing resistance to crack growth.

Dou, et al. (1991) performed static and fatigue tests on 34 welded large-sized T-joints, subjected to axial and in-plane bending loading, to study the effects of joint geometry parameters and loading modes on the fatigue life of the joints. In the laboratory tests, the time required for crack propagation was longer than that required for crack initiation. The fatigue life of these large-sized joints was ruled by their crack growth life. The authors concluded that the fatigue life of the joints shortened with an increase in the member wall thickness.

## A4.5 Steel Bridge Structures

### *A4.5.1 General Description*

The superstructure of a bridge is composed of primary and secondary member components. The primary members consist of rolled beams (i.e, wide-flange sections), rolled beams with cover plates (i.e., rectangular cover plates on beam flange), plate girders (i.e., built-up welded sections, regular or haunched), and box girders. The secondary members include diaphragms (X-frames and V-frames), lateral bracing, and sway bracing.

A number of localized failures have developed in components of steel bridges due to fatigue and subsequent brittle failure. To identify the cause of the fatigue failures and to develop crack investigation and fatigue prevention techniques, extensive laboratory and field studies relating to fatigue life of steel bridges have been undertaken.

### *A4.5.2 Fatigue Studies on Steel Bridges*

Fisher, et al. (1970, 1974) tested a series of beams, including cover plates (1970), and stiffeners and attachments (1974), to study the life expectancy of welded bridge beams and girders. Regarding fatigue life, they determined that: 1) stress range was the dominant stress parameter for all welded details; 2) structural steels with different yielding stresses did not exhibit significantly different fatigue life for the same loading history; and 3) the type of weld (i.e., fillet vs. groove) affected the fatigue life of the beams. Regarding the fatigue cracks, they noted that: 1) failures occurred mainly in the tension flange of all beams; 2) cracks were observed at the ends of cover plates; 3) cracks causing failure of stiffeners welded to the web alone initiated at the toe of the stiffener-to-web weld at its end; 4) when stiffeners were welded both to the web and the flanges, cracks initiated at the toe of the transverse stiffener-to-flange weld; and 5)

the crack causing failure at all welded flange attachments originated at the toe of the weld.

In a subsequent study, Fisher, et al. (1979) conducted laboratory and field studies to detect and repair the fatigue-related damage to welded highway bridges. The findings of this study were: 1) small cracks, as little as 0.25 in. (6 mm), can be detected by either ultrasonic or visual inspection with magnification; cracks smaller than 6 mm cannot be readily detected by available nondestructive methods of inspection; 2) a large reduction in the fatigue life of many welded details occurs when cracks initiate and grow from micro-sized defects that exist at the weld periphery; 3) peening was more effective than grinding as a repair method and can be applied with good results to both as-welded details and to surface cracks having depths less than 0.125 in. (3 mm); 4) crack initiation in repaired beams generally results from defects introduced by the repair method; and 5) fatigue damage due to out-of-plane displacement can be satisfactorily retrofitted by drilling holes at the crack tip.

Detailed case studies of several types of fatigue cracks are discussed and analyzed by Fisher (1984). In a study sponsored by the Federal Highway Administration, Fisher, et. al. (1990) surveyed cracks in a number of steel bridges. The findings of these studies and other investigations indicate that, for the majority of steel bridges, fatigue cracks can be attributed to one of two sources: out-of-plane distortions in small, unstiffened segments of girder webs (see Figure A4.7), and large initial cracks. The authors concluded that: 1) fatigue cracks initiate at an initial discontinuity in the weldment and grow perpendicular to the direction of applied tensile stress; 2) low fatigue strength details, such as welded web gusset plates or large cover-plated beams, should be avoided in bridge design; and 3) a high volume of truck traffic will accelerate fatigue cracking, especially in bridges with poorly detailed connections.

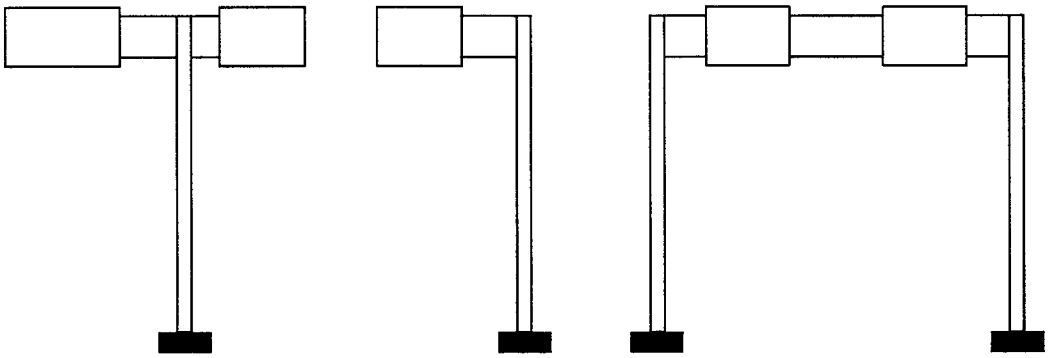

Unbalanced butterfly Cantilever Sign bridge

Sign support structures

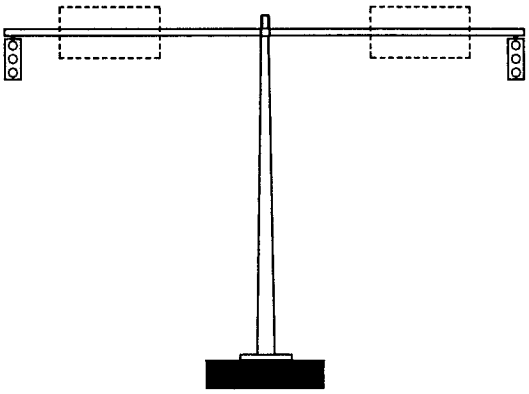

Cantilever arm mounted traffic signal

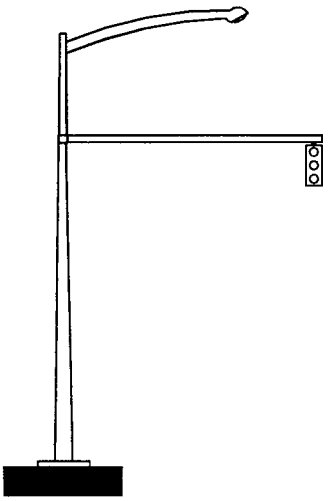

Combination cantilever arm mounted luminaires and traffic signals

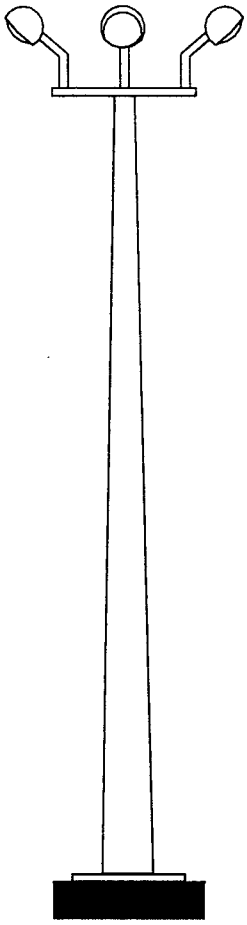

Luminary support structure (pole type)

Figure A4.1: Typical sign and luminary structures
(adapted from AASHTO, 1994)

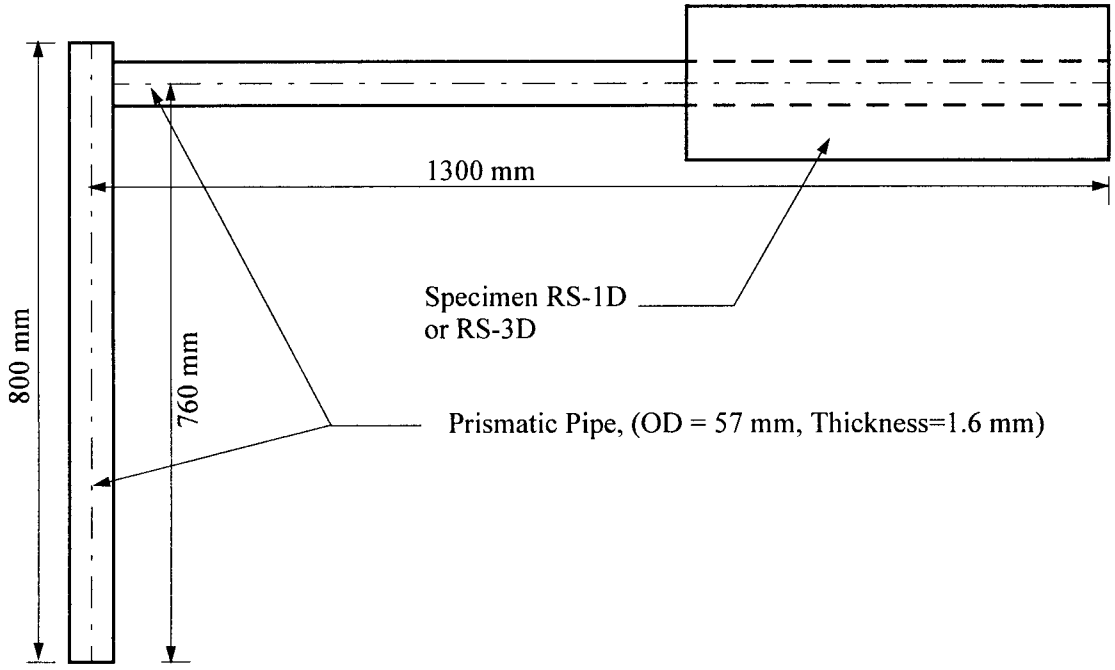


(a) Typical scaled 1/8 model structure used in wind tunnel tests

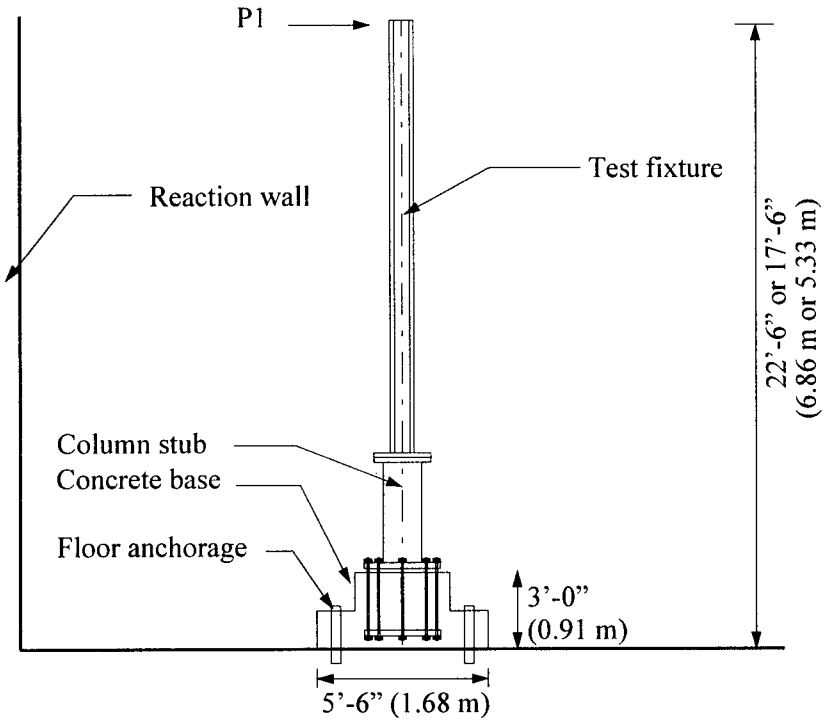


(b) Full-scale model used in the dynamic tests of the anchor bolt groups

Figure A4.2: Study of fatigue response of sign structures at Lehigh University (adapted from Kazcinski, et al., 1996)

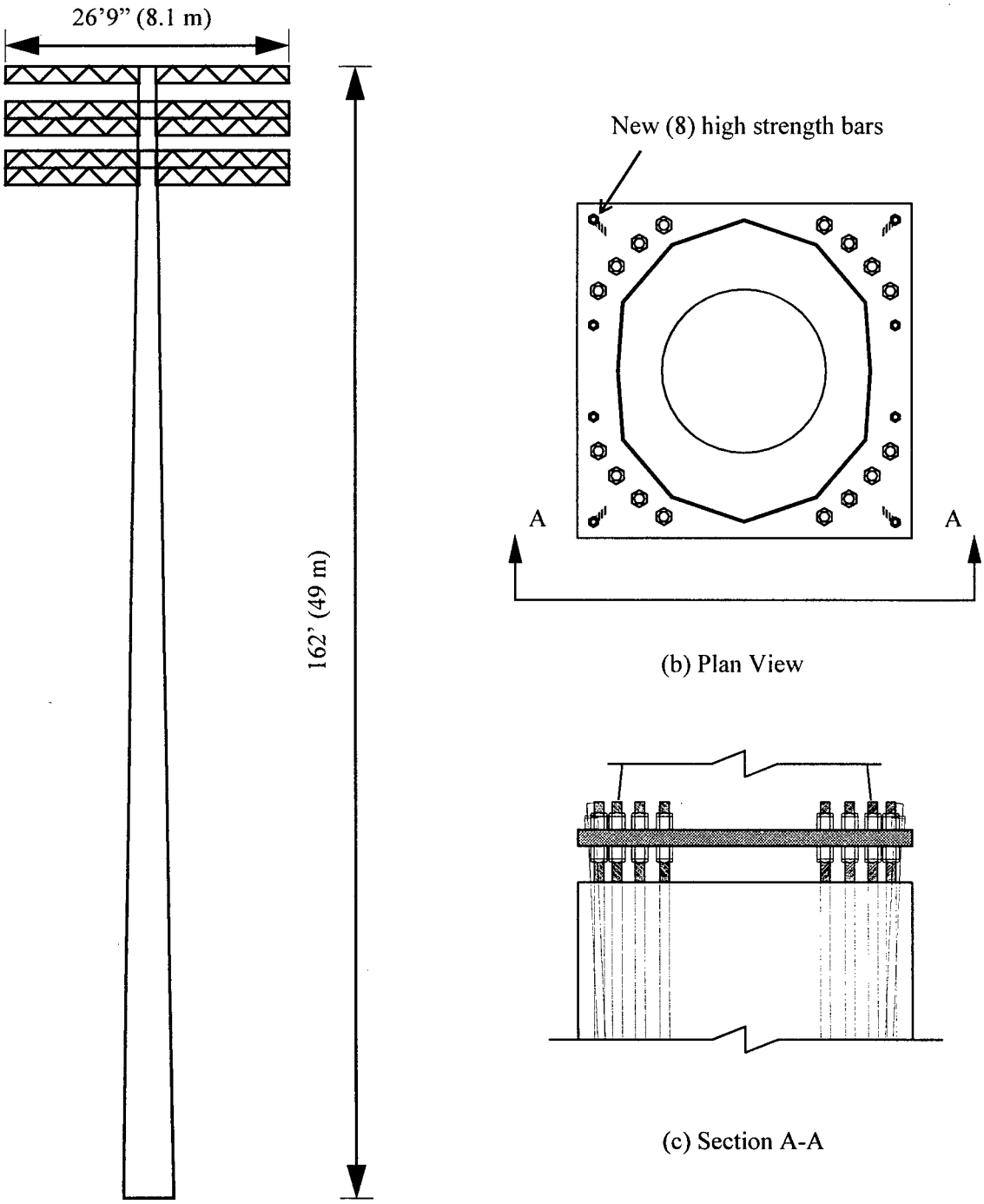


(a) Pole elevation

(b) Plan View

(c) Section A-A

Figure A4.3: Study of a light pole at Rich Stadium in Buffalo
(adapted from Mander, et al., 1992)

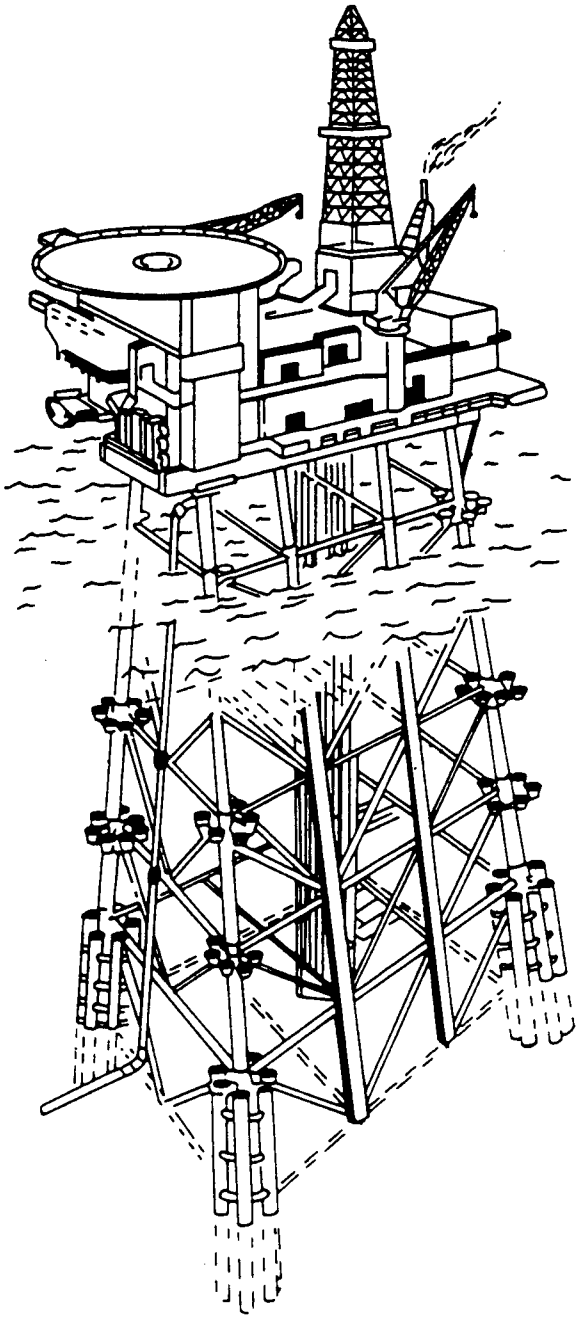

Figure A4.4: Schematics of a typical offshore structure (Tolloczko, 1991)

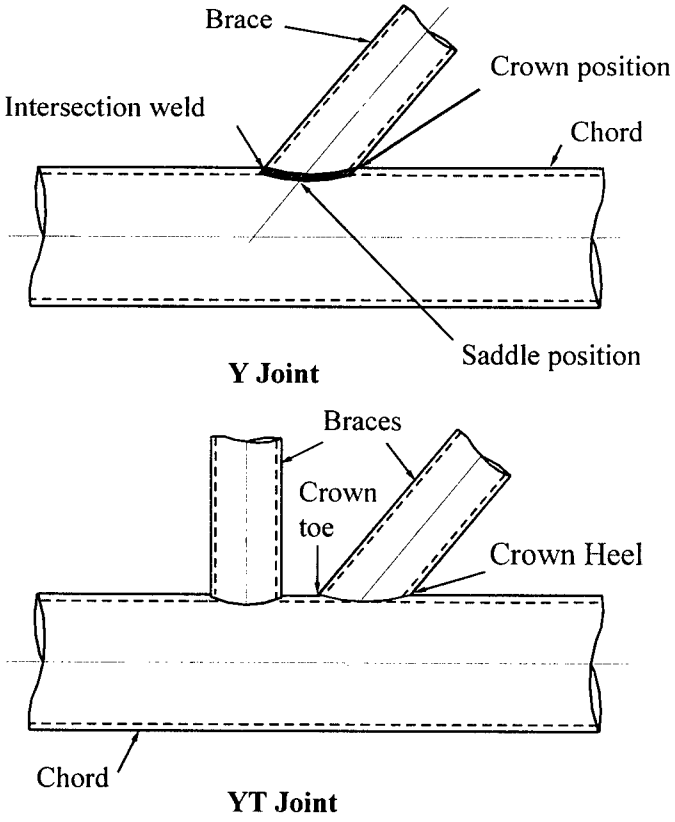


Figure A4.5: Typical single and multi-welded tubular offshore connections

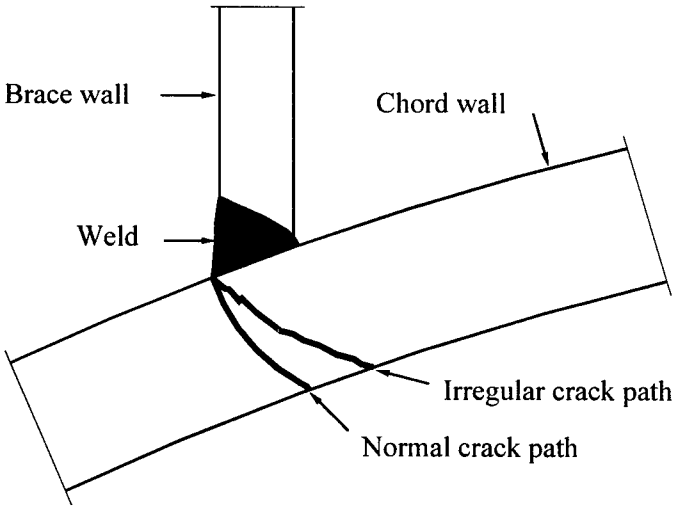


Figure A4.6: Crack propagation in tubular joints (adapted from Gowda, 1985)

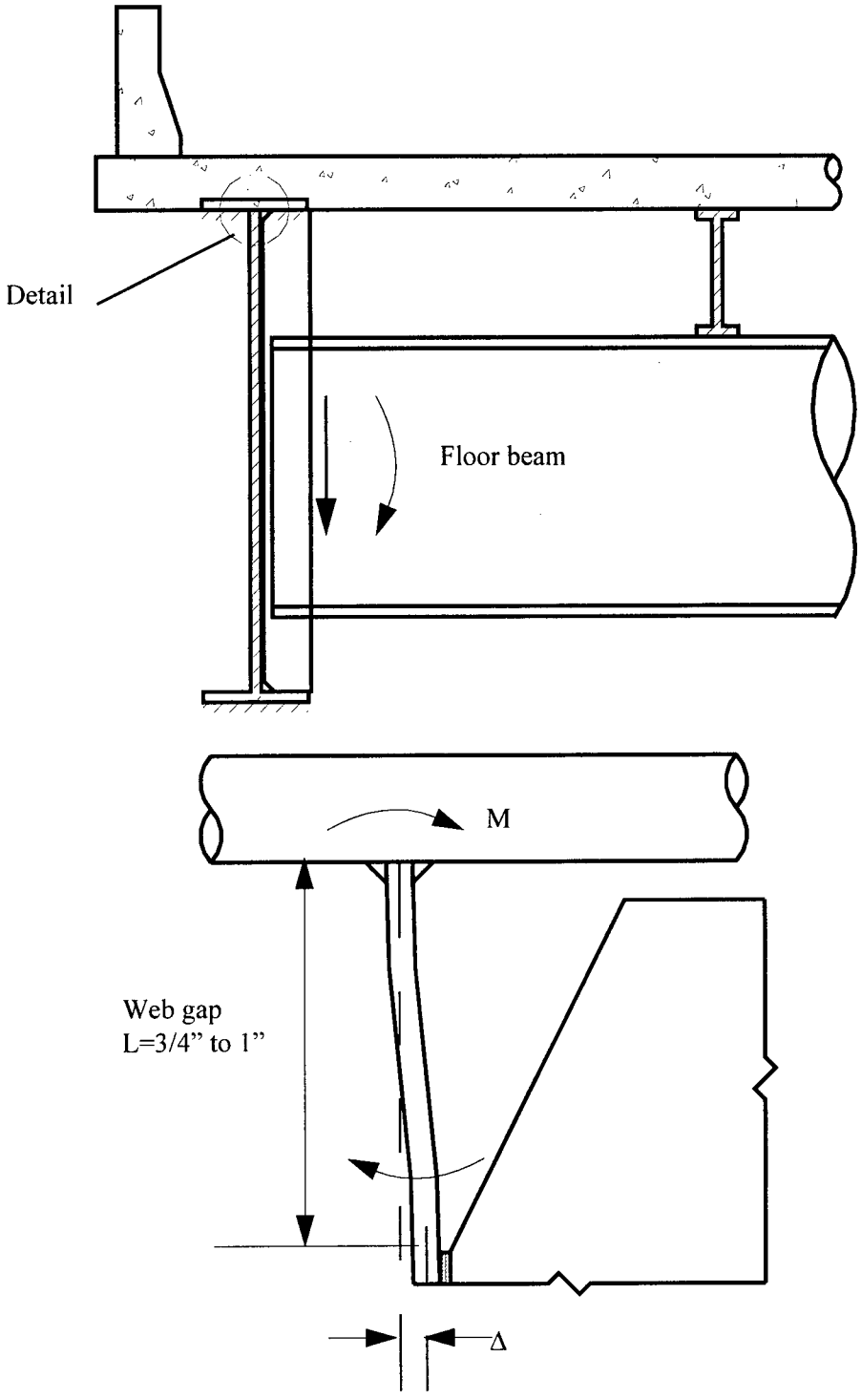


Figure A4.7: A typical source of fatigue cracking in a steel bridge
(adapted from Fisher, et al., 1983)

# APPENDIX A5: DESIGN CONSIDERATIONS

## A5.1 General

A brief summary of current standards for design of CMS structures is presented below, followed by a short review of criteria for design against fatigue failure.

## A5.2 AASHTO Design Guidelines for Sign Structures

The AASHTO (American Association of State Highway and Transportation Officials) Standard Specifications for Structural Supports for Highway Signs, Luminaries, and Traffic Signals (herein referred to as AASHTO-94) (AASHTO, 1994) are based on an equivalent static force method. A summary of the procedure is presented here.

### *A5.2.1 Loads*

Sign structures are designed for a combination of dead load (weight of the sign and attachments), live load (weight on the service platform), ice load (when applicable), and wind load (wind pressure on horizontal and vertical faces).

The wind pressure, $p$, on the sign structure is computed as:

$$p = 0.00256(1.3V)^2 C_D C_H \tag{A5.1}$$

where $V$ is the mean wind speed, $C_D$ and $C_H$ are the drag and height coefficients, respectively, and the factor 1.3 accounts for gusting. Tables in AASHTO-94 list values for these coefficients. The sign structure is then designed for a horizontal force equal to the product of the wind pressure, $p$, and the face area ($b$ x $d$ in Figure 2.1).

According to AASHTO-94, the design of a typical sign structure for wind load effects does not require dynamic analysis. Instead, equivalent static forces due to wind loading are determined and then combined with forces due to other types of loading for the purpose of analysis.

### *A5.2.2 Design of Steel Signs*

Sign structures must be designed for a combination of axial, flexural, and shear stresses. The axial, flexural, and shear stresses due to the different sources of loading are summed and checked using the following equation:

$$\frac{\sigma_a}{F_a} + \frac{\sigma_b}{C_A F_b} + \left(\frac{\sigma_v}{F_v}\right)^2 \leq 1.0 \qquad \text{(A5.2)}$$

In this equation, $\sigma_a$, $\sigma_b$, and $\sigma_v$ are the axial, flexural, and shear stresses, respectively; $F_a$ is the allowable axial stress; $F_b$ is the allowable bending stress; $F_v$ is the allowable shear (torsional) stress; and $C_A$ is an amplification coefficient that accounts for secondary bending effects due to axial load.

### *A5.2.3 Welding Requirements*

AASHTO-94 specifies that weldments should satisfy the requirements of AWS D1.1 (AWS, 1996) for post-to-base-connections. The guidelines recommend either a full-penetration weld or a socket type of joint utilizing two fillet welds. The guidelines specify that a random 25 percent of the connection welds be inspected. Ultrasonic tests and radiography are recommended for full-penetration welds, and magnetic particle tests are recommended for fillet welds. For welds of pole sections joined by circumferential welds, full-penetration welds are required, and these must be inspected by either ultrasonic or radiography means.

### *A5.2.4 Deflections*

For cantilever structures, AASHTO-94 specifies a limiting tip displacement and rotation for the vertical cantilever post. The angular deflection of the top of the post must be less than 1.7 degrees, and the tip horizontal displacement must be less than or equal to 2.5 percent of the height.

### *A5.2.5 Vortex Shedding*

AASHTO-94 shows that sign structures subjected to wind loading can be affected by vortex shedding. The frequency at which regular vortices will be shed is calculated using the Karman equation (see Appendix A1). For circular cross sections, the Strouhal number is given as 0.18, and the fundamental vibration frequency of the sign structure is computed as that for a cantilever column. The transverse wind pressure, $p_t$, causing the oscillations is computed from:

$$p_t = \frac{p}{2\xi} \qquad \text{(A5.3)}$$

where $p$ is the wind pressure on the vertical face (Equation A5.1) without the gust factor, and $\xi$ is the estimated structural damping of the sign structure (assumed to be 0.5 percent). Once the transverse wind pressure is obtained from Equation A5.3, the equivalent static loading due to the transverse wind pressure is computed (see Section A5.2.1).

### *A5.2.6 Fatigue*

AASHTO-94 recommends that the stress calculation for fatigue life follow the AASHTO Standard Specifications for Highway Bridges (herein referred to as AASHTO-92) (AASHTO, 1992). AASHTO-94 notes that the number of cycles that a sign structure may experience in its design life may exceed the maximum number of cycles indicated in the specifications, but that many of these cycles are expected to occur at a lower stress range than the design value. In addition, AASHTO-94 assumes that the critical stress may be reached under wind loading, but that the likelihood of this stress being exceeded again within its design life is small. The guidelines suggest that sound practice in the design of sign structures should be based on the stress range associated with infinite fatigue life of the material (equal to two million cycles for steel).

AASHTO-94 specifies that the critical areas for checking must include the welded connections at the base of the post and in the post proper. In addition, stress concentration due to bolt holes or re-entrant corners should be avoided in areas that are susceptible to failure by fatigue.

## A5.3 Design for Fatigue

### *A5.3.1 General*

The problem of fatigue has been studied by different individuals and organizations. As such, many engineering disciplines have developed their own requirements for design against fatigue failure. For example, the American Steel Institute of Construction (AISC), the American Petroleum Institute (API), the American Welding Society (AWS), and the American Railway Engineering Association (AREA) have each developed their own design criteria. Most of the design approaches are based on developing S-N curves for design based on experimental results and categorizing structural components into different classes and assigning each class an S-N curve and a fatigue stress limit (or rating).

### *A5.3.2 AASHTO Specifications*

AASHTO-92 parses fatigue into two categories: 1) load-induced, and 2) distortion-induced. The components and details which are susceptible to load-induced fatigue are classified into eight categories for fatigue resistance. Welded connections are classified into categories A, B, B', C, C', D, E, and E' (see Figure 2.4). The classifications are based on experimental data and incorporate a two-standard deviation factor of safety. For each category, a theoretical constant amplitude threshold is defined. Below the threshold stress range, a connection or component has an infinite fatigue life. Above the threshold, the fatigue resistance (measured in terms of number of cycles) is assumed proportional to the cube of the stress range.

For CMS structures, the full-penetration welded connections at the base of the post and flanged connections in the mast arm are categorized as class E'. As such, they have a theoretically infinite fatigue life for stress ranges below 2.6 ksi (18 MPa). The E' classification for such connections is used because of the difficulty associated with inspecting the back side of the weld due to the presence of the back-up ring.

## A5.4 Comments

The results of an extensive study at the Lehigh University (Kaczinski, et al., 1996) were presented as an NCHRP report. In that report, the authors suggest that AASHTO-94 be revised to incorporate the following wind effects: galloping, vortex shedding, natural wind, and truck gusts. It was further recommended that each of these phenomena be assigned an importance factor according to the particular type of sign structure. The experimental and analytical research found the equivalent static method to be adequate for the design of sign structures. The authors recommended that all components of sign structures be designed to resist the four wind effects individually. A limit of eight inches (203 mm) of vertical displacement at the tip of the horizontal mast arms under the effects of wind loading was also recommended.

# APPENDIX A6: TRIAL ANALYSIS AND DESIGN OF A CMS STRUCTURE

## A6.1 General

The preliminary analysis of a CMS structure is presented herein to provide the reader with sample information on the design and response of CMS structures. The vertical post in this structure was sized for gravity and wind loads; wind data from California were used to estimate the design wind pressures. The design follows AASHTO, 1994, Standard Specifications for Structural Supports for Highway Signs, Luminaries and Traffic Signals. The analysis procedure represents wind effects by equivalent static pressures. The following sections present information on the assumed geometry of the CMS structure (Section A6.2), the loads calculated per AASHTO (Section A6.3), the cross-section analysis (Section A6.4), and the design of the vertical post (Section A6.5).

## A6.2 Geometry of a CMS structure

The assumed geometry of the CMS structure is shown below in Figure A6.1. The dimension $H$ (= 29 ft 5 in.) is the maximum length pole used in Caltrans' standard design and represents the configuration that produces maximum loads and stresses in the structure (Woody and Gugino, 1997).

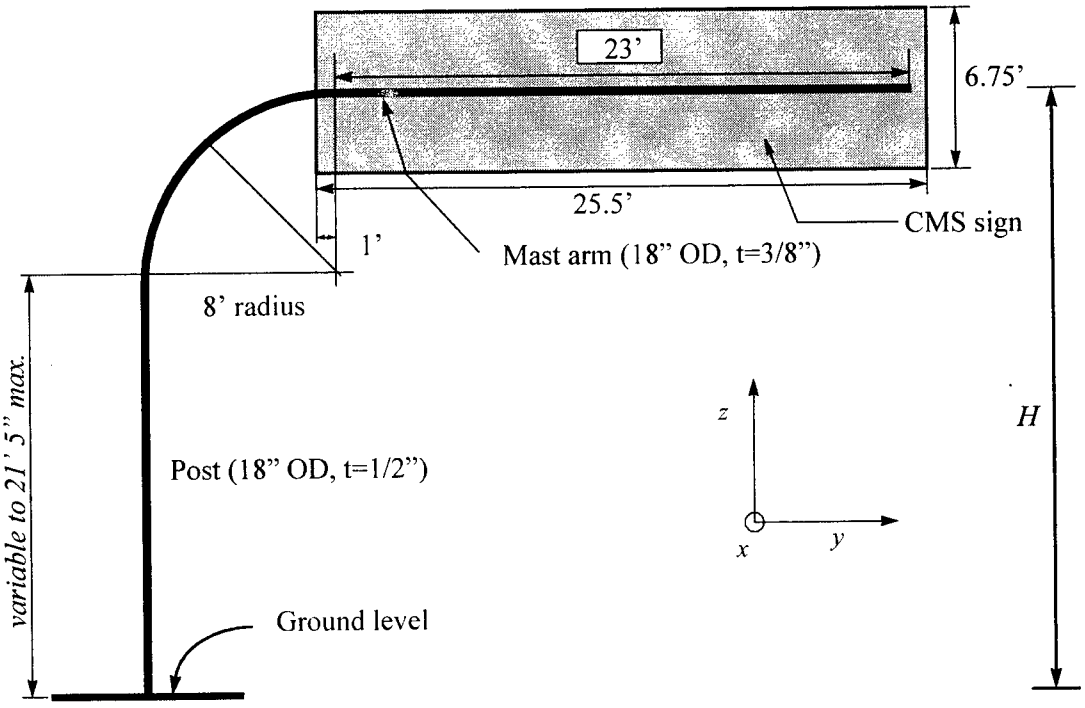


Figure A6.1: Geometry of the CMS structure

## A6.3 Loads

### *A6.3.1 Gravity Loads*

The following dead (DL) and live (LL) loads were assumed for the analysis and design of the CMS structure. Ice loads were not considered. The dead loads were provided by Caltrans.

Table A6.1: Gravity Loads

| Load | AASHTO (1994) Section No. | Information |
|---|---|---|
| DL | 1.2.1 | CMS sign + sign attachments (walkway, connecting brackets, and angles) = 4,800 lbs. |
| | | Post (OD=18", ID=17") = 94 lbs/ft, for a total weight=3,200 lbs. |
| | | Mast arm (OD=18", ID=17.25") = 74 lbs/ft, for a total weight=1,700 lbs. |
| | | Joint load (flange plates) = 200 lbs. |
| LL | 1.2.2 | 500 lbs point load. |

### *A6.3.2 Wind Load*

The wind pressure, $p$, acting on a component of a CMS structure may be computed (AASHTO Section 1.2.4) from the following equation:

$$p = 0.00256(1.3V)^2 C_D C_H \qquad \text{(A6.1)}$$

where $V$ is the mean wind speed in mph, $C_D$ and $C_H$ are the drag and height coefficients, respectively, and the factor 1.3 accounts for gusting.

Since CMS structures are termed overhead sign structures in AASHTO-1994, wind speeds were based on a 50-year mean recurrence interval. From AASHTO Figure 1.2.4C, $V$=80 mph is the maximum design wind speed in California. For a CMS structure ($H$ > 29 ft), a value of $C_H$ = 1.10 was assigned, as listed in AASHTO Table 1.2.5B. Values of $C_D$ for different components of a CMS structure were obtained from AASHTO Table 1.2.5C. Pertinent values of $C_D$ are listed in Table A6.2.

Table A6.2: Drag and height coefficients

| CMS Component | Cross section normal to the wind direction | | Drag Coefficient, $C_D$ | |
|---|---|---|---|---|
| | *x* | *y* | *x* | *y* |
| CMS sign | rectangular; L/W<5 | rectangular; L/W=large | 1.20 | 1.30 |
| CMS walkway | flat | flat | 1.75 | 1.75 |
| Post | circular | circular | 0.45 | 0.45 |
| Mast arm | circular | rectangular; L/W=large | 0.45 | 1.30 |

Figure A6.2 shows the notation for wind loads, as listed in AASHTO-1994 Figure 1.2.5.D(1), for cantilever sign support structures.

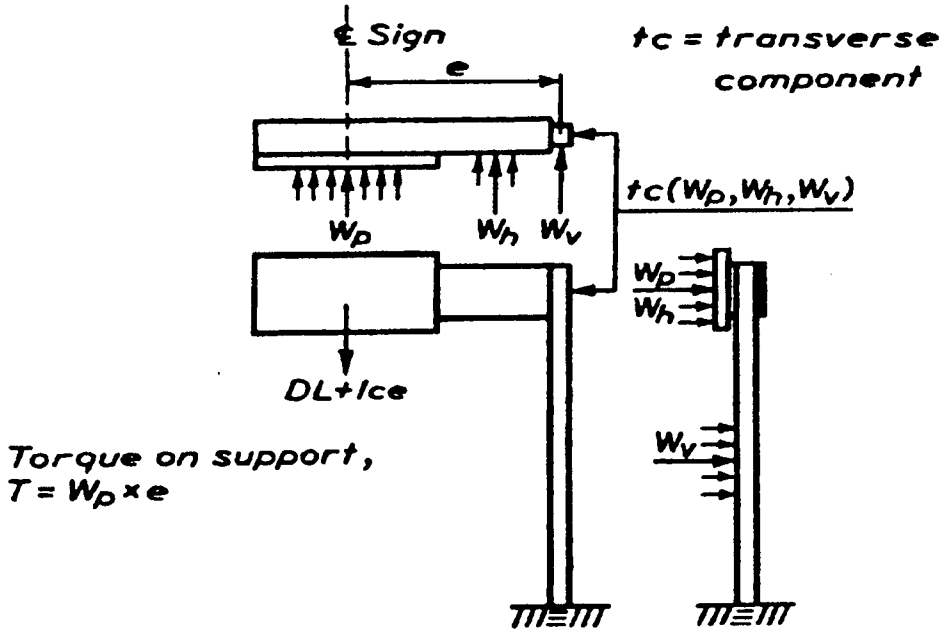


Figure A6.2: Notation for wind loads (AASHTO, 1994)

The wind loads on components of the sample CMS structure were computed using a design wind pressure and the area of the component normal to the wind direction. For CMS structures, the wind forces acting on the vertical post, the horizontal mast arm, the sign, and the walkway must be calculated. Wind flow in two directions must also be considered. Table A6.3 summarizes the wind forces acting on the CMS structure of Figure A6.1.

Table A6.3: Wind loads

| Component | Wind flow in *x*-direction | | | | Wind flow in *y*-direction | | | |
|---|---|---|---|---|---|---|---|---|
| | *p* lb/ft$^2$ | *A* ft$^2$ | *W* kips | e[a] in. | *p* lb/ft$^2$ | *A* ft$^2$ | *W* kips | *e* in. |
| CMS sign | 36.5 | 172 | 6.3 | 19.75 | 39.6 | 5.0 | 0.2 | 0 |
| Walkway[b] | 53.3 | 0 | 0 | 19.75 | 53.3 | 0 | 0 | 1.5 |
| Vertical post | 13.7 | 51 | 0.7 | 0 | 13.7 | 51 | 0.7 | 0 |
| Mast arm | 13.7 | NA[c] | 0 | 19.5 | 13.7 | 1.8 | 0 | 0 |

a. distance to the center-line of the post from the center-line of the component.
b. the projected area is negligible.
c. hidden behind the CMS sign.

### *A6.3.3 Load Summary*

For the CMS structure in Figure A6.1, the forces shown in Figure A6.2 will result in the load distribution shown in Figure A6.3. The numerical values of the design loads and their locations are listed in Table A6.4.

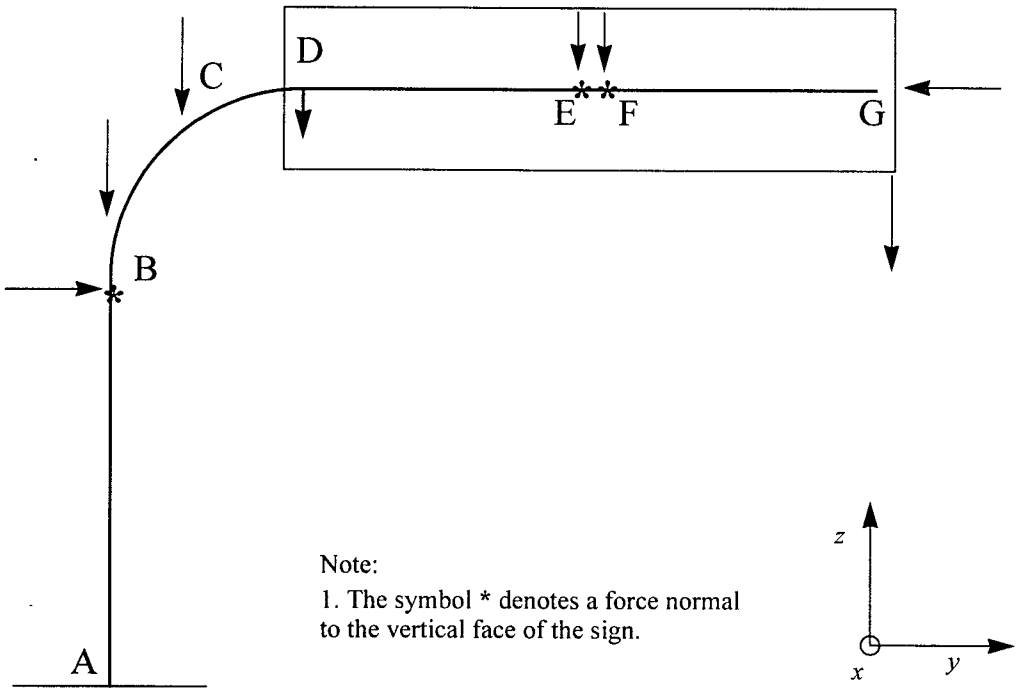


Figure A6.3: Assumed loading points on the CMS structure in Figure A6.1

Table A6.4: Loads acting on the CMS structure

| Point of application of load | Coordinate (ft) | | | Load components[a] (kips) | | |
|---|---|---|---|---|---|---|
| | $x$ | $y$ | $z$ | $x$ | $y$ | $z$ |
| A[b] | 0 | 0 | 0 | 0 | 0 | 0 |
| B[c] | 0 | 0 | 19.6 | $W_v = 0.7$ | $W_v = 0.7$ | $DL$=2.0 |
| C[d] | 0 | 4 | 25.4 | 0 | 0 | $DL$=1.2 |
| D[e] | 0 | 8 | 29.4 | 0 | 0 | $DL$=0.2 |
| E[f] | 0 | 19.5 | 29.4 | $W_H = 0$ | $W_H = 0$ | $DL$=1.7 |
| F[g] | 0 | 19.75 | 29.4 | $W_p = 6.3$ | $W_p = 0.2$ | $DL$=4.8 |
| G[h] | 0.5 | 32.5 | 29.4 | 0 | 0 | $LL$=0.5 |

a. Refer to Figure A6.2 for the definition of load components
b. Base of the post
c. Straight portion of the post
d. Curved portion of the post
e. Flange plates
f. Mast arm
g. Sign plus sign attachments (walkway, etc.)
h. End of the walkway

### *A6.3.4 Load Combinations*

The load combinations used for the design of a CMS structure are given in AASHTO Section 1.2.5D4 and are presented in Table A6.5:

Table A6.5: Load combinations

| Combination | Normal component | Transverse component |
|---|---|---|
| 1 | 100% | 20% |
| 2 | 60% | 30% |

For the remainder of this appendix, load combination 1 was used because it was the critical combination for the design of the vertical post in the sign structure.

### *A6.3.5 Group Loads*

The loads described above must be combined per AASHTO Section 1.2.6 into one of the group loads listed in Table A6.6.

Table A6.6: Group load combinations

| Group | Load combination | Percentage of allowable stress |
|---|---|---|
| I | *DL* | 100 |
| II | *DL+W* | 140 |
| III | *DL+IL+1/2W* | 140 |

Group II loads were used to size the vertical post for the gravity and equivalent static wind loads.

### *A6.3.6 Calculation of Forces at the Base of the Vertical Post*

Using the applied loads listed in the load summary (Table A6.4), the following resultant forces were obtained at the base of the vertical post (point A in Figure A6.3).

Table A6.7: Forces at the base of the post

| Component | Direction | Force or Moment |
|---|---|---|
| Axial Force | $P_z$ | 1.2+2.0+1.7+4.8+0.2=9.9 kips |
| Shear | $V_x$ | 6.3+0.7=7.0 kips |
| Shear | $V_y$ | 0.20*(0.7+0.2) = 0.2 kips |
| Torque | $T_z$ | 6.3*19.75=124 k-ft |
| Moment | $M_x$ | 0.2(0.7*19.6+0.2*29.4) + 1.2*4+1.7*19.5+4.8*19.75+ 0.2*8=140 k-ft |
| Moment | $M_y$ | 0.7*19.6+6.3*29.4=200 k-ft |

## A6.4 Analysis

### *A6.4.1 Section and Material Properties and Stress Calculations*

The cross-sectional properties of Table A6.8 were used for the analysis of the 18 in. diameter vertical post. The stresses at the base of the post were computed using information from Tables A6.7 and A6.8. Material properties were based on A36 steel, ($F_y$ = 36 ksi).

Table A6.8: Section properties

| *D*, in. | *t*, in. | *A*, in.$^2$ | *I*, in.$^4$ | *S*, in.$^3$ | *J*, in.$^4$ |
|---|---|---|---|---|---|
| 18 | 0.5 | 27.5 | 1053 | 117 | 2106 |

Table A6.9: Stresses at the base of the post

| Component | Direction | Stress (ksi) |
|---|---|---|
| Axial stress | $f_a = \frac{P_z}{A}$ | 9.9/27.5 = 0.4 |
| Shear stress ($x$-direction) | $f_{v_x} = V_x \frac{Q}{2It} = 2\frac{V_x}{A}$ | 2* 7.0/27.5 = 0.6 |
| Shear stress ($y$-direction) | $f_{v_y} = V_y \frac{Q}{2It} = 2\frac{V_y}{A}$ | 2* 0.2/27.5 = 0.1 |
| Torsional stress | $f_v = \frac{TR}{J}$ | (124*12)*9/2106 = 6.4 |
| Flexural stress ($x$-direction) | $f_{b_x} = \frac{M_x}{S}$ | (140*12)/117 = 14.4 |
| Flexural stress ($y$-direction) | $f_{b_y} = \frac{M_y}{S}$ | (200*12)/117 = 20.6 |

### *A6.4.2 Stress Combinations*

Resultant flexural and shear stresses, $f_\alpha$, were calculated using the equation:

$$f_\alpha = \sqrt{f^2_{\alpha_x} + f^2_{\alpha_y}} \tag{A6.2}$$

where $f_{\alpha_x}$ and $f_{\alpha_y}$ are the components in the $x$-and $y$-directions, respectively. The resultant stresses are given in Table A6.10.

Table A6.10: Resultant stresses for design

| Stress component | | Value, ksi |
|---|---|---|
| Axial | $f_a$ | 0.4 |
| Flexural | $f_b$ | 25.2 |
| Shear | $f_v$ | 7.0 |

### *A6.4.2 Allowable Stresses*

To account for secondary load effects due to geometric nonlinearity, AASHTO specifies the following reduction factor for flexure (Section 1.3.3A1) for a post of constant cross-section:

$$C_A = 1 - \frac{1}{0.52}(L^2)\left(\frac{P_T + 0.38D_P}{2.46IE}\right) \tag{A6.3}$$

where $L$ is the height of the post, $P_T$ is the concentrated axial load at the top of the post, $D_P$ is the weight of the post, $I$ is the moment of inertia of the post, and $E$ is Young's modulus. For the sample post and the loads calculated earlier, the reduction factor is:

$$C_A = 1 - \frac{1}{0.52}(352.8)^2\left(\frac{7.9 + 0.38(2.0)}{2.46(30000)(1053)}\right) = 0.97 \qquad \text{(A6.4)}$$

The slenderness ratio for the post is approximately equal to $kL/r$ = 2*(29.4*12)/6.18 = 114, which is smaller than the limiting value of $\sqrt{2\pi^2 E/F_y}$ = 128, where $F_y$ = 36 ksi for A36 steel.

Checking the local buckling criteria:

1) $\left(\frac{F_y}{E}\right)\left(\frac{R}{t}\right) = \left(\frac{36}{30000}\right)\left(\frac{9}{0.5}\right) = 0.022 \le 0.063$ and the section is compact.

2) $2\left(\frac{F_y}{E}\right)\left(\frac{R}{t}\right)^{3/2} = 2\left(\frac{36}{30000}\right)\left(\frac{9}{0.5}\right)^{3/2} = 0.18 \le 0.44$ and $F_v = 0.33F_y$.

The allowable stresses calculated per AASHTO-1994 are tabulated below. A value of 1.27 was assigned to the shape factor, $K_p$, per AASHTO Table 1.3.1.B(2).

Table A6.11: Allowable stresses

| Stress Component | | AASHTO (1994) Section No. | Design Value | Value[a], ksi |
|---|---|---|---|---|
| Axial | $F_a$ | 1.4.1 B 3 | $0.52F_y - \left(\frac{0.13F_y^2}{\pi^2 E}\left(\frac{kL}{r}\right)^2\right)$ | 11.3 |
| Flexure | $F_b$ | 1.4.1 B 2 | $\frac{0.66F_yK_p}{1.27}$ | 23.8 |
| Shear | $F_v$ | 1.4.1 B 1 (Table 1.4.1 B 1) | $0.33F_y$ | 11.9 |

a. value does not include stress increase of Table A6.6.

## A6.5 Steel Design

### *A6.5.1 Cantilever Post*

The governing design equation for the post is given in AASHTO Section 1.2.3A as:

$$CSR = \frac{f_a}{F_a} + \frac{f_b}{C_A F_b} + \left(\frac{f_v}{F_v}\right)^2 \le 1.0 \qquad \text{(A6.5)}$$

where $F_y$ is the yield stress, $F_b$ is the allowable flexural stress, $F_v$ is the allowable shear stress, and all other terms are defined above. Substituting values for the applied and allowable stresses and including the 1.4

increase in the allowable stress under *DL+WL* (see Table A6.6) gives:

$$CSR = \frac{0.4}{11.3(1.4)} + \frac{25.2}{0.97(23.8)(1.4)} + \left(\frac{7}{11.9(1.4)}\right)^2 = 0.98 < 1.0 \qquad \text{(A6.6)}$$

The 18 in. OD post is satisfactory for the assumed loading, geometry, and material properties, as judged by the use of the AASHTO procedure.

### *A6.5.2 Design of Welded Post-to-Base Plate Connection*

AASHTO (1994) Section 1.4.2 specifies that weldments satisfy the requirements of AWS D1.1 (AWS, 1996) for the post-to-base plate connection. The Specifications require the use of either a full-penetration weld or a socket type of joint utilizing two fillet welds.

### *A6.5.3 Deflection*

For cantilever support for sign structures, AASHTO-1994 (Section 1.9.1B) specifies that deflections need only be calculated for Group I loads (see Table A6.4), and that: i) the angular deflection of the top of the post due to effect of eccentric loads of horizontal arms and their appurtenances must be less than 1.7 degrees (3 percent rad.) and ii) the horizontal linear deflection of the post due to transverse loads from overhead cables must be less than 2.5 percent of the structure height. For the CMS structures, only the first limit applies. For a 29.4 ft tall post, from Table A6.4 and Figure A6.3, the applied moment is:

$$M = (1.7(19.5) + 4.8(19.75) + 0.2(8) + 1.2(4))12 = 1612 \text{ k-in} \qquad \text{(A6.7)}$$

and $V = 0$ (no overhead cables). The rotation and deflection at the tip may be computed as follows:

$$\begin{bmatrix} \theta \\ \frac{v}{L} \end{bmatrix} = \frac{L}{6IE}\begin{bmatrix} 6 & 3 \\ 3 & 2 \end{bmatrix}\begin{bmatrix} M \\ VL \end{bmatrix} = \frac{352.8}{6(1053)(30000)}\begin{bmatrix} 6 & 3 \\ 3 & 2 \end{bmatrix}\begin{bmatrix} 1612 \\ 0 \end{bmatrix} = \begin{bmatrix} 0.018 \\ 0.009 \end{bmatrix} \qquad \text{(A6.8)}$$

where $\theta$ is the angular deflection at the top of the post in radian, $v/L$ is the drift ratio, and other terms are defined above. The computed tip rotation of 1.8 percent radian is smaller than the limiting value of 3 percent radian.

## A6.6 Vibration and Fatigue

### *A6.6.1 Vortex Shedding*

AASHTO-1994 notes that sign structures subjected to wind loading may be affected by vortex shedding. The resonance will occur at a wind velocity of:

$$V_c = \frac{f_n d}{S_n} \tag{A6.9}$$

where $f_n$ is the frequency of the structure, $d$ is the dimension (in ft), and $S_n$ is the Strouhal number. For circular cross sections, the Strouhal number is given as 0.18. The fundamental vibration frequency of the sign structure is assumed to be 1.0 Hz. (Winter, 1996), $d$ = 18 in., and $V_c$ = 8.3 ft/sec (6 mph). The non-gusting wind pressure, $p$, is equal to:

$$p = 0.00256(V)^2 C_D C_H \tag{A6.10}$$

$$p = 0.00256(6)^2(0.45)(1.10) = 0.046 \text{ lb/ft}^2 \tag{A6.11}$$

The equivalent transverse wind pressure, $p_t$, causing the oscillations is calculated as:

$$p_t = \frac{p}{2\beta} \tag{A6.12}$$

where $p$ is the non-gusting wind pressure, and $\beta$ is the damping of the sign structure (assumed to be 0.5 percent of critical). The transverse wind pressure is equal to:

$$p_t = 4.6 \text{ lb/ft}^2 \tag{A6.13}$$

Assuming a linear variation of equivalent pressure up the height of the post, the resultant force $Q$ is 0.20 kips acting 19.6 ft above the base of the post. The bending moment at the base of the post due to the equivalent transverse wind pressure is:

$$M = 0.20(19.6)12 = 47 \text{ k-in} \tag{A6.14}$$

and the maximum bending stress in the post is:

$$\sigma = \frac{M}{S} = \frac{47}{117} = 0.40 \text{ ksi} \tag{A6.15}$$

### *A6.6.2 Fatigue*

AASHTO-1994 Specifications recommend that the stress calculation for fatigue life follow the AASHTO Standard Specifications for Highway Bridges (AASHTO, 1992). The guidelines suggests that sound practice in designing traffic-signal structures should be based on the infinite fatigue life of the materials comprising the structure. For steel components, AASHTO-1994 Section 1.9.6B identifies this as the two-million cycle failure stress.

The design wind pressure for fatigue stress calculation for a single pole-type support is $p_t$ from Equation A6.8, that is, 4.6 lb/ft$^2$. The maximum bending stress ($=\sigma$) in the post is 0.40 ksi, and the corresponding stress range ($=2\sigma$) is 0.80 ksi.

For CMS structures, the full-penetration welded connection at the base of the post is classified as Category E' with an infinite fatigue life for a stress range less than 2.6 ksi (18 MPa). This stress range exceeds the value of 0.80 ksi calculated for the vertical post.

## EERC REPORTS

EERC reports are available from the National Information Service for Earthquake Engineering (NISEE) and from the National Technical Information Service (NTIS). To order EERC Reports, please contact the Earthquake Engineering Research Center, 1301 S. 46th Street, Richmond, California 94804-4698, ph 510-231-9468.

**UCB/EERC-97/10:** Fatigue Life Evaluation of Changeable Message Sign Structures, by Gilani, A.M., Chavez, J.W., and Whittaker, A.S., November, 1997. $20

**UCB/EERC-97/09:** Second U.S.-Japan Workshop on Seismic Retrofit of Bridges, edited by K. Kawashima and S.A. Mahin, September, 1997. $57

**UCB/EERC-97/08:** Implications of the Landers and Big Bear Earthquakes on Earthquake Resistant Design of Structures, by Anderson, J.C. and Bertero, V.V., July 1997. $20

**UCB/EERC-97/07:** Analysis of the Nonlinear Response of Structures Supported on Pile Foundations, by Badoni, D. and Makris, N., July 1997. $20

**UCB/EERC-97/06:** Executive Summary on: Phase 3: Evaluation and Retrofitting of Multilevel and Multiple-Column Structures -- An Analytical, Experimental, and Conceptual Study of Retrofitting Needs and Methods, by Mahin, S.A., Fenves, G.L., Filippou, F.C., Moehle, J.P., Thewalt, C.R., May, 1997. $20

**UCB/EERC-97/05:** The EERC-CUREe Symposium to Honor Vitelmo V. Bertero, February 1997. $26

**UCB/EERC-97/04:** Design and Evaluation of Reinforced Concrete Bridges for Seismic Resistance, by Aschheim, M., Moehle, J.P. and Mahin, S.A., March 1997. $26

**UCB/EERC-97/03:** U.S.-Japan Workshop on Cooperative Research for Mitigation of Urban Earthquake Disasters: Learning from Kobe and Northridge -- Recommendations and Resolutions, by Mahin, S., Okada, T., Shinozuka, M. and Toki, K., February 1997. $15

**UCB/EERC-97/02:** Multiple Support Response Spectrum Analysis of Bridges Including the Site-Response Effect & MSRS Code, by Der Kiureghian, A., Keshishian, P. and Hakobian, A., February 1997. $20

**UCB/EERC-97/01:** Analysis of Soil-Structure Interaction Effects on Building Response from Earthquake Strong Motion Recordings at 58 Sites, by Stewart, J.P. and Stewart, A.F., February 1997. $57

**UCB/EERC-96/05:** Application of Dog Bones for Improvement of Seismic Behavior of Steel Connections, by Popov, E.P., Blondet, M. and Stepanov, L., June 1996. $13

**UCB/EERC-96/04:** Experimental and Analytical Studies of Base Isolation Applications for Low-Cost Housing, by Taniwangsa, W. and Kelly, J.M., July 1996. $20

**UCB/EERC-96/03:** Experimental and Analytical Evaluation of a Retrofit Double-Deck Viaduct Structure: Part I of II, by Zayati, F., Mahin, S. A. and Moehle, J. P., June 1996. $33

**UCB/EERC-96/02:** Field Testing of Bridge Design and Retrofit Concepts. Part 2 of 2: Experimental and Analytical Studies of the Mt. Diablo Blvd. Bridge, by Gilani, A.S., Chavez, J.W. and Fenves, G.L., June 1996. $20

**UCB/EERC-96/01:** Earthquake Engineering Research at Berkeley -- 1996: Papers Presented at the 11th World Conference on Earthquake Engineering, by EERC, May 1996. $26

**UCB/EERC-95/14:** Field Testing of Bridge Design and Retrofit Concepts. Part 1 of 2: Field Testing and Dynamic Analysis of a Four-Span Seismically Isolated Viaduct in Walnut Creek, California, by Gilani, A.S., Mahin, S.A., Fenves, G.L., Aiken, I.D. and Chavez, J.W., December 1995. $26

**UCB/EERC-95/13:** Experimental and Analytical Studies of Steel Connections and Energy Dissipators, by Yang, T.-S. and Popov, E.P., December 1995. $26

**UCB/EERC-95/12:** Natural Rubber Isolation Systems for Earthquake Protection of Low-Cost Buildings, by

Taniwangsa, W., Clark, P. and Kelly, J.M., June 1996. $20

**UCB/EERC-95/11:** Studies in Steel Moment Resisting Beam-to-Column Connections for Seismic-Resistant Design, by Blackman, B. and Popov, E.P., October 1995, PB96-143243. $20

**UCB/EERC-95/10:** Seismological and Engineering Aspects of the 1995 Hyogoken-Nanbu (Kobe) Earthquake, by EERC, November 1995. $26

**UCB/EERC-95/09:** Seismic Behavior and Retrofit of Older Reinforced Concrete Bridge T-Joints, by Lowes, L.N. and Moehle, J.P., September 1995, PB96-159850. $20

**UCB/EERC-95/08:** Behavior of Pre-Northridge Moment Resisting Steel Connections, by Yang, T.-S. and Popov, E.P., August 1995, PB96-143177. $15

**UCB/EERC-95/07:** Earthquake Analysis and Response of Concrete Arch Dams, by Tan, H. and Chopra, A.K., August 1995, PB96-143185. $20

**UCB/EERC-95/06:** Seismic Rehabilitation of Framed Buildings Infilled with Unreinforced Masonry Walls Using Post-Tensioned Steel Braces, by Teran-Gilmore, A., Bertero, V.V. and Youssef, N., June 1995, PB96-143136. $26

**UCB/EERC-95/05:** Final Report on the International Workshop on the Use of Rubber-Based Bearings for the Earthquake Protection of Buildings, by Kelly, J.M., May 1995. $20

**UCB/EERC-95/04:** Earthquake Hazard Reduction in Historical Buildings Using Seismic Isolation, by Garevski, M., June 1995. $15

**UCB/EERC-95/03:** Upgrading Bridge Outrigger Knee Joint Systems, by Stojadinovic, B. and Thewalt, C.R., June 1995, PB95-269338. $20

**UCB/EERC-95/02:** The Attenuation of Strong Ground Motion Displacements, by Gregor, N.J., June 1995, PB95-269346. $26

**UCB/EERC-95/01:** Geotechnical Reconnaissance of the Effects of the January 17, 1995, Hyogoken-Nanbu Earthquake, Japan, August 1995, PB96-143300. $26

**UCB/EERC-94/12:** Response of the Northwest Connector in the Landers and Big Bear Earthquakes, by Fenves, G.L. and Desroches, R., December 1994. $20

**UCB/EERC-94/11:** Earthquake Analysis and Response of Two-Level Viaducts, by Singh, S.P. and Fenves, G.L., October 1994, PB96-133756 (A09). $20

**UCB/EERC-94/10:** Manual for Menshin Design of Highway Bridges: Ministry of Construction, Japan, by Sugita, H. and Mahin, S., August 1994, PB95-192100(A08). $20

**UCB/EERC-94/09:** Performance of Steel Building Structures During the Northridge Earthquake, by Bertero, V.V., Anderson, J.C. and Krawinkler, H., August 1994, PB95-112025(A10). $26

**UCB/EERC-94/08:** Preliminary Report on the Principal Geotechnical Aspects of the January 17, 1994 Northridge Earthquake, by Stewart, J.P., Bray, J.D., Seed, R.B. and Sitar, N., June 1994, PB94203635(A12). $26

**UCB/EERC-94/07:** Accidental and Natural Torsion in Earthquake Response and Design of Buildings, by De la Llera, J.C. and Chopra, A.K., June 1994, PB94-203627(A14). $33

**UCB/EERC-94/05:** Seismic Response of Steep Natural Slopes, by Sitar, N. and Ashford, S.A., May 1994, PB94-203643(A10). $26

**UCB/EERC-94/04:** Insitu Test Results from Four Loma Prieta Earthquake Liquefaction Sites: SPT, CPT, DMT and Shear Wave Velocity, by Mitchell, J.K., Lodge, A.L., Coutinho, R.Q., Kayen, R.E., Seed, R.B., Nishio, S. and Stokoe II, K.H., April 1994, PB94-190089(A09). $20

**UCB/EERC-94/03:** The Influence of Plate Flexibility on the Buckling Load of Elastomeric Isolators, by Kelly, J.M., March 1994, PB95-192134(A04). $15

**UCB/EERC-94/02:** Energy Dissipation with Slotted Bolted Connections, by Grigorian, C.E. and Popov, E.P., February 1994, PB94-164605. $26

**UCB/EERC-94/01:** Preliminary Report on the Seismological and Engineering Aspects of the January 17, 1994 Northridge Earthquake, by EERC, January 1994, (PB94 157 666/AS)A05. $15

**UCB/EERC-93/13:** On the Analysis of Structures with Energy Dissipating Restraints, by Inaudi, J.A., Nims, D.K. and Kelly, J.M., December 1993, PB94-203619(A07). $20

**UCB/EERC-93/12:** Synthesized Strong Ground Motions for the Seismic Condition Assessment of the Eastern Portion of the San Francisco Bay Bridge, by Bolt, B.A. and Gregor, N.J., December 1993, PB94-165842(A10). $26

**UCB/EERC-93/11:** Nonlinear Homogeneous Dynamical Systems, by Inaudi, J.A. and Kelly, J.M., October 1995. $20

**UCB/EERC-93/09:** A Methodology for Design of Viscoelastic Dampers in Earthquake-Resistant Structures, by Abbas, H. and Kelly, J.M., November 1993, PB94-190071(A10). $26

**UCB/EERC-93/08:** Model for Anchored Reinforcing Bars under Seismic Excitations, by Monti, G., Spacone, E. and Filippou, F.C., December 1993, PB95-192183(A05). $15

**UCB/EERC-93/07:** Earthquake Analysis and Response of Concrete Gravity Dams Including Base Sliding, by Chavez, J.W. and Fenves, G.L., December 1993, (PB94 157 658/AS)A10. $26

**UCB/EERC-93/06:** On the Analysis of Structures with Viscoelastic Dampers, by Inaudi, J.A., Zambrano, A. and Kelly, J.M., August 1993, PB94-165867(A06). $20

**UCB/EERC-93/05:** Multiple-Support Response Spectrum Analysis of the Golden Gate Bridge, by Nakamura, Y., Der Kiureghian, A. and Liu, D., May 1993, (PB93 221 752)A05. $15

**UCB/EERC-93/04:** Seismic Performance of a 30-Story Building Located on Soft Soil and Designed According to UBC 1991, by Teran-Gilmore, A. and Bertero, V.V., 1993, (PB93 221 703)A17. $33

**UCB/EERC-93/03:** An Experimental Study of Flat-Plate Structures under Vertical and Lateral Loads, by Hwang, S.-H. and Moehle, J.P., February 1993, (PB94 157 690/AS)A13. $26

**UCB/EERC-93/02:** Evaluation of an Active Variable-Damping-Structure, by Polak, E., Meeker, G., Yamada, K. and Kurata, N., 1993, (PB93 221 711)A05. $15

**UCB/EERC-92/18:** Dynamic Analysis of Nonlinear Structures using State-Space Formulation and Partitioned Integration Schemes, by Inaudi, J.A. and De la Llera, J.C., December 1992, (PB94 117 702/AS/A05. $15

**UCB/EERC-92/17:** Performance of Tall Buildings During the 1985 Mexico Earthquakes, by Teran-Gilmore, A. and Bertero, V.V., December 1992, (PB93 221 737)A11. $26

**UCB/EERC-92/16:** Tall Reinforced Concrete Buildings: Conceptual Earthquake-Resistant Design Methodology, by Bertero, R.D. and Bertero, V.V., December 1992, (PB93 221 695)A12. $26

**UCB/EERC-92/15:** A Friction Mass Damper for Vibration Control, by Inaudi, J.A. and Kelly, J.M., October 1992, (PB93 221 745)A04. $15

**UCB/EERC-92/14:** Earthquake Risk and Insurance, by Brillinger, D.R., October 1992, (PB93 223 352)A03.

**UCB/EERC-92/13:** Earthquake Engineering Research at Berkeley - 1992, by EERC, October 1992, PB93-223709(A10). $13

**UCB/EERC-92/12:** Application of a Mass Damping System to Bridge Structures, by Hasegawa, K. and Kelly, J.M., August 1992, (PB93 221 786)A06. $26

**UCB/EERC-92/11:** Mechanical Characteristics of Neoprene Isolation Bearings, by Kelly, J.M. and Quiroz, E., August 1992, (PB93 221 729)A07. $20

**UCB/EERC-92/10:** Slotted Bolted Connection Energy Dissipators, by Grigorian, C.E., Yang, T.-S. and Popov, E.P., July 1992, (PB92 120 285)A03. $20

**UCB/EERC-92/09:** Evaluation of Code Accidental-Torsion Provisions Using Earthquake Records from Three Nominally Symmetric-Plan Buildings, by De la Llera, J.C. and Chopra, A.K., September 1992, (PB94 117 611)A08. $13

**UCB/EERC-92/08:** Nonlinear Static and Dynamic Analysis of Reinforced Concrete Subassemblages, by Filippou, F.C., D'Ambrisi, A. and Issa, A., August, 1992. $20

**UCB/EERC-92/07:** A Beam Element for Seismic Damage Analysis, by Spacone, E., Ciampi, V. and Filippou, F.C., August 1992, (PB95-192126)A06. $20

**UCB/EERC-92/06:** Seismic Behavior and Design of Semi-Rigid Steel Frames, by Nader, M.N. and Astaneh-Asl, A., May 1992, PB93-221760(A17). $33

**UCB/EERC-92/05:** Parameter Study of Joint Opening Effects on Earthquake Response of Arch Dams, by

Fenves, G.L., Mojtahedi, S. and Reimer, R.B., April 1992, (PB93 120 301)A04. $15

**UCB/EERC-92/04:** Shear Strength and Deformability of RC Bridge Columns Subjected to Inelastic Cyclic Displacements, by Aschheim, M. and Moehle, J.P., March 1992, (PB93 120 327)A06. $20

**UCB/EERC-92/03:** Models for Nonlinear Earthquake Analysis of Brick Masonry Buildings, by Mengi, Y., McNiven, H.D. and Tanrikulu, A.K., March 1992, (PB93 120 293)A08. $20

**UCB/EERC-92/02:** Response of the Dumbarton Bridge in the Loma Prieta Earthquake, by Fenves, G.L., Filippou, F.C. and Sze, D.T., January 1992, (PB93 120 319)A09. $20

**UCB/EERC-92/01:** Studies of a 49-Story Instrumented Steel Structure Shaken During the Loma Prieta Earthquake, by Chen, C.-C., Bonowitz, D. and Astaneh-Asl, A., February 1992, (PB93 221 778)A08. $20

**UCB/EERC-91/18:** Investigation of the Seismic Response of a Lightly-Damped Torsionally-Coupled Building, by Boroschek, R. and Mahin, S.A., December 1991, (PB93 120 335)A13. $26

**UCB/EERC-91/17:** A Fiber Beam-Column Element for Seismic Response Analysis of Reinforced Concrete Structures, by Taucer, F., Spacone, E. and Filippou, F.C., December 1991, (PB94 117 629AS)A07. $20

**UCB/EERC-91/16:** Evaluation of the Seismic Performance of a Thirty-Story RC Building, by Anderson, J.C., Miranda, E., Bertero, V.V. and The Kajima Project Research Team, July 1991, (PB93 114 841)A12. $26

**UCB/EERC-91/15:** Design Guidelines for Ductility and Drift Limits: Review of State-of-the-Practice and State-of-the-Art in Ductility and Drift-Based Earthquake-Resistant Design of Buildings, by Bertero, V.V., Anderson, J.C., Krawinkler, H., Miranda, E. and The CUREe and The Kajima Research Teams, July 1991, (PB93 120 269)A08. $20

**UCB/EERC-91/14:** Cyclic Response of RC Beam-Column Knee Joints: Test and Retrofit, by Mazzoni, S., Moehle, J.P. and Thewalt, C.R., October 1991, (PB93 120 277)A03. $13

**UCB/EERC-91/13:** Shaking Table - Structure Interaction, by Rinawi, A.M. and Clough, R.W., October 1991, (PB93 114 917)A13. $26

**UCB/EERC-91/12:** Performance of Improved Ground During the Loma Prieta Earthquake, by Mitchell, J.K. and Wentz, Jr., F.J., October 1991, (PB93 114 791)A06. $20

**UCB/EERC-91/11:** Seismic Performance of an Instrumented Six-Story Steel Building, by Anderson, J.C. and Bertero, V.V., November 1991, (PB93 114 809)A07. $20

**UCB/EERC-91/10:** Evaluation of Seismic Performance of a Ten-Story RC Building During the Whittier Narrows Earthquake, by Miranda, E. and Bertero, V.V., October 1991, (PB93 114 783)A06. $20

**UCB/EERC-91/09:** A Preliminary Study on Energy Dissipating Cladding-to-Frame Connections, by Cohen, J.M. and Powell, G.H., September 1991, (PB93 114 510)A05. $15

**UCB/EERC-91/08:** A Response Spectrum Method for Multiple-Support Seismic Excitations, by Der Kiureghian, A. and Neuenhofer, A., August 1991, (PB93 114 536)A04. $15

**UCB/EERC-91/07:** Estimation of Seismic Source Processes Using Strong Motion Array Data, by Chiou, S.-J., July 1991, (PB93 114 551/AS)A08. $20

**UCB/EERC-91/06:** Computation of Spatially Varying Ground Motion and Foundation-Rock Impedance Matrices for Seismic Analysis of Arch Dams, by Zhang, L. and Chopra, A.K., May 1991, (PB93 114 825)A07. $20

**UCB/EERC-91/05:** Base Sliding Response of Concrete Gravity Dams to Earthquakes, by Chopra, A.K. and Zhang, L., May 1991, (PB93 114 544/AS)A05. $15

**UCB/EERC-91/04:** Dynamic and Failure Characteristics of Bridgestone Isolation Bearings, by Kelly, J.M., April 1991, (PB93 114 528)A05. $15

**UCB/EERC-91/03:** A Long-Period Isolation System Using Low-Modulus High-Damping Isolators for Nuclear Facilities at Soft-Soil Sites, by Kelly, J.M., March 1991, (PB93 114 577/AS)A10. $26

**UCB/EERC-91/02:** Displacement Design Approach for Reinforced Concrete Structures Subjected to

Earthquakes, by Qi, X. and Moehle, J.P., January 1991, (PB93 114 569/AS)A09. $20

**UCB/EERC-90/21:** Observations and Implications of Tests on the Cypress Street Viaduct Test Structure, by Bollo, M., Mahin, S.A., Moehle, J.P., Stephen, R.M. and Qi, X., December 1990, (PB93 114 775)A13. $26

**UCB/EERC-90/20:** Seismic Response Evaluation of an Instrumented Six Story Steel Building, by Shen, J.-H. and Astaneh-Asl, A., December 1990, (PB91 229 294/AS)A04. $15

**UCB/EERC-90/19:** Cyclic Behavior of Steel Top-and-Bottom Plate Moment Connections, by Harriott, J.D. and Astaneh-Asl, A., August 1990, (PB91 229 260/AS)A05. $15

**UCB/EERC-90/18:** Material Characterization of Elastomers used in Earthquake Base Isolation, by Papoulia, K.D. and Kelly, J.M., 1990, PB94-190063(A08). $15

**UCB/EERC-90/17:** Behavior of Peak Values and Spectral Ordinates of Near-Source Strong Ground-Motion over a Dense Array, by Niazi, M., June 1990, (PB93 114 833)A07. $20

**UCB/EERC-90/14:** Inelastic Seismic Response of One-Story, Asymmetric-Plan Systems, by Goel, R.K. and Chopra, A.K., October 1990, (PB93 114 767)A11. $26

**UCB/EERC-90/13:** The Effects of Tectonic Movements on Stresses and Deformations in Earth Embankments, by Bray, J. D., Seed, R. B. and Seed, H. B., September 1989, PB92-192996(A18). $39

**UCB/EERC-90/12:** Effects of Torsion on the Linear and Nonlinear Seismic Response of Structures, by Sedarat, H. and Bertero, V.V., September 1989, (PB92 193 002/AS)A15. $33

**UCB/EERC-90/11:** Seismic Hazard Analysis: Improved Models, Uncertainties and Sensitivities, by Araya, R. and Der Kiureghian, A., March 1988, PB92-193010(A08). $20

**UCB/EERC-90/10:** Experimental Testing of the Resilient-Friction Base Isolation System, by Clark, P.W. and Kelly, J.M., July 1990, (PB92 143 072)A08. $20

**UCB/EERC-90/09:** Influence of the Earthquake Ground Motion Process and Structural Properties on Response Characteristics of Simple Structures, by Conte, J.P., Pister, K.S. and Mahin, S.A., July 1990, (PB92 143 064)A15. $33

**UCB/EERC-90/08:** Soil Conditions and Earthquake Hazard Mitigation in the Marina District of San Francisco, by Mitchell, J.K., Masood, T., Kayen, R.E. and Seed, R.B., May 1990, (PB 193 267/AS)A04. $15

**UCB/EERC-90/07:** A Unified Earthquake-Resistant Design Method for Steel Frames Using ARMA Models, by Takewaki, I., Conte, J.P., Mahin, S.A. and Pister, K.S., June 1990, PB92-192947(A06). $15

**UCB/EERC-90/05:** Preliminary Report on the Principal Geotechnical Aspects of the October 17, 1989 Loma Prieta Earthquake, by Seed, R.B., Dickenson, S.E., Riemer, M.F., Bray, J.D., Sitar, N., Mitchell, J.K., Idriss, I.M., Kayen, R.E., Kropp, A., Harder, L.F., Jr. and Power, M.S., April 1990, (PB 192 970)A08. $20

**UCB/EERC-90/03:** Earthquake Simulator Testing and Analytical Studies of Two Energy-Absorbing Systems for Multistory Structures, by Aiken, I.D. and Kelly, J.M., October 1990, (PB92 192 988)A13. $26

**UCB/EERC-90/02:** Javid's Paradox: The Influence of Preform on the Modes of Vibrating Beams, by Kelly, J.M., Sackman, J.L. and Javid, A., May 1990, (PB91 217 943/AS)A03. $13

**UCB/EERC-89/16:** Collapse of the Cypress Street Viaduct as a Result of the Loma Prieta Earthquake, by Nims, D.K., Miranda, E., Aiken, I.D., Whittaker, A.S. and Bertero, V.V., November 1989, (PB91 217 935/AS)A05. $15

**UCB/EERC-89/15:** Experimental Studies of a Single Story Steel Structure Tested with Fixed, Semi-Rigid and Flexible Connections, by Nader, M.N. and Astaneh-Asl, A., August 1989, (PB91 229 211/AS)A10. $26

**UCB/EERC-89/14:** Preliminary Report on the Seismological and Engineering Aspects of the October 17, 1989 Santa Cruz (Loma Prieta) Earthquake, by EERC, October 1989, (PB92 139 682/AS)A04. $15

**UCB/EERC-89/13:** Mechanics of Low Shape Factor Elastomeric Seismic Isolation Bearings, by Aiken, I.D.,

Kelly, J.M. and Tajirian, F.F., November 1989, (PB92 139 732/AS)A09. $20

**UCB/EERC-89/12:** ADAP-88: A Computer Program for Nonlinear Earthquake Analysis of Concrete Arch Dams, by Fenves, G.L., Mojtahedi, S. and Reimer, R.B., September 1989, (PB92 139 674/AS)A07. $20

**UCB/EERC-89/11:** Static Tilt Behavior of Unanchored Cylindrical Tanks, by Lau, D.T. and Clough, R.W., September 1989, (PB92 143 049)A10. $26

**UCB/EERC-89/10:** Measurement and Elimination of Membrane Compliance Effects in Undrained Triaxial Testing, by Nicholson, P.G., Seed, R.B. and Anwar, H., September 1989, (PB92 139 641/AS)A13. $26

**UCB/EERC-89/09:** Feasibility and Performance Studies on Improving the Earthquake Resistance of New and Existing Buildings Using the Friction Pendulum System, by Zayas, V., Low, S., Mahin, S.A. and Bozzo, L., July 1989, (PB92 143 064)A14. $33

**UCB/EERC-89/08:** Seismic Performance of Steel Moment Frames Plastically Designed by Least Squares Stress Fields, by Ohi, K. and Mahin, S.A., August 1989, (PB91 212 597)A05. $15

**UCB/EERC-89/07:** EADAP - Enhanced Arch Dam Analysis Program: Users's Manual, by Ghanaat, Y. and Clough, R.W., August 1989, (PB91 212 522)A06. $20

**UCB/EERC-89/06:** Effects of Spatial Variation of Ground Motions on Large Multiply-Supported Structures, by Hao, H., July 1989, (PB91 229 161/AS)A08. $20

**UCB/EERC-89/05:** The 1985 Chile Earthquake: An Evaluation of Structural Requirements for Bearing Wall Buildings, by Wallace, J.W. and Moehle, J.P., July 1989, (PB91 218 008/AS)A13. $26

**UCB/EERC-89/04:** Earthquake Analysis and Response of Intake-Outlet Towers, by Goyal, A. and Chopra, A.K., July 1989, (PB91 229 286/AS)A19. $39

**UCB/EERC-89/03:** Implications of Site Effects in the Mexico City Earthquake of Sept. 19, 1985 for Earthquake-Resistant Design Criteria in the San Francisco Bay Area of California, by Seed, H.B. and Sun, J.I., March 1989, (PB91 229 369/AS)A07. $20

**UCB/EERC-89/02:** Earthquake Simulator Testing of Steel Plate Added Damping and Stiffness Elements, by Whittaker, A., Bertero, V.V., Alonso, J. and Thompson, C., January 1989, (PB91 229 252/AS)A10. $26

**UCB/EERC-89/01:** Behavior of Long Links in Eccentrically Braced Frames, by Engelhardt, M.D. and Popov, E.P., January 1989, (PB92 143 056)A18. $39

**UCB/EERC-88/20:** Base Isolation in Japan, 1988, by Kelly, J.M., December 1988, (PB91 212 449)A05. $15

**UCB/EERC-88/19:** Steel Beam-Column Joints in Seismic Moment Resisting Frames, by Tsai, K.-C. and Popov, E.P., November 1988, (PB91 217 984/AS)A20. $39

**UCB/EERC-88/18:** Use of Energy as a Design Criterion in Earthquake-Resistant Design, by Uang, C.-M. and Bertero, V.V., November 1988, (PB91 210 906/AS)A04. $15

**UCB/EERC-88/17:** Earthquake Engineering Research at Berkeley - 1988, by EERC, November 1988, (PB91 210 864)A10. $26

**UCB/EERC-88/16:** Reinforced Concrete Flat Plates Under Lateral Load: An Experimental Study Including Biaxial Effects, by Pan, A. and Moehle, J.P., October 1988, (PB91 210 856)A13. $26

**UCB/EERC-88/15:** Dynamic Moduli and Damping Ratios for Cohesive Soils, by Sun, J.I., Golesorkhi, R. and Seed, H.B., August 1988, (PB91 210 922)A04. $15

**UCB/EERC-88/14:** An Experimental Study of the Behavior of Dual Steel Systems, by Whittaker, A.S., Uang, C.-M. and Bertero, V.V., September 1988, (PB91 212 712)A16. $33

**UCB/EERC-88/13:** Implications of Recorded Earthquake Ground Motions on Seismic Design of Building Structures, by Uang, C.-M. and Bertero, V.V., November 1988, (PB91 212 548)A06. $20

**UCB/EERC-88/12:** Nonlinear Analysis of Reinforced Concrete Frames Under Cyclic Load Reversals, by Filippou, F.C. and Issa, A., September 1988, (PB91 212 589)A07. $20

**UCB/EERC-88/11:** Liquefaction Potential of Sand Deposits Under Low Levels of Excitation, by Carter, D.P. and Seed, H.B., August 1988, (PB91 210 880)A15. $33

**UCB/EERC-88/10:** The Landslide at the Port of Nice on October 16, 1979, by Seed, H.B., Seed, R.B.,

Schlosser, F., Blondeau, F. and Juran, I., June 1988, (PB91 210 914)A05. $15

**UCB/EERC-88/09:** Alternatives to Standard Mode Superposition for Analysis of Non-Classically Damped Systems, by Kusainov, A.A. and Clough, R.W., June 1988, (PB91 217 992/AS)A04. $15

**UCB/EERC-88/08:** Analysis of Near-Source Waves: Separation of Wave Types Using Strong Motion Array Recordings, by Darragh, R.B., June 1988, (PB91 212 621)A08. $20

**UCB/EERC-88/07:** Theoretical and Experimental Studies of Cylindrical Water Tanks in Base-Isolated Structures, by Chalhoub, M.S. and Kelly, J.M., April 1988, (PB91 217 976/AS)A05. $15

**UCB/EERC-88/06:** DRAIN-2DX User Guide, by Allahabadi, R. and Powell, G.H., March 1988, (PB91 212 530)A12. $26

**UCB/EERC-88/05:** Experimental Evaluation of Seismic Isolation of a Nine-Story Braced Steel Frame Subject to Uplift, by Griffith, M.C., Kelly, J.M. and Aiken, I.D., May 1988, (PB91 217 968/AS)A07. $20

**UCB/EERC-88/04:** Re-evaluation of the Slide in the Lower San Fernando Dam in the Earthquake of Feb. 9, 1971, by Seed, H.B., Seed, R.B., Harder, L.F. and Jong, H.-L., April 1988, (PB91 212 456/AS)A07. $20

**UCB/EERC-88/03:** Cyclic Behavior of Steel Double Angle Connections, by Astaneh-Asl, A. and Nader, M.N., January 1988, (PB91 210 872)A05. $15

**UCB/EERC-88/02:** Experimental Evaluation of Seismic Isolation of Medium-Rise Structures Subject to Uplift, by Griffith, M.C., Kelly, J.M., Coveney, V.A. and Koh, C.G., January 1988, (PB91 217 950/AS)A09. $20

**UCB/EERC-88/01:** Seismic Behavior of Concentrically Braced Steel Frames, by Khatib, I., Mahin, S.A. and Pister, K.S., January 1988, (PB91 210 898/AS)A11. $26